ISBN: 978-94-92323-54-5

Electron-matter interaction probed with time-resolved cathodoluminescence

M. Magdalena Solà Garcia

2021

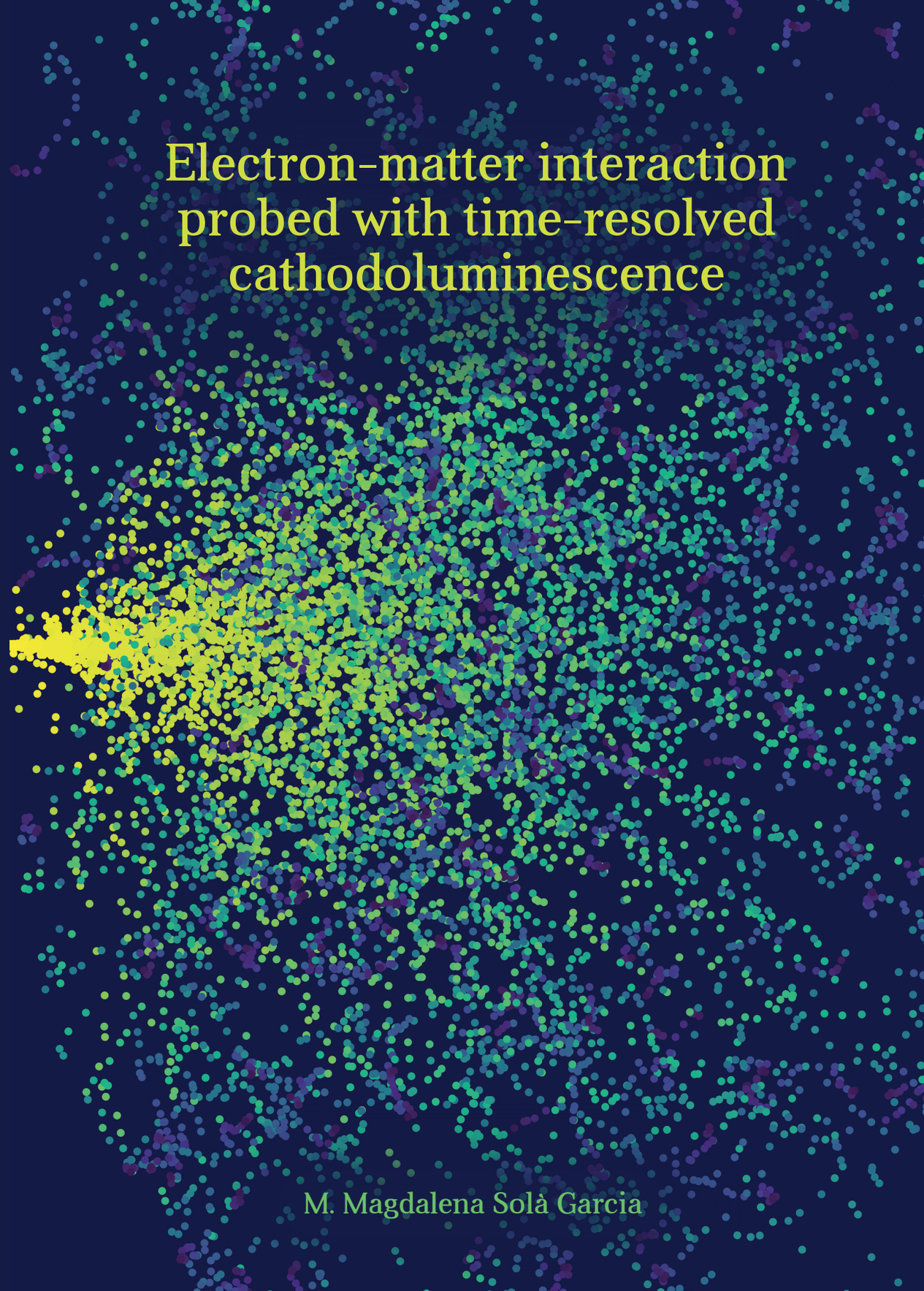

# Electron-matter interaction probed with time-resolved cathodoluminescence

M. Magdalena Solà Garcia

# ELECTRON-MATTER INTERACTION PROBED WITH TIME-RESOLVED CATHODOLUMINESCENCE

Ph.D. Thesis, University of Amsterdam, July 2021
*Electron-matter interaction probed with time-resolved cathodoluminescence*
M. Magdalena Solà Garcia

Cover: (back) Representation of a pulsed electron beam travelling in vacuum. (front) Electron cascade inside a material upon excitation with 300 electrons, adapted from simulations performed using the Casino software [1]. Each dot represents an inelastic collision of the electron with the sample and the colorscale indicates the electron energy.

ISBN 978-94-92323-54-5

The work described in this thesis was performed between August 2017 and July 2021 at AMOLF, Science Park 104, 1098 XG Amsterdam, The Netherlands.

This work is part of the Dutch Research Council (NWO). It has also been funded by the European Research Council (ERC) under the European Union's Horizon 2020 research and and innovation program (grant agreement no. 695343).

A digital version of this thesis is available at https://ir.amolf.nl.

# ELECTRON-MATTER INTERACTION PROBED WITH TIME-RESOLVED CATHODOLUMINESCENCE

ACADEMISCH PROEFSCHRIFT

ter verkrijging van de graad van doctor

aan de Universiteit van Amsterdam

op gezag van de Rector Magnificus

prof. dr. ir. K.I.J. Maex

ten overstaan van een door het College voor Promoties ingestelde commissie,

in het openbaar te verdedigen in de Agnietenkapel

op vrijdag 9 juli 2021, te 10.00 uur

door Maria Magdalena Solà Garcia

geboren te Binissalem

***Promotiecommissie***

| | | |
|---|---|---|
| *Promotor:* | prof. dr. A. Polman | Universiteit van Amsterdam |
| *Copromotor:* | dr. S. Meuret | CEMES-CNRS |
| *Overige leden:* | prof. dr. P. Schall | Universiteit van Amsterdam |
| | prof. dr. P.C.M. Planken | Universiteit van Amsterdam |
| | prof. dr. E.C. Garnett | Universiteit van Amsterdam |
| | dr. E. Alarcón Lladó | AMOLF |
| | prof. dr. R.A. Oliver | University of Cambridge |

Faculteit der Natuurwetenschappen, Wiskunde en Informatica

# CONTENTS

# 1

# INTRODUCTION

## 1.1. ELECTRON MICROSCOPY

Electron microscopy enables the study of matter down to the sub-nanometer scale. The emergence of electron microscopes has resulted in major breakthroughs in different fields of science and technology, including biology, materials science and electronics. Abbe's law, stating that the minimum distance between two points that can be resolved is directly proportional to the wavelength of the source, sets a limit for the spatial resolution of conventional optical microscopes ($\sim 200\,\text{nm}$) [2]. A broad range of optical techniques have been successfully demonstrated to overcome this limit, based on both far and near-field excitation and detection, such as stimulated emission depletion and near-field scanning optical microscopies [2–4]. Additionally, other imaging methods can be used to resolve features down to the nanoscale, including atomic force and scanning tunneling microscopy [5]. In electron microscopy, the small wavelength of the electron wavefunction ($\sim 7\,\text{pm}$ for a 30 keV electron) compared to that of light ($300-800\,\text{nm}$) results in a much larger spatial resolution than that of optical microscopes. In practice, the resolution of current electron microscopes is mainly limited by aberrations of the electromagnetic lenses and the interaction volume inside the sample, and not by the Abbe limit [6].

The first electron microscope was demonstrated in the early 1930s by E. Ruska and M. Knoll, and achieved a magnification of 17.4 [7, 8]. The first prototypes of transmission electron microscopes (TEMs) relied on the formation of an image with 50 keV electrons transmitted through a very thin specimen. Further developments by E. Ruska, M. Knoll and others resulted in higher spatial resolution, soon exceeding that of optical microscopes [8]. Figure 1.1a shows one of the first TEM images of a bacteriophage, obtained by H. Ruska in 1940 [9, 10]. However, the use of TEMs was limited to very thin samples. In order to overcome this limitation, the scanning electron microscope (SEM) was developed in the late 1930s and early

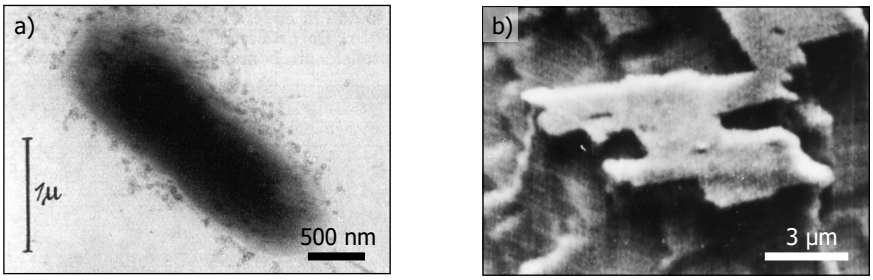


Figure 1.1: Early electron microscope images. (a) One of the first TEM images of a bacteriophage obtained by H. Ruska in 1940 [9]. Adapted from Ref. [10]. (b) SEM image of etched aluminum acquired by D. McMullan in 1952-1953 using the first commercial SEM from Cambridge Scientific Instrument (16 keV, 150 pA, 25° angle of incidence). Adapted from Ref. [11].

1940s, with initial works from M. Knoll, who first achieved a resolution of ~ 100 µm, followed by M. von Ardenne and V. Zworykin [11]. The latter reached a resolution of 50 nm [12]. Posterior improvements in the electron optics and secondary electron analysis resulted in the first commercial SEM being developed 1965 by Cambridge Scientific Instruments [12]. One of the first images obtained with such an SEM is shown in Fig. 1.1b, corresponding to etched aluminum [11]. SEMs rely on the raster scanning of a focused electron beam on a specimen and the collection of the generated secondary electrons, instead of the transmitted electrons as in TEMs. The development of SEMs enabled the study of the surface of bulk samples, thus setting a new milestone in the development of electron microscopy.

## 1.2. ANALYTICAL ELECTRON MICROSCOPY

Electron microscopes were initially developed to resolve features with a high spatial resolution, thus giving structural information about the sample. However, the interaction of electrons with a specimen results in a plethora of processes, which can be investigated to give direct access to other properties of the material.

One of the main electron-based spectroscopy techniques is electron energy loss spectroscopy (EELS), based on the quantification of the amount of energy lost by the electron when going through a (thin) sample. EELS gives information about the different inelastic scattering events that the electron undergoes in the sample, including the excitation of bulk plasmons, inner-shell electrons and vibrational modes [13]. The recent advances in monochromated EELS have enabled the study of low energy (< 10 meV) processes, including phonon spectra [14, 15]. Another analytical technique that is commonly used in electron microscopes is energy-dispersive X-ray spectroscopy (EDS), which relies on the analysis of X-ray emission. The latter originates upon excitation by the primary electron of core electrons to higher energy states, and their subsequent decay [8]. EDS is widely used for the study of chemical composition of samples with high spatial resolution.

Other analytical techniques used in combination with TEMs, including scan-

| Technique | Signal | Main applications | (S)TEM/SEM |
|---|---|---|---|
| EELS | Transmitted electrons | Multiple (see text) | (S)TEM |
| EDS | X-ray | Chemical composition | (S)TEM/SEM |
| CL | Emitted light | Optical properties | (S)TEM/SEM |
| EBSD | Back-scattered electrons | Crystal structure | SEM |
| EBIC | Induced electron current | Electrical properties | SEM |

Table 1.1: Overview of some common analytical electron microscopy techniques in both (S)TEM and SEMs.

ning transmission electron microscopes (STEMs), and SEMs are electron back-scattered detection (EBSD), electron-beam induced current (EBIC) and cathodoluminescence (CL). The latter will be further discussed below. Table 1.1 offers an overview of some common analytical techniques in electron microscopy, together with their most typical applications.

## 1.3. CATHODOLUMINESCENCE

Cathodoluminescence (CL) refers to the light emitted after excitation of a material with a high-energy electron beam. CL was initially observed in the 19$^{th}$ century, prior to the discovery of electrons, as a glow in vacuum tubes from cathode rays [16]. During the 20$^{th}$ century, CL found its technological application in cathode-ray tubes, which were widely developed as display screens. In parallel, the commercialization of electron microscopes also triggered interest in CL for the study of minerals [17] and semiconductors [18], among others [19]. Additionally, the small size of the electron probe makes CL an attractive tool to study localized excitation of plasmonic and dielectric resonances [20–24].

We can classify CL emission into two types, coherent and incoherent CL, depending on the mechanism of electron excitation and light emission [25]. When exciting a sample with high-energy electrons both types of CL emission can be present, but one typically dominates over the other, depending on the characteristics of the material [26].

### 1.3.1. INCOHERENT CATHODOLUMINESCENCE

Incoherent cathodoluminescence refers to the spontaneous emission of light after excitation of a sample with an electron beam [25]. The term 'incoherent' accounts for the fact that the emitted CL light does not exhibit a phase relation with the excitation source, that is, the time-varying electromagnetic field created by the incoming electron. Hence, incoherent CL can be considered as a similar form of light emission as photoluminescence, but using electrons instead of photons as the initial excitation source. In this case, the electron acts as a localized source of energy. Moreover, given the high energy of electrons compared to optical transitions, electron excitation enables the excitation of transitions with higher energy than in PL, with the latter typically limited by the energy of the incoming photon.

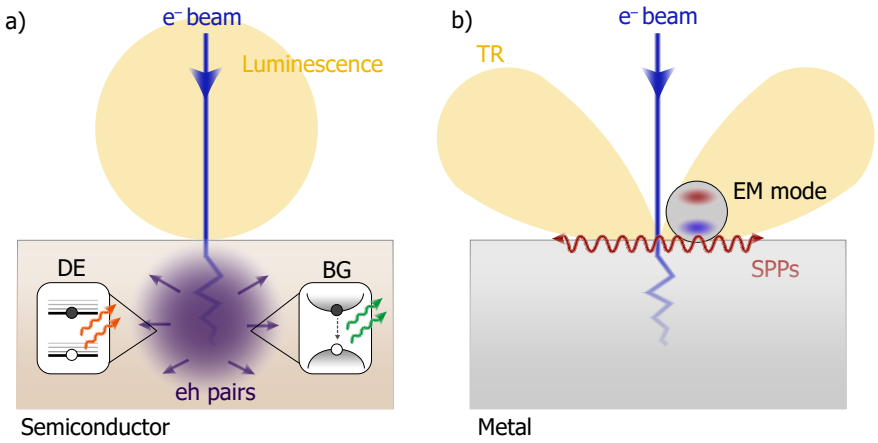


Figure 1.2: Schematic of the different mechanisms of CL emission. (a) Incoherent CL emission: in a semiconductor, the primary electron loses energy through inelastic collisions with the sample, which can result in the creation of charge carriers (eh pairs). The latter can either recombine radiatively through band-edge emission (BG) or excite an interband defect, which can decay by emitting a photon (DE). (b) Coherent CL emission: in a metal, the electron can induce transition radiation (TR), resulting from the polarization of the metal-vacuum interface, and excite surface plasmon polaritons (SPPs), among others. The electron can also excite an electromagnetic (EM) mode of a nanoparticle, for example, a plasmonic resonance.

A schematic of the mechanism of emission of incoherent CL is shown in Figure 1.2a. An electron travelling through a material undergoes multiple inelastic scattering events. One of the main forms of electron energy loss is through the excitation of bulk (or volume) plasmons. Bulk plasmons are collective excitations of valence electrons in a material, and typically have energies in the tens of eV range [13]. The deexcitation of these plasmons (on a fs timescale) results in the generation of one or more energetic charge carriers. In semiconductors, these typically thermalize to the lower energy states of the conduction band within a timescale of several hundreds of fs to ps [27–29]. The thermalized charge carriers can recombine by emitting a photon (band edge emission) or through intermediate energy states in the band gap [19]. Incoherent CL is the dominant form of CL emission in semiconductor and wide-bandgap materials. In this thesis we further explore the mechanisms resulting in the emission of incoherent CL.

### 1.3.2. COHERENT CATHODOLUMINESCENCE

In coherent CL, the emitted light maintains a phase relation with respect to the electromagnetic field of the electron [19]. Coherent CL results from the polarization of matter by the electromagnetic evanescent field of the electron, and the subsequent decay through emission of light. Fig. 1.2b shows a schematic of different processes that lead to the emission of coherent CL. One of the predominant forms of coherent CL is transition radiation (TR), which originates when an electron transits the in-

terface between two different media. This results in a polarization of the interface, and the subsequent decay through far field emission, which resembles that of a vertical point dipole [25]. Another type of coherent CL is Cherenkov radiation, which arises when an electron travels inside a material at a speed larger than the speed of light in that medium, thus allowing the transformation into far field radiation of the electron evanescent field [25]. Electrons travelling along a periodic array can also result in far field coherent radiation, a phenomenon known as the Smith-Purcell effect.

One of the major applications of coherent CL is the study of plasmonic and dielectric resonances in nanoparticles [20–24]. The evanescent field of the electron can couple to electromagnetic modes in metals and dielectric structures, and the subsequent decay is emitted in the form of coherent CL. Hence, the electron beam can be used to locally probe different resonances, thus taking advantage of the high spatial resolution given by the electrons [30] compared to optical excitation, in addition to its large spectral excitation bandwidth [31].

### 1.3.3. CL DETECTION MODALITIES

The most common method to analyze CL emission is by studying its spectrum. In this case, CL light is typically directed towards a spectrometer, thus enabling the analysis of its spectral components. CL spectroscopy is both used in incoherent CL, in which it can give valuable information about band edge recombination, the presence of defects in materials and composition of minerals, and in coherent CL, to distinguish between different resonant modes, for example. In recent years, CL analysis has developed beyond spectroscopic studies to offer more detailed information about the process of light emission.

The angular emission pattern of CL light can be studied using angle-resolved CL (ARCL). In this case, the CL beam is directly projected on a 2D detector, such that each point on the camera corresponds to a specific angle of emission [32, 33]. An optical filter is usually placed along the CL beam path to select the desired spectral range. More recently, angle-resolved CL has been extended to provide full energy-momentum (wavelength-angle) information by combining angle-resolved acquisition with spectroscopy [34, 35]. CL polarimetry has also been developed, offering information about the full polarization state of the emitted light. The technique is based on the use of a quarter-wave plate and a linear polarizer along the CL beam path, and the detection of the transmitted light using a 2D detector [36]. More recently, phase-resolved experiments have been performed. In this case, transition radiation was used as a reference field for interferometric investigation, thus enabling the extraction of the phase information of scattered surface-plasmon polaritons [37, 38].

An important feature of light emission is the temporal emission statistics, which give information about excitation and emission dynamics of emitters. Time-resolved CL (TR-CL) measurements usually require the excitation of a sample with a pulsed electron beam. Pulsed electron beams can be obtained by either blanking the electron beam or using a laser-driven electron source, as will be discussed below. In

both cases, the CL emission is guided to a sensitive detector (usually a single-photon detector) and a histogram of the decay statistics is recorded using a time correlator. The time resolution of this method is determined by the detection system, typically corresponding to tens of ps. Hence, this technique is usually suitable for the study of carrier dynamics and lifetime of emitters (for example, quantum dots or quantum wells). Additionally, the temporal information of the emitted light can be extracted by measuring the second-order autocorrelation function ($g^{(2)}(\tau)$) [39], in which two photon-counting detectors are used to record a histogram of the time delay between CL photons. In this case, the emitter lifetime can be obtained without the need of a pulsed electron beam. Moreover, $g^{(2)}(\tau)$ measurements in CL can be used to characterize bunching ($g^{(2)}(0) > 1$) and antibunching ($g^{(2)}(0) < 1$) of optical emitters [39, 40]. Photon bunching in CL occurs due to the fact that one electron can generate more than one photon, and can be used to extract the interaction probability of electrons with optical emitters [41, 42], as will be further explored in this thesis (Chapter 5).

Finally, in this thesis we introduce a new CL technique: pump-probe CL (PP-CL) microscopy, based on the combined excitation of electron and laser pulses on the sample, similar to optical pump-probe measurements. In this case, the sample is excited using either electron or laser pulses, and the resulting state is probed with laser or electron pulses, respectively. The precise control of the time delay between pump and probe beams ensures a high temporal resolution, in principle only limited by the electron pulse width (~ ps or less). Moreover, PP-CL microscopy enables fundamental studies of the dynamics of electron-matter interaction. The development of PP-CL microscopy emerges together with new developments in ultrafast electron microscopy aimed to further explore electron and matter interaction, as will be described below.

## 1.4. ULTRAFAST ELECTRON MICROSCOPY

Conventional electron microscopes allow us to image materials and nanostructures down to the nanometer scale. However, they typically offer a stationary image, without information about the dynamics of the system. Yet, many key processes that determine material properties occur at very short timescales (fs-ns regime), including charge carrier transport, chemical bond formation and molecular vibrations. Over the years, several instruments have been developed to bring the time dimension to electron microscopy, leading to the emergence of the field of ultrafast electron microscopy (UEM).

We can distinguish two different modalities to obtain time-resolved information in an UEM [43, 44]. The first, and most common one, is the stroboscopic mode [45]. It relies on the repeated excitation of a sample with electron pulses, and the collection of the signal over many ($> 10^7$) experimental cycles to achieve high enough statistics. This method can only be used to study reversible processes, given that the specimen should decay into a stationary state before the arrival of each pulse. The integration over many cycles facilitates the use of pulses containing a very low number of electrons per pulse (usually less than 1), which results in a

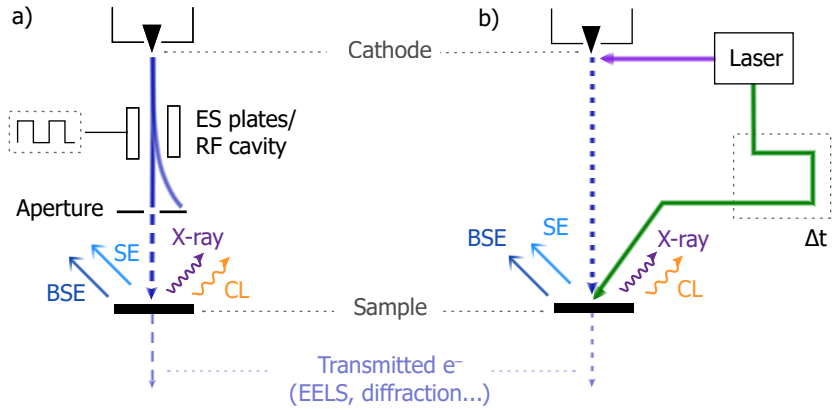


Figure 1.3: Schematic of the two main techniques to obtain a pulsed electron beam in an UEM. (a) Electron beam-blanker: the electron beam is swept over an aperture with a fixed frequency, thus resulting in a pulsed electron beam on the sample. The deflection of the beam is typically achieved by driving electrostatic (ES) plates or using a radio-frequency (RF) cavity. (c) Laser-driven electron cathode: a pulsed laser (usually with fs pulse width) is focused on the electron cathode to induce the photoemission of electron pulses. The same laser beam can be split to synchronously excite the sample at a tunable delay $\Delta t$ with respect to the electron beam, in a pump-probe fashion. In both techniques (a and b) the transmitted, secondary (SE) and back-scattered (BSE) electrons can be further analyzed, together with X-ray and cathodoluminescence (CL) emission.

high spatial and temporal resolution. In contrast, the second modality of UEM, the single-shot mode, is based on the acquisition of signal after a single electron pulse. The pulses usually contain a large number of electrons ($> 10^5$) to ensure that the collected signal is high enough. Single-shot mode can be used to study irreversible processes, but the use of dense electron pulses typically results in low spatial and temporal resolution.

There are currently two main techniques to obtain a pulsed electron beam in an UEM: electron beam blanking and the use of a laser-driven electron source [44]. Both of them can use either single-shot or stroboscopic modes, and can be applied to SEM and TEMs.

### 1.4.1. UEM WITH BEAM-BLANKING

The method of beam blanking consists in the sweeping of the electron beam across a small aperture, such that the beam is effectively cut. Figure 1.3a shows a schematic of this technique. The first realizations of beam blanking relied on the deflection of the electron beam by applying a pulsed voltage to a set of electrostatic plates, leading to temporal resolutions in the ns range [45–47]. Further developments of this technique have resulted in even higher temporal resolution, reaching electron pulse widths of a few tens of picoseconds [48, 49], mainly limited by the jitter in the electronics and rise time of the electric pulse [44]. Recently, a design has been proposed in which the plates are driven by a photoconductive switch upon laser

excitation, leading to an electron pulse width of 100 fs [50]. Alternatively, the electron beam can also be deflected using an RF cavity, resulting in a higher temporal resolution, down to 100 fs, at a fixed frequency [51, 52]. Ultrafast electron microscopes using beam blankers can achieve high spatial resolution, close to that for the continuous mode. The main loss in spatial resolution comes from the positioning of the crossover in conjugate mode and deflection of the beam across the electrostatic plates or microcavity [44, 48, 49, 53].

### 1.4.2. UEM WITH LASER-DRIVEN ELECTRON CATHODE

A key technique to obtain ultrashort electron pulses is by directly changing the way in which electrons are emitted from the electron source. To do so, a pulsed laser (usually with fs pulses) is focused on the electron cathode, resulting in the photoemission of electrons upon photon absorption. Over the years, different configurations have been proposed, using a variety of electron sources, ranging from flat cathodes to sharp nanotips, as used in conventional electron microscopes.

In order to overcome the initial ns temporal resolution of the first beam-blanker techniques, several works in the 1980s and 1990s developed laser-driven cathodes in SEM, TEMs and electron-diffraction systems [43, 54–56]. In the late 1990s, Bostanjoglo and co-workers performed several studies using single-shot UTEM, focusing on the investigation of irreversible processes such as laser-induced melting [57, 58]. In this case, two ns Nd:YAG lasers were used to excite the electron cathode in a conventional thermionic source, and the sample, respectively, achieving 200 nm spatial resolution and ~ 10 ns electron pulses. Subsequent work by LaGrange *et al.* resulted in a higher spatial resolution (~ 20 nm) for 30 ns pulses containing ~ $10^7$ electrons [59, 60].

The first UTEMs with atomic spatial resolution and femtosecond electron pulse widths were achieved by the group of Zewail in the 2000s [61, 62]. In this case, the electron cathode of the TEM, a $LaB_6$ microtip, was irradiated with fs laser pulses, and the same laser was used to synchronously excite the sample. Working in the single-electron regime, with pulses containing one or a few electrons on average, reduces Coulomb interaction between electrons, which is one of the main sources of temporal and spatial broadening of pulsed electron beams [63, 64]. In these experiments, the acquisition of signal was usually performed using the stroboscopic mode, such that many cycles of the experiment were recorded to ensure good statistics. The brightness of UTEMs was further improved by using a Schottky field emission gun (FEG) as the electron source, achieving Å spatial resolution with 200 fs electron pulse width [65]. A UTEM using a cold-FEG has also been demonstrated [66], thus enabling the development of ultrafast electron holography. These new improvements resulted in a rapid growth of applications of UTEMs over the past years [67–71] .

In parallel to the emergence of UTEMs, ultrafast SEMs (USEMS) were also developed. Following some earlier work in the 1980s [54], Merano *et al.* demonstrated an USEM to perform time-resolved CL measurements on GaAs nanostructures [72, 73]. In this case, a flat gold cathode was used, achieving temporal and

spatial resolutions of 10 ps and 50 nm, respectively. USEM with a Schottky FEG was demonstrated by Zewail and co-workers, yielding an improvement of both spatial and temporal resolution (~ 10 nm and ~ 300 fs) [74, 75]. Since then, different groups have performed time-resolved SEM studying both changes in secondary electron yield [76] and cathodoluminescence [77–81], including two commercial systems for time-resolved CL developed by Attolight and Delmic.

## 1.5. NEW DEVELOPMENTS IN UEM: PUMP-PROBE INSIDE THE ELECTRON MICROSCOPE

The fast development of ultrafast electron microscopy has opened new possibilities to perform novel experiments inside an electron microscope. As can be observed from the first works on UEM, time-resolved measurements are tightly linked to pump-probe experiments: usually a laser beam is used to bring the sample out of equilibrium, and the electron is used to probe the state at different delays with respect to the arrival of the laser pump, in a stroboscopic fashion. Combining the time resolution from UEM with the spectroscopic methods for electron microscopy presented in Table 1.1 in a pump-probe configuration brings a variety of novel techniques to study electron-matter interaction.

Some examples of applications of pump-probe UTEM include the study of the dynamics of structural changes using real and Fourier-space imaging [62, 82], chemical bond formation at the atomic scale [83], laser-induced magnetization dynamics [84] and phase transitions [85, 86]. One of the most prominent new applications of UTEM is photon-induced near-field electron microscopy (PINEM), in which the laser-induced optical fields in nanostructures are probed through the analysis of the electron energy spectrum [87–89]. In this case, the electron exhibits quantized energy gain or loss due to strong interaction between electrons and optical near fields. In USEMs, several pump-probe works have been performed to study photoinduced carrier dynamics in semiconductors [90]. In these cases, the change in secondary electron emission is investigated as a function of delay between optical pump and electron probe.

In addition to the study of material properties, the development of UEM have also attracted more interest into the study of the electron itself. Several works have demonstrated tailoring of the electron wavefunction, resulting in attosecond electron pulses [89, 91, 92], electron acceleration [93] and vortex beam formation [94, 95], among others.

## 1.6. MOTIVATION AND OUTLINE OF THE THESIS

The developments in UEM allow us to access new domains in the study material dynamics at the nanoscale. However, the interaction of electrons with matter involves many different processes, including both elastic and inelastic scattering, and coherent and incoherent excitation of the specimen. These processes occur at different timescales, ranging from fs, typical for bulk plasmon decay, up to μs, in the

case of thermal effects, for example [29, 43]. This broad range of interactions can result in complex analysis of (time-resolved) electron microscopy experiments. To take advantage of the full capabilities of the new EM developments, it is important to have an in-depth understanding of the dynamics of electron-matter interaction. In this thesis we investigate fundamental properties of the interaction between electrons and matter through the analysis of light emission (CL). We introduce pump-probe cathodoluminescence microscopy as a novel technique to study the interaction of fast electrons with matter through the absorption and emission of light. Similar to the works discussed above, in PP-CL we use electrons and light to excite the sample. In contrast to previous works, we study the light emitted by the sample, either PL or CL, thus enabling for the first time the opportunity to use the electrons as a pump, which gives new insights into electron-matter interaction.

In **Chapter 2**, we describe the design, technical implementation and full characterization of our ultrafast SEM, based on a laser-driven Schotky FEG, including the analysis of the energy, spatial and temporal resolution of the new microscope.

In **Chapter 3** we introduce the technique of pump-probe cathodoluminescence microscopy. We show the technical development of the setup, characterization and alignment procedure. We also discuss the main considerations to account for in PP-CL experiments, including a comparison between CL and PL measurements in semiconductors, and introduce the first results of PP-CL experiments on $Cu_2ZnSnS_4$.

**Chapter 4** presents the first results of PP-CL using electrons as a pump. We investigate the charge-state conversion of NV centers induced upon electron excitation, together with the back-transfer in the ms timescale, and model the state transfer dynamics using a rate equation model, from which all the characteristic timescales are derived.

Finally, in **Chapter 5** we further investigate how electrons interact with matter through the analysis of second-order autocorrelation ($g^{(2)}(\tau)$) measurements. We present a fully analytical model and experimental data of the photon emission statistics of InGaN/GaN quantum wells under different conditions. We describe the amplitude of bunching ($g^{(2)}(0)$) as a function of electron fluence, excitation probability, emitter lifetime and electron pulse width when using continuous, ns-pulsed and ultrashort pulsed electron beams.

Overall, this thesis provides new insights into electron-matter interaction through the study of cathodoluminescence, and presents a new technique to further explore electron excitation and photon emission dynamics at the nanoscale.

# 2

# ULTRAFAST SCANNING ELECTRON MICROSCOPY

*Ultrafast scanning electron microscopy (USEM), based on a laser-driven electron source, is a promising technique for the study of material dynamics at the nanoscale. While ultrafast TEMs have been widely discussed and characterized, work on ultrafast SEMs (USEM) is still limited. In this chapter we provide a full overview of a USEM based on the photoemission of electrons upon fs laser excitation of a Schottky field-emission gun. We start by discussing the fundamentals of electron emission in continuous and pulsed conditions and the main parameters involved in each process. Next, we focus on the technical aspects of our USEM, including the alignment procedure. Finally, we develop a full characterization of our setup. We present measurements of the electron energy distribution in USEM for different emission conditions and we show its dependence on the number of electrons per pulse. The energy spread ranges from 0.77 (*$<1$ *electron per pulse) to* 14.4 eV *(*$\sim 1000$ *electrons per pulse), with the latter dominated by Coulomb repulsion between electrons. We estimate an electron pulse width of* 416 fs *in the case of low number of electrons per pulse, and* 6.4 ps *for pulses containing* $\sim 1000$ *electrons. The spatial resolution (*$\sim 90$ nm*) is evaluated for different settings in the emission process and we discuss the main factors that can be lead to a higher spatial resolution.*

## 2.1. INTRODUCTION

Ultrafast electron microscopy (UEM) has emerged as a powerful tool to study material dynamics combining high temporal (typically tens or hundreds of femtoseconds) and spatial (~ nm, down to Å in TEMs) resolution [43, 96–98]. One of the main techniques to obtain a pulsed electron beam is through photoemission of electrons upon excitation of the electron cathode with femtosecond laser pulses. This method results in a high temporal resolution, similar to that of optical exper-

iments, and enables pump-probe studies, in which the same laser is used to excite the sample, while the electrons act as a probe. Some examples of works using laser-driven electron sources in TEMs are the study of the dynamics of structural changes [61, 97], phase transformations [86, 99], optical near fields [87, 89] and off-axis electron holography [100], among others. In SEMs, applications include the investigation of photoinduced carrier dynamics in semiconductors [75, 90] and time-resolved cathodoluminescence [72, 79]. Pulsed electron beams can also be obtained using a beam blanker, in which the electron beam is swept over an aperture, but typically results in lower temporal resolution ($\sim 30$ ps) [44, 49] and is less suitable for pump-probe measurements.

A complete understanding of the resolution and limitations of pulsed electron beams is critical for optimum performance of an UEM. The characterization of laser-driven sources in TEMs has been addressed in several works, in which the temporal, spatial and energy resolution was analyzed [44, 63, 65–67, 101]. The effects of Coulomb interaction (space-charge effects) are also discussed in literature, showing that the performance of UTEMs is strongly dependent on the average number of electrons per pulse [64, 102, 103]. In contrast, the literature on characterization of ultrafast SEMs (USEM) is more limited, and has mainly focused on temporal and spatial resolution [98, 104]. Even though the photoemission process is mostly dependent on the electron cathode (planar, $LaB_6$, Schottky FEG or cold-FEG), differences in the electron column between TEM and SEMs can also play a role in the characteristics of the electron pulses on the sample. Moreover, the final application of the pulsed electron beam is different in both cases, thus it is important to analyze and discuss the features of the pulsed beam specifically to SEMs.

In this chapter we provide a full characterization of an ultrafast SEM, based on a laser-driven Schottky FEG. We start by reviewing the fundamentals of electron emission in normal (continuous) and pulsed mode, and we present the technical design and development of our USEM, which is based on a commercial SEM. We operate the USEM in two different regimes, containing either a low ($< 1$) or high (up to 1000) average number of electrons per pulse. We discuss the impact of the different emission regimes and microscope settings on the energy spread of electron pulses in continuous and pulsed mode, and on the temporal and spatial resolution of the USEM.

## 2.2. CONTINUOUS EMISSION OF ELECTRONS

Before discussing the characterization of a pulsed electron source, it is important to understand the working principle of an electron source in normal conditions, that is, to obtain a continuous electron beam. Here we briefly review the main types of electron sources and characteristic features.

### 2.2.1. ELECTRON SOURCES

Standard electron microscopes, both SEM and TEMs, use micro and nanotips as electron sources. A secondary electron (SE) image of such nanotip is shown in Fig.

| | **$LaB_6$ (TE)** | **W (TE)** | **Shottky FEG** | **Cold FEG** |
|---|---|---|---|---|
| Material | $LaB_6$ | W | ZrO/W [100] | W [310] |
| $\phi$ (eV) | 2.4-2.7 | 4.5 | 2.8-2.92 | 4.25-4.5 |
| $T$ (K) | 1700 | 2700 | 1800 | 300 |
| $E_{\text{ext}}$ ($\text{Vm}^{-1}$) | - | - | $\sim 10^8$ | $> 10^9$ |
| $I_e$ (A) | $\sim 10^{-3}$ | $\sim 10^{-3}$ | $\sim 10^{-4}$ | $\sim 10^{-5}$ |
| $B$ ($\text{Am}^{-2}\,\text{sr}^{-1}$) | $\sim 10^{10}$ | $\sim 10^9$ | $\sim 10^{11} - 10^{12}$ | $\sim 10^{13} - 10^{14}$ |
| $\Delta E_0$ (eV) | 1-2 | 1.5-3 | 0.5-1 | 0.2-0.4 |
| Pressure (Pa) | $\sim 10^{-4}$ | $\sim 10^{-2}$ | $\sim 10^{-7}$ | $\sim 10^{-9}$ |

Table 2.1: Main types of electron sources with the corresponding parameters. TE refers to thermionic emission and FEG to field-emission gun. $\phi$ is the work function, $T$ is the operating temperature, $E_{\text{ext}}$ refers to the magnitude of the extractor field, $I_e$ is the total emitted current, $B$ is the brightness, $\Delta E_0$ is the energy spread and pressure refers to the vacuum pressure at which the source operates. Data extracted from refs. [8, 43].

2.1a (reproduced from [105]), corresponding to a tungsten cathode with a ZrO coating (ZrO/W), typically used in Schotkky FEGs, as will be discussed below.

There are three main types of electron sources, depending on how electrons are released from the tip: thermionic, Schottky and cold field-emission [8]. Each of them offers its own advantages and disadvantages. Table 2.1 shows an overview of the different types of electron sources and their main properties: work function ($\phi$), working temperature ($T$), amplitude of the extractor field ($E_{\text{ext}}$), emitted current ($I_e$), brightness ($B$), electron energy spread ($\Delta E_0$) and pressure at which the source operates. The work function of the material is defined as the work needed to release an electron from the material to the vacuum [106], while the brightness of an electron source is defined as

$$B = \frac{I_e}{A_s \Omega}\,. \tag{2.1}$$

Here, $I_e$ is the total current emitted by the source, $A_s$ is the emitting area and $\Omega$ is the solid angle in which electrons are emitted [8]. The brightness of a source determines the trade-off between electron current, spatial resolution and coherence of the electron beam [107].

#### THERMIONIC SOURCE

In thermionic emission, the temperature of the tip is increased through Ohmic heating, such that electrons acquire energy to overcome the work function and be released from the tip. The two main materials used for thermionic emission are $LaB_6$ and W, with work function corresponding to $2.4 - 2.7\,\text{eV}$ and $4.5\,\text{eV}$, respectively (see Table 2.1). Figure 2.1b shows the Fermi-Dirac distribution of electrons in a material for a temperature of 0 (black) and 1800 K (dark red). Here the probability that a given energy state is occupied, $f(E)$, is given on the x-axis as a function of the energy (y-axis). In the limit of 0 K, the occupation probability of any state with energy larger than the Fermi level is zero, and thus no electron emission is possible.

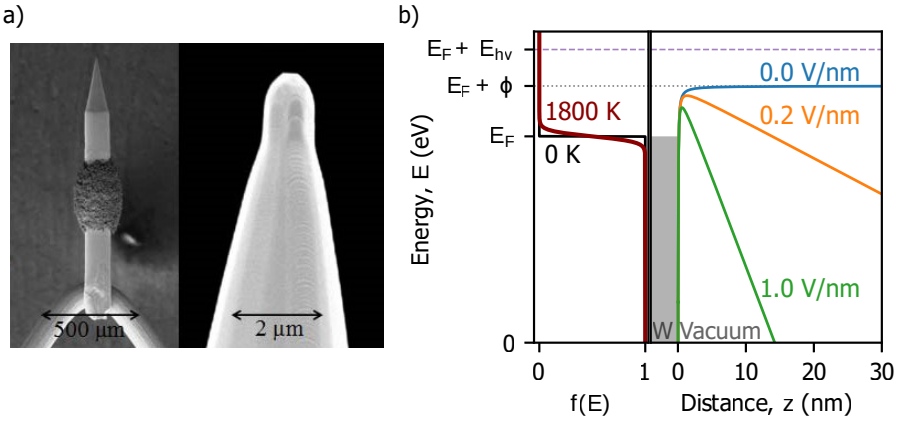


Figure 2.1: Emission of electrons from an electron cathode. (a) SE image of a typical ZrO/W nanotip, showing the ZrO reservoir (left) and the apex of the tip (right). Reproduced from [105]. (b) (left) Fermi-Dirac distribution of electrons in the electron source for different energy states at a temperature of 0 K and 1800 K. (Right) Energy barrier of an electron as a function of its distance to the surface of the tip, calculated for an applied external electric field of 0, 0.2 and 1 $\mathrm{V\,nm^{-1}}$ (blue, orange and green, respectively). $\phi$ is the work function of the tip, and $E_{h\nu}$ refers to the energy of a photon in the case of a laser-driven source.

Increasing the temperature of the tip leads to an increase of the occupation probability of higher energy states, thus allowing for emission of electrons (thermionic emission). Thermionic sources typically exhibit brightness of $10^9 - 10^{10}\,\mathrm{A\,m^{-2}\,sr^{-1}}$ and energy spreads in the $1-3$ eV range (Table 2.1).

### SCHOTTKY FEG

The energy needed for electrons to escape from the tip can be further reduced by means of the Schottky effect [107]. In this case, a positive bias voltage is applied relative to the emitter, which we will refer to as extractor voltage ($V_{\mathrm{ext}}$). The presence of an electric field ($E_{\mathrm{ext}}$) around the tip effectively lowers the energy barrier. We can describe this effect theoretically by considering the potential energy of an electron that has been released from the tip. The electron leaves a positive screening charge behind, and thus experiences a restoring force due to Coulomb attraction. The potential energy associated to this positive-negative charge configuration can be calculated by considering the work needed to bring a charge from infinity to the position $z$. Hence, the potential energy of an electron right outside of the cathode in the presence of an external electric field $E_{\mathrm{ext}}$ can be approximated as [105]

$$U_E(z) = E_F + \phi - \frac{k_e q^2}{4z} - qE_{\mathrm{ext}}z\,, \tag{2.2}$$

where $E_F$ is the Fermi energy, $\phi$ the work function of the material, $k_e$ the Coulomb constant, $q$ the electron charge and $z$ represents the distance from the surface of the electron cathode. Figure 2.1b (right) shows the potential energy of an electron

right after escaping the tip when no external voltage is applied (blue curve), as well as for $E_{ext}$ =0.2 and 1.0 $Vnm^{-1}$ (orange and green, respectively). In the absence of an external electric field , the energy barrier, defined as the difference between the maximum potential energy and the Fermi level, corresponds to the work function of the tip, and emission is purely thermionic. This barrier is lowered by 0.54 and 1.2 eV for $E_{ext}$ =0.2 and 1.0 $Vnm^{-1}$, respectively. Additionally, the energy barrier also becomes narrower for increasing extractor field, thus allowing for quantum tunnelling of electrons with energy lower than the work function.



An electron source using this combination of thermionic emission and the Schottky effect is referred to as a Schottky field-emission gun (FEG). These sources typically use a W tip with ZrO coating, which reduces the work function of the material down to ~ 2.9 eV [65, 105]. The application of high extractor fields on the nanotip of Schottky FEGs results in higher brightness than thermionic sources (~ $10^{11} - 10^{12} Am^{-2} sr^{-1}$), due to the reduced emitting area. The lower operating temperature also results in a lower electron energy spread (~ 0.5 – 1 eV), due to the reduced excess energy of the emitted electrons (Table 2.1). This type of electron source is the one used in this thesis.

#### COLD FEG

Finally, field-emission guns can also operate without heating the tip, i.e., at room temperature. In this case, the extractor field applied to the nanotip is larger than in the Schottky FEGs, and emission is possible through quantum tunneling of electrons with energy close to the Fermi energy to the vacuum [43]. This allows one to achieve a higher brightness (~ $10^{13} - 10^{14} Am^{-2} sr^{-1}$) and lower energy spread (~ 0.2 – 0.4 eV) than the sources discussed above. These features make cold-FEGs desirable for applications in scanning transmission electron microscopy, such as EELS.

### 2.2.2. GEOMETRY OF A SHOTTKY FEG

In this thesis we use an SEM equipped with a Schottky FEG source. A schematic of the Schottky FEG geometry can be seen in Figure 2.2a (top left). Here, the ZrO/W tip is surrounded by a negatively biased plate (suppressor), from which it protudes by about 250 µm. In our case, the suppressor voltage is fixed to −500 V. The presence of this negative voltage ensures that only electrons from the end of the tip can be released to the vacuum. The extractor plate, which is positively biased (4550 V), is placed at around 500 µm from the apex of the tip and has a central aperture through which electrons can go through [105]. We should note that the typical values of extractor voltage and distance between the emitter and extractor plate would lead to an extractor field much lower than the ones given in Figure 2.1b if a planar geometry of the electron source is assumed. However, the sharp apex of the tip produces an enhancement of the electric field, thus achieving a larger extractor field near the tip. The combination of extractor and suppressor voltages around the tip also has an impact on the brightness of the source, that is, the area of the tip from which electrons are emitted, and their direction. In particular, lowering the extractor volt-

age with respect to the suppressor voltage results in a decrease of the brightness, as will be discussed below. Hence, by tuning these voltages we can control how many electrons emitted away from the apex of the tip go through the extractor aperture and are thus collected [105]. Having control over it will allow us to choose between different photoemission regimes, as will be discussed below.



## 2.3. PULSED EMISSION OF ELECTRONS: LASER-DRIVEN SCHOTTKY FEG

Until now we have discussed the operation of a Schottky FEG in normal conditions, that is, to obtain a continuous electron beam. In the case of a laser-driven source, a pulsed laser beam is focused on the electron cathode and electrons are released from the tip through the photoelectric effect (photoemission). In this case, the tip is usually operated at a low temperature in order to suppress continuous emission. Hence, the energy needed to overcome the work function is provided by the photon energy instead of thermal excitation. In our case we use a laser beam with photon energy $E_{h\nu} = 4.82\,\text{eV}$ ($\lambda = 258\,\text{nm}$), which is much larger than the work function of ZrO/W (2.9 eV). Other works have demonstrated photoemission using lower photon energies, even below the ZrO/W work function, in which case the emission of electrons takes place by means of the absorption of two (or more) photons [108–110]. In the case of low photon energy and higher laser peak intensity ($I > 10^{12}\,\text{W cm}^{-2}$) [108], the emission of electrons can also take place by optical field emission, in which the light field around the tip is strong enough to allow for tunneling of electrons. Multiphoton photoemission and optical field emission are not studied in this chapter.

Using a high photon energy has some significant advantages. During a typical experiment with a cold tip, the ZrO coating cannot be replenished due to its lower diffusivity, thus leading to an increase of the work function [105]. Using high energy photons allows us to still have efficient emission of electrons even when the work function is increasing due to the consumption of the ZrO coating [74]. In our experiments, we have observed that the photoemission efficiency, that is, the average number of electrons emitted per incoming laser photon, decreases by $\sim 30\,\%$ after $\sim 90\,\text{min}$, similar to other work [76]. This can be solved by briefly heating up the tip in between experiments. An additional advantage of using high energy photons is the fact that the reduction of the energy barrier by the extractor field is no longer needed. This gives us flexibility to lower the extractor voltage to achieve different working regimes while still having emission of electrons.

## 2.4. IMPLEMENTATION OF A USEM

Next, we present the technical details related to the development of our USEM, and we discuss a procedure to align the laser on the electron cathode.

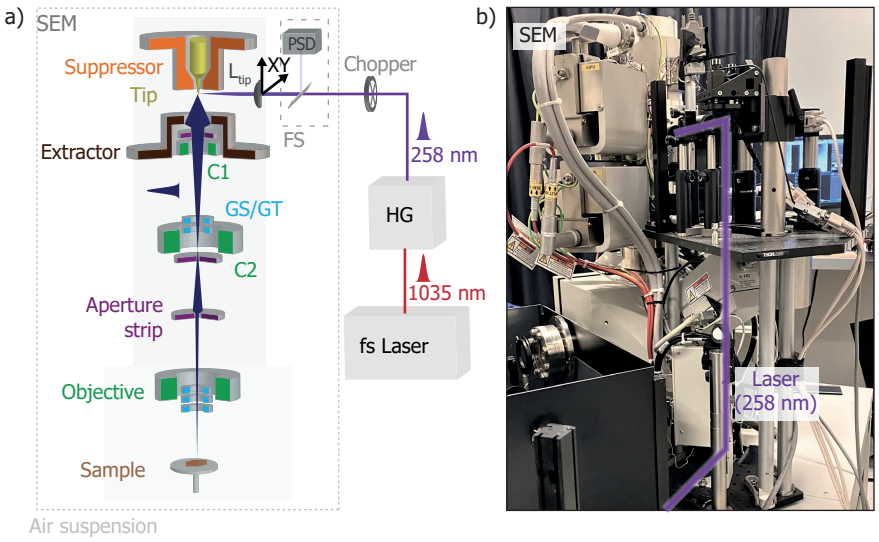


Figure 2.2: USEM based on a laser-driven Schottky FEG. a) Schematic of the setup. The 4$^{th}$ harmonic ($\lambda$ = 258 nm) of a femtosecond laser, generated through a set of BBO crystals (HG), is focused on the electron cathode of the SEM. Alignment between the laser and the microscope is kept using a feedback system (FS). The electron cathode (tip) slightly protudes from the suppressor plate (−500 V). The emission of electrons is enhanced by the extractor plate (4550 V). The electron beam is further focused along the column using two condenser lenses, $C_1$ and $C_2$, before reaching the final objective lens, which focuses the beam on the sample. GT/GS: gun tilt/shift, respectively. b) Photograph of the setup.

### 2.4.1. LASER-DRIVEN SEM SETUP

Figure 2.2 shows a schematic (a) and a photograph (b) of the setup that we use in our laser-driven electron microscope. The USEM has been developed from a standard Thermo Fisher Quanta 250 FEG SEM, with the exception of the initial measurements that used a Thermo Fisher/FEI XL30 (chapter 4). Access to the electron cathode is given through a UV-transparent window. A two-level breadboard has been attached to the electron microscope on which optical components are mounted. The breadboard configuration is thus coupled to the air suspension of the SEM, used to isolate the microscope from vibrations in the room. The alignment between this floating part of the setup and the rest of optical components, including the laser, is maintained by using an optomechanical feedback system (more details in Chapter 3, section 3.2).

We use a femtosecond laser (Clark MXR Impulse, diode-pumped Yb-doped fiber oscillator/amplifier system) providing ~ 250 fs pulses, with tunable repetition rate (200 kHz - 25.19 MHz) and wavelength output at $\lambda \simeq 1035$ nm. The fundamental laser beam is sent through a set of beta barium borate (BBO) crystals to produce the 2$^{nd}$ ($\lambda_{SH}$ = 517 nm), 3$^{rd}$ ($\lambda_{TH}$ = 345 nm) and 4$^{th}$ ($\lambda_{FH}$ = 258 nm) harmonics. The 4$^{th}$ harmonic is used for the photoemission of electron pulses. We use a beam expander composed of two lenses (focal length 10 and 50 cm, respectively) to increase

the beam size of the $4^{\text{th}}$ harmonic beam by a factor 5. The beam is guided up to the height of the electron cathode through a periscope. The top part of the periscope contains a dichroic mirror which reflects the $4^{\text{th}}$ harmonic, while transmitting at longer wavelengths. Finally, the beam is focused on the electron cathode through a lens (tip lens, $f = 12.5\,\text{mm}$) down to a $\sim 10\,\mu\text{m}$ spot. The position of the lens in the direction of the optical axis ($z$) is adjusted using a manually controlled linear stage, while the position in the transverse direction ($x$, $y$) is controlled by means of two motorized stages (PI M-227).

#### ELECTRON COLUMN

The electron column is composed of the electron gun module, containing the suppressor and extractor voltage plates, together with the tip, as discussed in section 2.2. A $\sim 350\,\mu\text{m}$-diameter aperture is placed below the extractor plate to block electrons emitted further away from the optical axis. A set of two condenser lenses, is used to change the position of the crossover the electron beam along the column, and the microscope contains a set of apertures (aperture strip, $30 - 1000\,\mu\text{m}$). The particular condenser lens voltages ($C_1$ and $C_2$) determine the fraction of the beam that goes through the aperture. Finally, an objective lens is used to focus the electron beam on the sample.

### 2.4.2. EXPERIMENTAL PROCEDURE TO FIND THE TIP

A critical step in performing time-resolved experiment with an electron microscope is the proper alignment of the laser on the electron cathode. The next sections show the typical procedure performed during the installation of the setup and prior to starting an experiment.

#### INITIAL ALIGNMENT OF THE LASER

The first alignment of the laser on the tip can be performed with the help of a CMOS camera and a set of irises. In normal operating conditions, the electron cathode is set to 1800 K and its blackbody radiation can be observed by eye. This radiation is collected by the lens in front of the SEM window ($f = 12.5\,\text{mm}$) and imaged on a CMOS camera (Thorlabs DCC1645C). In our case, we placed the CMOS camera behind the dichroic mirror from the periscope, and an achromatic lens ($f = 3\,\text{cm}$) was used to focus the light onto the camera. A photograph of the visible blackbody radiation of the tip is shown in Fig. 2.3a. This configuration allows us to roughly align the lens focus on the electron cathode. The focus is later optimized by maximizing the current emitted by the cathode, as explained below. In order to align the laser on the tip (in the transverse direction, x,y), we placed a set of two irises through which the emitted light goes. Then the laser is aligned such that it goes through the center of the irises, thus giving a rough alignment of the laser on the tip. The exact position of the laser beam with respect to the tip is optimized by scanning the lens in front of the tip with two motorized stages, as will be explained in the next section. We should note that this initial alignment procedure is only needed during the installation of the setup or after major changes in the laser beam path.

### SCANNING OF THE LENS

Once the photoemission setup is fully installed, the steps presented in the previous section can be omitted. Hence, we only need to fine-tune the position of the laser on the electron cathode within a $\sim 100 \times 100\,\mu m^2$ scanning window. It is usually desirable to start the alignment of the laser beam on the tip with a hot tip, that is, using the standard settings of the electron column. When lowering the temperature of the tip, it thermally contracts by up to a few tens of µm [105], which results in a change of the alignment of the electron beam path inside the column. Hence, starting the alignment of the laser on the cathode with a hot tip ensures an optimum collection of the photoemitted electrons. It is also helpful to optimize the parameters inside the electron column (gun tilt/shift, condenser lens voltage and aperture) for maximum collection of the electrons in continuous mode. We collect the electron current on the sample by focusing the electron beam on a Faraday cup, placed on the sample stage, which is connected to a picoammeter (Keithley 6485) or to a lock-in amplifier (Zurich Instruments MFLI, 500 kHz/5 MHz) through a current amplifier (Femto DLPCA-200). When the tip is hot (that is, working in continuous mode) most of the collected electron current comes from the continuous emission, even if the laser beam is already focused on the tip. However, modulating the $4^{th}$ harmonic laser beam using an optical chopper (Hz - kHz) (Thorlabs MC2000B-EC), which is also connected to a lock-in amplifier, allows us to discern between continuous (field-enhanced thermionic emission) and pulsed (photoemission) electron currents. Additionally, it can be helpful to further tune the parameters inside the electron column (gun tilt/shift, condenser lens voltage and aperture) in order to maximize the collection of the photoemitted electrons.

Figure 2.3b shows a measurement obtained when scanning the tip lens around the electron cathode (in the x, y plane) and collecting the electron signal from the lock-in amplifier. In this case the Schottky FEG was operating in normal conditions (1800 K, $V_{ext}$ = 4550 V), the electron beam acceleration was set to 10 kV and the continuous (background) electron current was ~ 200 nA (using a 1 mm aperture). We used a laser power ($\lambda_{FH}$ = 258 nm) of 1.6 mW at 5.04 MHz (0.3 nJ/pulse). The gain of the current amplifier was set to $10^6$ $AV^{-1}$ and the chopping frequency was 287 Hz. We observe that photoemitted current is collected even when the laser is focused more than 60 µm away from the apex of the tip. The configuration of suppressor and extractor voltage ensures that only electrons emitted from the apex of the tip can be released and go through the extractor aperture, and it is thus unlikely that electrons far from the apex (shank emission) can be efficiently released. Instead, the current observed when focusing far from the apex of tip is probably due to emission of electrons from the apex that are excited by the tail of the laser beam profile (assumed to be Gaussian).

Once the laser is aligned on the tip, we lower the temperature of the tip to suppress continuous emission. This is done by decreasing the filament current from 2.35 A to 1.7 A, resulting in a final temperature of ~ 1200 K. Figure 2.3c shows a scan of the tip lens obtained under the same conditions as in 2.3b, but at this lower temperature. Given the thermal contraction of the tip at this low temperature, here we

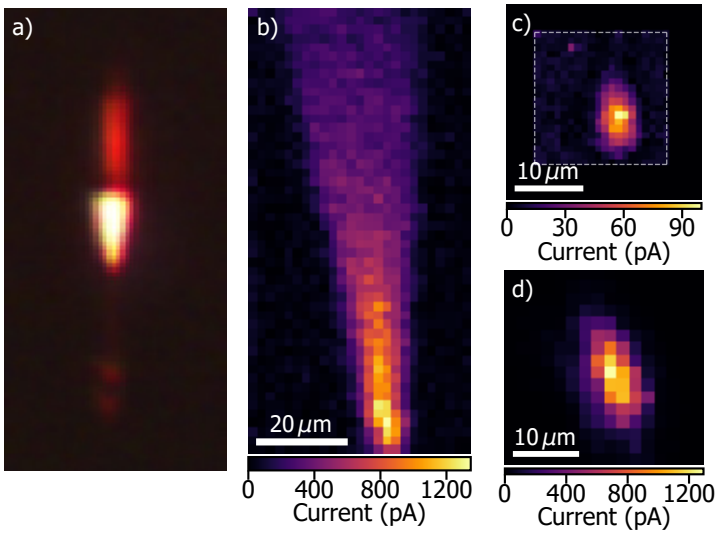


Figure 2.3: Experimental procedure to focus the laser on the electron cathode. (a) Photograph of blackbody radiation of the tip under normal operating conditions ($T \simeq 1800\,\mathrm{K}$). (b) Map of the pulsed current collected on a Faraday cup while scanning the laser focus around the hot tip in the $xy$ plane ($T = 1800\,\mathrm{K}$, $V_{ext} = 4550\,\mathrm{V}$). The current produced by photoemission is distinguished from the continuous one using a lock-in amplifier. (c) Similar map as in (b) but with a colder tip ($T \simeq 1200\,\mathrm{K}$). (d) Similar map as in (c) but obtained at $V_{ext} = 650\,\mathrm{V}$. Here the continuous emission is fully suppressed and the pulsed current is measured directly with a picoammeter.

realigned the electron column and adjusted the condenser voltage ($C_1$) for optimal electron collection. Here, $C_1$ was increased from 1125 V in normal conditions to 1190 V. We observe that the overall emission decreased by ~ 92 %, down to the tens of pA regime. Moreover, now emission can be observed only from a relatively small area, corresponding to the apex of the tip, due to the lower photoemission efficiency. Regardless of this reduction in the temperature of the tip, complete suppression of continuous emission is only achieved after letting the tip cool down for at least 1 h, which is not practical for experiments.

A way to instantaneously remove the remaining continuous emission is by lowering the extractor voltage, such that the effective work function of the ZrO/W tip is increased (Fig. 2.1b). We have observed that lowering the extractor voltage to ~ 3000 V results in the full suppression of continuous emission. Given that the photon energy of the laser beam is much larger than the work function, photoemission of electron pulses is barely affected. Further reducing the extractor voltage to 650 V results in an enhancement of the photoemitted electron current collected on the Faraday cup, as will be seen below (section 2.5.3), contrary to what we would expect from the Schottky theory explained in section 2.2. In normal operating conditions, the extractor-suppressor configuration acts such that a large fraction of the emit-

ted electrons are blocked by the extractor aperture. Instead, when the magnitude of the extractor voltage is similar to that of the suppressor, most of the emitted electrons can go though the aperture, thus increasing the collection efficiency of the photoemitted electrons [105]. Figure 2.3d shows a scan of the tip lens obtained at $V_{ext} = 650\,V$. Given that there is not continuous emission anymore, the laser beam is not chopped and the electron current collected by the Faraday cup is sent directly to a picoammeter. Here again, the condenser lens was readjusted ($V_{C1} = 650\,V$) together with gun tilt and shift to maximize the collection of electrons. All other parameters were kept the same as in Fig. 2.3c. We observe that in this case the maximum electron current is 1.29 nA, corresponding to an average of ~ 1600 electrons per pulse. We should note that this corresponds to one of the lowest values of the extractor voltage at which photoemission is still possible. Lowering $V_{ext}$ below the magnitude of the suppressor voltage (500 V) would result in the total suppression of emission of electrons from the tip.



## 2.5. ENERGY SPREAD OF THE ELECTRON BEAM

Electrons emitted from an electron cathode have an energy equal or close to the energy barrier, which is determined by the combined effect of work function of the tip and extractor field (in the case of a Schottky FEG). Electrons with energy larger than the energy barrier can be easily released, but the occupation probability of these higher energy states, given by the Fermi-Dirac statistics, is low. Instead, energy states below the energy barrier have a larger occupation probability, but electrons in these states can only be released through quantum tunneling. Hence, the emitted electrons have a certain energy distribution ($\Delta E$), determined by the Fermi-Dirac statistics and the strength of extractor field [105]. Other parameters in the emission process, such as defects on the tip and slight changes of the work function for different facets of the tip, also contribute to the electron energy spread. Moreover, Coulomb repulsion, also referred to as space-charge effects, at the gun and, to a lesser extent, at the different crossovers along the electron column, can also play a role in the final electron energy width [111, 112]. This means that in experiments, electrons have an energy of $E_0 \pm \Delta E$, where $E_0$ is the operating energy ($E_0 \sim 0.5 - 30\,keV$ for SEMs and $60 - 300\,keV$ for TEMs).

The uncertainty in the energy of the electron beam is a crucial parameter in several analytical techniques such as electron-energy-loss spectroscopy (EELS), usually performed in (S)TEMs, given that it directly affects the energy resolution of the measurements. In SEMs, the energy spread can have a strong impact on the spatial resolution and, in the case of pulsed electron beams, also on the temporal resolution. Therefore, knowing the energy spread of the electron beam and the parameters that influence it is essential to optimize the performance of (time-resolved) SEMs.

### 2.5.1. RETARDING FIELD ANALYZER

The energy width of an electron beam in (S)TEMs is typically measured using an EELS detector, which is based on the controlled deflection of electrons depending on their energy by means of a magnetic prism. Here instead we use a retarding field energy analyzer (RFA) to measure the energy spread for low-energy electron beams in the SEM. The RFA was obtained from Prof. P. Kruit (Technical University of Delft) and is based on the work by M. van der Heijden [113]. A schematic of the setup is shown in Fig. 2.4a. The RFA is mounted on the sample stage of the SEM (see photograph, Fig. 2.4b) and the electron beam is directly sent through an initial aperture, after which it is focused on the retarding electrode (orange in the figure). The voltage on this electrode ($V_{RF}$) is supplied by a fixed negative offset voltage $V_{\text{offset}}$, usually set slightly below the electron accelerating voltage (-5 kV), plus a tunable small (negative) voltage $\Delta V$ in the range of a few tens of volts. Our RFA is designed to operate at an electron accelerating voltage of $V_0 = -5\,\text{kV}$. Hence, when $V_{RF} = V_{\text{offset}} + \Delta V < V_0$ most electrons will go through the electrode and end up being collected by a Faraday cup, which is connected to an electrometer (Keithley 6514 System Electrometer). Instead, when $V_{RF} > V_0$ most electrons will be repelled and will not reach the Faraday cup. In an experiment, $\Delta V$ is scanned and the current collected by the Faraday cup in each step is recorded. Hence, the dependence of the collected current on $V_{RF}$ directly gives the electron energy distribution, given the relation $E = qV$ (with $q$ the electron charge). An additional negative voltage (−9 V) is also set at the entrance of the Faraday cup to hinder the escape of secondary electrons created in the Faraday cup.

Figure 2.4c shows a measurement performed with a 5 keV continuous electron beam, obtained using a 40 µm diameter aperture. The figure shows the current $I$ collected by the Faraday cup as a function of the potential energy on the retarding field electrode, defined as $E_{RF} = qV_{RF}$. Here $V_{\text{offset}}$ is set to $\sim -4.99\,\text{kV}$ and $\Delta V$ is scanned over a 0 to −15 V range with step size of 117 mV. We fit the data with the cumulative distribution function (CDF) of a pseudo-Voigt distribution ($\text{V}_p$), defined as

$$\begin{aligned} I(E) &= \text{V}_p(E; I_0, k, E_c, \gamma, B) = \\ &= k\text{L}(E) + (1-k)\text{G}(E) + B = \\ &= -k\frac{I_0}{2}\left[\frac{1}{\pi}\arctan\left(\frac{E-E_c}{\gamma}\right)+1\right] + \\ &+ (1-k)\frac{I_0}{2}\left[1-\text{erf}\left(\frac{\sqrt{\log 2}}{\gamma}(E-E_c)\right)\right] + B\,, \end{aligned} \tag{2.3}$$

where L($E$) is the CDF of a Cauchy-Lorentz distribution with width parameter $\gamma$ and G($E$) is the CDF of a normal distribution with standard deviation $\sigma = \sqrt{2\log 2}\gamma$. Both CDFs are centered around $E_c$, and have amplitudes proportional to the total electron current $I_0$. The parameter $k$ indicates the contribution of each CDF to the measured curve, and $B$ a background, representing the noise level of the measurement. The red curve in Fig. 2.4c is the fit of the data, obtained with $\gamma = 0.39\,\text{eV}$, $I_0 = 2.12\,\text{pA}$, $E_c = 6.14\,\text{eV}$ and $k = 0.13$. The energy spread of the electron beam is

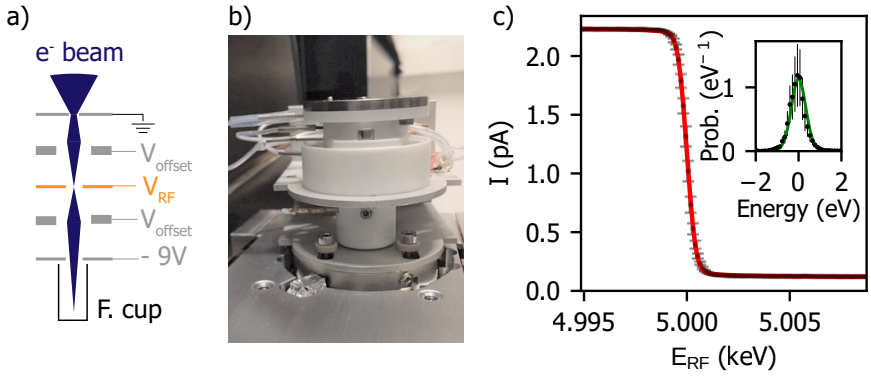


Figure 2.4: Energy-spread measurements with the retarding field analyzer (RFA). (a) Schematic of the RFA setup: the electron beam is accelerated up to $V_{\text{offset}}$, typically set slightly below the operating voltage of the SEM (−5 kV). The beam is focused on the retarding electrode, set at $V_{\text{RF}} = V_{\text{off}} + \Delta V$, and $\Delta V$ is scanned over a fixed voltage range, typically from 0 to −30 V. The electrons that go through the electrode are collected in the Faraday cup. Escape of secondary electrons from the Faraday cup is hindered by setting a negative potential (−9 V). (b) Photograph of the RFA setup mounted on the sample stage of the SEM. (c) RFA measurement of the energy spread of a 5 keV continuous electron beam. The red curve represents a fit obtained when using a pseudo-Voigt distribution. Inset: electron energy distribution, obtained from the derivative of the RFA data, together with the probability density function of a pseudo-Voigt function (green).

defined as $\Delta E = 2\gamma$, corresponding to the full width at half maximum of the curve, which in this case is $\Delta E = 0.79$ eV. We should note that in the plot, $E_c$ has already been subtracted from the x-axis, such that the center corresponds to the electron beam energy. The precise value of $V_{\text{offset}}$ is not known, given the limited precision of the high voltage supply readout, thus the exact $\Delta V$ at which $E_{RF} = 5$ kV is always extracted by subtracting the fitted value of $E_c$ from the electron energy $E_0$, thus assuming that the center corresponds to $E_0$.

The derivative of the RFA data with respect to the retarding field energy gives the shape of the energy distribution of the electron beam. The result is shown in the inset of Fig. 2.4c. Given that the noise is amplified when performing the derivative, it is best to fit the data directly with Eq. 2.3 rather than fitting its derivative (green curve in the inset).

### 2.5.2. ENERGY SPREAD OF A CONTINUOUS BEAM

Several parameters have an impact on the energy distribution of a continuous electron beam. Here we evaluate how the emission conditions at the Schottky gun influences the final energy spread of the electron beam. The initial energy spread of the emitted electrons ($\Delta E_0$) and the current emitted from the tip (~ 300 µA) are determined by the tip temperature and suppressor and extractor voltages. In typical operating conditions (continuous emission), we have $T \sim 1800$ K, $V_{\text{supp}} = -500$ V and $V_{\text{ext}} = 4550$ V. The initial electron beam is cut through a set of apertures along

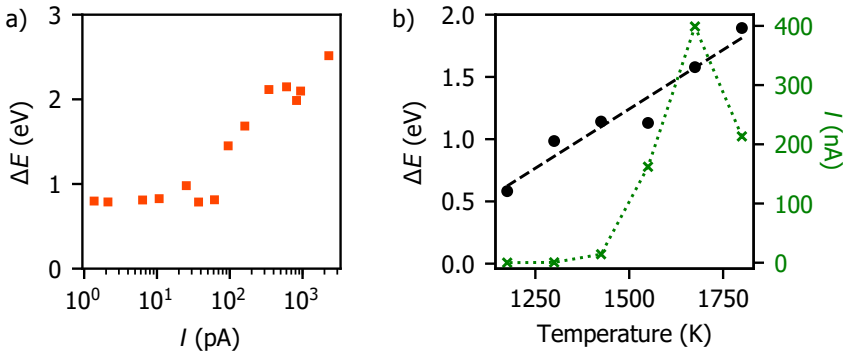


Figure 2.5: Energy spread of a continuous electron beam. (a) Energy spread ($\Delta E$) of a 5 keV continuous electron beam as a function of the electron current collected on the Faraday cup. (b) Energy spread of the electron beam (black) and collected current $I$ (green) as a function of the temperature of the tip.

the microscope column, which result in lower electron currents on the sample plane. Figure 2.5a shows the energy spread of the electron beam as a function of the electron current collected on the Faraday cup (that is, in the sample plane). The electron current is tuned by changing the value of the condenser lenses ($C_1$ and $C_2$), which determine the fraction of electrons that go through the final aperture (40 µm in this case). We observe that reducing the current from 6.5 nA to 59 pA results in a decrease of the energy spread from 2.74 to 0.72 eV. This dependence of $\Delta E$ on the electron current can be due to two effects. First, when reducing the current we remove electrons that are emitted further away from the optical axis, that is, coming from different positions from the tip that might have slightly different work functions [105]. Second, at larger electron currents, Coulomb repulsion at the different crossovers along the microscope column can become more dominant, thus resulting in an increase of the energy distribution, as will be discussed in section 2.5.3.

Another parameter that affects the electron energy spread is the temperature of the electron cathode. As explained in section 2.2, decreasing the temperature of the emitter also reduces the occupation probability of higher energy states, thus decreasing the energy spread of the emitted electrons. Figure 2.5b shows the value of the energy spread measured as a function of the temperature of the tip. In each measurement the value of the condenser lens $C_1$ is changed in order to maximize the collected electron current, and we used the largest aperture (1 mm). We find that the energy spread decreases linearly with temperature, with a slope of 2 eV K$^{-1}$, from a value of 1.86 eV for a temperature of 1800 K, corresponding to the typical operating conditions of our Schottky FEG, down to 0.59 eV for 1175 K. At lower temperatures, the electron current reaching the sample becomes too unstable to give reliable results. We typically waited up to 40 min in between measurements to let the electron current stabilize.

In the figure we also plot the maximum electron current $I$ collected on the Fara-

day cup as a function of the tip temperature. The current exhibits a decrease when reducing the temperature, as expected due to the lower occupation of high energy states at low temperature [8, 107]. The fact that the electron beam current at $T = 1800$ K is lower than at 1675 K is attributed to non-optimum alignment of the electron column in the 1800 K case. Nevertheless, the energy spread is still lower at 1675 K than at 1800 K, thus further suggesting that the main effect on the energy spread comes from the change in temperature rather than the change in the value of the electron current measured on the Faraday cup.



### 2.5.3. ENERGY SPREAD OF A PULSED ELECTRON BEAM

Next, we evaluate the energy spread of pulsed electron beams obtained through photoemission. Similar to the continuous case, the initial energy distribution of electrons ($\Delta E_0$) is determined by the electron gun conditions (temperature, extractor voltage). However, now the laser wavelength also plays a role: the excess of energy between the photon energy and energy barrier of the tip also contributes to the initial energy spread of the electron beam [114]. Moreover, in the case of ultrashort pulses, Coulomb repulsion in dense electron bunches becomes a critical factor, as will be discussed below.

In a typical photoemission experiment, electrons are emitted from a small area on the tip (~ μm), governed by the size of the tip apex and extractor-suppressor configuration, and within a short time (usually a few hundreds of fs). This spatial and temporal concentration of electrons can lead to significant Coulomb interactions (space-charge effects), both in the lateral/transverse and longitudinal/axial directions, with respect to the electron beam propagation. In the first case, the main effect is a reduction of the spatial resolution, due to the spatial broadening of the electron beam. In the second case, referred to as Boersch effect, Coulomb repulsion among electrons within the same pulse leads to a broadening of the electron kinetic energy distribution [115]. The initial energy distribution of electrons ($\Delta E_0$) translates into a difference in electron speed, and thus position along the optical axis. Coulomb repulsion will increase this broadening, given that the leading electrons will be further accelerated, while the electrons in the tail will experience a deceleration [105, 115–117]. This effect results in a gradual broadening of the energy width with increasing number of electrons per pulse, as previously reported in literature [102, 103]. Moreover, in the extreme case in which each pulse contains a large number of electrons, this effect can result in the appearance of two distinguished energy peaks, corresponding to the accelerated and decelerated electrons [101–103, 118].

In order to investigate the effect of Coulomb repulsion under different photoemission conditions, we performed RFA measurements of the energy spread as a function of the number of electrons per pulse ($N_e$). Figures 2.6a-b show two examples of such curves, obtained for an average value $N_e$ of 0.53 and 1029 electrons per pulse, respectively. Here the current measured on the Faraday cup, and thus, $N_e$, was tuned by varying the laser power focused on the tip, corresponding to 4.23 and 273.41 pJ per pulse, respectively, in these particular cases. All other settings of

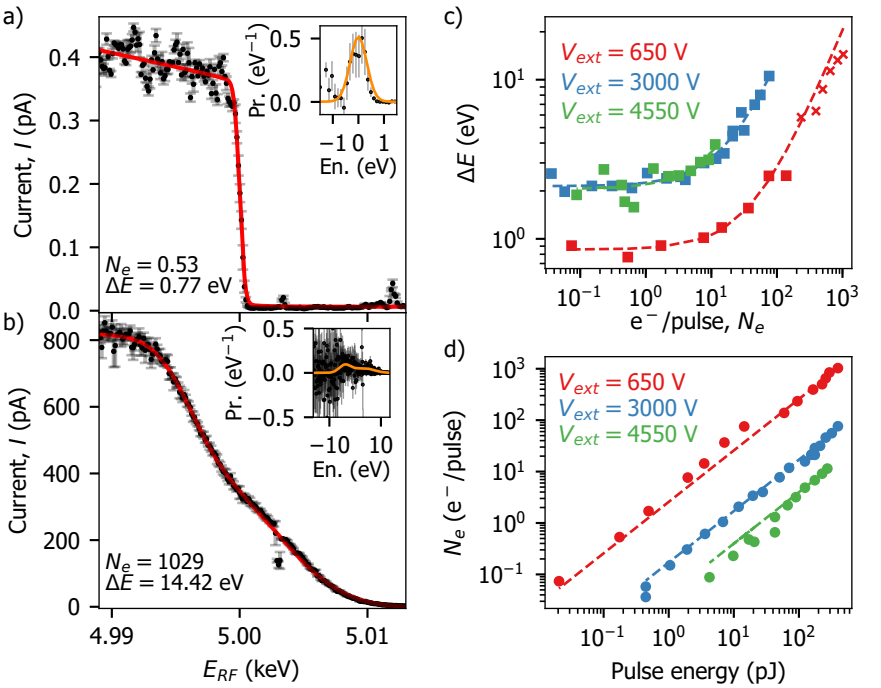


Figure 2.6: Energy spread of a pulsed electron beam. (a, b) RFA measurements obtained for a low (0.53) and high (1029) average number of electrons per pulse, obtained at 5 keV, and using a low extractor voltage ($V_{\text{ext}}$ = 650 V). The solid red curves represent the fits using a single (a) and double (b) pseudo-Voigt distributions. The insets show the energy distributions obtained from the data, together with the analytical curves calculated from the results of the fits (orange). (c) Energy spread vs number of electrons per pulse for high (4550 V), medium (3000 V) and low (650 V) extractor voltages. The dashed lines are linear fits of the data. (d) Number of electrons per pulse collected on the sample plane as a function of the laser energy per pulse ($\lambda_{exc}$ = 258 nm), together with the corresponding linear fits (dashed curves).

the electron column were kept the same, and the repetition rate of the laser was set to 5.04 MHz. In both cases the tip was cooled down ($I_{\text{fil}}$ = 1.7 A, $T \simeq$ 1200 K), and we used $V_{\text{ext}}$ = 650 V and $C_1$ = 450 V. We observe that the curve corresponding to $N_e$ = 0.53 electrons per pulse (Fig. 2.6a) exhibits a sharp transition in the RFA spectrum. Fitting the curve with Eq. 2.3 (red curve) yields an energy spread of 0.77 eV. The curve also exhibits a linear downward trend in the $E_{RF}$ = 4.990 − 4.998 keV range, where we would expect a constant current, which is attributed to a decrease of the electron current during the acquisition, probably due to drifting of the position of the laser beam with respect to the tip. This is accounted for in the fit. The inset in Fig. 2.6a shows the derivative of the data, together with the derivative from Eq. 2.3, calculated using the results from the fit.

In contrast, Fig. 2.6b shows the RFA measurement obtained for a very large number of electrons per pulse ($N_e \simeq$ 1029). In this case we observe a broadening of

the curve, corresponding to a larger energy spread, as expected from the Boersch effect. Moreover, we observe that the transition from high (800 pA) to zero current is not completely smooth but exhibits two features. This curve is best described when considering that the current collected by the Faraday cup as a function of the energy on the retarding field electrode depends on two pseudo-Voigt distributions, each centered around $E_{c,i}$ and with width parameter $\gamma_i (i = 1,2)$, that is,

$$I(E) = \eta \mathrm{V}_p(E; I_0, k, E_{c,1}, \gamma_1, 0) + (1-\eta)\mathrm{V}_p(E; I_0, k, E_{c,2}, \gamma_2, 0) + B\,, \tag{2.4}$$

with the expression for $\mathrm{V}_p$ given in Eq. 2.3. Here the parameter $\eta$ determines the contribution of each individual pseudo-Voigt function. The curve in Fig. 2.6b was best fitted when $k = 0$, meaning that the peaks are fully Gaussian, $\eta = 0.52$, $\gamma_1 = 2.62\,\mathrm{eV}$, $\gamma_2 = 4.56\,\mathrm{eV}$, $E_{c,1} = -3.92\,\mathrm{eV}$ and $E_{c,2} = 3.32\,\mathrm{eV}$. Here the zero in the x-axis, which would correspond to $E_{RF} = 5\,\mathrm{keV}$, cannot be calculated directly from the fits, given that we have two values of $E_c$. Instead, we took the value from the curves that do not show a double peak, thus having a clear $E_c$. $E_{c,1}$ and $E_{c,2}$ are thus expressed with respect to this central energy. Moreover, the energy width $\Delta E$ of the electron beam is now defined as,

$$\Delta E = \gamma_1 + \gamma_2 + |E_{c,1} - E_{c,2}|\,. \tag{2.5}$$

The presence of these two peaks can be interpreted as a further proof of the contribution of Coulomb repulsion to the final electron energy distribution of highly dense electron pulses.

Figure 2.6c shows $\Delta E$ as a function of $N_E$ obtained for three different extractor voltages: low ($V_{ext} = 650\,\mathrm{V}$, red), medium ($V_{ext} = 3000\,\mathrm{V}$, blue) and high ($V_{ext} = 4550\,\mathrm{V}$, green). The squares indicate the cases in which the data was fitted with a single pseudo-Voigt function, hence $\Delta E = 2\gamma$, while the crosses denote the cases in which a double pseudo-Voigt function was used, with energy spread calculated using Eq. 2.5. The energy spread gradually increases when increasing the number of electrons per pulse, as we would expect from the Boersch effect. We fit the data using a linear function (dashed curves), with slopes corresponding to 0.02, 0.11 and $0.15\,\mathrm{eV/e^-}$, for low, medium and high extractor respectively. These values indicate that the energy spread is more strongly affected by $N_e$ in the high and medium extractor cases. This could be explained by the fact that for high extractor voltages, the extractor aperture blocks a large fraction of the photoemitted electrons. Hence, the same number of electrons collected on the sample plane corresponds to a larger number of photoemitted electrons in the high and medium extractor cases.

To investigate the collection efficiency of emitted electrons at different extractor voltage, Figure 2.6d shows the number of electrons per pulse collected on the Faraday cup as a function of the laser energy focused on the tip. The number of electrons emitted by the tip is higher than the values measured on the Faraday cup, given that the extractor aperture and rest of apertures along the microscope column block a fraction of the electron beam. In all cases the data in Fig. 2.6d can be fitted with a linear function, with slope 2.57, 0.17 and $0.04\,\mathrm{e^-/pJ}$ for low, medium and high extractor voltages, respectively. Hence, we observe again a clear difference between

the low and medium/high extractor cases. This result is initially counter intuitive, given that at lower extractor voltage the energy barrier is larger and, thus, we would expect that the electron emission efficiency is lower. However, the extractor voltage also has an impact on the collection efficiency. At low extractor voltage, the angular spread of electrons right after emission is lower than at high extractor voltage. Hence, fewer electrons are blocked by the extractor aperture, thus increasing the collection efficiency of photoemitted electrons. These results are compatible with the effect of the extractor voltage discussed in ref. [105].

Finally, we should note that we obtain the smallest energy spread when using a low extractor voltage, as seen in Fig. 2.6c. In particular, from the linear fits we extracted lower limits of 0.86, 2.14 and 2.05 eV (low, medium and high $V_{\text{ext}}$). These values represent the value of energy spread in the limit of low $N_e$, that is, with pulses containing less than one electron. In these cases Coulomb repulsion does not play a role, and the energy spread is determined by the conditions of photoemission. The lower energy spread obtained in the case of a low extractor voltage could be explained by the fact that lowering this voltage results in an effective increase of the energy barrier for the emission of electrons from the electron cathode. Hence, less electrons have excess energy, thus reducing the initial energy distribution. At a high extractor voltage ($V_{\text{ext}} = 4550\,\text{V}$), the energy barrier is lowered by $\sim 1\,\text{eV}$ (Eq. 2.2, $E_{\text{ext}} \sim 0.7\,\text{V nm}^{-1}$), close to the difference in energy spread obtained here between high and low extractor voltages.

## 2.6. SPATIAL RESOLUTION

In the geometry of the laser-driven cathode, we drastically change the way electrons are emitted from the tip with respect to the continuous beam configuration. However, in principle the settings of the electron column itself can be kept the same as in continuous mode, which implies that fundamentally a similar spatial resolution can be achieved. Indeed, several reports have shown spatial resolutions down to 5 nm in a pulsed-laser driven SEM [90] and a resolution of 0.9 nm in TEM, in which a new laser driven cathode system using a cold-FEG was demonstrated [66]. Nevertheless, in practice several parameters in the electron column are usually adjusted, which can affect the spatial resolution. Here we discuss which parameters play a role in the spatial resolution and the different regimes in which we can work.

In the rest of this chapter we evaluate the spatial resolution by using a sample containing Sn spheres with diameters ranging from 50 nm up to 10 µm. All images are taken at the same working distance at which cathodoluminescence (CL) experiments are performed (14 mm), but without the CL mirror in place, as it blocks part of the SE emission. In all cases we use the $4^{\text{th}}$ harmonic of the laser ($\lambda_{exc} = 258\,\text{nm}$) and the repetition rate is set to 25.19 MHz. We evaluate the spatial resolution ($\eta$) by means of the Fourier transform method presented in ref. [49]. We should note that differences in the electron beam focus and alignment of the column between experimental sessions have an impact on the exact value of $\eta$. Moreover, different levels of noise in the images, depending on the magnitude of the SE signal, also affect the accuracy of $\eta$.

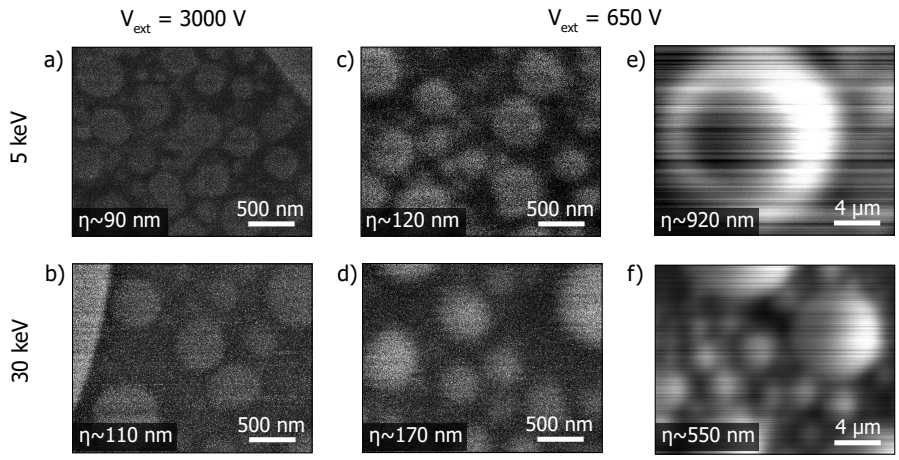


Figure 2.7: Secondary electron images of a Sn ball sample using a pulsed electron beam at 5 keV (top row) and 30 keV (bottom row). (a-b) Images obtained using $V_{ext}$ = 3000 V and 60 µm aperture. (c-d) Images obtained using $V_{ext}$ = 650 V and 60 µm aperture. (e-f) Images obtained under conditions for the highest electron current ($V_{ext}$ = 650 V and 1 mm aperture).

A critical parameter for a good spatial resolution is the initial region of the tip from which electrons are emitted. The smaller this area, the tighter we can focus the electron beam on the sample. Given a certain brightness of the source, which is determined by the conditions of electron emission, a reduction of the emitted area results also in a decrease of the electron current (Eq. 2.1). Hence, there is always a tradeoff between high spatial resolution and signal, which in our case is either secondary electrons (SE) or CL.

A way of keeping a relatively small emitting area is by using a high suppressor and extractor voltages, as discussed above. Even when using the same value of $V_{ext}$ as in continuous mode, we need to readjust $C_1$ for optimum resolution, both due to the thermal contraction of the tip when lowering its temperature (see 2.4.2) and difference in the photoemission area with respect to continuous emission. In experiments, it is usually more convenient to lower the extractor voltage to 3000 V, which allows us to fully suppress continuous emission (see section 2.4.2) while keeping a relatively high extractor field. Figure 2.7a shows an SE image of Sn balls obtained using $V_{ext}$ = 3000 V and a 5 keV electron beam, for which we extract a spatial resolution of $\eta \sim 90$ nm. Here we used a 60 µm aperture and condenser lens $C_1$ = 760 V, obtaining a current of 0.3 pA. Fig. 2.7b shows an image obtained using the same extractor voltage but at 30 keV ($C_1$ = 1220 V, $I$ = 5 pA, $\eta \sim 110$ nm).

Working at a very low extractor voltage (magnitude comparable to the suppressor voltage, $V_{supp}$ = 500 V) can pose some advantages, such as a larger electron current and smaller energy width, as discussed in 2.5.3. However, the larger collection efficiency of electrons, as discussed in section 2.5.3 results in a larger area from

which electrons are emitted, thus effectively reducing the brightness of the source. Figs. 2.7c,d show images obtained at low extractor voltage ($V_{ext}$ = 650 V) at 5 and 30 keV. Here we also used a 60 µm aperture and obtained a spatial resolution of $\eta \sim 120$ nm at 5 keV ($C_1$ = 200 V, $I$ = 0.5 pA) and $\eta \sim 170$ nm at 30 keV ($C_1$ = 600 V, $I$ = 7 pA). Finally, in applications that require a high electron current, we can tune the conditions at low extractor voltage such that a large portion of the emitted current reaches the sample, but at the expense of a very poor spatial resolution. Figs. 2.7e, f show images obtained also at low extractor using a 1 mm aperture, meaning that a big fraction of the photoemitted electrons reach the sample. In these cases we obtained a large electron current (~ nA) but at the expense of much lower spatial resolution: $\eta \sim 920$ nm at 5 keV ($I$ = 1 nA, $C_1$ = 450 V) and $\eta \sim 550$ nm at 30 keV ($I$ = 1.2 nA, $C_1$ = 1000 V).

Space-charge effects can also impact the spatial resolution for pulses containing multiple electrons. It is therefore desirable to keep a low number of electrons per pulse when possible. On the one hand, the width of the electron beam can be broadened due to Coulomb repulsion, thus directly increasing the size of the electron spot on the sample plane. Moreover, spherical aberrations might become more important due to this widening of the beam. Finally, the electron optics also suffer from chromatic aberrations, given that electrons with slightly different energies will be focused in different planes. Hence, the large energy spreads obtained for a high number of electrons per pulse (section 2.5.3) will have a negative impact on the spatial resolution. We should note that effects due to Coulomb repulsion are most important when the initial emitting area is small, such as in the high extractor case. When having a very low extractor voltage, the widening of the electron beam due to space-charge effects, and spherical and chromatic aberrations, might be negligible compared to the already large initial spot size.

The spatial resolutions obtained from these measurements are larger than the highest ones reported for other USEMs (~ 5 nm), in which a Schottky FEG source and a laser with similar characteristics as ours were used [90]. Here we discuss the main factors that can contribute to this discrepancy and possible improvements. We should note that there are different methods to quantify the size of the electron beam on the sample from a given SE image, each yielding different values [119]. Hence, the definition of spatial resolution between different works can differ, thus making it difficult to precisely compare values derived using different techniques. The value of the extractor voltage can play an important role in the spatial resolution, due to the difference in effective emission area from the electron source, as we have discussed above. Hence, a high extractor voltage, ideally the same as in continuous mode, should be used when high spatial resolution is needed. A resolution of ~ 35 nm using our initial USEM was reported when using a high extractor voltage [49].

A major source of loss in spatial resolution can come from the settings of the electron column, including working distance, electron optics and column alignment. In our measurements we used a working distance of 14 mm, corresponding to the one at which CL measurements are performed, instead of the optimum one

for our SEM (~ 10 mm). This effect could be reduced by using an SEM designed for optimum performance at such working distance. The settings of the electron optics, including condenser lenses ($C_1$ and $C_2$) and gun tilt/shift, need to be optimized for each value of electron energy and extractor voltage. The process of optimization of $C_1$ and $C_2$ requires readjusting the focus and astigmatism of the beam at each condenser value, which can result in some uncertainty in the final optimum values of $C_1$ and $C_2$. A systematic study of the optimum condenser values, including different sets of experiments to account for differences in beam alignment, could help improve the current settings. Additionally, ensuring an optimum mechanical alignment of the electron column is important to achieve a high spatial resolution. Finally, as we have already discussed above, there is a tradeoff between spatial resolution and electron current on the sample, and a low current results in a small SE signal. In these cases, the optimization of focus and astigmatism on the sample becomes challenging.



Overall, the analysis of spatial resolution reported in this section serves as a guide to understand the parameters that play a role in the resolution and the different regimes in which the USEM can operate. Further improvements, such as the ones proposed above, could be developed to bring the spatial resolution towards the 5 – 10 nm range.

## 2.7. TEMPORAL RESOLUTION

Finally, a key parameter in a laser-driven SEM is its temporal resolution. Here we estimate and set an upper limit for the pulse width of the electron on the sample, and we show an application of time-resolved CL in the USEM.

### 2.7.1. ELECTRON PULSE WIDTH

The electron pulse width ($\Delta t_{e^-}$) has two contributions: the laser pulse width ($\Delta t_{\text{laser}}$) and the temporal spread due to the electron energy distribution ($\Delta t_{\Delta E}$). The latter is due to the fact that the arrival time of electrons on the sample depends on their kinetic energy. As we have previously shown, the electron energy distribution is strongly affected by Coulomb repulsion between electrons from the same pulse. The electron temporal spread taking into account space-charge effects is typically calculated using Monte-Carlo simulations or mean-field theory, among others [63, 102, 117, 118, 120–122]. For simplicity, here we assume that the energy spread due to Coulomb repulsion takes place instantaneously after emission, which is reasonable given the low energy and high temporal and spatial concentration of electrons around the source [102, 118]. We also assume that the photoemission process is instantaneous compared to the rest of timescales. Hence, the temporal broadening happens during the acceleration phase of the electron beam up to the desired electron energy $E_0$, and while the beam propagates along the rest of the microscope column, where no external voltage is applied. In this case, the

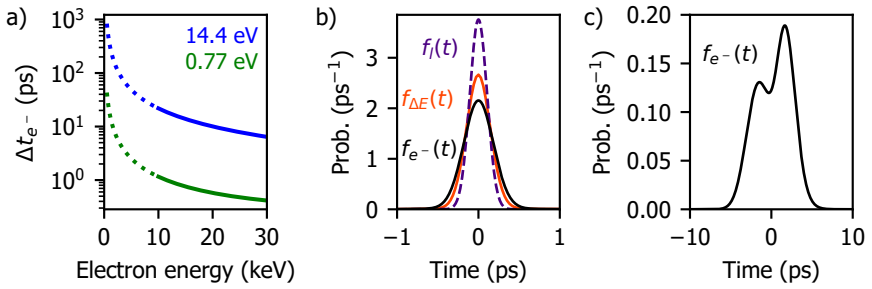


Figure 2.8: Calculated temporal spread of electron pulses. (a) Electron pulse width $\Delta t_{e^-}$ as a function of the final electron beam energy for initial energy distributions of 0.77 and 14.4 eV (green and blue, respectively). The calculations were performed using Eq. 2.6. (b) Temporal distribution of the laser ($f_I(t)$) (purple curve, $\Delta t_{\text{laser}} = 250$ fs), temporal spread of a 30 keV electron pulse ($f_{\Delta E}(t)$) only due to the initial energy distribution of $\Delta E = 0.77$ eV measured for ~ 0.53 electrons per pulse (orange, $\Delta t_{\Delta E} = 330$ fs) and the convolution of both (black, $f_{e^-}(t)$), corresponding to the final electron pulse temporal shape ($\Delta t_{e^-} = 416$ fs). (c) Temporal distribution of the electron pulse obtained for the initial energy distribution obtained from the measurements in Fig. 2.6b ($\Delta E = 14.4$ eV for 1029 electrons per pulse), resulting in a spread of $\Delta t_{e^-} = 6.4$ ps.

temporal width of the electron pulse is given by [63]

$$\Delta t_{e^-} \simeq \sqrt{\Delta t_{laser}^2 + \Delta t_{\Delta E}^2} = \\ = \sqrt{\Delta t_{laser}^2 + \frac{m}{2E_i}\Delta E_i^2 \left[ -\frac{d}{E_0}\left(1 - \frac{v_i}{v_f}\right) - \frac{l}{m\gamma_f^3}\frac{v_i}{v_f^3} \right]^2}. \tag{2.6}$$

Here, $E_i$ is the energy of the electrons right after being emitted from the cathode, from which we can extract $v_i = \sqrt{\frac{2E_i}{m}}$, and $\Delta E_i$ is their initial energy spread, which we will consider the same as the total energy spread measured in section 2.5.3 ($\Delta E$). The final speed of the electron is represented by $v_f = \gamma_f \sqrt{\frac{2E_0}{m}}$, where $\gamma_f$ corresponds to the Lorentz contraction factor, $m$ is the electron mass, $d$ indicates the distance between the tip apex and the accelerating anode and $l$ is the length from the accelerating anode to the sample plane.

From Eq. 2.6 it follows that the temporal spread is directly determined by the final electron beam energy: at lower operating voltages the initial energy spread plays a larger role than at higher voltages. Figure 2.8a shows the temporal width of the electron pulse as a function of the final electron beam energy, calculated using Eq. 2.6. The two curves represent two different initial energy spreads, 0.77 and 14.4 eV (green and blue, respectively), corresponding to the lowest and largest distributions measured with the RFA (Fig. 2.6). In the calculations we considered $d = 25$ mm, $l = 0.5$ m, $\Delta t_{laser} = 250$ fs, and an electron initial energy given by $E_i = E_f + \phi_{ZrO/W} = 14.37$ eV, thus assuming that the reduction of the energy barrier due to the extractor voltage is negligible. This assumption is reasonable given that

the experiments were performed using a low extractor field ($V_{ext}$ = 650 V). As expected, the lowest temporal spread, corresponding to $\Delta t_{e^-}$ = 416 fs, is obtained at the highest electron beam energy (30 keV) and for the lowest initial energy spread. We should note that the results obtained for electron beam energies lower than 10 keV are less precise, due to the design of the SEM. In these cases, electrons are initially accelerated to 10 keV and subsequently decelerated down to the desired final energy. Hence, Eq. 2.6 should be modified to include additional terms for the deceleration and acceleration steps. Instead, for energies larger than 10 keV, the electrons are directly accelerated to their final energy.



Using a similar derivation as for Eq. 2.6, we can calculate the distribution of arrival time of electrons within a pulse, given a known energy distribution (see [63]). Figures 2.8b,c show the temporal shape of an electron pulse containing an average of 0.53 and 1029 electrons per pulse, obtained assuming the initial energy distributions from Figs. 2.6a,b ($\Delta E$ = 0.77 and 14.4 eV, respectively). In order to avoid extra calculations for the deceleration at lower operating energies, which would obscure the trends investigated here, we performed the calculations for an electron beam energy of 30 keV. We assume that the energy distributions obtained with the RFA measurements at 5 keV are still valid at larger energies, which is reasonable given that it is typically assumed that space-charge effects dominate before the acceleration of electrons [102]. Fig. 2.8b shows the distribution of arrival time of electrons for the case of a low number of electrons per pulse ($N_e$ = 0.53). The orange curve represents the electron temporal spread exclusively due to the initial energy distribution ($\Delta t_{\Delta E}$ = 330 fs), while the pulse width of the laser is shown in purple ($\Delta t_{laser}$ = 250 fs, dashed curve). The convolution of both curves gives the electron pulse distribution (black curve), for which we obtain a temporal width of $\Delta t_{e^-}$ = 414 fs. For larger number of electrons per pulse, the contribution of the laser pulse is negligible and the electron pulse shape is mostly determined by the energy spread due to space-charge effects, as shown in Fig. 2.8c. In this case we obtain an electron pulse width of $\Delta t_{e^-}$ = 6.4 ps. We should emphasize that these numbers are rough approximations, given the assumptions taken, but give an idea of the magnitude of the effect of Coulomb repulsion on the overall time resolution.

Given that the retrieved temporal pulse widths are relatively small, direct measurements of the electron pulse width are typically performed by means of pump-probe techniques, such as in photon-induced near-field electron microscopy (PINEM) [65] or when analyzing the change in SE signal due to photogenerated carriers [98]. In our setup we can perform time-resolved cathodoluminescence (CL) measurements using a time-correlated single-photon counting (TCSPC) technique. In brief, the CL emitted by the sample is collected using a parabolic mirror and guided to a 105 µm fiber (Thorlabs FG105UCA), from which it is focused on a single-photon avalanche detector (PicoQuant PDM Series), which is connected to a time-correlator (PicoQuant PicoHarp 200). The 2$^{nd}$ harmonic of our fs laser ($\lambda$ = 517 nm) is detected by a photodiode (PicoQuant TDA 200) also connected to the time-correlator, thus serving as a trigger. Further information on the CL setup and TCSPC measurements is provided in chapter 3 (section 3.4.3). Figure 2.9 shows a measurement

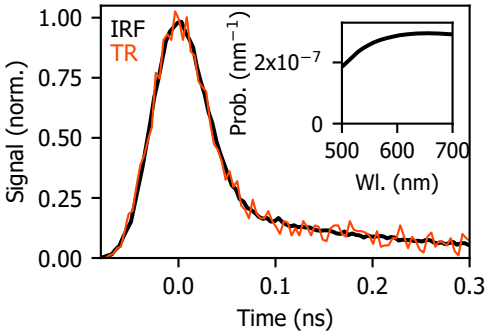


Figure 2.9: Time resolution of a time-resolved CL experiment. The time resolution of the TCSCP detection system is measured by acquiring a time trace of the fs-laser (black curve), corresponding to ~ 60 ps. The orange curve shows the decay statistics of transition radiation on a Au sample when exciting with a 30 keV pulsed electron beam (650 ± 100 electrons per pulse). The TR emission was spectrally filtered in the 620 ± 5 nm range. Inset: theoretical calculation of the spectrum of emission probability for TR per electron and spectral bandwidth. Wl.: wavelength.

obtained when directly sending the 2$^{\text{nd}}$ harmonic ($\lambda_{\text{exc}}$ = 517 nm) of the fs laser into the TCSPC setup (black curve). Given that the laser pulse width is ~ 250 fs, the curve indicates the resolution of our detection system (IRF), which we find to be $\Delta t_{\text{IRF}} \approx 60$ ps.

Figure 2.9 also shows the decay statistics of transition radiation (TR) obtained after excitation of a single-crystal Au sample with a 30 keV electron beam (650 ± 100 electrons per pulse, $V_{\text{ext}}$ = 650 V, $C_1$ = 1050 V, 1 mm aperture) (orange curve). In the experiment we used a 620 ± 5 nm bandpass filter to avoid temporal spread due to dispersion in the fiber, given the broad spectral emission of TR. A theoretical calculation of the spectrum of TR is shown in the inset of Fig. 2.9 [25]. TR emission can be considered as instantaneous (~ 20 fs [31]), thus the decay statistics are dominated by the TCSPC response function ($\Delta t_{\text{IRF}}$) and electron pulse width ($\Delta t_{e^-}$). We find that the time trace of TR matches well with the resolution of this method measured with the laser. From this experiment we can set an upper limit for the electron pulse width of ~ 10 ps, in agreement with the maximum pulse width estimated from the electron energy spread, as described above (6.4 ps). The upper limit is estimated by accounting for errors in the fitting procedure and differences between experimental sets.

### 2.7.2. APPLICATION: CL LIFETIME MAP

One of the advantages of performing time-resolved CL measurements is the ability to study the electron excitation and photon emission dynamics at the nanoscale. Hence, we tested our USEM by studying a GaN nanowire containing five vertically-aligned InGaN/GaN quantum wells [42]. An SE image of the nanowire is shown in Figure 2.10a, which was obtained using a 10 keV continuous electron beam. Fig.

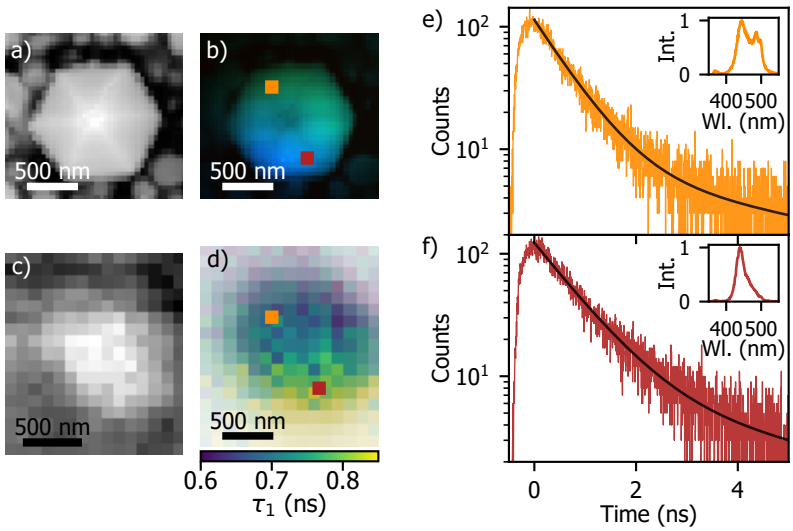


Figure 2.10: CL lifetime maps of InGaN/GaN quantum wells embedded in a GaN nanowire. (a) SE image of the top of the nanowire obtained with a 10 keV continuous electron beam. (b) False-color RGB map of the CL emission, obtained with a continuous electron beam. (c) SE image of the same nanowire obtained in pulsed conditions ($V_{ext}$ = 650 V, ~ 5 pA). (d) Lifetime map of the nanowire, in which the colorscale indicates the fast component of the decay ($\tau_1$) and the transparency reflects the amount of signal collected in each pixel. (e, f) Examples of time traces obtained at the positions indicated in (d). The decays are fitted with a double exponential function (black curves). Inset: CL spectra obtained at the two positions indicated in (b). Abbreviations: Wl. is wavelength and Int. is intensity.

2.10b shows a false-color RGB CL map, obtained by dividing the spectral range in three color channels: blue (corresponding to emission in the 400 – 450 nm range), green (450 – 500 nm) and red (500 – 550 nm). We observe that CL emission is not uniform on the nanowire, but there is a slight red-shift in the top region compared to the bottom one. This difference in spectra is clearly observed in the insets of Figs. 2.10e, f, showing two spectra taken at the positions on the nanowire indicated in Fig. 2.10b. The spectrum obtained on the top part of the nanowire exhibits two peaks centered around 440 nm and 490 nm, while the one corresponding to the bottom part of the nanowire exhibits a single peak at 440 nm.

Next, we measured the temporal CL statistics as a function of electron beam position. Fig. 2.10c shows the SE image obtained in pulsed conditions. In this case we used $V_{\text{ext}}$ = 3000 V, $C_1$ = 885 V and 60 µm aperture. The laser repetition rate was set to 25.19 MHz and we used a laser energy of 29 pJ, resulting in an electron current of $I \sim 5$ pA. The spatial resolution is clearly worse than in the continuous case, which could be improved by further reducing the electron current, but at the expense of a lower CL signal. Figs. 2.10e,f show two examples of traces obtained at two different positions on the nanowire, corresponding to approximately the same positions as for the spectra in the inset. Here the CL signal was optically filtered

with a 500 nm shortpass filter. The solid curves represent the fits obtained when fitting the time traces with a double-exponential decay, defined as

$$f(t) = S\left(A_1 e^{-t/\tau_1} + A_2 e^{-t/\tau_2}\right). \tag{2.7}$$



Here $\tau_1$ and $\tau_2$ are the characteristic lifetimes for each exponential, $S$ is the total amplitude of the curve and $A_1$ and $A_2$ are the corresponding weights of each exponential ($A_2 = 1 - A_1$). We obtain that the decay from the traces can be fitted with a fast ($\tau_1 \approx 0.7$ ns) and a slow ($\tau_2 \approx 7.5$ ns) component. Fig. 2.10d shows a map of $\tau_1$, in which the color scale represents the extracted value of $\tau_1$, and the transparency of each pixel indicates the CL intensity and weight of this decay compared to $\tau_2$. We obtain a value of $\tau_1 \approx 0.6$ ns on the top-left of the nanowire, while the measurements on the bottom part of the nanowire exhibit a slightly slower decay, $\tau_1 \approx 0.85$ ns. Figure 2.11a shows the map obtained for the second characteristic decay, $\tau_2$, which does not exhibit a clear spatial dependence. Fig. 2.11 also shows the relative contributions of each decay component (b and c, respectively) as a function of the position on the nanowire. The lack of spatial features suggests that both decay components are equally present on the different positions of the nanowire, with the main spatial dependence being in the value of the fast decay $\tau_1$. In order to elucidate the origin of this spatial dependence we should perform further experiments and analysis, which are beyond the scope of this section. This experiment shows that we can perform quantitative time and spatially-resolved CL measurements using a pulsed electron beam, despite the lower spatial resolution.

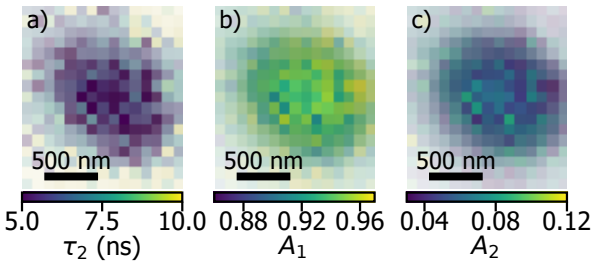


Figure 2.11: Lifetime map fits of InGaN/GaN quantum wells in a GaN nanowire. Spatial maps of the slow decay ($\tau_2$, a) and weights of the fast and slow decays ($A_1$ and $A_2$, b and c respectively). The parameters correspond to the variables in Eq. 2.7.

## 2.8. CONCLUSION

In this chapter we have presented the design and characterization of a laser-driven USEM. In the first part of the chapter we have discussed the fundamental emission process of a Schottky FEG in continuous and pulsed modes, together with the technical implementation of our USEM. Next, we have used a retarding field analyzer to measure the energy spread of continuous and pulsed electron beams. We

show that the energy spread of a continuous electron beam is strongly influenced by the temperature of the electron cathode, decreasing from 1.86 to 0.59 eV, in accordance with the Schottky FEG emission theory. In the case of a pulsed electron beam, we observe a clear increase of the energy spread with increasing number of electrons per pulse, which is attributed to the effect of Coulomb repulsion between electrons from the same pulse. We obtain energy spreads ranging from 0.77 eV for an average of less than one electron per pulse, up to 14.4 eV for more than 1000 electrons per pulse. We characterize the spatial resolution of our USEM, obtaining a resolution of around $\sim 90$ nm in the limit of low current on the sample ($\leq 1$ pA), and we discuss the possible differences between our experiment and other studies, in which higher spatial resolutions are obtained. We show that decreasing the extractor voltage results in a loss of spatial resolution but increase of electron current, thus offering an alternative solution for applications in which a high electron current is critical. Finally, we discuss the time resolution of our time-resolved SEM and CL measurements. From the measurements of energy spread we estimate an electron pulse width of 416 fs for pulses containing less than one electron, on average, in which case the electron temporal resolution is limited by the laser pulse width. In the case of more than 1000 electrons per pulse, we calculate a widening of the electron pulse width up to 6.4 ps. The time resolution in CL experiments is $\sim 60$ ps, limited by the detection system. The feasibility of our USEM to perform time-resolved CL experiments is evaluated by showing an example of CL measurements on nanowires containing InGaN/GaN quantum wells.

# 3

# PUMP-PROBE CATHODOLUMINESCENCE MICROSCOPY

*We introduce pump-probe cathodoluminescence microscopy (PP-CL) as a novel technique to study ultrafast dynamics in materials using combined and synchronous excitation of electron and laser pulses. We present the design, implementation and characterization of the PP-CL setup. The light emitted by the sample, either PL, CL or a combination of both, is analyzed through spectral, time-correlated and lock-in measurements. We discuss the main considerations to take into account in PP-CL experiments and present the differences and similarities between PL and CL emission in terms of excitation volume, injection density, spectrum, quantum efficiency and carrier dynamics. The comparison is illustrated with experiments on GaAs and GaN substrates. Finally, we present the initial studies of carrier dynamics in $Cu_2ZnSnS_4$ using PP-CL.*

## 3.1. INTRODUCTION

Cathodoluminescence (CL) microscopy is a powerful technique to resolve optical properties down to the nanometer scale, given the use of electrons as the excitation source. The spatial resolution of CL is limited by the electron beam size (~ nm), the interaction volume of the electron and carrier diffusion in the material. Recently, the emergence of ultrafast electron microscopy has enabled time-resolved CL studies, in which the emission and excitation dynamics of materials are investigated at the nanometer scale [72, 123, 124]. The time resolution of TR-CL is typically limited by the detection system (~ tens of ps). Instead, by combining optical and electron excitation in a pump-probe configuration we can achieve temporal resolutions down to the hundreds of fs regime, similar to optical pump-probe systems,

while taking advantage of the high spatial resolution given by the electron beam [96].

Pump-probe measurements, usually based on double-laser beam excitation, are routinely used across different research fields, including biochemistry, materials science and molecular physics [125–127]. In these experiments, a sample is excited with a pump beam (typically a laser pulse) and the resulting state is probed with a second beam (for example, another laser pulse), thus enabling the study of ultrafast processes. Even though fully optical pump-probe configurations are the most common ones, many different pump-probe schemes have been proposed, with changes either in one or both of the pump/probe beams [128, 129] or the detection scheme [130, 131]. In electron microscopy, pump-probe measurements using a laser-pump electron-probe configuration have been demonstrated [62, 75, 132]. A pump-probe based technique that has recently become popular is photon-induced near-field electron microscopy (PINEM), typically performed in a (scanning) transmission electron microscope, (S)TEM, which is based on the study of the electron energy loss and gain after interaction with an optically-excited nanostructure [87–89]. Other pump-probe-type works in a TEM include the study of the formation of chemical bonds [83], magnetization dynamics [84, 133] and optically-excited phonon modes [134, 135]. In scanning electron microscopes (SEM), previous studies have investigated the recombination dynamics in semiconductors of optically-induced carriers by analyzing the variations in the secondary electron signal [75, 136, 137]. In all these cases the sample is excited by the laser pump, while the electrons act as a probe. The probe signals are thus transmitted electrons (used for real and Fourier-space imaging or EELS, among others) or secondary electrons, from which a real-space image is formed.

In this chapter, we discuss the implementation and characterization of the first pump-probe cathodoluminescence (PP-CL) setup. Similar to previous work, our setup consists of a dual-beam system, with both a pulsed electron and laser beam. In contrast to earlier work, the emission and excitation dynamics are investigated through the analysis of the emitted luminescence, either CL or photoluminescence (PL). Hence, our setup allows us to use the electron beam either as a pump, thus probing the effect with the laser, or as a probe, after pumping with the laser. We illustrate the use of PP-CL with initial investigations of CL enhancement on optically-excited $Cu_2ZnSnS_4$, in which the electron acts as a probe. In the next chapter (Chapter 4) we study electron-induced charge state transfer on diamond nitrogen-vacancy centers, in which the electron acts as the pump.

## 3.2. OVERVIEW OF THE PP-CL SETUP

Our pump-probe experiments rely on the use of an electron and laser beam, in which one (pump) brings the sample out of equilibrium and the other one (probe) records the new state of the material. Tuning the delay between pump and probe gives access to the dynamics of the induced effect. The process of pumping and probing is repeated over many cycles ($> 10^6$) in order to accumulate enough signal (stroboscopic mode) [43]. Hence, this method can only be used to study reversible

phenomena, given that the sample has to go back to a steady (unexcited) state before each cycle of pump-probe.

Our pump-probe CL setup integrates an SEM with an optical setup containing a femtosecond laser (Fig. 3.1). We use a Thermo Fisher Quanta 250 FEG SEM (0.5 – 30 keV), which has been modified to give optical access to the electron gun through a UV-transparent window. The femtosecond laser (Clark MXR) consists of a diode-pumped Yb-doped fiber oscillator/amplifier system, providing 250 fs pulses at an output wavelength of ~ 1035 nm and tunable repetition rate (200 kHz-25.19 MHz). The laser beam is directed towards an optical setup (harmonic generator, HG) containing a set of BBO crystals (Clark MXR) to obtain the $2^{nd}$, $3^{rd}$ and $4^{th}$ harmonics of the fundamental beam ($\lambda$ = 517,345 and 258 nm, respectively). Figure 3.2 shows an image of the HG setup with the corresponding beam paths for the different harmonics. The HG setup is built such that we can use different combinations of two harmonics simultaneously, thus offering a large flexibility in a pump-probe experiment.



The PP setup can be divided into three main parts: electron, light-injection, and collection paths. The electron path consists of the coupling of the $4^{th}$ harmonic laser beam ($\lambda$ = 258 nm) to the electron gun to induce photoemission of electrons. A detailed description of the electron path and the photoemission process is provided in Chapter 2. The light-injection path refers to the set of optical components designed to direct the laser beam towards the SEM chamber and focus it on the sample. The collection path denotes the set of optics and detection systems that we use to analyze the luminescence from the sample (either PL or CL).

The SEM, the collection path and part of the electron path are mounted on an air suspension system (see Fig. 3.1a), meaning that they move freely to compensate for vibrations in the room. Instead, the rest of optical components, including the laser, is mounted on a non-floating optical table. We use two identical feedback systems (TEM-Messtechnik $\mu$-Aligna) (for the electron and light-injection paths, respectively) to actively track the movement of the floating section and move the laser beam accordingly, such that the alignment between both sections is maintained. The feedback system is composed of a position-sensitive detector (PSD), mounted on the floating section, and two motorized mirror mounts, mounted along the non-floating part (either the electron or the light-injection path). All components are connected through a controller. We use a beam sampler to send a small fraction of the laser beam to the PSD, which tracks the motion of the SEM with respect to the laser beam, and the mechanical actuators are moved accordingly to compensate for it.

We use an off-axis parabolic mirror (0.5 mm focal distance, parabola coefficient a=0.1 and 1.46$\pi$ sr solid angle collection) placed above the sample both to focus the laser beam on the sample and to collect the luminescence (PL or CL). The mirror has a 600 µm diameter hole placed above the focal point through which electrons pass. A motorized stage (Delmic Redux) controls the position of the mirror in the direction parallel to the sample plane. We bring the sample to the focal point of the mirror by lifting the sample stage up to a working distance of around 14 mm (see

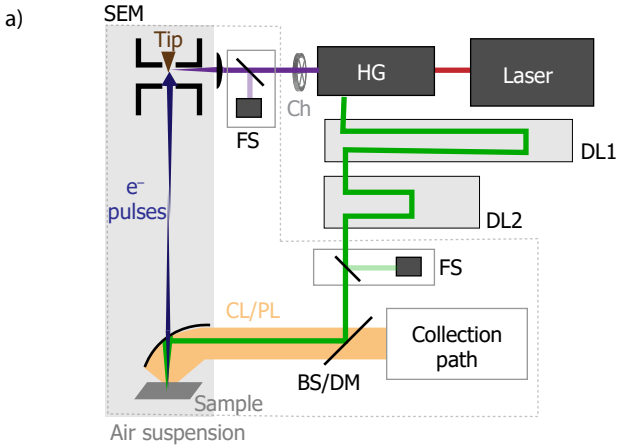


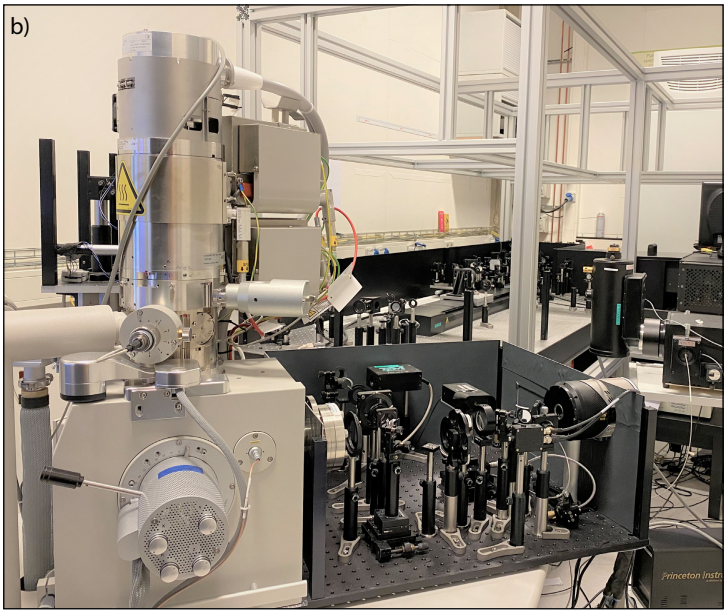


Figure 3.1: Pump-probe cathodoluminescence setup. Schematic (a) and photograph (b) of our PP-CL setup. The setup consists of the electron (purple), light-injection (green) and collection (orange) paths. The fundamental output ($\lambda = 1035\,\text{nm}$) of a femtosecond laser is converted to the 2$^{\text{nd}}$, 3$^{\text{rd}}$ and 4$^{\text{th}}$ harmonics ($\lambda = 517, 345$ and $258\,\text{nm}$, respectively) in the harmonic generator (HG) setup. The 4$^{\text{th}}$ harmonic is focused on the electron cathode of the SEM to generate electron pulses. The 2$^{\text{nd}}$ or 3$^{\text{rd}}$ harmonics are directed towards the SEM chamber using either a beam splitter or dichroic mirror (BS, DM) to optically excite the sample. The delay between electron and light pulses is controlled using two delay lines (DL1 and DL2). The alignment between the air-suspended parts and the optical table is maintained using a feedback system (FS).

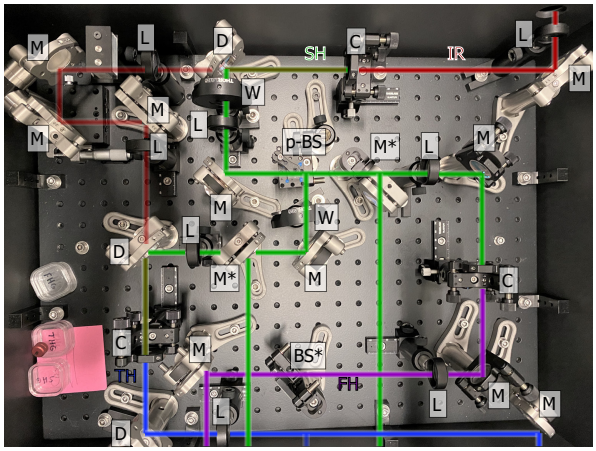


Figure 3.2: Photograph and beam path of the harmonic generator setup (Clark MXR). The fundamental laser beam (IR, $\lambda$ = 1035 nm) is directed towards a set of BBO crystals to generate the 2$^{nd}$ (SH, $\lambda$ = 517 nm), 3$^{rd}$ (TH, $\lambda$ = 345 nm) and 4$^{th}$ (FH, $\lambda$ = 258 nm) harmonics. This setup allows us to use different harmonics simultaneously. Abbreviations: mirror (M), lens (L), dichroic mirror (D), beam-splitter (BS), polarizing beam-splitter (p-BS) and BBO crystal (C). The asterisk denotes the components that can be flipped in and out of the beam path.

section 3.4.1). In the next sections we will describe in detal the coupling of the laser beam into the SEM chamber (light-injection path) and the detection and analysis of the emitted CL and PL (collection path).

## 3.3. LIGHT-INJECTION PATH

In our pump-probe setup, we excite the sample with both electron and laser pulses. Hence, we need to guide one of the harmonics of the fs laser towards the inside of the SEM chamber. In this thesis we use either the 2$^{nd}$ or 3$^{rd}$ harmonic beams ($\lambda$ = 517 and 345 nm, respectively) to optically excite the sample. The 4$^{th}$ harmonic ($\lambda$ = 258 nm) and fundamental laser beam ($\lambda$ = 1035 nm) could also be used in the light-injection path by choosing appropriate optics. Figure 3.1 shows a schematic of the complete setup, in which the green line represents the light-injection path. The path is also designed to control the arrival time of the light pulses with respect to that of the electron pulses, which is essential in a pump-probe experiment. We use two free-space optical delay lines (DL1 and DL2 in the figure), consisting of a set of two mirrors (in the case of DL1) or a hollow retroreflector (Newport UBR2.5-5UV, for DL2) mounted on a mechanical stage. Moving the delay stage by 15 cm corresponds to a time delay of 1 ns, given the double path of the light along the stage.

The first delay line (DL1) is manually controlled and is used to adjust the zero-delay between electron and light pulses. We only align this stage at the start of an experiment, and it is kept fixed during a measurement. The operating electron energy of the SEM (0.5 – 30 keV) determines the electron arrival time on the sample.

Hence, we adjust DL1 in each experiment such that the arrival time of the laser on the sample matches the one from the electrons. As a reference, a 30 keV electron arrives 7.5 ns earlier to the sample than a 5 keV one, which corresponds to a delay stage movement of 1.125 m. This delay line is also used to compensate for the different path lengths of the harmonics inside the harmonic generator, resulting in variations in their arrival time (~ 1 ns). The total length of DL1 is 1.26 m.

In a pump-probe experiment, we tune the delay between electrons and light by moving the second delay line (DL2). We use a motorized linear stage (Newport M-IMS600BPP, and motion controller Newport ESP301-1G), with total range of 60 cm (4 ns), minimum step size of 1.25 µm (8.3 fs) and precision of 0.65 µm (4 fs). The stage movement is controlled using a script developed for the Odemis software (Delmic), such that its movement is integrated with the data acquisition. In an experiment we typically choose the center of this delay line to correspond to the zero delay between electrons and light, meaning that we can scan in a −2 to 2 ns range (with sign defined depending on the arrival time of the laser with respect to the electron). The temporal alignment of electron and laser beams on the sample is discussed in section 3.6.

After DL2, the laser beam is directed towards the SEM chamber using an 8:92 pellicle beam splitter (Thorlabs BP208) or a dichroic mirror optimized for either the 2$^{nd}$ or the 3$^{rd}$ harmonic (Semrock Di02-R532-25x36 and Di01-R355-25x36, respectively). The position and angle of the beam splitter or dichroic mirror is controlled by a kinematic mount and a linear stage, thus allowing us to precisely align the laser with respect to the parabolic mirror. Finally, the light is focused on the sample using the parabolic mirror described in section 3.2. The alignment of the laser beam on the sample is discussed in section 3.5.

## 3.4. LUMINESCENCE (CL/PL) COLLECTION PATH

After excitation with an electron or laser beam (or both), the luminescence is collected by the parabolic mirror (described in section 3.2). The resulting luminescence beam is collimated and has a size determined by the mirror dimensions (23 mm × 11 mm) [33, 138]. The luminescence is further directed outside of the SEM towards the detection path setup. A photograph of this optical setup is provided in Fig. 3.3, together with the corresponding schematic. We have four types of detection methods: angular, spectral, time-correlated and phase-locked. The optical components in the collection path are either on magnetic mounts or can be easily removed, such that we have full flexibility for different optical configurations, depending on the experiment. In the next sections we describe each of these detection schemes.

### 3.4.1. ANGULAR DETECTION WITH CCD CAMERA

The alignment of the parabolic mirror and sample height is performed by sending the CL light directly to a 2D back-illuminated thermoelectrically-cooled CCD silicon array (PI PIXIS 1024B, 1024x1024 pixels), operating at a temperature of −70 °C.

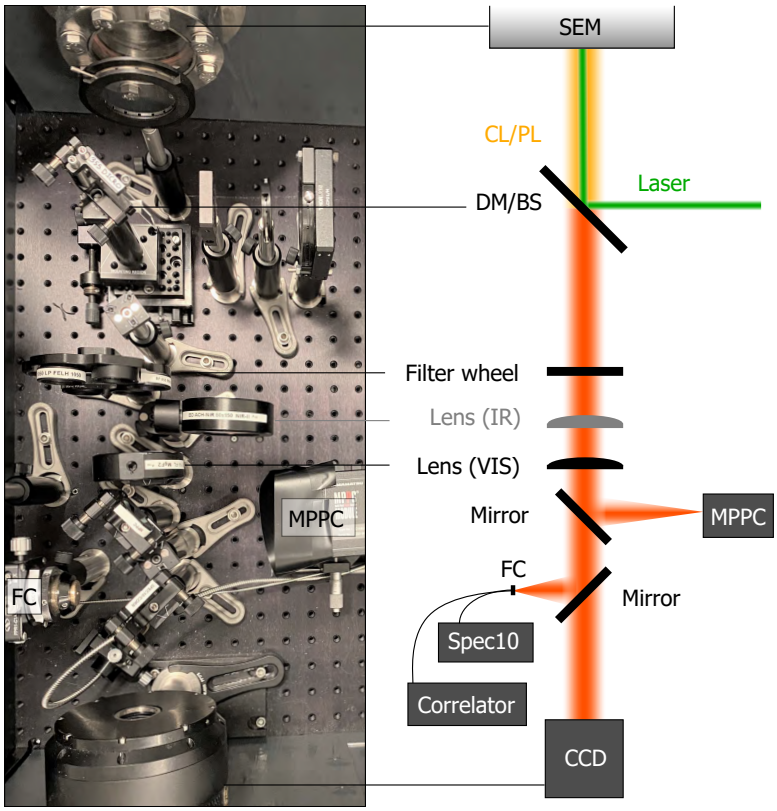


Figure 3.3: Luminescence (CL/PL) collection path. The light collected by the parabolic mirror is directed outside the SEM chamber for analysis. Different optical paths are available depending on the type of measurement: angular, spectroscopic, time-correlated or phase-locked. DM: dichroic mirror, BS: beam splitter, FC: fiber coupler, MPPC: multipixel phtoon counter.

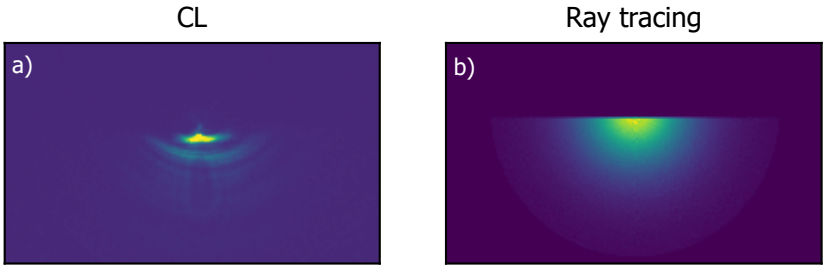




Figure 3.4: CL alignment. (a) Pattern of the collimated CL beam on the CCD obtained when the parabolic mirror is aligned with respect to the sample. The image was obtained when exciting a GaN sample with a 5 keV continuous electron beam. (b) Ray tracing calculation of the image on the CCD obtained for a point source placed at the focal point of the parabolic mirror.

In this case we do not place any additional optical components in the detection path, such that we directly collect the collimated CL beam. An example of the image obtained on the CCD for an aligned parabolic mirror and sample is provided in Figure 3.4a, together with a ray tracing calculation of the pattern on the CCD obtained for a point source placed at the focal point of the mirror (Fig. 3.4b) [33, 139].

### 3.4.2. SPECTROSCOPY

Spectrally-resolved measurements in the visible range are performed by sending the emitted light through an achromatic lens ($f$ = 160 mm, $d$ = 40 mm) and a silver mirror (Thorlabs PF10-03-F01) to couple it to a multimode fiber with 550 µm core diameter (OZ Optics QMMJ-55-IRVIS-550/600-3AS-2). The fiber is mounted on a manually controlled 2D mechanical stage to optimize the coupling of light into the fiber in the plane perpendicular to the optical axis. The fiber guides the light to a spectrometer (PI Acton SP2300i) containing a liquid-nitrogen-cooled silicon CCD array (PI Spec-10 100F/LN, 1340x100 pixels), which reaches a temperature of −120 °C for enhanced signal-to-noise ratio (SNR).

The system response of the spectral measurements is characterized by measuring the spectrum of transition radiation (TR) of a single-crystal Al sample, similar to previous works [26, 41]. Figure 3.5a shows TR spectra obtained upon excitation with a 30 keV continuous electron beam (143.9 nA) when using a 150 gr/nm grating with 500 and 800 nm blaze (black and dark red, respectively). Fig. 3.5a also displays the calculated probability of photon emission per electron and wavelength bandwidth (green dashed curve), obtained using the formalism described in section IVC of ref. [25]. Using both curves we can extract the collection efficiency of our system ($\eta_{\text{collection}}$), defined as the number of counts detected per photon emitted by the sample. The results are shown in Fig. 3.5b for both gratings. The collection efficiency is not sample dependent, and can be used for any kind of CL and PL experiment, as long as we keep the same acquisition settings as in the TR measurements. Differences in the alignment of the parabolic mirror and fiber coupling can lead to

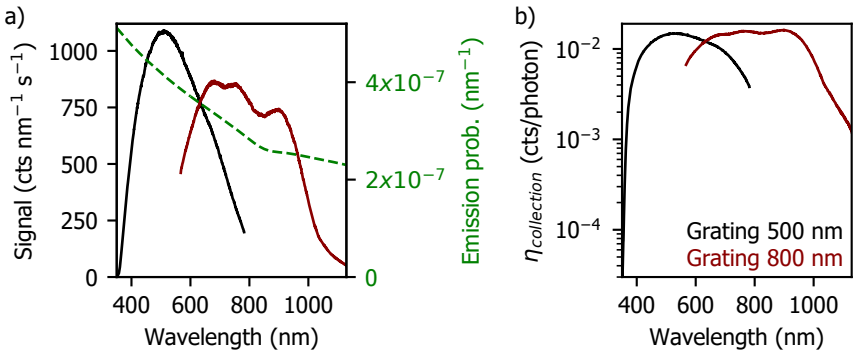


Figure 3.5: System response of spectral measurements. (a) Spectra of transition radiation of a single-crystal Al sample obtained under 30 keV electron excitation for a 150 gr/nm grating with 500 (black) and 800 nm (dark red) blaze. Right axis (green): Theoretical TR emission probability per electron. (b) Collection efficiency of the setup using both gratings of the spectrometer.

changes of ~ 30 % in the collection efficiency [26].

### 3.4.3. TIME-CORRELATED MEASUREMENTS

We study the dynamics of laser or electron excitation and light emission using two types of time-correlated measurements: time-correlated single-photon counting (TCSPC) and second-order autocorrelation ($g^{(2)}(\tau)$) measurements.

#### TIME-CORRELATED SINGLE-PHOTON COUNTING

Time-correlated single-photon counting (TCSPC) measurements rely on the excitation of the sample with a pulsed beam (either electron or laser), and the subsequent analysis of the temporal statistics of the emitted light. We use the same optics (lens and mirror) as for the spectral measurements to couple the luminescence to a multimode fiber with 105 µm core diameter (Thorlabs FG105UCA). The fiber is connected to an external optical setup, mounted on a portable breadboard. A photograph of the setup is shown in Fig. 3.6a, together with a schematic of the optical path (in orange). The luminescence is initially attenuated using a tunable neutral density filter and can be spectrally filtered with an optical filter. Next, the light goes through a set of lenses (both $f = 7.5$ cm) to collimate and refocus it onto a single-photon avalanche photodiode (SPAD) (PicoQuant PDM Series). The SPAD has an active area of 100 µm$^2$ × 100 µm$^2$ and is mounted on a 3D mechanical stage for optimum alignment with respect to the light beam. The count rate is always kept below ~ $10^6$s$^{-1}$ to avoid damaging the detector. The entire correlator path is enclosed inside a light-tight enclosure in order to reduce background signal and protect the SPAD.

TCSPC measurements are performed by recording a histogram of the photon arrival time with respect to a reference signal (trigger), which is done using a time-correlator (PicoQuant PicoHarp 200). We direct part of the laser beam (usually the

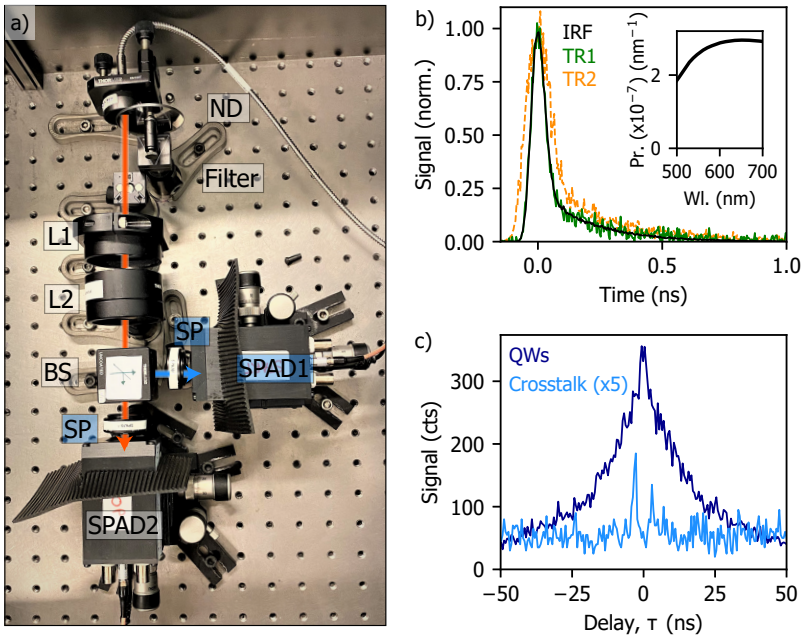


Figure 3.6: Time-correlated single-photon counting and autocorrelation $g^{(2)}(\tau)$ measurements. (a) Photograph of the optical setup used to perform time-correlated measurements. Here ND refers to a (tunable) neutral density filter, L1 and L2 are lenses, BS is a beam-splitter, SP is a short-pass filter and SPAD1 and SPAD2 are single-photon avalanche photodiodes. (b) Time resolution of the TCSPC system (~ 60 ps, black curve) obtained when sending the 2$^{nd}$ harmonic of the fs-laser towards the SPAD. The dispersion of the fiber is evaluated by measuring the time statistics of transition radiation on a single-crystal Au sample in the $620 \pm 5$ nm (TR1, green curve) and $532 - 670$ nm (TR2, orange curve) spectral ranges. Inset: theoretical calculation of photon emission probability of TR for a 30 keV electron pulse (Wl: wavelength). (c) CL $g^{(2)}(\tau)$ measurements of InGaN/GaN quantum wells (dark blue) and NV centers in diamond (light blue) obtained with a continuous 10 keV electron beam. The curve for the NV sample exhibits strong crosstalk.

2$^{nd}$ or 3$^{rd}$ harmonic) to a photodiode (PicoQuant TDA 200), which sends an electrical signal to the time-correlator, thus acting as a trigger. The time-correlator calculates the difference in arrival time between the trigger pulse and the electric pulse generated by the SPAD after detection of a CL/PL photon, thus resulting in a histogram of photon arrival time. In TCSPC measurements, only the first photon of each luminescence pulse is recorded. Hence, it is important to keep a low count rate to avoid an overestimation of the number of photons collected in the first time bins (pile-up effect), which would lead to the recording of artificially fast dynamics. This is solved by attenuating the emitted light such that, on average, less than one photon per pulse reaches the detectors.

The time resolution of the TCSPC setup is determined by the instrument response function (IRF) and dispersion in the optical fiber. We measure the IRF by directly sending the 2$^{nd}$ harmonic ($\lambda = 517$ nm) of the fs-laser into the TCSPC setup,

as shown in Fig. 3.6b (black curve). Considering that the laser pulse width is negligible (~ 250 fs), we obtain an IRF of 60 ps (FWHM), which is determined by the precision of the correlator, SPAD and photodiode. In the case of a spectrally broad luminescence signal, we also need to account for dispersion in the optical fiber. In order to quantify this effect, we measured CL time traces of transition radiation (TR) on a single-crystal Au sample using different optical filters. Fig. 3.6b shows traces obtained when filtering the signal in the $620 \pm 5$ nm (TR1) and $532 - 670$ nm (TR2) spectral ranges (green and orange curves, respectively). In this case we used a 30 keV pulsed electron beam containing an average of $40 \pm 15$ and $80 \pm 30$ (green and orange curves, respectively) ($V_{ext} = 650$ V, $C_1 = 1050$ V, see Chapter 2). The inset shows the theoretical emission spectrum, calculated using the formalism from ref. [25]. TR emission can be assumed as instantaneous (~ 20 fs [31]), hence the width of the time trace is determined by the IRF, dispersion of the fiber and electron pulse width (~ ps, see Chapter 2). We observe that the curve obtained when filtering the luminescence in the $620 \pm 5$ nm range resembles the one for the IRF obtained with the laser, thus suggesting that both dispersion in the fiber and electron pulse width are negligible. Instead, measuring luminescence in a broader range ($532 - 670$ nm) results in a broader time trace, which we attribute to dispersion in the optical fiber. From the measurements we estimate a dispersion of $\sim 0.2\,\mathrm{ps\,nm^{-1}\,m^{-1}}$, which is reasonable for a glass-type fiber. The temporal broadening due to dispersion in the fiber could be removed by having a completely free-space coupling system.



#### SECOND-ORDER AUTOCORRELATION ($g^{(2)}(\tau)$) MEASUREMENTS

To gain further insights in laser and electron excitation dynamics, we can study the CL and PL photon correlation statistics, which are measured using second-order autocorrelation ($g^{(2)}(\tau)$) measurements. Given a time-dependent luminescent intensity $I(t)$, $g^{(2)}(\tau)$ is defined as [140]

$$g^{(2)}(\tau) = \frac{\langle I(t)I(t+\tau)\rangle}{\langle I(t)\rangle^2}, \tag{3.1}$$

where the angle brackets denote the time average. Hence, in a $g^{(2)}(\tau)$ measurement we build a histogram of the number of coincidence events, defined as the detection of two photons, with respect to the time delay between them ($\tau$). Our $g^{(2)}(\tau)$ experiments are performed using a Hanbury-Brown and Twiss geometry [141]. We use the same optical setup as for TCSPC measurements, with the difference that we now use two SPADs (1 and 2 in Fig. 3.6a, blue path). Both detectors are connected to the time-correlator. A 50:50 beam splitter is placed after the last lens, such that the CL/PL photons have equal probability of being detected by each SPAD. After detection of a photon by SPAD1 at a given time $t_1$, the time-correlator acts as a stopwatch until a photon is detected on SPAD2 (at a time $t_2$). A count is added on the histogram at a delay corresponding to $\tau = t_2 - t_1$. A $g^{(2)}(\tau)$ measurement is always symmetric, given that there is an equal probability of detecting a photon first on SPAD1 and then SPAD2 ($+\tau$) or viceversa ($-\tau$). An example of a $g^{(2)}(\tau)$ measurement in CL is shown in Fig. 3.6c (dark blue), performed when exciting InGaN/GaN quantum wells with a continuous 10 keV electron beam. More details on

the spectrum of the sample and $g^{(2)}(\tau)$ measurements are shown in Chapter 5. In this example we used a $450 \pm 40$ nm bandpass filter.

A potential concern in $g^{(2)}(\tau)$ measurements is the phenomenon of crosstalk. After detection of a photon, SPADs can emit secondary photons, typically in the infrared spectral range (> 700 nm) [142]. In $g^{(2)}(\tau)$ measurements, the detection of this secondary photon by the second SPAD leads to the appearance of peaks at specific delays in the $g^{(2)}(\tau)$ curve. Figure 3.6c shows an example of this effect, obtained when exciting nitrogen-vacancy (NV) centers in diamond with a continuous 10 keV electron beam. The amplitude of the curve was multiplied by 5 for visibility purposes. The curve exhibits two peaks at delays corresponding to $\tau \approx \pm 2.8$ ns. Here we used a $650 \pm 75$ nm bandpass filter together with a 670 nm short-pass filter placed in front of each SPAD. The probability of having crosstalk can be reduced by further filtering out the longer wavelengths, as shown in Fig. 3.6c (dark blue). Hence, in this setup, $g^{(2)}(\tau)$ measurements are limited to wavelengths ranges below $\sim 600$ nm.

### 3.4.4. LOCK-IN DETECTION

The previously described detection systems are based on the direct collection and analysis of the emitted light. In pump-probe mesurements we have two signals: photoluminescence and cathodoluminescence, usually with very different magnitudes. This means that any spectrally or temporally-resolved measurement performed with the methods described above will be dominated by the largest signal. Hence, the analysis of the weaker signal becomes challenging, given that it can become buried in the noise of the larger signal. In our PP measurements, PL is typically several orders of magnitude larger than the CL signal, partially due to the larger PL spot area compared to the CL one, as will be discussed below (section 3.5.1). Moreover, when using the laser as a pump, a large excitation fluence is usually needed to achieve nonlinear regimes, thus further increasing the PL/CL ratio.

A method to extract the weaker signal (here, CL) is by decreasing the measurement bandwidth, such that noise is reduced, by means of lock-in detection. In this case, we focus the luminescence (CL/PL) on a thermoelectrically-cooled multipixel photon counter (MPPC module, Hamamatsu C14455-3050GA, 2836 pixels). The MPPC is connected to a lock-in amplifier (Stanford Research Systems RS830 DSP). Lock-in amplifiers work as phase-sensitive detectors, which can isolate small signals modulated at a known frequency and filter out other frequency components, thus improving the signal-to-noise ratio. This allows us to separate the desired signal from noise or background signal. In our experiments, we use an optical chopper (Thorlabs MC2000B-EC) to modulate the laser beam that we use to generate electron pulses ($4^{\text{th}}$ harmonic), typically at a few hundreds of Hz, thus resulting in a modulated CL emission. The chopper is also connected to the lock-in amplifier and serves as a reference signal. This mechanism allows us to isolate the CL signal from a large PL background, given the difference in CL and PL modulations.

In a pump-probe measurement we usually compare the magnitude of the probe

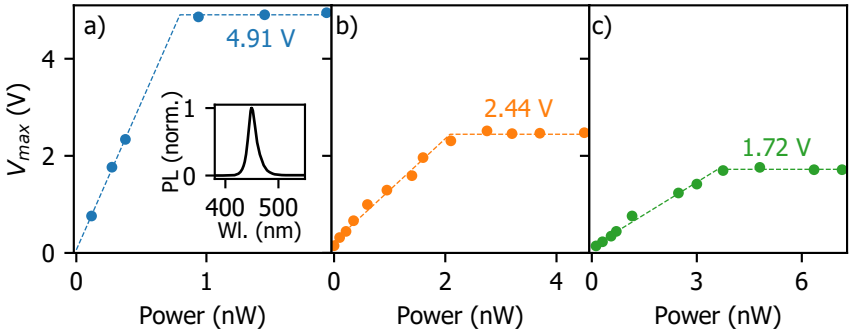


Figure 3.7: Response curve of the multi-pixel photon counter (MPPC) module. Dependence of the output voltage on the PL power incident on the MPPC at 1, 5.04 and 25.19 MHz repetition rates (a,b and c, respectively). The measurement was performed when exciting InGaN/GaN quantum wells with the 3rd harmonic of the laser. The inset in (a) shows the PL spectrum.

signal (either CL or PL) with and without pumping the sample (with laser or electrons, respectively). Hence, the detector (MPPC in our case) should have a low noise level so that it can detect small signals, in our case CL (< pJ), and a large dynamic range so that large PL signals do not saturate the detector, thus causing nonlinear behavior. Saturation of the MPPC during the experiment would result in artificially low signals in the pump-probe measurement compared to the reference (only CL or PL) one.

The output voltage of the MPPC as a function of incident power is shown in Figure 3.7 for different laser repetition rates. Here the input power is PL emission from InGaN/GaN quantum wells upon excitation with a $\lambda = 345$ nm laser beam (3rd harmonic). The PL spectrum is shown in the inset of Fig. 3.7a, and shows emission in the $400-450$ nm spectral range [41] (see also chapter 5). We chose to perform the characterization using PL emission, instead of directly sending the laser towards the MPPC, to mimic the conditions of an actual pump-probe experiment. The PL power was measured using a silicon photodiode (Thorlabs S120VC) placed along the PL path. Given the lower sensitivity of the photodiode compared to the MPPC, we placed a neutral density (ND2) filter in front of the MPPC to attenuate the incoming PL. The MPPC shows a linear response up to a certain power $P_{\max}$, above which saturation is observed. The curves obtained at different repetition rates exhibit a different $P_{\max}$, ranging from 3.6 nW at 25.19 MHz down to 0.8 nW at 1 MHz. We obtain a maximum output voltage of 4.98 V at 1 MHz, very close to the expected maximum output of the MPPC (5 V). Instead, the maximum voltage goes down to 2.44 and 1.72 V for 5.04 and 25.19 MHz, respectively. The dependence of the maximum power and output voltage on the repetition rate is attributed to the pixel recovery time. This analysis shows that in a pump-probe experiment it is crucial to ascertain that the output voltage of the signals (CL, PL and CL+PL) is sufficiently below the maximum output at the operating repetition rate.

## 3.5. LASER FOCUSING ON THE SAMPLE

We use the same parabolic mirror for luminescence collection (section 3.2) to focus the laser beam on the sample. This configuration allows us to focus the light down to a micrometer size spot without introducing additional components in the SEM chamber. Focusing with a parabolic mirror requires a precise alignment, given that any small misalignment can lead to aberrations, thus degrading the shape of the laser spot [143, 144]. Moreover, a precise spatial overlap of electrons and light is essential in pump-probe experiments. In this section we investigate the spot size of the laser on the sample and its alignment with respect to the electron beam.



In the experiments, we align the parabolic mirror by bringing the sample into focus while optimizing the CL pattern on a CCD camera, as explained in section 3.4.1. This guarantees maximum collection of the CL emitted light. The laser beam is then aligned on the sample by mechanically tuning the angle of the dichroic mirror or beam-splitter (see Fig. 3.9a) and position it with respect to the parabolic mirror. We can also use the feedback system to precisely tune the mirror actuators, thus yielding a higher angular and spatial control.

### 3.5.1. CHARACTERIZATION OF THE LASER FOCUS

Direct imaging of the laser spot on the sample plane is challenging due to its size (µm) and limited space in the SEM chamber. Instead, we can examine the change in secondary electron (SE) yield after optical excitation. Previous works have studied changes in SE emission in a pump-probe configuration ([136, 137]), from which the laser spot was imaged on the sample. For simplicity, here we rely on non-reversible changes in the SE contrast induced after repeated excitation with the laser (typically >10 s). Figure 3.8a shows an SE image of a 30 µm-thick GaN film on a sapphire substrate (PI-KEM, undoped n-type) after 10 s exposure with the 3$^{rd}$ harmonic laser beam ($\lambda$ = 345 nm, 1.7 mW average power at 5.04 MHz). The scan was taken using a 5 keV electron beam with 380 pA electron current and 10 µs pixel integration time. We observe a centered elongated spot with a higher SE yield, which we attribute to the laser-exposed area. This is further confirmed by tracking the movement of this spot as we misalign the laser beam with respect to the sample, as will be explained below. The mechanism behind the change in SE signal upon laser excitation is unknown. We use a laser fluence ($\sim 0.4\,\mathrm{mJ\,cm^{-2}}$) well below the reported damage threshold of GaN under UV fs-laser excitation ($\sim 5\,\mathrm{J\,cm^{-2}}$) [145]. Hence, it is unlikely that laser ablation plays a role. Previous studies have reported a reduction of the surface roughness of GaN upon excitation with UV ns laser pulses [146, 147], which could explain the change in SE yield. The change in SE contrast could also be due to increased contamination on the optically-excited surface, similar to the contamination typically observed in SEMs in the electron-irradiated areas [148, 149]. Further experiments with varying laser power, repetition rate and exposure time could be performed to elucidate the origin of this effect.

We further analyze the shape of the laser spot by taking horizontal ($x$) and vertical ($y$) cross-sections of the SE image, as shown in Fig. 3.8b and c, respectively. In each case, the curve is obtained by integrating over the rectangle delimited by

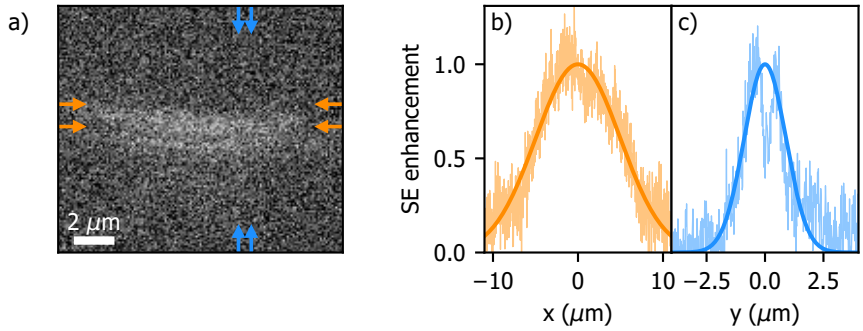


Figure 3.8: Visualization of the laser spot on the sample. (a) SE image of a GaN substrate obtained after excitation with the 3rd harmonic laser beam. Horizontal (b) and vertical (c) cross-sections of the SE image together with the corresponding Gaussian fits, from which we obtain a laser spot size of 11.7 and 2.1 µm in the horizontal and vertical direction, respectively.

the corresponding arrows (orange and blue in Fig. 3.8a). The position of this rectangle is chosen in both cases such that it yields the largest spread, thus ensuring that we characterize the largest section of the laser spot. In this experiment we ensured that the laser power was low enough to avoid any saturation effect. The solid lines represent Gaussian fits, from which we derive a laser spot size (full width at half maximum) of 11.7 and 2.1 µm in the horizontal and vertical directions, respectively. We attribute the asymmetry of the laser spot to non-perfect alignment of the laser beam with respect to the parabolic mirror.

### 3.5.2. LASER ALIGNMENT ON THE SAMPLE

As shown above, imaging the change in SE yield after laser excitation allows us to characterize the shape and size of the laser spot on the sample. However, we have only observed this effect on specific samples and under excitation with the 3rd harmonic laser beam. Hence, it is not practical for alignment in regular pump-probe experiments. Instead, we can align the laser beam on the sample by analyzing the image on the CCD of the PL beam, similar to the method used to align the parabolic mirror and sample height with CL (section 3.4.1).

We define good alignment of the laser beam as when it is centered with respect to the electron beam, that is, when it is at the focal point of the parabolic mirror. Figures 3.9(b-h) show various images of PL emission from GaN upon laser excitation (3rd harmonic beam, $\lambda = 345$ nm), together with the corresponding SE image of the laser spot on the sample, obtained using the method discussed above. Panel (b) shows an example of satisfactory alignment of the laser. Here the CCD image resembles the one expected for a collimated beam from an off-axis parabolic mirror, as shown in Fig. 3.4, and we observe that the laser spot is centered with respect to the electron beam. The rest of panels in Fig. 3.9 show the CCD pattern and SE

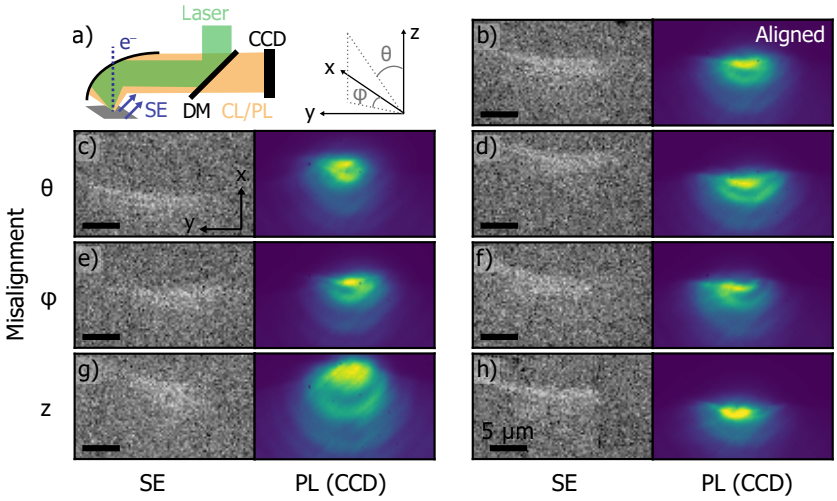


Figure 3.9: Laser alignment on the sample. (a) Left: schematic of the experiment, including PL collection on the CCD camera and secondary electron (SE) image formation. The position of the laser on the sample is tuned by moving the dichroic mirror (or beam splitter) (DM). Right: system of coordinates. (b-h) SE images of the GaN surface after excitation with the 3$^{rd}$ harmonic laser beam (left) together with the corresponding PL pattern on the CCD (right) for an aligned laser beam (b) and misalignments in the polar ($\theta$) (c,d) and azimuthal ($\phi$) (e,f) directions, as well as in the sample height (g,h).

image for different types of misalignments of the incoming angle of the laser (polar, $\theta$, and azimuthal, $\phi$, angles) (c-f) and height of the sample (g, h). As a reference, a schematic of the experiment and the coordinate system is shown in Fig. 3.9a. The angle of the laser with respect to the parabolic mirror is tuned by controlling the tilt of the dichroic mirror (DM). We observe a clear correlation of the misalignment of the laser spot with respect to the electron beam and the pattern on the CCD. This shows that we can rely on the alignment of the laser using this technique, instead of having to image the laser spot, as in the previous section.

We should note that the height of the sample is fixed through the CL alignment, corresponding to the optimum collection of CL. This alignment should also correspond to best focus of the laser for a perfectly-collimated laser beam. Imperfections in the collimation can result in a focal point slightly different than the one for CL collection.

## 3.6. TEMPORAL ALIGNMENT

Pump-probe experiments require precise control of the timing between pump and probe (electron and laser, or vice versa). Here we describe the temporal alignment of the laser and electron pulses. We record the decay statistics of PL and CL separately using the TCSPC setup (see 3.4.3), from which we obtain the difference in arrival time between electron and laser pulses on the sample. Figure 3.10

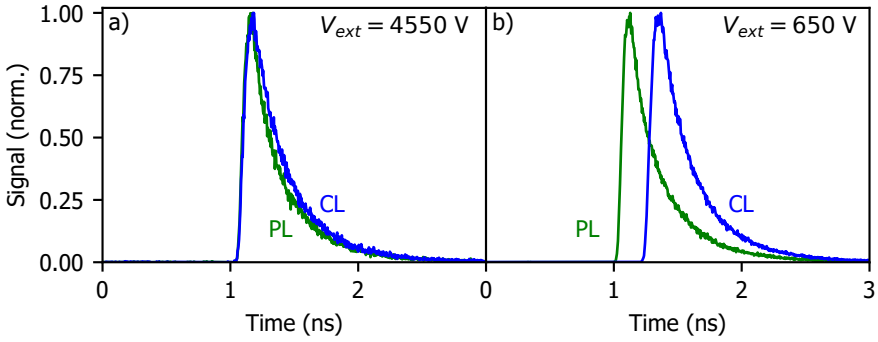


Figure 3.10: Temporal alignment of electron and light pulses. (a) PL (green) and CL (blue) decay traces from GaAs showing a good temporal overlap between electron and light pulses exciting the sample. (b) Same as in (a) but after lowering the extractor voltage, which results in a change in the arrival time of electrons.

shows decay traces of GaAs bandgap emission upon excitation with the laser beam ($\lambda_{exc}$ = 345 nm, ~ 5 mW) (green curve) and 30 keV electron pulses (~ 15 electrons per pulse) (blue curve). The extractor voltage at the electron gun was set to 4550 V. The x-axis indicates the time at which photons are detected on the SPAD with respect to the trigger signal. The temporal overlap of both traces, shown in Fig. 3.10a, indicates a good time alignment between electron and laser pulses. The accuracy of this method for determining the zero-delay is limited by the minimum bin size of the time-correlator (4 ps) and uncertainty in the determination of the arrival time of electrons or light from the decay curves. The latter becomes more complex when PL and CL exhibit different decay dynamics. Hence, we typically achieve an accuracy of ~ 10 ps. A higher accuracy in the determination of the zero-delay between electron and laser pulses can be obtained directly through a pump-probe experiment. In that case, the precision of the delay line stages creates an error of ~ 8 fs (see section 3.3), hence the temporal resolution is only limited by the electron (~ ps) and laser (~ 250 fs) pulse duration.

We should note that small changes in the electron or light path directly impact the temporal alignment. As we discussed previously, changing the energy of the electrons from 5 to 30 keV results in a delay of 7.5 ns (section 3.3). The conditions in the photoemission of electrons, discussed in Chapter 2, also determine the arrival time of the electrons. Figure 3.10b shows decay traces of GaAs obtained under the same conditions as in (a) but at low extractor voltage ($V_{ext}$ = 650 V). We observe that the CL is now delayed by ~ 200 ps with respect to the PL, which is attributed to the different speed at which electrons travel along the extractor plate. Hence, a precise temporal alignment is essential before starting a pump-probe experiment. Such accurate measurements of the timing of electron arrival can give further insights in electron dynamics in both the electron source and column, both in SEM and TEM.

## 3.7. COMPARISON BETWEEN CL AND PL

Until now we have focused on the technical aspects of our pump-probe CL setup, including its characterization and different analysis techniques. Here we describe further considerations that are important to take into account when performing a pump-probe experiment, related to the difference between electron and light excitation. PL and (incoherent) CL are often considered as two analogous methods to study the optical properties of materials. They both rely on the spontaneous emission of photons after excitation of a material with either a laser (PL), or high-energy electrons (CL). However, there are significant differences between both types of excitations. In this section we discuss the differences in excitation volume, deposited energy density, spectral emission, quantum efficiency and carrier dynamics in both PL and CL experiments. We illustrate these differences with calculations and experiments on bulk GaAs and GaN samples. All of the experiments are taken in our PP-CL setup, which allows us to excite the same spot on the sample and use the same collection system for both CL and PL emission. Even though each sample studied in PP-CL will require a specific analysis, these results allow us to evaluate the main trends and key parameters for pump-probe experiments.

### 3.7.1. EXCITATION VOLUME AND ENERGY DENSITY

One of the main discrepancies between electron and laser excitations is the initial excitation volume. In the case of laser excitation, the beam size typically ranges from hundreds of nm to several μm (see section 3.5.1). The penetration depth of the laser light in the sample is determined by the absorption coefficient of each specific material at the excitation wavelength. In contrast, electron beams typically exhibit much smaller spot sizes, from a few nm for a continuous beam to a few hundreds of nm for a pulsed beam, as explained in chapter 2. The primary electron beam travels through the material while suffering inelastic collisions, until it loses all of its energy. The excitation depth, and thus interaction volume, is highly dependent on the initial electron energy.

The difference in excitation volume in PL and CL is illustrated in Figure 3.11. The figure shows calculated maps of the deposited energy density in GaAs for 5 and 30 keV electron beams (a,b) and laser excitation with a wavelength of 345 and 517 nm (c,d, corresponding to the 3$^{rd}$ and 2$^{nd}$ harmonics of our laser). The CL maps are derived from the results of Monte Carlo simulations of the electron trajectory inside the sample, performed using the Casino software [1]. We have assumed an electron beam radius of 20 nm, which is an intermediate between our SEM resolution using continuous and pulsed electron beams. The PL maps are calculated assuming an initial symmetrical Gaussian laser spot with $\sigma = 3\,\mu$m and absorption profile derived using the Beer-Lambert law. The optical parameters of GaAs are extracted from ref. [150].

In all cases we assume a total deposited energy of 100 fJ, which would correspond to an average of ~ 120 electrons per pulse in the case of 5 keV and ~ 20 electrons per pulse for 30 keV. This corresponds to an electron current of 96 and 16 pA, respectively, and laser power of 0.5 μW (at 5 MHz). The color scale in each map is set

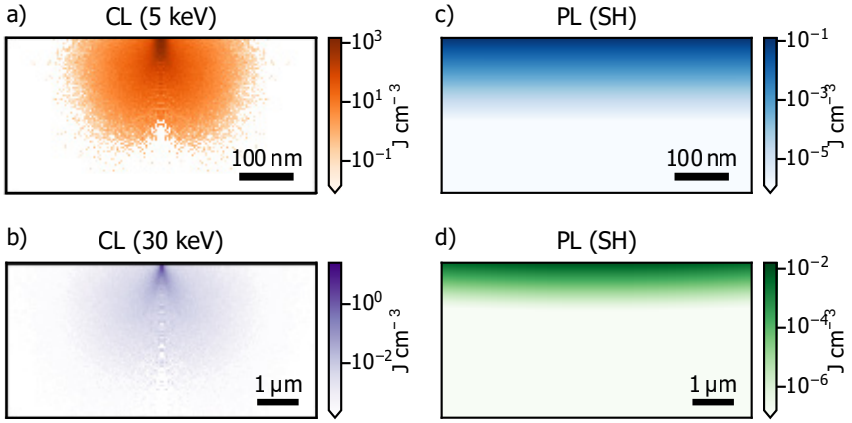


Figure 3.11: PL and CL deposited energy density volume in GaAs. (a) Calculated density of energy deposited on a GaAs sample by 5 keV electrons. (b) Same as in (a) but for electrons with initial energy of 30 keV, showing an increase in the interaction volume and decrease in the energy density with respect to the 5 keV electrons. (c) Deposited energy density after optical excitation with the 3$^{rd}$ harmonic beam for a Gaussian laser spot with $\sigma = 3\,\mu$m. (d) Same as in (c) but for the 2$^{nd}$ harmonic laser beam. In all four cases the total deposited energy corresponds to 100 fJ.

such that it covers 5 orders of magnitude with respect to the highest energy density.

Excitation with 5 keV electrons yields the largest energy density, corresponding to $\sim 10^{3}\,\mathrm{J\,cm^{-3}}$, due to the small excitation volume. Instead, at 30 keV the maximum energy density decreases by two orders of magnitude, down to $\sim 20\,\mathrm{J\,cm^{-3}}$, given the larger volume excited by the electron. The PL maps exhibit lower densities, $\sim 0.1$ and $0.01\,\mathrm{J\,cm^{-3}}$ for the 3$^{rd}$ and 2$^{nd}$ harmonic, respectively. Even though the penetration depth is close to that for CL, the larger size of the laser spot on the sample compared to the electron spot results in these lower densities.

To further compare the penetration depth of electrons and light, Figure 3.12 shows the characteristic energy deposition depth in CL as a function of the initial electron energy for GaAs (a) and GaN (b). This length represents the distance from the surface at which the energy of the electron has decreased by $1/e$ on average. In both materials the penetration depth goes from less than 10 nm for a 1 keV electron to more than 1 µm at 30 keV. The plot also shows the absorption length of the 2$^{nd}$ and 3$^{rd}$ harmonic laser beams for the two materials (horizontal lines). The optical data for GaAs and GaN are obtained from refs. [150] and [151], respectively. In GaAs the 3$^{rd}$ harmonic barely penetrates inside the material due to its large extinction coefficient, while the 2$^{nd}$ harmonic beam reaches a depth of $\sim 100$ nm, matching the energy deposition depth for electrons between 5 and 10 keV. In the case of GaN, the absorption length of the 3$^{rd}$ harmonic matches the ones for 5-10 keV electrons ($\sim 100$ nm). Data for the 2$^{nd}$ harmonic is not shown given that the photon energy is below the GaN band gap ($\sim 365$ nm). This analysis shows that in pump-probe

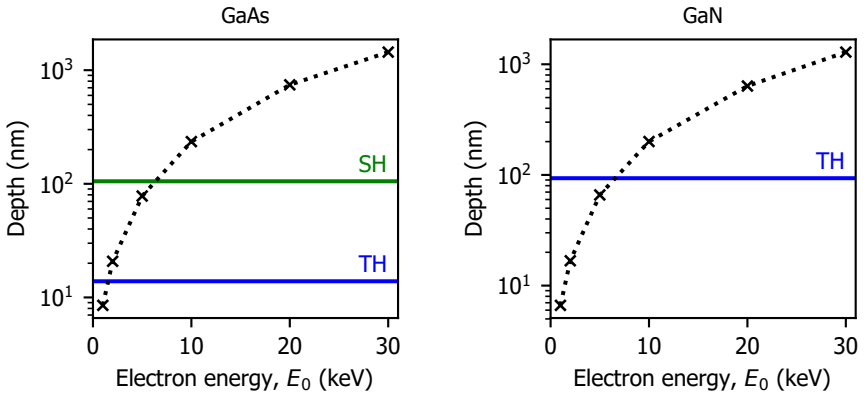


Figure 3.12: Electron and light absorption length in GaAs and GaN. (a) Calculated $1/e$ depth of energy deposition of an electron inside GaAs as a function of its initial energy, extracted from Monte Carlo simulations using the Casino software [1]. The horizontal lines correspond to the optical absorption length for $\lambda_{exc}$ = 345 and 517 nm (blue and green, corresponding to the 3$^{rd}$ and 2$^{nd}$ harmonic beams). (b) Same as in (a) but for a GaN sample.

experiments it is important to consider the overlap of electron and laser excitations inside the material, in addition to the spatial and temporal alignment discussed above (sections 3.5 and 3.6).

### 3.7.2. SPECTRAL EMISSION

In our PP-CL setup we can acquire PL and CL spectra on the same area on the sample, thus enabling a direct comparison between both spectral emissions. Figure 3.13a shows CL spectra obtained on an undoped GaAs sample (Nanografi, 350 ± 25 µm-thick) at different electron excitation energies (1 to 30 keV, curves from purple to yellow, respectively). The spectra were obtained using a continuous electron beam with electron current in the 400-900 pA range. The spectra exhibit a dominant peak around 860 nm, which matches with the band gap of GaAs at 300 K [152]. The spectra also show an additional peak around 1000 nm, which has been previously attributed to Ga vacancy defects [153, 154]. We observe that the band gap emission redshifts by around 7 nm with increasing electron energy. Redshift of band gap emission is frequently observed in GaAs for increasing temperature [152, 155], due to temperature-dependent band gap energy [156–158]. This suggests that higher electron energies induce a larger heating of the lattice, similar to the redshift observed on GaN nanowires for increasing electron current [159]. This redshift could also be related to differences in material quality along the depth of the sample, given that more energetic electrons probe deeper regions (see Fig. 3.13a). However, PL spectra using the 2$^{nd}$ and 3$^{rd}$ harmonics do not show this effect despite their different absorption depths (Fig. 3.12a), as will be seen below, thus discarding this hypothesis. Other effects, such as saturation of shallow defects, typically result

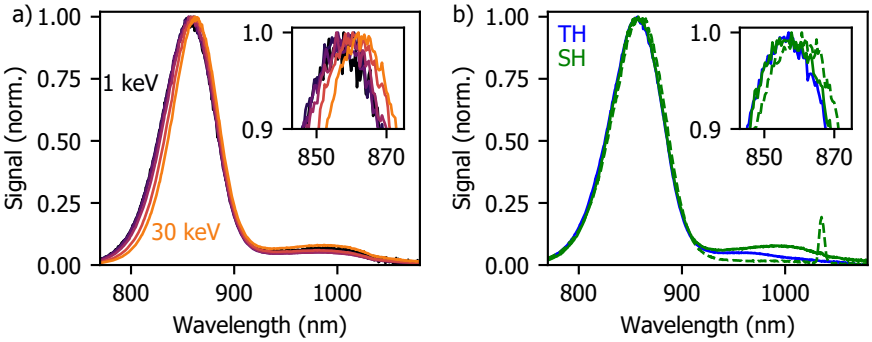


Figure 3.13: PL and CL spectra of GaAs. (a) CL spectra of a GaAs sample after excitation with a continuous electron beam with energy from 1 up to 30 keV (black to orange) (400-900 pA). The spectra exhibits a redshift with increasing electron energy. (b) PL spectrum on GaAs obtained after excitation with the 2$^{nd}$ ($\lambda_{exc}$ = 517 nm) and 3$^{rd}$ ($\lambda_{exc}$ = 345 nm) harmonics of the laser (solid green and blue curves, 33 and 2 µW, respectively). The plot also shows a measurement obtained at higher excitation power (2.5 mW, 2$^{nd}$ harmonic, dashed green curve), which also exhibits a redshift.

in a blueshift of the spectra [160], and are thus unlikely.

Figure 3.13b shows PL spectra obtained upon excitation with the 3$^{rd}$ harmonic (blue curve, 33 µW) and the 2$^{nd}$ harmonic (solid green curve, 2 µW). Both spectra exhibit a peak at around 856 nm, similar to the CL curves at low electron energy. However, exciting the sample with a larger laser power (2.5 mW, 2$^{nd}$ harmonic) also results in a ~ 4 nm redshift, as shown in Fig. 3.13b (dashed green curve), thus further suggesting that it is related to heating of the sample. The sharp peak at 1035 nm observed in this curve corresponds to the 2$^{nd}$ order of the spectrometer grating for the excitation wavelength ($\lambda_{exc}$ = 517 nm).

CL measurements on an undoped n-type GaN sample (PI-KEM, 30 µm-thick GaN on sapphire) also exhibit a small redshift (~ 2 nm) in the emission wavelength for increasing electron energy, as shown in Figure 3.14a (200 – 500 pA electron current). In this case, the spectra are centered around the band gap energy of GaN (~ 365 nm at 300 K [161]), and the redshift could also be attributed to an increase of lattice temperature, as previously reported [159, 161]. However, in this case the emission is composed of contributions from different peaks in the 360 – 370 nm spectral range. The contributions are more clearly visible in the PL spectrum obtained upon excitation with the 3$^{rd}$ harmonic laser beam (3 µW), as shown in Fig. 3.14b. Here we observe two peaks centered at 362 and 368 nm, as well as a broader and weaker peak around 380 nm. The presence of several spectral lines in GaN luminescence has been previously reported and is attributed to different defect-induced luminescence transitions [162]. Hence, the change in spectra observed in this case could also be attributed to differences in the contributions of the individual peaks for different electron energies. Given the different penetration depth of at varying electron energies, differences in defect concentration along the depth of

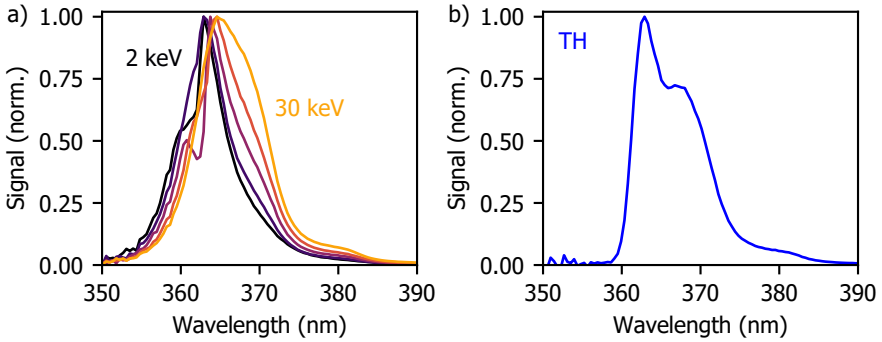


Figure 3.14: PL and CL spectra of GaN. (a) CL spectra of a GaN sample upon excitation with a continuous electron beam with energy from 2 up to 30 keV (black to orange) (200 – 500 pA). The spectra exhibits a redshift with increasing electron energy. (b) PL spectrum on GaN obtained after excitation with the 3rd harmonic laser beam ($\lambda_{exc}$ = 345 nm, 3 µW).

the sample could play a role. Further CL studies at low temperature, as well as comparison between samples with varying crystal quality, are needed to better understand the role of electron energy on the CL spectra. We should note that in our samples, the contribution of yellow-band emission, typically in the 500-700 nm spectral range [163], is negligible compared to emission around the band gap energy.

### 3.7.3. QUANTUM EFFICIENCY

In the previous section we have analyzed the difference between PL and CL in a qualitative way, by investigating the differences in emission spectra. Next, we compare quantitatively the PL and CL band gap emission in GaAs and GaN. To do so, we define a common figure of merit: the quantum efficiency ($QE$), that is,

$$QE = \frac{N_{\text{emitted}}}{N_{\text{carr}}} \tag{3.2}$$

where $N_{\text{emitted}}$ is the number of photons emitted in the sample and $N_{\text{carr}}$ refers to the maximum number of charge carriers generated after excitation with either electrons or light.

#### PL QUANTUM EFFICIENCY

In PL, absorption of a photon with energy larger than the band gap results in the excitation of an electron from the valence to the conduction band. The generated charge carrier thermalizes to lower energy states in the conduction band before recombining, either radiatively or non-radiatively. Hence, the maximum number of generated carriers directly corresponds to the number of absorbed photons, that is, $N_{\text{carr}} = (1-R)P_0 T \frac{\lambda_{\text{exc}}}{hc}$. Here, $R$ is the reflectance of the material at the excitation wavelength $\lambda_{\text{exc}}$, $P_0$ is the incident power, $T$ is the exposure time, $h$ is Planck's constant and $c$ is the speed of light.

To calculate the number of emitted photons ($N_{\text{emitted}}$), defined as number of radiative recombination events, from the signal detected on the spectrometer, we need to account for several loss factors in the luminescence collection. First, we account for reabsorption of the emitted photons. This loss factor ($\eta_{\text{reabs}}$) is calculated by applying Beer-Lambert's law on the initial absorption profile (see map of absorbed energy in Fig. 3.11c,d). We assume that re-emission of the reabsorbed photons is negligible, which is reasonable given the low quantum efficiencies obtained (as will be discussed below). Second, only photons emitted within the critical angle of the material can escape the sample. Assuming isotropic emission inside the material, the escape efficiency becomes $\eta_{\text{esc}} = 1 - \cos\theta_c$, where $\theta_c$ is the critical angle of the material. Third, we account for the mismatch between the laser spot size ($\sim 11\,\mu\text{m} \times 2\,\mu\text{m}$, section 3.5.1) and collection area of the parabolic mirror ($\sim 10\,\mu\text{m} \times 10\,\mu\text{m}$), meaning that not all photons emitted from the sample are collected. Taking into account the collection area of our mirror and the dimensions of our laser spot, we calculate this loss factor to be $\eta_{\text{spot}} \approx 0.7$. Finally, the collection efficiency of the rest of the optical system is accounted for using the calibration obtained from transition radiation (TR), as described in section 3.4.2. However, we need to correct for the fact that TR exhibits a toroidal angular emission pattern [26, 32], in contrast to the Lambertian pattern typically observed for semiconductors [26]. Taking into account the geometry of our parabolic mirror, the collection efficiency is $\eta_{\text{TR}} = 0.82$ for TR and $\eta_{\text{Lamb}} = 0.86$ for Lambertian emission [41]. Hence, we can express the quantum efficiency in PL as

$$QE_{\text{PL}} = \frac{hc}{(1-R)P_0 T \lambda_{\text{exc}}} \frac{\eta_{\text{Lamb}}}{\eta_{\text{TR}}\eta_{\text{esc}}\eta_{\text{reabs}}\eta_{\text{spot}}} \int_{\lambda_1}^{\lambda_2} \frac{S(\lambda)}{\eta_{\text{coll}}(\lambda)}\, d\lambda\,. \tag{3.3}$$

Here, $S(\lambda)$ is the acquired spectrum, in units of counts per spectral bandwidth, and $\eta_{\text{coll}}(\lambda)$ is the collection efficiency of the system (Fig. 3.5b). The limits of the integral, $\lambda_1$ and $\lambda_2$, are taken such that they include the entire PL emission spectrum.

#### CL QUANTUM EFFICIENCY

The excitation process in CL is fundamentally different from the PL case. After entering a material, the primary electron, with energy $E_0$, deposits energy in the sample through inelastic collisions. One of the dominant interactions of high energy electrons with a material is the generation of bulk plasmons (also referred to as volume plasmons), defined as the collective oscillation of valence electrons [13, 28, 29]. The energy of a bulk plasmon ($E_{\text{plasmon}}$), typically $10-30\,\text{eV}$, is determined by the density of valence electrons of the material [13], and is thus characteristic for each material. The excited bulk plasmons decay through the excitation of high-energy carriers, which thermalize to the lower states of the conduction band by generating carriers with lower energy, phonons and secondary electrons [28, 164, 165].

We then define the maximum number of thermalized carriers, with energy $E_{\text{BG}}$, generated in CL as

$$N_{\text{carr}} = N_p N_{c,p} \frac{IT}{q} \approx (1-\Gamma)\frac{E_0}{E_{\text{BG}}}\frac{IT}{q} \tag{3.4}$$

where $\Gamma$ is the fraction of back-scattered electrons, $I$ is the electron current, $T$ is the acquisition time and $q$ is the electron charge. $N_p = E_0/E_{plasmon}$ is the maximum number of plasmons created per electron, and $N_{c,p} = E_{plasmon}/E_{BG}$ is the maximum number of thermalized carriers created per plasmon. The approximate sign in the last equality of Eq. 3.4 represents the fact that in practice the number of carriers ($N_p$ and $N_{c,p}$) is an integer, which is taken into account in the calculations.

In order to calculate the number of emitted photons ($N_{emitted}$) we consider the same losses as in the PL case, except for the loss related to the mismatch between the laser spot and collection area of the mirror ($\eta_{spot}$). In CL, the excitation of electrons is very localized, and thus all photons are efficiently collected by the parabolic mirror. The expression for the quantum efficiency in CL is

$$QE_{CL} = \frac{E_{BG}}{(1-\Gamma)E_0}\frac{q}{IT}\frac{\eta_{Lamb}}{\eta_{TR}\eta_{esc}\eta_{reabs}\eta_{spot}}\int_{\lambda_1}^{\lambda_2}\frac{S(\lambda)}{\eta_{coll}(\lambda)}\,d\lambda\,, \tag{3.5}$$

with $S(\lambda)$ the CL spectrum in units of counts per spectral bandwidth.

We should note that the method and model presented here to calculate PL and CL quantum efficiencies might result in less accurate results than conventional techniques, such as PL quantum yield quantification [166] or direct EQE measurements. This lower accuracy is due to the error in the quantification of the spectra ($\sim 30\,\%$, as discussed in section 3.4.2). However, it enables direct comparison of PL and CL efficiencies at the same conditions and on the same area on the sample, which is critical to study the differences between electron and light excitation.

#### EXPERIMENTAL CL/PL QUANTUM EFFICIENCY

Figure 3.15 shows the CL quantum efficiency obtained for GaAs (a) and GaN (b) samples as a function of electron energy, extracted from the data presented in Figs. 3.13 and 3.14, respectively. We observe quantum efficiencies in the $10^{-4} - 10^{-2}$ range for GaAs and in the $10^{-4} - 10^{-3}$ range for GaN, which is reasonable considering reported values in literature [167, 168]. The quantum efficiency exhibits an increase with increasing electron energy in both GaAs and GaN of more than 1 order of magnitude. We hypothesize that this enhancement is due to the effect of surface recombination, as previously proposed in CL studies of GaN [169]. Surface recombination is known to impact the quantum efficiency in both GaAs and GaN [167, 170]. Electrons with larger energies penetrate deeper inside the material, as discussed above (section 3.7.1), thus creating carriers that are further away from the surface.

The PL quantum efficiency is also plotted in Fig. 3.15 for both GaAs and GaN (a and b) upon excitation with the 2$^{nd}$ and 3$^{rd}$ harmonic of the laser (green and blue horizontal lines, respectively). In GaAs, the extracted quantum efficiency is higher when exciting with the 2$^{nd}$ harmonic compared to excitation with the 3$^{rd}$ harmonic ($\sim 10^{-4}$ and $10^{-3}$, respectively). Given the larger absorption depth when using the 2$^{nd}$ harmonic beam (Fig. 3.12), these results match with the hypothesis that surface recombination is the mechanism responsible for the increase in quantum efficiency with increasing electron energy.

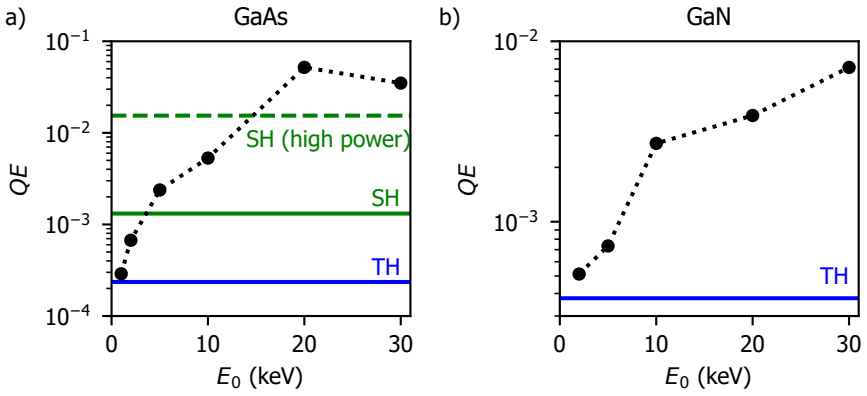


Figure 3.15: PL and CL quantum efficiency of GaAs and GaN. (a) CL quantum efficiency for GaAs extracted from the experiments shown in Fig. 3.13 and calculated using Eq. 3.5 for different electron energies, together with the PL quantum efficiencies (Eq. 3.3) for excitation with the 2$^{nd}$ and 3$^{rd}$ harmonic laser beams (green and blue horizontal lines). (b) Same as in (a) but for GaN (data from Fig. 3.14).

An additional explanation could be that the increase in quantum efficiency is related to the redshift in the emission spectra observed for both GaAs and GaN (Figs. 3.13 and 3.14). However, heating of the lattice, which produces a redshift, typically results in lower quantum efficiencies [155, 171, 172]. Hence, it is less likely that these effects are correlated, and the decrease of efficiency due to temperature might be weaker than the enhancement due to reduced surface recombination.

Finally, we found that the PL quantum efficiency upon excitation with the 2$^{nd}$ harmonic at high power (2.5 mW, same as in Fig. 3.13b) is also larger than at lower power (2.0 µW, solid lines in Fig. 3.15). A possible explanation for this could be saturation of non-radiative traps, either surface or bulk defects, thus leading to an improved quantum efficiency.

These results show that electron and laser excitation can result in different quantum efficiencies, which should be taken into account when performing PP-CL measurements. To fully elucidate the mechanisms behind the increase the changes in CL quantum efficiency we should perform further experiments, such as a systematic comparison of passivated samples, which are beyond the scope of this section. The method presented here to extract PL and CL quantum efficiencies offers a way to perform quantitative studies of both luminescence mechanisms.

### 3.7.4. CARRIER DYNAMICS

Finally, our PP-CL setup also allows us to study both PL and CL temporal decays. Here we perform time-resolved measurements on GaAs using the TCSPC setup discussed in section 3.4.3. Figure 3.16 shows CL decay traces obtained when exciting with 10 and 30 keV electron pulses (a and b, respectively) for different number of electrons per pulse. The number of electrons per pulse ranges from 2 up to ~ 720

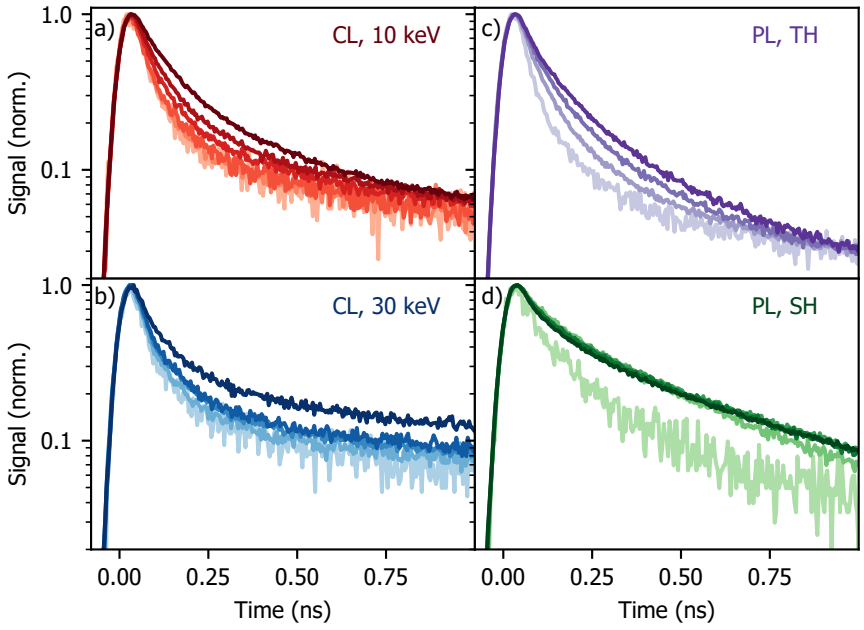


Figure 3.16: Decay dynamics in GaAs. (a) CL time traces obtained upon excitation with a pulsed electron beam (10 keV) containing an average of 2, 30, 110, 250, 380 and 720 electrons per pulse (light to dark orange). (b) Same as in (a) but for a 30 keV beam, with 0.4, 6, 30, 60 and 190 electrons per pulse (light to dark blue). (c) PL time traces obtained after laser excitation (3$^{rd}$ harmonic, $\lambda_{exc}$ = 345 nm) for increasing energy per pulse (3, 46, 113 and 211 pJ, light to dark purple). (d) Same as in (c) but for excitation with the 2$^{nd}$ harmonic ($\lambda_{exc}$ = 517 nm, ) (4, 105, 232, 334 and 498 pJ, light to dark green).

in the case of 10 keV (light to dark red curves), and from less than 1 to ~ 180 for 30 keV (light to dark blue curves). The experiments were done using an extractor voltage of 650 V. We also performed PL experiments obtained when exciting the sample with the 3$^{rd}$ and 2$^{nd}$ harmonics of the laser (c and d, respectively), and for increasing energy per pulse (from ~ 3 up to ~ 500 pJ), using a laser repetition rate of 5.04 MHz. In all cases we observe a dominant fast decay in the 100 – 200 ps regime. Interestingly, both CL and PL signals exhibit slower decays for increasing fluence, either electrons or photons. This observation is in contrast with the trends expected when only bimolecular or Auger processes dominate the recombination processes. In those cases, an increase in the initial carrier density leads to a faster decay of the signal [172, 173].

To further explore this effect, in Figure 3.17 we plot the characteristic $1/e$ time ($\tau_c$) as a function of the deposited energy per pulse, for both CL (a) and PL (b). The CL data shows a linear increase of $\tau_c$ from ~ 100 up to ~ 180 ps. The trends for 10 and 30 keV electrons are very similar, despite the difference in energy density (which is directly related to carrier density) expected for different electron energies

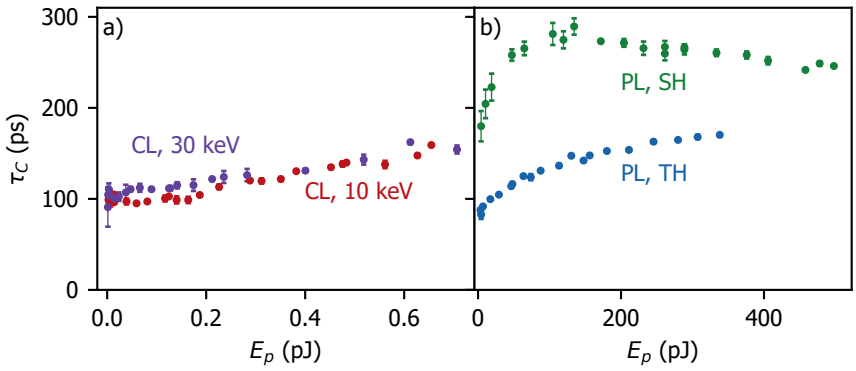


Figure 3.17: PL and CL decay times vs. injected energy. (a) Characteristic time ($\tau_c$) in CL as a function of the deposited energy per pulse for 10 and 30 keV electron beams. (b) Same as in (a) but for PL obtained upon laser excitation with the 2$^{nd}$ and 3$^{rd}$ harmonics.



(see section 3.7.1). This observation also suggests that bimolecular and Auger recombination are not the dominant decay mechanisms, since they directly depend on carrier density.

In the case of PL, we observe a difference between excitation with the 2$^{nd}$ or 3$^{rd}$ harmonic laser beams. Irradiation with the 3$^{rd}$ harmonic results in a characteristic time increasing from ~ 80 to ~ 160 ps for increasing deposited energy, which is in a similar range as the decay times found in CL. In this case the trend is sub-linear, and shows a gradual saturation for increasing energy per pulse. Instead, when using the 2$^{nd}$ harmonic beam we obtain larger $\tau_c$. We observe an increasing trend from ~ 180 to ~ 280 ps, up to an energy per pulse of ~ 90 pJ, above which the decay time slightly decreases to ~ 240 ps.

An increase in decay time for larger injected carrier densities has been previously observed and attributed to saturation of defect states [174–177]. At low injection levels, carriers have a high probability of being trapped. Instead, at higher injection levels, an increasing number of defects is occupied, thus effectively reducing the recombination rate of carriers. This hypothesis should be validated with further experiments and modelling. Time-resolved experiments at low temperature could help to evaluate the contribution of defects states to the observed decay times. Moreover, a complete decay rate model including the different recombination paths should be developed for a full understanding of carrier dynamics in GaAs.

Overall, the comparison between CL and PL excitation volumes, deposited energy densities, spectra, quantum efficiency and carrier dynamics provides insights into the differences between electron and light excitation of semiconductors, which should be accounted for in PP-CL experiments.

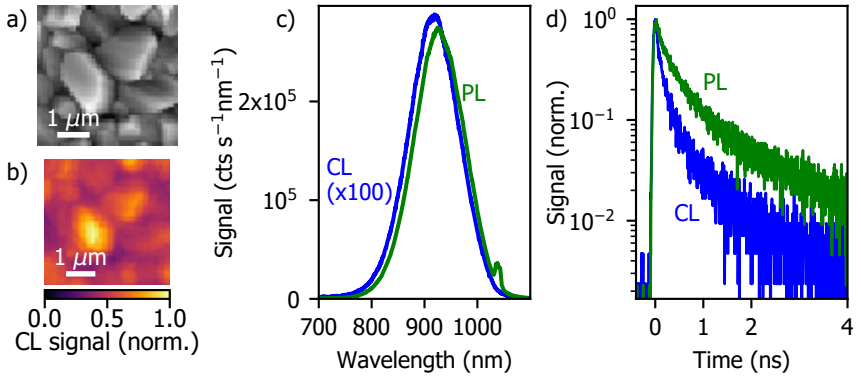


Figure 3.18: CL and PL measurements on CZTS. (a) SE image of a CZTS sample together with the corresponding CL map (b), showing the CL signal integrated over a 600 – 1000 nm wavelength range. (c) PL (green) spectrum obtained upon excitation with the 2$^{nd}$d harmonic laser beam, together with the CL spectrum (blue) obtained when using a 10 keV pulsed electron beam. The CL signal is a factor 100 lower than the PL signal. (d) PL (green) and CL (blue) decay traces obtained under the same conditions as (c).

## 3.8. EXAMPLE OF A PP-CL MEASUREMENT

Finally, we discuss the procedure and analysis of a complete PP-CL experiment. The PP-CL setup enables two possible configurations, with the electron acting either a pump or a probe. A full study of a PP-CL experiment in which the electron acts as a pump is presented in Chapter 4. Here, we describe the first results obtained using the second configuration of the setup, in which the electron acts as a probe.

We perform our study on a $Cu_2ZnSnS_4$ (CZTS) sample, which was fabricated by the group of Prof. X. Hao at the University of New South Wales (Sydney). The sample consists of a ~ 800 nm-thick CZTS layer deposited on top of a Mo/glass substrate. A ~ 3 nm layer of $Al_2O_3$ is deposited on top for passivation. CZTS is a promising new photovoltaic material, based on fully earth-abundant materials, and thus knowledge of its carrier recombination dynamics is important for further use in solar cells [178, 179].

Figure 3.18a shows a SE image of the sample obtained with a 10 keV continuous electron beam (~ 154 pA), from which we observe the different grain boundaries. We also show a CL map acquired simultaneously (Fig. 3.18b). The CL colormap represents the normalized CL signal integrated over the entire wavelength range, thus showing the dependence of CL emission on the position on the sample. The CL map reflects the position of the grain boundaries, with the darker regions corresponding to the edges of the grains. This spatial dependence of the CL intensity could be due to non-radiative carrier recombination near the grain edges, as well as differences in electron excitation efficiency and CL escape probability. A more detailed analysis is necessary, such as a $g^{(2)}(\tau)$ analysis, as discussed in Chapter 5,

from which we can extract the electron excitation efficiency.

CL and PL spectra of the sample are shown in Fig. 3.18c. The PL spectrum was obtained when exciting the sample with the 2$^{nd}$ harmonic laser beam ($\lambda$ = 517 nm, 25 pJ per pulse at 25.19 MHz). We use a 532 nm long-pass filter in the detection path to suppress the remaining pump light. The CL spectrum was obtained under a 10 keV pulsed electron beam containing 636 ± 33 electrons per pulse. We attribute the uncertainty in the number of electrons per pulse to the the variation of 4$^{th}$ harmonic laser power used to generate electron pulses. Here we used photoemission conditions for high current ($V_{ext}$ = 650 V, $C_1$ = 540 V, 1 mm aperture, see Chapter 2), thus resulting in a low spatial resolution. The CL spectrum has been multiplied by a factor 100 for easier comparison to the PL spectrum. The electron and laser beam conditions described here correspond to the ones used in the pump-probe experiments shown below. Both spectra exhibit an emission peak centered around 918 and 926 nm for CL and PL, respectively. These spectra are similar to the ones obtained in other works under optical excitation [160], and are usually attributed to close-to-bandgap emission. The differences in peak wavelength emission between PL and CL could be due to different levels of saturation of shallow tail states in each case. In our sample, we have also observed a change of PL peak emission as a function of laser power, similar to previous studies, which is attributed to saturation of trap states [160]. The small sharp peak around 1035 nm observed in the PL spectrum corresponds to the second-order diffraction of the excitation laser beam from the spectrometer grating. Fig. 3.18d shows PL and CL decay traces obtained using the TCSPC setup, which we used to temporally align the arrival of electron and laser pulses on the sample.

Next, we performed pump-probe experiments. Given the large difference between the CL and PL signals (PL is a factor 100 larger) we used lock-in detection, as described in section 3.4.4. The electron beam was modulated at a frequency of 287 Hz. The output voltage of the MPPC module was below 300 mV when collecting both PL and CL, which is well below the saturation value of the detector at 25.19 MHz (Fig. 3.7c). A PP experiment consists of the acquisition of $N$ sets of measurements, each at a different position of the delay stage, corresponding to a certain delay between electron and light pulses. These $N$ measurements are performed in a random order, such that we can disregard any artificial trends due to sample degradation or drift in the system. At each position of the delay stage we perform one set of measurements, consisting of 2 acquisitions: CL, that is, only electrons exciting the sample, and PP, i.e., laser and electron on the sample. In the CL-only measurement, the light-injection path is mechanically blocked with a software-controlled flip mount, such that the laser beam does not excite the sample. Hence, we acquire only CL emission. We record the average signal read by the lock-in amplifier during the exposure time $T_{exp}$, and repeat the acquisition $n$ times to improve the statistics. Here we used $T_{exp}$ = 30 s and $n$ = 4. The CL emission is recorded at every delay position to compensate for effects such as sample degradation or fluctuations in the electron current. Next, the light-injection path is unblocked such that electrons and light excite the sample synchronously, thus producing both CL and PL. The

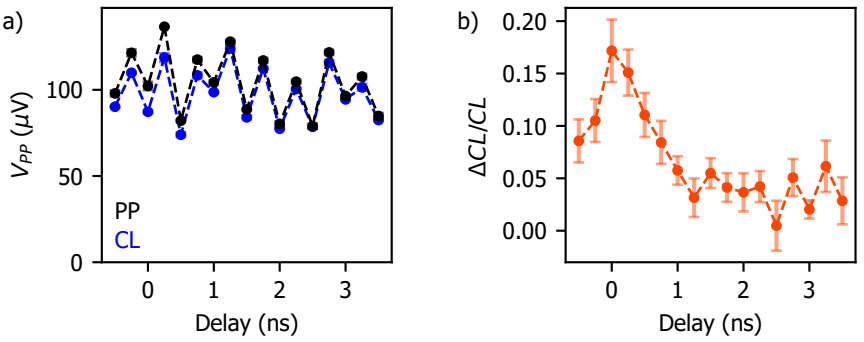


Figure 3.19: Pump-probe measurements on CZTS using a lock-in amplifier. (a) Signal obtained when exciting with only electron pulses (CL, blue) and electron and light pulses (PP, black) at different delays between electrons and light. A positive delay is defined as the arrival of the electron pulse after the light pulse. (b) Normalized CL change as a function of delay. We observe an increase in the CL signal right after optical excitation of the sample, which decreases for increasing delay.

signal is recorded by the lock-in using the same settings as in the CL-only measurement ($T_{\text{exp}}$ and $n$). Hence, a set of measurements at each position of the delay scan takes a time of $2nT_{\text{exp}}$ (here, 4 min). We could add a third measurement of PL-only, such that the laser beam that is focused on the electron cathode ($4^{\text{th}}$ harmonic) is blocked. However, the PL background signal read by the lock-in amplifier was negligible (< 1 μV, compared to ~ 100 μV of CL), thus this was not needed.

The results of a PP experiment on CZTS are shown in Figure 3.19. We used an electron current of $1.28 \pm 0.13$ n$A$ ($318 \pm 39$ electrons per pulse). All other excitation parameters were kept the same as for the spectra and decay traces shown in Fig. 3.19. We scanned the delay line over a range from −0.5 to 3.5 ns with step size of $\delta t = 0.25$ ns. Positive delay is defined as the arrival time of the electron pulse (probe) after the laser pulse (pump). The entire experiment took ~ 1 h, which was split into two shorter scans of ~ 30 min each, scanning from −0.5 to 3.5 ns with $\delta t = 0.5$ ns, and from −0.25 to 3.25 ns, also with $\delta t = 0.5$ ns. Long acquisitions can be challenging due to drift of the alignment of the laser beam on the electron cathode, thus decreasing the current on the sample. Hence, splitting an experiment into short scans allows us to perform realignment in between measurements if needed. Moreover, keeping the electron cathode at a low temperature for a long period of time results in a decrease in the emitted current, thus it is desirable to quickly warm up the tip in between measurements (see Chapter 2 for details).

Panel (a) of Fig. 3.19 shows the peak-to-peak voltage read by the lock-in amplifier for CL (blue) and PP (black) at the different positions of the delay stage. The CL signal is around 100 μV, with variations of up to 25 %, which we attribute to fluctuations in the power of the laser beam that excited the electron cathode (~ 1 Hz). The PP data exhibits similar variations, but its absolute value is systematically larger than the CL one at small delays. To further analyze the pump-probe effect, we di-

vide the change in CL, defined as $\Delta CL = PP - CL - PL$, by the CL signal. A value of zero means that the CL emission is unaffected by the presence of the laser. Instead, in Fig. 3.19b we observe a clear initial enhancement of the CL signal near zero delay. The increase in CL is ~ 17% at zero delay, and decreases for longer pump-probe delay. Similar trends were reproduced on different positions on the CZTS film. The error bars in the figure are calculated from the standard deviations of the CL and PP measurements in panel (a). The mechanism responsible for this CL enhancement is preliminary attributed to the filling of defect states by the laser beam, and the subsequent emptying of these states in the ns timescale. Further measurements and modeling are now ongoing to study these PP-CL transients more in detail, which account for the different carrier recombination rates, including bimolecular recombination, and monomolecular recombination through defect states. These measurements represent the first initial studies of PP-CL using electrons as a probe and with dependence on the delay between electron and light pulses.



## 3.9. CONCLUSION

In this chapter we have presented the design of a new instrument for pump-probe cathodoluminescence experiments. In the first part of the chapter we have discussed the technical implementation of the setup, based on the coupling of a fs laser to the electron cathode and sample chamber of a Quanta 250 FEG SEM. The setup allows for different types of analysis of the luminescence emitted by the sample (either PL or CL), including spectroscopy, time-resolved and autocorrelation measurements, and lock-in based detection. The spatial overlap of electron and light pulses on the sample is performed by visualizing the laser spot on the sample, or by analyzing the angular emission of the PL light, while the temporal overlap is achieved by monitoring the arrival time of electrons and light through time-resolved PL and CL measurements.

In the second part of the chapter, we discussed some important considerations to take into account when performing pump-probe experiments. We compared electron and light excitation mechanisms in terms of interaction volume, density of deposited energy, emission spectra, quantum efficiency and carrier dynamics. Experimental data on GaN and GaAs show that excitation with increasing electron energy results in a redshift of band gap emission, as well as an increased quantum efficiency compared to PL experiments performed on the same area on the sample. Time-resolved measurements on GaAs show the same trends for both electron and laser excitation. We observe that the characteristic time increases for increasing fluence, which is preliminarly attributed to saturation of defect states.

Finally, we presented initial studies of PP-CL measurements on $Cu_2ZnSnS_4$, in which we used the electron as a probe. We observe that excitation of the sample with the laser results in a transient CL enhancement on the ns timescale. A second configuration of our PP-CL setup is illustrated in the next chapter, in which the electrons act as a pump.

# 4

# ELECTRON-INDUCED STATE CONVERSION IN DIAMOND NV CENTERS

*Nitrogen-vacancy (NV) centers in diamond are reliable single-photon emitters, with applications in quantum technologies and metrology. Two charge states are known for NV centers: $NV^0$ and $NV^-$, with the latter being mostly studied due to its long electron spin coherence time. Therefore, control over the charge state of the NV centers is essential. However, an understanding of the dynamics between the different states still remains challenging. Here, conversion from $NV^-$ to $NV^0$ due to electron-induced carrier generation is shown. Ultrafast pump-probe cathodoluminescence spectroscopy is presented for the first time, with electron pulses as pump, and laser pulses as probe, to prepare and read out the NV states. The experimental data is explained with a model considering carrier dynamics (0.8 ns), $NV^0$ spontaneous emission (20 ns) and $NV^0 \rightarrow NV^-$ transfer (500 ms). The results provide new insights into the $NV^- \rightarrow NV^0$ conversion dynamics, and into the use of pump-probe cathodoluminescence as a nanoscale NV characterization tool.*

## 4.1. INTRODUCTION

Nitrogen-vacancy (NV) centers in diamond are promising elements for quantum optical systems since they are single-photon emitters [180, 181] with high photostability, quantum yield and brightness, even at room temperature [182–184]. Moreover, they are integrated inside a wide-bandgap solid-state host, the diamond lattice, making them robust against decoherence and allowing device scalability [185–187]. NV centers exhibit two different configurational states, the $NV^0$ state, with a zero-phonon line (ZPL) at 2.156 eV ($\lambda$ = 575 nm), and the $NV^-$ state, with a ZPL at 1.945 eV ($\lambda$ = 637 nm) [181]. NV centers in the $NV^-$ state have received most of the

attention in the past years since they exhibit a long electron spin coherence time that can be optically manipulated and read out [186, 188], which, together with the characteristics mentioned previously, make them suitable as building blocks for quantum technologies [186, 189, 190], nanoscale magnetometry [191, 192], and other applications [193, 194]. Typically, synthetically prepared diamonds with NV centers contain both $NV^0$ and $NV^-$ states. Previous work has shown that the state of an NV center can be converted from $NV^-$ to $NV^0$ (*ionization*) and vice versa (*recombination*). For example, the state of the NV centers can be changed by laser irradiation [195–197], as well as by shifting the Fermi level, either chemically [198–200], or by applying an external voltage [201, 202]. Overall, the control and understanding of NV state dynamics is key to the development of efficient quantum optical systems based on NV centers.



So far, most work on NV characterization and state conversion dynamics has focused on optical excitation and readout of the NV state. However, NV centers can also be excited by high-energy (1-200 keV) electrons, using either a scanning or transmission electron microscope (SEM or TEM), while the emitted cathodoluminescence (CL) is collected. Given the small electron beam spot size, the study of NV centers with electron excitation allows for a spatial resolution only limited by the diffusion of carriers, which can be down to the nanometer scale [203]. This opens the possibility to excite directly NV centers in nanodiamonds with high spatial resolution [203] and study the coupling of locally-excited nanostructures to NV centers [204, 205], among others. Furthermore, NV centers are good platforms to study the fundamentals of quantum optics with electrons, in contrast to optical measurements. Electron-beam excitation of NV centers involves a multi-step process, in which the primary electron beam inelastically interacts with the diamond lattice, creating bulk plasmons that decay by generating charge carriers [13, 206, 207]. These carriers then diffuse through the diamond and recombine, partially through the excitation of NV centers. Single-photon emission of individual NV centers excited with electrons has already been demonstrated using measurements of the CL photon autocorrelation function ($g^{(2)}(\tau)$) [40]. Interestingly, in CL experiments typically only emission from the $NV^0$ state is observed [40, 203, 208–213], with one exception [212], in which a very small $NV^-$ CL signal was observed at low temperature (16 K). This raises the question whether (1) the electron beam does not excite NV centers in the $NV^-$ state, (2) the electron beam quenches the $NV^-$ transition, or (3) the electron beam converts NV centers from the $NV^-$ to the $NV^0$ state. Answering this question is essential to understand the NV state dynamics in general, and to further exploit the use of CL in nanoscale characterization of atomic defects acting as single-photon emitters.

In this chapter we study the interaction of electrons with NV centers, and in particular their state conversion dynamics. We perform the experiments using pump-probe CL spectroscopy, a novel technique that allows to study excited state dynamics at ultrafast timescales. Previous works combining electron and light excitations in a TEM include photon-induced near-field electron microscopy (PINEM)[87, 89], in which the electron gains or loses energy when interacting with the optically-

induced near-field, and femtosecond Lorentz microscopy [84], in which the laser-induced magnetization dynamics are probed with the electrons. Similarly, photoinduced carrier dynamics have been studied in an SEM by analyzing the secondary electron yield after laser excitation [136]. However, in these configurations the electron acts as a probe, since the signal is either transmitted or secondary electrons. In contrast, in pump-probe CL the final signal is the emitted light, either CL or photoluminescence (PL), therefore the electron can also act as a pump. In this work, we use an ultrafast SEM in which picosecond electron pulses are used to pump the diamond sample, while synchronously we optically probe the NV state. The electron pulses are generated using a laser-driven cathode configuration, a technique initially demonstrated by Merano et al. using a gold cathode [72], and further developed in combination with field-emission guns (FEGs) to improve the spatial and temporal resolution [65, 79]. After ultrafast excitation of the NV centers, the CL and PL spectra are collected for spectral and temporal characterization. We find that repeated pulsed electron excitation (5.04 MHz) causes a state conversion from $NV^-$ to $NV^0$, until a steady state is achieved in which the electron-induced $NV^- \rightarrow NV^0$ conversion is balanced by the reverse $NV^0 \rightarrow NV^-$ back transfer. The steady state $NV^0$ population under electron irradiation can be controlled by the number of electrons per pulse. We describe the results with a model that includes electron-induced carrier generation and diffusion, with the NV centers acting as carrier traps and electrons converting NV centers from the $NV^-$ to the $NV^0$ state. The time dynamics of carrier diffusion (~0.8 ns), $NV^0$ decay (~20 ns) and $NV^0 \rightarrow NV^-$ back transfer (~500 ms) are clearly observed from the pump-probe transients.



## 4.2. PUMP-PROBE CL SETUP

The pump-probe CL experiments are performed inside a SEM. We focus the $4^{th}$ harmonic ($\lambda$ = 258 nm) of an Yb-doped fiber fs-laser on the electron gun to generate electron pulses by photoemission [72, 214] (Figure 4.1a). Photoemission of electron pulses using this setup was characterized previously [49] (see also chapter 2), showing that the generated electron pulses are in the picosecond regime, similar to other work [76, 79]. The electron beam is focused on a single spot on the sample, corresponding to the center of the area irradiated by the laser beam. We synchronously excite the sample at the electron-irradiated region with $2^{nd}$ harmonic ($\lambda$ = 517 nm) pulses generated by the same fs laser, which are focused inside the SEM chamber to a ~10 µm-diameter spot on the sample using an Al parabolic mirror. The $2^{nd}$ harmonic path length can be tuned within a ± 2 ns time window, such that the optical excitation pulse on the sample is delayed (or advanced) with respect to the electron pulse. CL and PL are collected by the parabolic mirror and directed to either a spectrometer or a time-correlated single photon counting (TCSPC) module. We use a 300 µm thick single-crystal diamond sample (obtained from Element 6 Inc.), grown by chemical-vapor deposition (<1 ppm nitrogen concentration, <0.05 ppm boron concentration), containing an approximate NV concentration of $[NV_{tot}]$ = 1.2 ppb (200 $\mu m^{-3}$). The sample is coated with a thin charge dissipation layer (E-spacer 300) to avoid charging when exciting with the electron pulses.

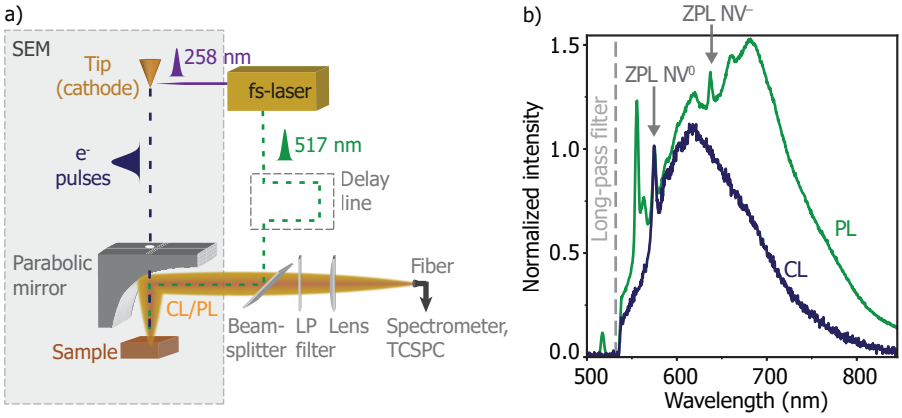


Figure 4.1: Pump-probe CL setup and NV centers spectra. (a) Schematic of the pump-probe CL setup. The 4$^{th}$ harmonic ($\lambda$ = 258 nm) of a fs laser is focused on the electron cathode to induce photoemission of electron pulses (0-400 electrons/pulse, picosecond temporal spread). The 2$^{nd}$ harmonic ($\lambda$=517 nm) of the same laser synchronously excites the sample to readout the NV state. The light pulse is delayed 1.3 ns with respect to the electron pulse. The emitted light, CL, PL or both, is collected using a parabolic mirror and analyzed with a spectrometer or TCSPC module. A long-pass (LP, $\lambda$ >532 nm) filter is used to remove the light from the excitation laser. (b) Photoluminescence (green) and cathodoluminescence (blue) spectra obtained independently when exciting a bulk diamond sample with either 517 nm pulsed laser beam (0.9 nJ/pulse) or a 5 keV pulsed electron beam (400 electrons/pulse), respectively. Both spectra are obtained when exciting with a repetition rate of 5.04 MHz and at the same position on the sample. CL and PL spectra have been normalized by the amplitude of the NV$^0$ ZPL at 575 nm.

## 4.3. CL, PL AND PUMP-PROBE MEASUREMENTS

Using the pump-probe CL setup, we acquire first PL and CL spectra, shown in Figure 4.1b. The PL spectrum shows emission from the ZPL of NV$^-$ ($\lambda$ = 637 nm) and NV$^0$ ($\lambda$ = 575 nm), with both ZPL transitions accompanied by phonon replicas, forming a broadband spectrum in the 575-800 nm spectral range. A Raman peak at $\lambda$ = 555 nm is also observed [215], as well as a peak around 563 nm, which has been observed in previous work and preliminarily attributed to a divacancy defect [210, 216, 217]. The CL spectrum, obtained when exciting with a 5 keV pulsed electron beam clearly shows the ZPL of the NV$^0$ state, with phonon sideband, but no emission from the NV$^-$ state is observed, similar to previous work [40, 203, 208–213]. The relative contribution of NV$^-$ and NV$^0$ states to the PL spectrum is obtained by a fitting procedure, with the CL spectrum as a reference for the spectral shape of the NV$^0$ emission (see Supporting Information, section 4.7.2). Using estimated optical absorption cross sections at the laser excitation wavelength (see section 4.7) we derive the NV$^-$ and NV$^0$ fractions: $[NV^-]/[NV_{tot}] \simeq 0.4$ and $[NV^0]/[NV_{tot}] \simeq 0.6$.

Our pump-probe measurements consist of the independent acquisition of a set of spectra: only CL, only PL, and pump-probe (PP). The latter is obtained under

simultaneous electron and light excitation, with the light pulse arriving 1.3 ns after each electron pulse. A set of spectra is shown in Figure 4.2a. All measurements were performed at the same spot on the sample, to avoid effects due to concentration inhomogeneities. In addition to the differences in the PL and CL spectra mentioned above, we also observe that the PL signal is an order of magnitude higher than the CL one. Even though a detailed comparison between both magnitudes is complex due to the different incident powers and excitation mechanisms, we can estimate the number of NVs excited in each case. The laser spot size has a diameter of around 10 µm and large penetration depth, due to the low absorption of diamond and low NV concentration. Therefore, the volume is mostly determined by the collection volume of the setup (see section 4.7.1). Instead, the primary interaction volume of the 5 keV electron beam is around 0.4 $\mu m^3$, as calculated from Monte Carlo-based simulations using the software Casino [218]. Even though the effective volume is enlarged due to carrier diffusion, as will be shown below, it is still smaller than the volume excited by the laser. A sketch of both volumes is shown in Fig. 4.2c. Taking into account the optical cross-sections and collection geometry, we estimate that we collect PL from around 1.4x$10^4$ NVs per pulse for an incident power of 0.9 nJ (per pulse). Comparing the magnitude of the PL and CL signals, we can also extract that an average of 900 NV centers in the $NV^0$ state are excited per electron pulse, in the steady state situation, as will be discussed further on. In this case, each electron pulse contained 400 electron with 5 keV energy (corresponding to 0.32 pJ per pulse).

Using the PL, CL and PP spectra shown above, we can analyze the effect of electron irradiation on NV centers. We define the quantity of difference spectrum, obtained when subtracting CL and PL spectra from the PP spectrum. This analysis allows to study the correlation between electron and light excitation of the NV centers. Therefore, no correlation would lead to a flat difference spectrum. Instead, the difference spectrum obtained from the data in Figure 4.2a exhibits clear features, as shown in Figure 4.2b (black curve). We observe an increase of the signal (positive counts) in the lower-wavelength spectral band, corresponding to the $NV^0$ emission. As a reference, we observe a clear peak corresponding to the $NV^0$ ZPL. We also observe a concomitant decrease in the longer-wavelength band, corresponding to $NV^-$ emission. In this case, the $NV^-$ ZPL is visible as a dip. This implies that after electron excitation the number of emitting $NV^0$ centers is increased, while the number of $NV^-$ centers is decreased. The results suggest that centers in the $NV^-$ states are converted into $NV^0$ states under electron irradiation, corresponding to hypothesis (3) exposed earlier in the text. Difference spectra derived for different sets of measurements at 0.3, 1, 10 and 147 electrons per pulse are also shown in Figure 4.2b, as well as a reference measurement (no electron irradiation). Each set of measurements corresponds to the acquisition of independent CL, PL and PP spectra, in which the number of electrons per pulse is varied, while keeping the laser excitation power constant at 0.9 nJ per pulse. We again observe $NV^- \rightarrow NV^0$ conversion, with the number of converted centers rising for increasing average number of electrons per pulse. This behavior in the difference spectra was consistently observed in other measurements at different areas of the sample, and also with other

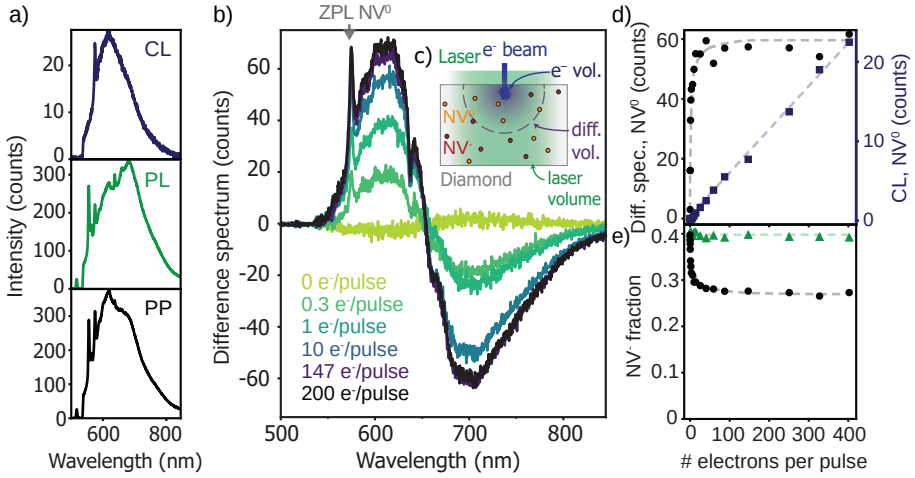


Figure 4.2: $NV^- \rightarrow NV^0$ conversion under electron excitation (a) Top: CL spectrum (5 keV, 400 electrons/pulse), middle: PL spectrum ($\lambda$ = 517 nm, 0.9 nJ/pulse), bottom: pump-probe (PP) spectrum obtained when both electrons and light (same conditions as before) excite the sample (5.04 MHz). The acquisition time was 1 min in all cases. (b) Difference spectrum, obtained by subtracting CL and PL spectra from the PP spectrum. (c) Sketch of the laser and electron excitation on the sample, representing the different volumes of primary electron interaction ($e^-$ vol.), diffusion of carriers (diff. vol.) and laser volume (laser vol.). (d) $NV^0$ ZPL intensity ($\lambda$ = 575 nm) of the difference spectrum (black circles) and from the CL-only spectrum (blue squares) as a function of the average number of electrons per pulse. The $NV^0$ ZPL of the difference spectrum shows saturation at around 20 electrons/pulse, while in the case of CL the dependence is linear. Dashed lines are shown as guides for the eye. (e) $NV^-$ fraction obtained from the PP as a function of the number of electrons per pulse. The green triangles indicate the $NV^-$ fraction derived from the PL spectra (all at the same PL pump power). Dashed lines are guides for the eye.

electron energies (30 keV, see Fig. 4.5 in the Supporting Information).

To further investigate the electron-induced $NV^- \rightarrow NV^0$ conversion trend, we plot the amplitude of the $NV^0$ ZPL as a function of the number of electrons per pulse (Figure 4.2d). Saturation of the signal from the $NV^0$ ZPL is observed above ~20 electrons per pulse, suggesting that this is the required electron flux (at 5.04 MHz) to induce the saturation of the $NV^-$ conversion in the volume of the sample excited by electrons. For reference, Figure 4.2d also shows the CL intensity for the $NV^0$ ZPL as a function of the number of electrons per pulse. The plot shows a linear trend, indicating that the $NV^0$ CL signal is not saturating with increasing electron dose, i.e., there is no strong depletion of the ground state population. Therefore, from these results we derive that electrons can either excite NV centers in the $NV^0$ state, which leads to a linear dependence on the electron flux, or convert $NV^-$ into $NV^0$, which saturates with increasing number of electrons per pulse.

From the data in Figure 4.2b we can also derive the $NV^-$ population as a function of the number of electrons per pulse, as plotted in Figure 4.2e. This derivation is done by fitting the $NV^0$ and $NV^-$ contributions from the PP measurements (see Supporting information, section 4.7.2). Starting from the initial $NV^-$ fraction of 0.4

for the reference measurement, as already derived before, the population of centers in the $NV^-$ state rapidly decreases with increasing number of electrons per pulse, reaching a saturation level corresponding to 0.26 $NV^-$ fraction. We attribute this saturation level to the full conversion of $NV^-$ centers into $NV^0$ centers within the volume excited by the electrons, as will be discussed further on. The fact that the $NV^-$ fraction does not reach zero at saturation is attributed to the difference between excitation and collection volumes of electron and laser beam, as sketched in Figure 4.2c. For completeness, in Figure 4.2e we also show the $NV^-$ fraction derived from the PL measurements taken in each set of measurements from Figure 4.2b. We observe that the $NV^-$ fraction under only laser irradiation remains approximately constant, meaning that the $NV^-$ population before each set of measurements is identical. The fact that the $NV^-$ population is unchanged also implies that the electron-induced $NV^-\rightarrow NV^0$ conversion is reversible, i.e., there is an $NV^0\rightarrow NV^-$ back transfer process, and that damage induced by the electron to the sample is negligible. Given that $NV^-\rightarrow NV^0$ conversion has also been observed due only to laser irradiation [195–197], we also acquired PL spectra at different incident powers. The results are presented in Figure 4.6 (Supporting Information) and show that the $NV^-$ fraction remains constant for increasing laser power, therefore proving that NV conversion due to only laser irradiation is negligible in our experiment. Pump-probe measurements with different delays between electron and light were also acquired (Supporting Information, Figure 4.7a), but no significant differences are observed. This is attributed to the fact that the $NV^0\rightarrow NV^-$ back transfer is on the order of milliseconds, as will be demonstrated below, larger than the time between pulses (198 ns at 5.04 MHz).

## 4.4. EXCITATION, EMISSION AND CONVERSION DYNAMICS

In order to further describe the interaction of electrons with NV centers, we study the excitation and emission dynamics of NV centers at the nanosecond timescale, as well as the $NV^0\rightarrow NV^-$ back transfer that occurs in the millisecond scale. The time-dependent CL emission from NV centers upon electron excitation is shown in Figure 4.3a, which has been measured using the TCSPC technique. Notice that the CL intensity corresponds only to emission from excited $NV^0$ centers, given that $NV^-$ emission is not probed with CL. The CL signal exhibits a gradual increase in the first 2 ns, reaching a maximum emission at around 2.2 ns (see inset). We ascribe this initial increase to the diffusion of carriers beyond the primary electron-excited volume, which increases the excited $NV^0$ population well after the initial ps-electron pulse excitation. After the first 2 ns we observe a decay of the CL intensity, from which we extract a characteristic decay time of ~20 ns, in agreement with the typical radiative decay time of excited $NV^0$ centers [40, 219]. We also observe a ~100 ps spike at 0 ns, which accounts for around 1% of the total intensity. The origin of this fast decay is unknown. The intensity of this peak depends on the position on the sample, as well as electron energy. Nevertheless, the amplitude of this peak does not show any correlation with the magnitude of the $NV^-\rightarrow NV^0$ conversion, from which we infer that both effects are unrelated.

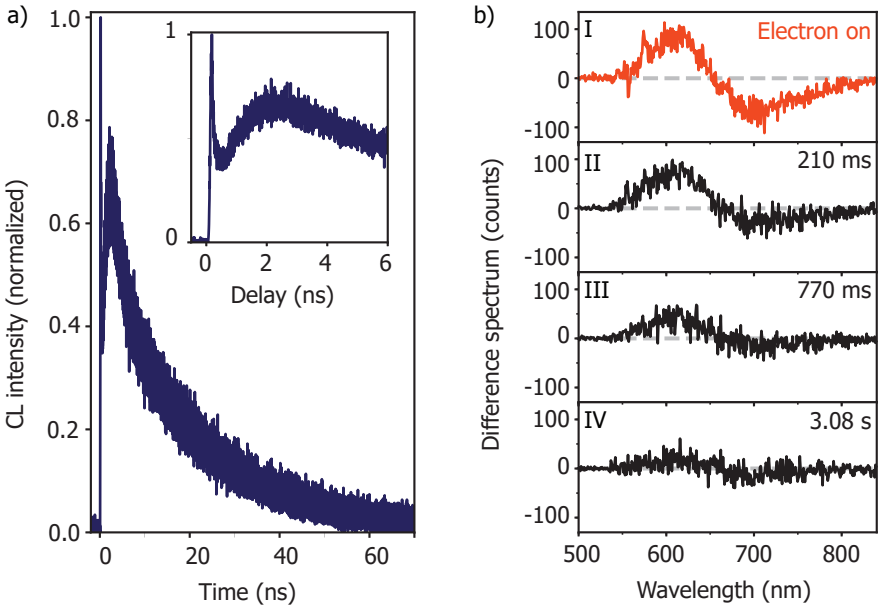


Figure 4.3: Carrier diffusion, excitation and back transfer dynamics. (a) Peak-normalized CL intensity upon pulsed electron excitation (5 keV, ~450 electrons/pulse, 5.04 MHz) at t=0 ns, measured with time-correlated single photon counting. Data are taken in the $NV^0$ 575-725 nm spectral band. Inset: enlarged early-timescale. (b) Difference spectrum (defined as PP–CL–PL) obtained with the electron beam on (I) and 210 ms, 770 ms and 3.08 s after the electron beam was blanked (II-IV, respectively). The $NV^0 \rightarrow NV^-$ back transfer takes around 500 ms. The time-resolution of this experiment is 70 ms.

In contrast to the fast carrier diffusion and $NV^0$ emission dynamics, previous studies of optically induced $NV^-$→$NV^0$ conversion suggest that the $NV^0$→$NV^-$ back transfer is in the millisecond regime [195]. To study this, we performed time-resolved spectral measurements over a millisecond time scale. We used the minimum exposure time possible in our spectrometer, acquiring a spectrum every 70 ms. The repetition rate is kept at 5.04 MHz, as in the previous experiments. We performed a spectral acquisition sequence in which initially both the electron and laser beam were irradiating the sample (PP spectrum). At some point during the acquisition, the electron beam was blanked, while the laser continued exciting the sample, and spectra kept being collected every 70 ms. In this way, the NV population can be probed immediately after the electron beam is switched off. Afterwards, we also acquired CL and PL spectra with the same exposure time, such that a difference spectrum can be derived, similar to Figure 4.2b. An example of the obtained difference spectrum is shown in Figure 4.3b-I, which again reflects the $NV^-$→$NV^0$ conversion by the electron-excited carriers. In this case, the electron beam was still irradiating the sample. Figure 4.3b-II shows the difference spectrum obtained 210 ms after switching off the electron beam. Notice that here the difference spectrum is obtained by subtracting only PL from the PP measurement, given that there is no CL. We observe a 30% decrease of the intensity of the difference spectrum, indicating that most of the converted $NV^-$ centers still remain in the $NV^0$ state, and only some have converted back into $NV^-$. Results after 770 ms and 3.08 s are also plotted (Figure 4.3b-III,IV), in which we observe a progressive decay of the signal, indicating that $NV^0$ centers are converted back to the $NV^-$ state. A complete transient of the average signal in the difference spectrum as a function of time is provided in Fig. 4.7b. (Supporting Information) These data indicate that the electron-induced $NV^-$→$NV^0$ state conversion is reversible, with the back transfer taking place within a characteristic time of ~500 ms. This time scale is in agreement with earlier work, in which back transfer of optically-induced $NV^-$→$NV^0$ conversion, was found to occur with a characteristic time of 465 ms [195].

## 4.5. DISCUSSION AND PHENOMENOLOGICAL MODEL

Optically-induced state conversion from $NV^-$ to $NV^0$ has been previously explained to take place by the release of an electron from the $NV^-$ center to the conduction band of diamond [197, 219–221]. Literature values for the difference in energy between the $NV^-$ ground state and the conduction band range from 2.6 to 4.3 eV [195, 197, 219], and the $NV^-$→$NV^0$ optical conversion typically requires a two-photon absorption process. In our experiment, we propose a model in which electron-hole pairs generated from the electron cascade can recombine, thus providing the energy to induce the release of the bound electron from the $NV^-$ center, given that the bandgap of diamond is 5.5 eV. This conversion mechanism is similar to that in optical experiments, with the difference that the energy is provided by a carrier recombination event instead of two pump photons. This model is in agreement with previous work in which emission only from the $NV^0$ state was observed when exciting with far-UV photons ($\lambda$ = 170 nm, above the bandgap of diamond)

[222] and in electroluminescence [223, 224]. In both cases, charge carriers are generated and NV centers are excited through the recombination of carriers, similar to CL. In addition to this, the energy provided by a single carrier recombination event is larger than the energy needed to induce the $NV^-\rightarrow NV^0$ conversion, suggesting that a single carrier recombination event could already release the electron, without the need to first excite the $NV^-$ center as in the case of optical experiments [197, 219–221]. The latter suggestion requires further studies in the mechanism of $NV^-\rightarrow NV^0$ conversion by carrier recombination, which are beyond the scope of this chapter.

To qualitatively analyze the data shown above we model the electron-induced $NV^-\rightarrow NV^0$ state conversion by means of a three-dimensional model, considering carrier diffusion and NV center conversion and excitation. We start by modelling the dynamics in the nanosecond regime, corresponding to carrier diffusion and $NV^0$ decay. We use Monte Carlo simulations, using the software Casino [218], to obtain the three-dimensional spatial distribution of inelastic scattering events of the primary 5 keV electron beam. Most of the energy lost by the electron corresponds to the generation of bulk plasmons, described as excitations of the outer shell electrons [13], with an energy corresponding to 31 eV for diamond [206]. We then model the initial carrier distribution with a 3D Gaussian distribution, with standard deviation $\sigma = 0.185\,\mu m$ estimated from the plasmon distribution derived from Casino simulations, and amplitude proportional to the number of electrons per pulse. We assume that each bulk plasmon effectively generates an average of 2 electron-hole pairs [27]. The concentration of charge carriers as a function of time and space ($\rho_{eh}(r,t)$) is then obtained by solving the diffusion equation, with carrier recombination described with a lifetime $\tau_R$.

Taking into account carrier diffusion, we model the concentration of $NV^-$ in the ground state ($\rho_-$) and $NV^0$ in the ground ($\rho_0^g$) and excited ($\rho_0^e$) states by means of a rate equation model:

$$\frac{\partial \rho_-(r,t)}{\partial t} = -v_{th}\rho_{eh}(r,t)\sigma_c^{eh}\rho_-(r,t) + \frac{\rho_{-,i}-\rho_-(r,t)}{\tau_{back}} \tag{4.1a}$$

$$\frac{\partial \rho_0^g(r,t)}{\partial t} = v_{th}\rho_{eh}(r,t)\left[\sigma_c^{eh}\rho_-(r,t) - \sigma_0^{eh}\rho_0^g(r,t)\right] + \frac{\rho_0^e(r,t)}{\tau_0} - \frac{\rho_{-,i}-\rho_-(r,t)}{\tau_{back}} \tag{4.1b}$$

$$\frac{\partial \rho_0^e(r,t)}{\partial t} = v_{th}\rho_{eh}(r,t)\sigma_0^{eh}\rho_0^g(r,t) - \frac{\rho_0^e(r,t)}{\tau_0} \tag{4.1c}$$

where $v_{th}$ is the thermal velocity of carriers, $\sigma_0^{eh}$ is the cross section to excite $NV^0$ states by carriers, $\sigma_c^{eh}$ is the $NV^-\rightarrow NV^0$ conversion cross section, $\tau_0$ is the lifetime of excited $NV^0$ state, $\tau_{back}$ accounts for the $NV^0\rightarrow NV^-$ back transfer, and $\rho_{-,i}$ is the initial uniform concentration of $NV^-$. In this model we assume that $NV^0$ states can be excited by carriers, but $NV^-$ states cannot, given that we do not observe $NV^-$ signal in the CL measurements. Moreover, the interaction of the primary electron

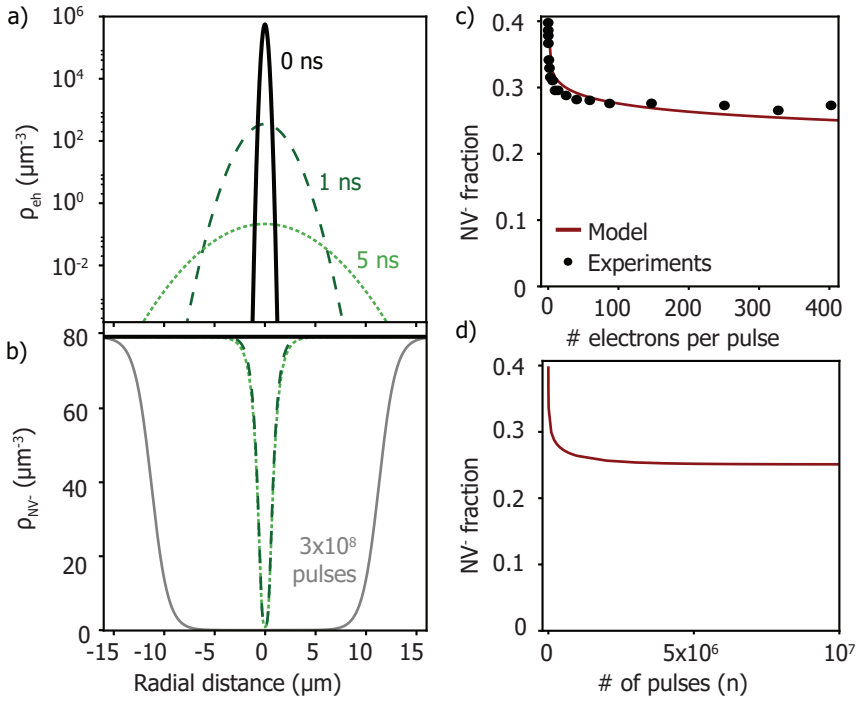


Figure 4.4: Carrier diffusion and rate equation models. (a) Spatial distribution of the concentration of carriers at t = 0, 1 and 5 ns (solid black, dashed dark green and dotted light green, respectively). (b) Initial spatial distribution of the concentration of $NV^-$ states (solid black) and after 1 and 5 ns (dashed dark and dotted light green) after a single electron pulse. The spatial distribution of $NV^-$ states after $3 \times 10^8$ pulses, corresponding to a typical acquisition time (~ 1 min), is also plotted (solid gray). (c) Modelled $NV^-$ fraction as a function of the number of electrons per pulse (dark red curve), together with the experimental data (black circles). (d) $NV^-$ fraction as a function of the number of pulses (400 electrons/pulse), obtained using the discrete rate equation model.

beam (picosecond temporal spread) with the sample, including generation of bulk plasmons and decay into carriers, is treated as instantaneous, given that it is much shorter than the characteristic time scale of the dynamics in Equations 4.1a-c.

Numerically solving the system of differential equations over time, and integrating $\rho_0^e(r,t)$ over the collection volume, allows to fit the trend in the first 2 ns of the time-dependent CL intensity shown in Figure 4.3a. The carrier lifetime derived from the fit is $\tau_R = 0.8$ ns, corresponding to a diffusion length of 0.9 μm, which is in agreement with values reported for samples with a similar concentration of NV centers [225]. From the model we also find that excitation with 400 electrons (5 keV) leads to about 740 $NV^0$ centers excited per pulse, close to the value independently derived from the comparison of PL and CL intensities in Figure 4.2a,b. Taking into account the obtained carrier lifetime, in Figure 4.4a we plot the spatial distribution of the carrier concentration at t = 0 ns (solid black) and after 1 and 5 ns

(dashed dark green and dotted light green, respectively), obtained from the expression of $\rho_{eh}(r,t)$ (see Supporting Information, section 4.7.3). The carrier distribution rapidly spreads out due to diffusion, with the total amount of carriers decreasing as a result of carrier recombination.

The calculated spatial distribution of the $NV^-$ concentration is shown in Figure 4.4b, again at t = 0, 1 and 5 ns, obtained by solving Equations 4.1a-c. Given that the electron excitation cross sections for $NV^0$ excitation and $NV^- \rightarrow NV^0$ conversion are unknown, we estimate them by considering the known exciton capture cross section of a nitrogen impurity in diamond [226], $\sigma_0^{eh} = \sigma_c^{eh} = 3\times10^{-6}\,\mu m^{-2}$. We consider $v_{th} = 100\,\mu m\,ns^{-1}$, $\tau_{back} = 500\,ms$, as obtained from the experimental data in Figure 4.3b, and an initial homogeneous $NV^-$ fraction of 0.4 (black line in Figure 4.4b for t = 0 ns), corresponding to the experimental data in Figure 4.2e. We observe that 1 ns after the first pulse, NV centers in the $NV^-$ state that are located within a 1 µm range from the initial electron cascade have been converted to $NV^0$ due to the interaction with carriers. For larger times (5 ns) the distribution of converted $NV^-$ centers is nearly the same as for t = 1 ns, as nearly all carriers have recombined.

In order to account for longer time scales, corresponding to the back transfer from $NV^0$ to $NV^-$ and the time of acquisition of our experiments (typically 1 min, $\sim 3\times10^8$ pulses), we developed a discrete rate equation model. In this case, the concentration of $NV^-$ centers is modelled as a function of the pulse number ($n$),

$$\rho_-(r,t) = \rho_-(r,0)\frac{\beta+\alpha(r)\left[1-\alpha(r)-\beta\right]^n}{\alpha(r)+\beta}, \tag{4.2}$$

where

$$\alpha(r) = 1 - e^{-v_{th}\sigma_c^{eh}\int_0^T \rho_{eh}(r,t)\,dt} \tag{4.3}$$

is the probability of carrier-induced conversion of centers in the $NV^-$ states between subsequent pulses, with $T$ being the time between pulses (198 ns at 5.04 MHz), and

$$\beta = 1 - e^{-T/\tau_{back}} \tag{4.4}$$

is the probability that an $NV^0$ center transfers back to the $NV^-$ state, again between subsequent pulses (see section 4.7.3). Using this model, in Figure 4.4b we plot the spatial distribution of $NV^-$ centers after $3\times10^8$ pulses (solid gray), corresponding to a typical acquisition time (1 min), in which steady state has been reached. The calculated steady state $NV^-$ fraction as a function of the number of electrons per pulse is shown in Figure 4.4c, which is overlaid with the experimental data from Figure 4.2e (black circles). Each point in the plot corresponds to the steady state value calculated using Eq. 4.2, and integrated over the excitation and collection volume (see Supporting information, section 4.7.1). In our model, taking the parameters discussed above, the only fit parameter is the collection depth of the CL system, which is 23 µm for the best fit. This is a reasonable value given the confocal geometry of the CL/PL collection system (see 4.7.3). Figure 4.4d shows the calculated $NV^-$ fraction as a function of the number of pulses. We observe that the $NV^-$ fraction saturates for $\sim5\times10^6$ pulses (1 s), consistent with the fact that steady

state is reached for a time longer than the $NV^0 \rightarrow NV^-$ back transfer time. Overall, the model qualitatively describes properly the experimental data, therefore giving further proof for the proposed electron-induced mechanism for $NV^- \rightarrow NV^0$ conversion dynamics.

## 4.6. CONCLUSIONS

In conclusion, we have used pump-probe CL spectroscopy to show that high energy (5 keV) electron irradiation of NV centers induces a state conversion from the $NV^-$ to the $NV^0$ state. We show that the $NV^-$ population decreases when increasing the number of electrons per pulse that excite the sample, until saturation is reached, which is attributed to the full conversion of the $NV^-$ centers in the volume excited through the electrons. Experiments also show that the $NV^- \rightarrow NV^0$ conversion is reversible, with a typical back transfer time of 500 ms. We present a three-dimensional rate equation model, considering diffusion of electron-generated charge carriers and taking into account the integrated effect of subsequent pulses, which qualitatively describes the experimental results. This work shows that $NV^-$ centers are effectively converted to $NV^0$ centers by electron irradiation, and explains why $NV^-$ emission is not observed in CL measurements. We envision that the pump-probe CL approach presented in this work can be applied to other complex solid-state emitter systems, to obtain further insight in their complex dynamical behavior.



## 4.7. SUPPORTING INFORMATION

### 4.7.1. METHODS

#### ULTRAFAST SEM

A schematic of the setup is shown in Figure 4.1a. The pump-probe CL experiments are performed inside a SEM (Thermo Fisher Scientific/XL30 FEI) containing a Schottky field-emission electron cathode consisting of a ZrO coated W tip. The conditions used to generate the electron pulses are discussed in [49] (see chapter 2 for details about the photoemission process). We use a diode-pumped Yb-doped fiber system (IMPULSE Clark-MXR) providing 250-fs light pulses at a wavelength of $\lambda$ = 1035 nm and repetition rate of 5.04 MHz. The primary laser beam is guided through a harmonic generator to create $2^{nd}$, $3^{rd}$ and $4^{th}$ harmonics (517, 345 and 258 nm, respectively). The $4^{th}$ harmonic is guided to the electron column and focused with a $f$ = 15 cm lens onto the electron cathode, which is accessible through a vacuum window. Earlier work using the same setup has shown that this photoemission process results in electron pulses with a temporal spread in the picosecond range [49]. We use a gradient neutral-density filter to change the $4^{th}$-harmonic pulse energy from 0 to 1.5 nJ/pulse, which results in an average number of electrons per pulse up to 400. The corresponding time-averaged beam current on the sample was 0-325 pA measured with a Faraday cup. The error in the current measurement is ~25%, limited by the stability in the laser power, and measurement method. In

the experiments, the electron spot size has a diameter of ~600 nm. Using the same setup, a higher spatial resolution can be achieved at the expense of lower current on the sample [49]. All the experiments are performed at room temperature and at a pressure of $10 \times 10^{-6}$ mbar.

#### LASER-ELECTRON BEAM OVERLAP

The $2^{nd}$ harmonic ($\lambda$ = 517 nm) of the same primary laser beam is passed through a linear stage (Newport M-IMS600PP) with motor controller (Newport ESP301-1G), after which it is sent through a pellicle beam splitter (8:92), guided into the SEM sample chamber through a vacuum window, and focused onto the sample to a ~10 µm-diameter spot using an Al parabolic mirror ($1.46\pi$ sr acceptance angle, 0.1 parabola parameter and 0.5 mm focal distance). In the pump-probe measurements the $2^{nd}$ harmonic path length was tuned such that the light pulse was delayed 1.3 ns with respect to the electron pulse. The $2^{nd}$ and $4^{th}$ harmonic laser powers were independently controlled such that measurements with varying number of electrons per pulse could be done for constant $2^{nd}$ harmonic PL power.

#### CL AND PL COLLECTION

Luminescence from the sample is collected using the Al parabolic mirror and directed to a light collection and analysis system. Light collected by the mirror is focused ($f$ = 16 cm) onto the entrance facet of a multimode fiber (550 µm core diameter) creating a confocal collection geometry, which limits the PL and CL collection depth in the sample. The fiber guides the light to a Czerny-Turner spectrometer equipped with a CCD array detector (Princeton Spec10) and grating containing 150 lines/mm and blaze wavelength corresponding to 500 nm. A long-pass filter ($\lambda$ >532 nm) is used to suppress scattered pump laser light in the detection path. TCSPC measurements are performed by sending the CL signal to a single photon avalanche photodiode (MPD PD-100) analyzed by time correlation (Picoquant PicoHarp 300), which builds a delay histogram. In this case, an additional bandpass filter ($\lambda = 650 \pm 75$ nm) is used, corresponding to the spectral range within which NV emission occurs. We use the $3^{rd}$ harmonic laser pulse measured with a photodiode as the trigger for the time-correlated measurements. The PL, CL and PP data in Figure 4.1b and Figure 4.2a are collected over a time of 1 min each. The light collection geometry in this setup typically allows the collection of light within a 20 µm$^2$ × 20 µm$^2$ area. Only light emitted in this area, and within the escape cone of diamond, can be collected efficiently. Given the critical angle for diamond ($\theta_c < 24.6°$), we can estimate that light emitted at a depth down to 20 µm inside the diamond can still be collected. Nevertheless, emission beyond this 20 µm depth might reach the surface at a position outside of the collection area, thus the collection efficiency decreases at larger depths.

### 4.7.2. DATA ANALYSIS

Absorption cross sections of $NV^0$ and $NV^-$ at the excitation wavelength of $\lambda$ = 517 nm are estimated to be $2 \times 10^{-17}$ cm$^2$ and $1.4 \times 10^{-17}$ cm$^2$, respectively. In order to

estimate these cross sections, first the $NV^-$ and $NV^0$ contributions to the PL spectrum are disentangled by taking the normalized CL spectrum as the $NV^0$ spectral shape, and assuming that the remaining PL spectrum corresponds to the $NV^-$ contribution. We then consider complementarity between emission and absorption spectra, and normalize by known absorption cross sections at the ZPL of each center.1 The amount of excited NVs in PL from Figure 4.2b is calculated by considering the NV concentration ($200\,\mu m^{-3}$), and a light collection depth of $23\,\mu m$. The $NV^-$ population in the pump-probe measurements (Figure 4.2d) is obtained by fitting the PP spectra, after subtraction of the CL spectra, and considering the estimated absorption cross sections for the $NV^-$ and $NV^0$ states. The fitting of the NV spectra are performed with a total of 14 Gaussian functions: for each NV state ($NV^0$ or $NV^-$), one Gaussian function is used to fit the ZPL and 6 broader Gaussian functions are used to account for the phonon replica. We estimate a relative error in the calculation of the $NV^-$ population of < 25%, due to uncertainties in the fitting procedure.



### 4.7.3. MODEL

#### ELECTRON CASCADE SIMULATIONS

The spatial distribution of the creation of bulk plasmons by the primary electron beam was obtained with the Monte Carlo-based simulation software Casino [218]. We used a diamond density of $3.51\,g\,cm^{-1}$ and bulk plasmon energy of 31 eV [27]. The beam diameter is set to 600 nm. From the simulations we derive an average of 70 bulk plasmons created per electron.

#### MODEL FOR DIFFUSION OF CHARGE CARRIERS

The evolution in space and time of the concentration of electron-hole pairs, $\rho_{eh}(r,t)$, is obtained by solving the three-dimensional diffusion equation in spherical coordinates, which gives

$$\rho_{eh}(r,t) = \frac{a\sigma^3}{\left(2Dt+\sigma^2\right)^{3/2}} e^{-\frac{t}{\tau_R}} e^{-\frac{r^2}{4Dt+2\sigma^2}}, \tag{4.5}$$

where $D$ is the carrier diffusion coefficient and $\tau_R$ the carrier lifetime, which accounts for the recombination of carriers. We consider $D = 1\,\mu m^2\,ns^{-1}$, as obtained from literature [225, 227]. The parameters $a$ and $\sigma$ correspond to the amplitude and standard deviation of the 3D initial Gaussian distribution of carriers, derived from Casino simulations. In our case, $\sigma = 0.185\,\mu m$ and $a = 1404 n_{el}$, where $n_{el}$ is the number of electrons per pulse. We do not consider the effect of the diamond surface on the diffusion equation and recombination of carriers.

#### DISCRETE RATE EQUATION MODEL

The concentration of $NV^-$ as a function of position, $r$, and number of pulse, $n$, described by Equation 4.2 is derived by solving the rate equation

$$\rho_-(r,n+1) = \rho_-(r,n) - \alpha(r)\rho_-(r,n) + \beta\left[\rho_-(r,0) - \rho_-(r,n)\right]. \tag{4.6}$$

Here, $\alpha(r)$ is described in Equation 4.3 and is obtained by considering the change in $\rho_-(r,t)$ between subsequent pulses only due to $NV^-\rightarrow NV^0$ conversion, i.e. $\alpha(r) = \rho_{-,\mathrm{conv}}(r,T) - \rho_{-,\mathrm{conv}}(r,0)$). This process is described with the rate equation

$$\frac{\partial \rho_{-,\mathrm{conv}}}{\partial t} = -\nu_{\mathrm{th}}\sigma_c^{\mathrm{eh}}(r,t)\rho_{-,\mathrm{conv}}(r,t). \tag{4.7}$$

Similarly, we derive the expression of $\beta = \rho_{-,\mathrm{back}}(r,T) - \rho_{-,\mathrm{back}}(r,0)$ from Equation 4.4 by considering the change in $\rho_-(r,t)$ during the time between two pulses only due to the of $NV^0\rightarrow NV^-$ back transfer, which is obtained by solving the rate equation

$$\frac{\partial \rho_{-,\mathrm{back}}(r,t)}{\partial t} = \frac{\rho_{-,\mathrm{back}}(r,t) - \rho_{-,i}}{\tau_{\mathrm{back}}}. \tag{4.8}$$

In this description we assume that the change in $\rho_-(r,t)$ due to the $NV^-\rightarrow NV^0$ conversion and due to the $NV^0\rightarrow NV^-$ back transfer are independent between subsequent pulses. This assumption is valid since the back transfer time (500 ms) is much longer than the time between pulses (198 ns). In order to compare the model with the experimental data, we calculate the steady state value, $\rho_-(r,\infty)$, and integrate over a cylindrical volume, with cross section corresponding to the Gaussian profile of the excitation beam ($\sigma_{\mathrm{laser}} = 5\,\mu\mathrm{m}$). Given that diamond is transparent at the excitation wavelength ($\lambda = 517\,\mathrm{nm}$), absorption is only due to excitation of NV centers, thus NVs will be excited through the entire sample. Nevertheless, PL will only be effectively collected up to a certain depth, which becomes the fit parameter.

### 4.7.4. ADDITIONAL EXPERIMENTAL DATA

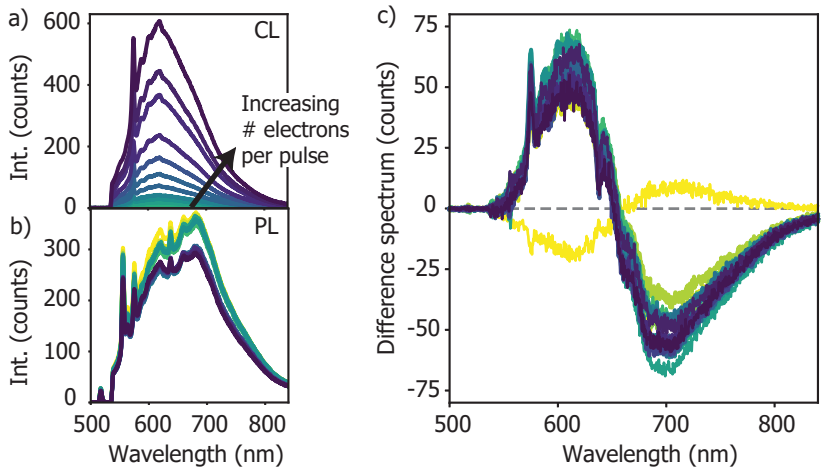


Figure 4.5: Pump-probe experiments performed with an electron energy of 30 keV. (a) Cathodoluminescence (CL), (b) Photoluminescence (PL) and (c) difference spectrum (PP – PL – CL, where PP stands for pump-probe). The colors of the curves indicate the number of electrons per pulse, going from 0 (yellow) up to 208 (dark purple). The difference spectrum reflects again the $NV^{-} \rightarrow NV^{0}$ conversion due to electron irradiation. Nevertheless, when performing these measurements at 30 keV we consistently observe deterioration of the sample after each CL measurement, as can be observed from the PL measurements (a) taken before each pump-probe measurement (and after each CL measurement). This deterioration of the sample can also be observed in the reference measurement (yellow curve, 0 electrons per pulse), which does not show a completely flat spectrum.

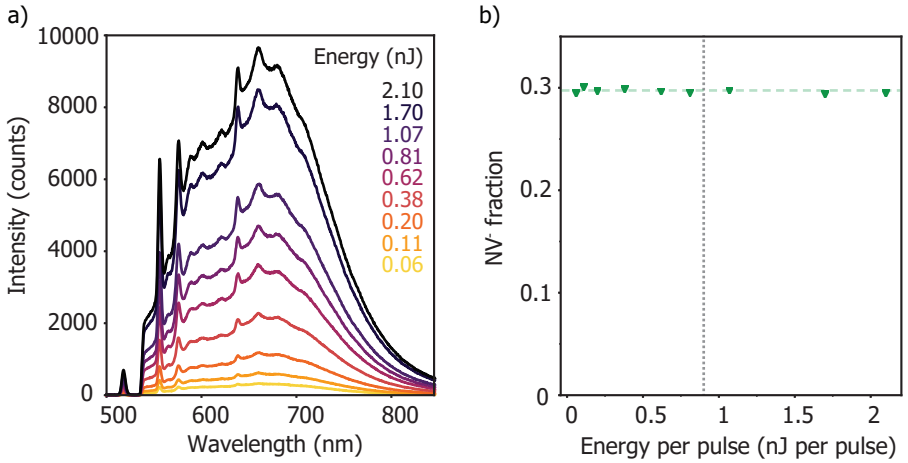


Figure 4.6: $NV^-$ fraction as a function of the incident laser power. (a) PL spectra obtained at the same spot on the sample but different incident laser power, ranging from 0.06 up to 2.1 nJ per pulse. (b) $NV^-$ fraction as a function of the energy per pulse, derived from the PL spectra in (a). The $NV^-$ fraction remains constant for the different values of the incident power, indicating that optically-induced $NV^- \rightarrow NV^0$ conversion (or vice versa) is negligible in this case. The dotted gray line indicates the power at which the experiments from Fig. 4.2 were performed, while the dashed green line serves as a guide for the eye. These measurements were all acquired at the same spot on the sample, but different from the spot in which measurements from Figure 4.2 were performed, thus explaining why the $NV^-$ fraction is different in both cases.

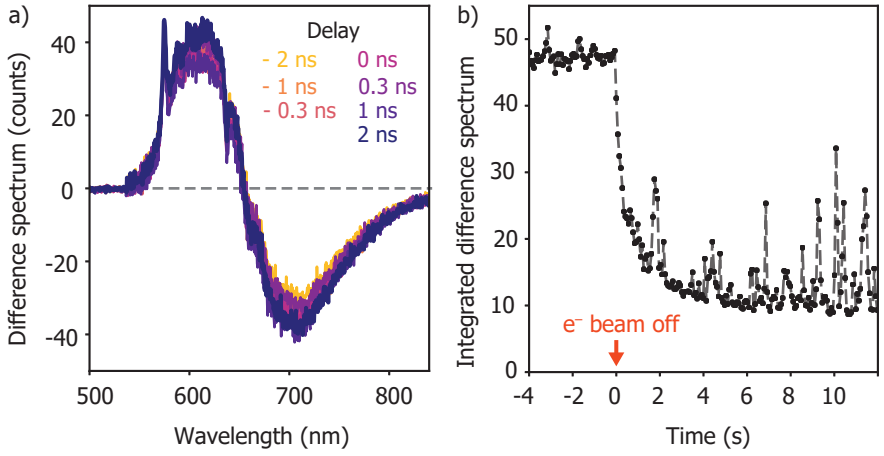


Figure 4.7: (a) Difference spectrum obtained for different laser arrival times. The delay indicates the difference in arrival time of electrons and laser pulses to the sample, with negative delay indicating that the laser arrives before the electron beam. The $NV^- \rightarrow NV^0$ conversion is again observed in the difference spectrum, but there are no differences among the different delays, due to the fact that the electron-induced conversion has a timescale in the millisecond regime (Fig. 4.3b), much larger than the time between pulses in the experiments (198 ns at 5.04 MHz). (b) Temporal evolution of the $NV^0 \rightarrow NV^-$ back transfer after turning off the electron beam. The y-axis corresponds to the mean value of the intensity of each difference spectrum, after taking the absolute value. Each spectra is extracted every 70 ms during the measurement (Fig. 4.3b).

# 5

# PHOTON STATISTICS OF INCOHERENT CATHODOLUMINESCENCE USING CONTINUOUS AND PULSED ELECTRON BEAMS

*Photon bunching in incoherent cathodoluminescence (CL) spectroscopy originates from the fact that a single high-energy electron can generate multiple photons when interacting with a material, thus revealing key properties of electron-matter excitation. Contrary to previous works based on Monte Carlo modeling, here we present a fully analytical model describing the amplitude and shape of the second-order autocorrelation function ($g^{(2)}(\tau)$) for continuous and pulsed electron beams. Moreover, we extend the analysis of photon bunching to ultrashort electron pulses, in which up to 500 electrons per pulse excite the sample within a few picoseconds. We obtain a simple equation relating the bunching strength ($g^{(2)}(0)$) to the electron beam current, emitter decay lifetime, pulse duration, in the case of pulsed electron beams, and electron excitation efficiency ($\gamma$), defined as the probability that an electron creates at least one interaction with the emitter. The analytical model shows good agreement with the experimental data obtained on InGaN/GaN quantum wells using continuous, ns-pulsed (using beam blanker) and ultrashort ps-pulsed (using photoemission) electron beams. We extract excitation efficiencies of 0.13 and 0.05 for 10 and* 8 keV *electron beams, respectively, and we observe that nonlinear effects play no compelling role, even after excitation with ultrashort and dense electron cascades in the quantum wells.*

## 5.1. INTRODUCTION

Photon statistics in incoherent cathodoluminescence (CL) reveals fundamental properties of the interaction of high-energy electrons (~1-300 keV) with matter [39]. In particular, the second-order autocorrelation function ($g^{(2)}(\tau)$) exhibits strong bunching ($g^{(2)}(0) \gg 1$) when exciting a material, such as a semiconductor or insulator, with an electron beam [39, 205, 228], contrary to conventional photoluminescence measurements with laser excitation (typically $g^{(2)}(0) = 1$) [140]. This is because each electron initially excites bulk plasmons in the material, which end up generating thermalized carriers that diffuse and recombine. This recombination can lead to either the emission of a photon with energy corresponding to the bandgap of the material (bimolecular recombination), or to the excitation of another emitter embedded in the material, such as a defect or quantum well, which can then decay radiatively. Either cases can result in the emission of multiple photons per incoming electron [207] Recently, $g^{(2)}(\tau)$ measurements have been used to quantify the excitation efficiency of electrons in InGaN/GaN quantum wells (QWs) with different geometries [41, 42]. The excitation efficiency is defined as the probability of an electron to interact with the emitter, in that case the QWs. Moreover, the $g^{(2)}(\tau)$ technique allows to extract the emitter decay dynamics without the need of a pulsed electron beam [39]. These new insights into the use of $g^{(2)}(\tau)$ measurements in CL are key for a complete and quantitative analysis of electron microscopy experiments.

All CL bunching experiments performed so far have been described using Monte Carlo-based numerical models, showing good agreement with the measured $g^{(2)}(\tau)$ curves and the dependence of $g^{(2)}(0)$ on the electron current. However, Monte Carlo models are time consuming and fail to provide a full understanding of the bunching process and the key parameters that determine its amplitude. Moreover, fitting the experimental data with a Monte Carlo model is complex and requires additional computation and interpolation procedures, thus making the $g^{(2)}(\tau)$ analysis less accessible.

In addition to this, so far CL autocorrelation measurements have been limited to the cases of continuous and ns-pulsed electron beams. Recently, ultrafast electron microscopy using fs-ps electron pulses as excitation sources, has emerged as a powerful technique to access the dynamics of electron excitation of materials with high temporal resolution, combined with the nanoscale electron-beam spatial resolution [24, 72, 96]. Ultrafast electron microscopy has already been used to study electron-generated carrier dynamics [79, 136] and phase transitions [229, 230], among others. Additionally, the development of techniques such as photon-induced near-field microscopy (PINEM) has exploited the quantum nature of the electron wave packet [87, 89], thus leading the way to the study of quantum-mechanical aspects of electron-light-matter interactions inside an electron microscope. Autocorrelation measurements, such as $g^{(2)}(\tau)$, using ultrashort electron pulses can offer new insights into the dynamics of excitation of a material with dense electron pulses [231].

In this chapter, we resolve the above-mentioned limitations of current $g^{(2)}(\tau)$

analyses which use Monte Carlo simulations. We develop a fully analytical model to describe the value of $g^{(2)}(0)$ as a function of four experimental parameters, for three different electron beam configurations. Our analytical model describes how the electron current (or number of electrons per pulse), emitter lifetime, excitation efficiency and pulse duration, in the case of pulsed electron beams, determine the value of $g^{(2)}(0)$. Using our analysis, we directly extract the electron excitation efficiency $\gamma$, defined as the fraction of electrons that create at least one interaction with the emitter [41], from one simple equation. We also show that our model reproduces the Monte Carlo simulations developed in previous work.

In order to further test the validity of the model, we perform $g^{(2)}(\tau)$ experiments on InGaN/GaN quantum wells with both continuous and pulsed electron beams. In particular, we study two types of pulsed electron beams: with relatively long (up to 200 ns) and ultrashort (a few ps) pulse durations. In the case of ultrashort pulses, we vary the number of electrons per pulse from (on average) less than 1 up to $\sim 500$, thus allowing us to access regimes in which several electrons interact with the sample within the bulk plasmon decay and carrier thermalization timescales. Here, our analytical model shows that $g^{(2)}(0)$ depends only on the number of electrons per pulse and the excitation efficiency. From the model it can also be derived that in the case of a pulsed electron beam the excitation efficiency can be obtained alternatively through a simple analysis, without the need of any fitting procedure. Our analysis of the $g^{(2)}(\tau)$ function shows that even for dense cascades generated by 500 electrons per pulse (i.e., within a few picoseconds) nonlinear effects do not have a compelling contribution in the excitation and carrier recombination of InGaN/GaN QWs.



## 5.2. EXPERIMENTAL SECTION

Cathodoluminescence experiments are performed in a scanning electron microscope (SEM) equipped with a parabolic mirror that collects the emitted light. The statistics of CL emission is analyzed using a Hanbury-Brown and Twiss (HBT) geometry [141], composed of a 50:50 beam splitter (BS) and two avalanche photodiodes (APDs) as single-photon counting detectors (5.1b). Experiments with varying pulse widths ($6-200$ ns) are performed using an electrostatic electron beam blanker. Ultrashort pulses, with pulse widths of few picoseconds, are obtained by focusing a fs-laser ($\lambda = 258$ nm) onto the electron cathode, inducing photoemission of electron pulses (see chapter 2). All of our experiments are performed at room temperature.

We study a bulk semiconductor heterostructure of InGaN/GaN quantum wells, grown by molecular beam epitaxy [41]. A schematic of the structure is shown in the inset of Fig. 5.1a. The sample consists of 10 2-nm-thick InGaN layers, separated with 15-nm GaN layers. A 2-nm AlGaN barrier layer is grown on top of the quantum well stack, and the whole structure is buried below a 250-nm-thick p-type GaN layer. The substrate is composed of n-type GaN. The inset also shows the results of Monte Carlo simulations of the trajectory of a 10 keV electron beam inside the sample, performed using the Casino software [1]. Each dot in the plot represents a

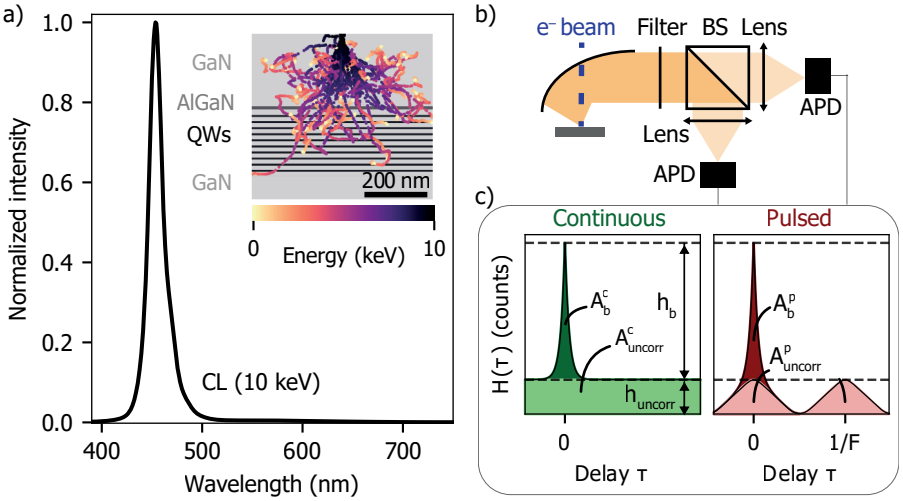


Figure 5.1: (a) Cathodoluminescence (CL) spectrum of InGaN/GaN quantum wells (QWs) obtained with a continuous 10 keV beam (242 pA). Inset: schematic of the InGaN/GaN heterostructure overlaid with the results from Monte Carlo simulations of the electron trajectory inside the sample, perfomed using the Casino software [1]. Each curve indicates the trajectory of one electron, and the color bar indicates the energy of the electron at each position. (b) Schematic of the CL collection and analysis using a Hanbury-Brown and Twiss (HBT) experiment. (c) Schematic of the expected histograms obtained using the HBT experiments using continuous (left) and pulsed (right) electron beams.

collision of the primary electron with the sample, which can lead to the excitation of one or more bulk plasmons. The color of the dot indicates the energy of the primary electron beam at that point. The results show that only a small fraction of the electrons will directly reach the QWs, as previously shown using $g^{(2)}(\tau)$ measurements [41]. Moreover, the AlGaN layer acts as a carrier blocking layer [232], hence only carriers generated below this layer can excite the QWs.

Figure 5.1a shows a typical CL spectrum obtained when exciting the sample with 10 keV electrons. The emission originates mostly from the QWs, corresponding to the InGaN band edge emission peak around 450 nm. Defect luminescence from the yellow band [163, 233], in the 520-650 spectral range, is barely visible in the spectrum, given that the intensity in this range is 30 times lower than the QW emission. This is in accordance with previous CL measurements on this sample [41], and is attributed to the fact that 10 keV electrons do not reach the GaN substrate, thus limiting the excitation of carriers in the bulk GaN. In the HBT experiments we use a bandpass filter ($450 \pm 40$ nm) to ensure that only the CL emission from the QWs is recorded.

## 5.3. CONTINUOUS ELECTRON BEAM

A typical $g^{(2)}(\tau)$ experiment consists of the acquisition of a histogram ($H(\tau)$) of the number of coincidence events (i.e., a correlation) as a function of the delay between two recorded photons ($\tau$). A schematic of the recorded histogram obtained after excitation with a continuous electron beam is shown in Fig. 5.1c (left). In this case, the $g^{(2)}(\tau)$) curve is obtained by normalizing the histogram with respect to the value at very long delay ($\tau \to \infty$), $h^c_{\text{uncorr}}$, which represents the amplitude for uncorrelated events. Hence,

$$g^{(2)}(0) = \frac{H(0)}{H(\tau \to \infty)} = 1 + \frac{h^c_b}{h^c_{\text{uncorr}}}, \tag{5.1}$$

where $h^c_b$ is the amplitude of the bunching peak, as depicted in Fig. 5.1c. $g^{(2)}(0)$ can be interpreted as the likelihood of having two photons with delay $\tau = 0$ compared to any other delay. In the case of Poissonian statistics, such as for coherent light, $g^{(2)}(\tau) = 1$ for any delay [140], while $g^{(2)}(0) < 1$ indicates sub-Poissonian statistics (antibunching), as in the case of a single-photon emitter [234, 235], and $g^{(2)}(0) > 1$ represents super-Poissonian statistics (bunching). Some examples of processes in which bunching occurs are blackbody radiation [236, 237] and superradiance [238, 239], as well as the CL emission presented here. From a statistical point of view, $h_b$ is related to the total number of correlations (defined as the detection of two photons) leading to bunching, that is, coming from the same electron, while $h^c_{\text{uncorr}}$ represents the uncorrelated events, that is, correlations between photons that are generated by different electrons.

The temporal decay of the bunching peak is determined by the radiative decay of the emitter and enables determination of the emitter lifetime, as will be explained below. The area of the bunching peak, related to the height as $A^c_b = \alpha_b h^c_b$, is proportional to the average number of possible combinations between pairs of photons that lead to bunching, that is, that come from the same electron. Here we have defined $\alpha_b$ as the shape factor of the bunching peak. Similarly, the area $A^c_{\text{uncorr}}$ is related to the mean number of possible combinations of photon correlations from different electrons, that is, uncorrelated events, during the acquisition time of the experiment $T = B\,t_B$. Here $B$ is the total number of bins in the experiment and $t_B$ is the time of each bin. From this it follows that $A_{\text{uncorr}} = h^c_{\text{uncorr}}(2B+1)\,t_B/2$. The factor $2B+1$ comes from the fact that the $g^{(2)}(\tau)$ histogram is theoretically built over positive and negative times, in a symmetric fashion. The additional factor 2 in the denominator accounts for the fact that the number of possible events decreases for increasing delay following a triangular function (see section 5.7.2 in the Supporting Information). Taking these definitions into account, Eq. 5.1 becomes

$$g^{(2)}_{\text{cont}}(0) = 1 + \frac{A^c_b}{A^c_{\text{uncorr}}} \frac{(2B+1)\,t_B}{2\alpha_b}. \tag{5.2}$$

The model is constructed following the subsequent steps that start with an electron entering the material, until a photon is emitted, similar to the previous Monte Carlo model [39, 41]. The steps are as follows:

1. Excitation of $b_i$ bulk plasmons in GaN close to the QWs, described by a Poisson distribution with expected value $b$. It should be noted that the number of plasmons generated per electron will probably be larger than $b_i$, but here we only consider those that can create carriers which can excite the QWs, that is, excited within the carrier diffusion length.

2. Decay of each bulk plasmon into $m_i$ thermalized carriers, again described by a Poisson distribution with expected value $m$.

3. Diffusion of carriers, which can either:

   (a) excite a QW, which emits a photon. The joint probability of these two steps is accounted in the parameter $\eta$.

   (b) not excite a QW or excite a QW which then decays non-radiatively.

   This step is assumed to follow a binomial distribution, with $m_i$ representing the number of events and $\eta$ probability that an event results in the emission of a photon.



We should note that here we refer to the process of QW excitation, but the model can be applied to any other kind of emitter, or simply to carrier recombination. In the case of a thin sample and high electron energy, such as in transmission electron microscopy (TEM) experiments, the average number of bulk plasmons ($b$) defined in step 1 corresponds to the ratio between the thickness and the electron mean free path [13, 39]. In the case of thicker samples, b takes into account the probability that carriers, and, in particular, minority carriers, created after electron excitation actually reach the emitter. It therefore depends on the sample geometry and diffusion length of minority carriers, as will be seen further in the text.

A key aspect of our $g^{(2)}(0)$ model is that it accounts for the combined stochastic nature of all the involved processes. The model is therefore based on the calculation of the average possible combinations of pair-correlation events that lead to bunching ($A_b^c$) and to uncorrelated events ($A_{\text{uncorr}}^c$). A full derivation of the model is provided in the Supporting Information (section 5.7.2). In brief, from step 2 and 3 we obtain that the average number of possible combinations of pair-correlation events created after the excitation of $b_i$ bulk plasmons is given by $b_i^2 m^2 \eta^2$. We then need to find the average number of combinations of correlations between pairs of photons from the same electron (i.e., ignoring pair-correlation events created by photons from different electrons), taking into account that $b_i$ follows a Poisson distribution. Given n electrons arriving at the sample during the time of the experiment $T$, the average number of combinations of pair-correlation events leading to bunching becomes

$$A_b^c = nb(b+1)m^2\eta^2 . \tag{5.3}$$

Similarly, it can be shown that the expected value of the number of combinations of pair-correlation events leading to uncorrelated events, that is, pairs of photons coming from different electrons, is (see 5.7.2)

$$A_{\text{uncorr}}^c = n(n-1)b^2 m^2 \eta^2 . \tag{5.4}$$

We now insert Eqs. 5.3 and 5.4 into Eq. 5.2, and rewrite $n$ as a function of the electron current, $I = nq/(Bt_b)$, where $q$ is the electron charge. We also consider the limit $B \gg 1$, which is reasonable given that the acquisition time is typically minutes or more, while the time resolution is usually less than 1 ns. We then obtain the following expression for the amplitude of $g^{(2)}(\tau)$ at 0 delay:

$$g^{(2)}_{\text{cont}}(0) = 1 + \frac{q}{I\alpha_b}\frac{b+1}{b}. \tag{5.5}$$

Several aspects are noticeable from Eq. 5.5. First of all, we can see that the value of $g^{(2)}(0)$ is inversely proportional to the electron beam current, which is in agreement with previous experimental results [39, 41, 228]. This can now be understood from the fact that the amplitude of the bunching peak scales linearly with the number of electrons reaching the sample (Eq. 5.3), as it depends on the number of correlations between photons from the same electron. Instead, the background scales quadratically (Eq. 5.4), since it depends on the events created by photons from different electrons.

Second, Eq. 5.5 shows that $g^{(2)}(0)$ does not depend on the number of carriers generated per bulk plasmon $m$, nor on the efficiency of these carriers to excite a QW or the quantum efficiency of the QW (both processes included with $\eta$). The only relevant parameter is the number of bulk plasmons created close to the QWs ($b$). This is in agreement with the fact that $g^{(2)}(\tau)$ measurements are independent of the absolute intensity incident on the detectors, as long as the statistics of the emission process is preserved [140]. Notice that even in the case $b = 1$, that is on average one bulk plasmon per electron interacts with the QWs, $g^{(2)}(0) > 1$ due to the stochastic nature of the plasmon excitation process. It follows from Eq. 5.5 that the bunching contribution to $g^{(2)}(0)$ increases with decreasing $b$, given that decreasing the number of interacting plasmons generated per electron would have a similar effect as decreasing the current. Given the Poissonian nature of the $b_i$ parameter, the average number of interacting bulk plasmons $b$ is related to the probability of creating at least one interaction (bulk plasmon) close to the emitter [41], defined as

$$\gamma = 1 - \text{Poiss}(0; b) = 1 - e^{-b}, \tag{5.6}$$

where $\gamma$ can be interpreted as the excitation efficiency of the electron in the given material geometry. Finally, the value of $g^{(2)}(0)$ also depends on the shape of the bunching curve ($h_b(\tau)$), which is represented by the dependence on $\alpha_b$. Given an emitter decay $y_{\text{emitter}}(t)$, it can be shown that the number of correlations between photons emitted with a delay $\tau$ is proportional to (see 5.7.4)

$$h_b = \int_0^\infty y_{\text{emitter}}(t)\, y_{\text{emitter}}(t+\tau)\, dt. \tag{5.7}$$

In the case that the emitter decays as a simple exponential with lifetime $\tau_{\text{emitter}}$, $h_b(\tau)$ is an exponential with $\tau_{\text{emitter}}$, and thus the decay of the $g^{(2)}(\tau)$ curve directly gives the emitter decay. In this case, the relation between the area and the height of the bunching peak is: $\alpha_b = 2\tau_{\text{emitter}}$ (see 5.7.2). In the case of more complex decay

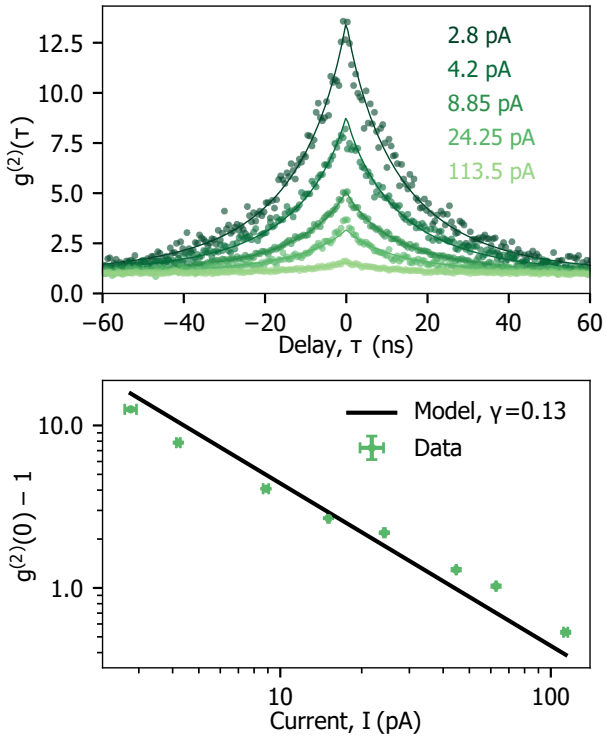


Figure 5.2: $g^{(2)}(\tau)$ measurements with a continuous electron beam. (a) $g^{(2)}(\tau)$ experiments obtained for different electron currents, with an electron energy of 10 keV. The points represent the data and the solid lines the fit. (b) Fits of $g^{(2)}(0)-1$ vs electron current obtained from the curves in (a). The black solid line is the fit obtained using Eq. 5.5, from which a value of $\gamma = 0.13$ is obtained. The error bars represent the uncertainty in the measured value of the electron current (horizontal) and fit errors (vertical).

mechanisms, we should apply Eq. 5.7 to extract the emission dynamics from the $g^{(2)}(\tau)$ measurement. Eqs. 5.5 and 5.7 can now be directly used to fit experimental data of $g^{(2)}(\tau)$ versus beam current, to determine $b$, and hence $\gamma$, thus providing essential information on the electron beam excitation efficiency in incoherent CL excitation.

Figure 5.2a shows a selection of $g^{(2)}(\tau)$ measurements of the QW sample at different electron currents, all obtained using a continuous 10 keV electron beam. The time binning in all measurements is set to $t_b = 512$ ps. At the lowest current (2.8 pA), $g^{(2)}(0) = 12.6$ is obtained, while the value of $g^{(2)}(0)$ strongly decreases for increasing current. The curves cannot be properly fitted with a simple exponential decay, probably due to multiple decay processes taking place simultaneously. Instead, the emitter decay ($y_{\text{emitter}}(t)$) can be described with a stretched exponential, given by

$$y_{\text{emitter}}(t) = y_0 e^{-\frac{t}{\tau_{\text{emitter}}}^{\beta_{\text{emitter}}}}, \tag{5.8}$$

with parameters $\tau_{\text{emitter}}$ representing the average emitter lifetime and $\beta_{\text{emitter}}$ the deviation from a pure exponential decay [240]. This is further confirmed by direct measurements of the decay statistics of the QWs (see 5.7.4). In this case, the shape of $g^{(2)}(\tau)$ does not give directly the emitter decay properties, but we need to fit the data with Eq. 5.7, which can be solved numerically. The solid lines in the figures correspond to the fits, from which we obtain an emitter lifetime of $\tau_{\text{emitter}} = 10.65 \pm 0.32$ ns and $\beta_{\text{emitter}} = 0.76 \pm 0.01$.

In order to compare the experimental results with the analytical model, Fig. 5.2b shows the value of $g^{(2)}(0) - 1$, obtained from the fits of each curve, as a function of electron current. The horizontal error bars indicate the uncertainty in measuring the electron current, while the vertical errors are derived from the fitting procedure. We observe that the value of $g^{(2)}(0) - 1$ exhibits a linear decrease (on a log-log plot) with slope $-1$, as predicted by Eq. 5.5. The shape factor $\alpha_b$ is calculated numerically from the solution of Eq. 5.7 using the derived values of $\tau_{\text{emitter}}$ and $\beta_{\text{emitter}}$, thus becoming $\alpha_b = 25.04$. Therefore, we can extract $b$ from Eq. 5.5. We obtain the best fit for $b = 0.13$, which yields an excitation efficiency of $\gamma = 0.13 \pm 0.01$, meaning that on average, only 13 out of 100 electrons actually interact with the QWs. This low interaction between the electrons and the QWs is attributed to the fact that at 10 keV most electrons lose their energy before arriving to the QWs, as shown in Figure 5.1a and discussed in ref. [41]. Moreover, the carriers generated on the top GaN layer cannot reach the QWs, due to the presence of the AlGaN blocking layer on top of the QWs. For reference, we also show in the Supporting Information (section 5.7.1) that the results from the model are in excellent agreement with those obtained with the Monte Carlo-based approach proposed in previous works [39, 41], confirming that our model serves as an effective analytical version of the Monte Carlo one.



## 5.4. PULSED ELECTRON BEAM

$g^{(2)}(\tau)$ experiments can also be performed using pulsed electron beams, which can offer advantages such as lower acquisition times and simpler analysis, as will be discussed below. In this configuration, the photon emission dynamics is shaped by the temporal spread of electrons, and thus a modified model needs to be developed. A schematic of the histogram obtained in an HBT experiment in pulsed conditions is shown in Figure 5.1c (right). In contrast to the continuous case, here the histogram is composed of a peak at $\tau = 0$, containing correlations between photons from the same electron pulse, and peaks at delays corresponding to the time between pulses ($\tau_i = i/F$, with $i$ being an integer number and $F$ the repetition rate). The latter correspond to correlations between photons from consecutive pulses ($i = \pm 1$), from every second pulse ($i = \pm 2$) and so on. These peaks are thus analogous to the background ($A^c_{\text{uncorr}}$) in the continuous case.

The derivation of the model for the pulsed case is similar to the one for the continuous one, with the main difference being the shape factor of the bunching ($\tau_0$) and uncorrelated ($\tau_i, i \neq 0$) peaks. Given that the peaks at $\tau_i (i \neq 0)$ contain correlations between photons from different pulses, their shape is determined by

both the electron pulse and emitter decay, as explained in the Supporting Information (5.7.4). The ratio between the area ($A^p_{\text{uncorr,i}}$) and the height ($h_{\text{uncorr,i}}$) of any of these peaks is given by $A^p_{\text{uncorr,i}} = \alpha_{\text{conv}} h_{\text{uncorr,i}}$. $\alpha_{\text{conv}}$ is thus a shape factor, which will depend on the particular shape of the electron pulse and emitter decay.

The peak centered at $\tau = 0$, accounts for correlations between photons from the same pulse, and has two components ($A^p_0 = A^p_{\text{uncorr,0}} + A^p_b$). The first component corresponds to correlations between photons from the same pulse, but different electrons, and therefore has a shape factor $\alpha_{\text{conv}}$. The second component corresponds to correlations between photons from the same electron, which is what constitutes the bunching. Similar to the continuous case, we can consider that all the excitations take place instantaneously, given that the time scale of bulk plasmon decay and carrier diffusion (typically in the fs/ps regime) [207] is much smaller than the emitter lifetime (hundreds of ps or ns). Therefore, the shape of the electron pulse does not play a role in this component, contrary to the case of the uncorrelated component. The time between photons is only determined by the emitter lifetime, and $A^p_b = \alpha_b h^p_b$, where $h^p_b$ is the height of this peak.

5

Taking into account the shape factors, and calculating the average number of possible combinations of pair-correlations events for bunching ($A^p_b$) and uncorrelated ($A^p_{\text{uncorr,i}}$) events in an analogous way as in the continuous case (see section 5.7.3 for a full derivation), we obtain that for pulsed excitation

$$g^{(2)}_{\text{pulsed}}(0) = 1 + \frac{\alpha_{\text{conv}}}{\alpha_b}\frac{b+1}{n_e b}. \tag{5.9}$$

We observe that the expression for $g^{(2)}(0)$ for a pulsed beam is very similar to the one for the continuous case (Eq. 5.5). Here, $g^{(2)}(0)$ is inversely proportional to the number of electrons per pulse, which is related to the electron beam current through $n_e = \frac{I}{qF}$, with $F$ being the repetition rate. The dependence of $g^{(2)}(0)$ on the average number of bulk plasmons that interact with the sample ($b$) is exactly the same as for a continuous electron beam, showing that the pulsed $g^{(2)}(\tau)$ measurement fundamentally probes the interaction of electrons with the sample in the same way. The main difference between the continuous and pulsed case is the factor $\alpha_{\text{conv}}$: in the pulsed case the $g^{(2)}(0)$ depends also on the shape of the electron pulse. From the derivation of $g^{(2)}(0)$ (section 5.7.3) it also follows that now we can simply divide the area of the peak at $\tau = 0$ by the area of any other peak at $\tau \neq 0$ to obtain the excitation efficiency:

$$\frac{A^p_b + A^p_{\text{uncorr,0}}}{A^p_{\text{uncorr,i}}} = 1 + \frac{b+1}{n_e b} = 1 + \frac{1-\log(1-\gamma)}{n_e \log(1-\gamma)}. \tag{5.10}$$

In this case we do not need any fitting procedure nor prior knowledge of electron pulse shape or emitter decay, thus making the analysis even simpler. This becomes particularly useful when having small signal-to-noise ratios or nontrivial emitter decays or electron pulse shapes, in which cases fitting becomes challenging.

In order to test the model for the pulsed case, we performed experiments using an ultrafast beam blanker, in which a set of electrostatic plates is inserted inside the

electron column. One of the plates is driven using a pulse generator, which is set to send a square signal with peak-to-peak voltage of 5 V and offset 2.5 V, while the other plate is grounded. This configuration allows us to obtain effectively square electron pulses with pulse width ($\Delta p$) determined by the repetition rate $F$ and duty cycle $D$. A characterization of the electron pulses is shown in the Supporting Information (5.7.6). In our experiments we kept the duty cycle fixed at $D = 95\,\%$ and varied the repetition rate from 0.2 to 6 MHz, resulting in pulse widths ranging from 200 down to 6 ns. Notice that an even smaller pulse width, down to 30 ps, can be obtained using the same ultrafast blanker in a different configuration [49], but long pulse widths were chosen to show the effect on the amplitude and shape of the bunching peak. The current in continuous mode (that is, without blanking) was kept constant ($I = 214$ pA) for all experiments, therefore changing the repetition rate results in a varying number of electrons per pulse, that is,

$$n_e = \frac{I}{q}\frac{1 - D/100}{F} = \frac{I}{q}\Delta p \tag{5.11}$$

Figure 5.3a shows a selection of $g^{(2)}(\tau)$ curves centered around the peak at zero delay. The experiments were performed using an electron energy of 8 keV instead of 10 keV as in the measurements using a continuous electron beam. This choice of lower electron energy allows us to achieve relatively high $g^{(2)}(0)$ amplitudes despite having a high current on the sample (214 pA), due to the blanking conditions. The solid lines in Fig. 5.3 are the fits of the data, which correspond to the sum of the solution from Eq. 5.7 (assuming a decay following a stretched exponential), and a convolution between a triangular curve and the same solution from Eq. 5.7. The triangular function comes from the convolution between two square pulses with pulse width ($\Delta p$), representing two electron pulses (see 5.7.4). The best fit of the curves is found for $\tau_{\text{emitter}} = 5.40 \pm 0.33$ ns and $\beta_{\text{emitter}} 0.56 \pm 0.01$. The difference between these values and the ones found in the continuous experiment (10.7 ns and 0.67, respectively) is attributed to the inhomogeneity of the sample, which results in emission lifetimes that depend on sample position (see Supporting Information, 5.7.8). The discrepancy could also come from the fact that at 10 keV we might be probing deeper QWs, which can exhibit different lifetimes. The curve at the lowest number of electrons per pulse (8 $e^-$/pulse) exhibits the highest amplitude ($g^{(2)}(0) = 4.1$). In this case, the pulse width (6 ns) is comparable to the emitter lifetime, and thus no clear distinction between the bunching ($A_b^p$) and uncorrelated ($A^p_{\text{uncorr},0}$) curves can be observed. Instead, the $g^{(2)}(\tau)$ curve for long pulses show a small sharp peak, corresponding to the bunching peak, on top of a broader background, as can be observed in the curve corresponding to $\Delta p = 500$ ns (637 electrons per pulse). The full shape of the uncorrelated peak can be observed in the right inset of Figure 5.3a, showing the peak around delay 0 and the first consecutive peak ($\tau_1 = 1/F$).

The value of $g^{(2)}(0) - 1$ as a function of the number of electrons per pulse is shown in Figure 5.3b, which has been derived from the fits in Fig. 5.3a. We observe that the bunching decreases with increasing number of electrons per pulse, as expected, but, contrary to what we observed in the continuous case, the data does

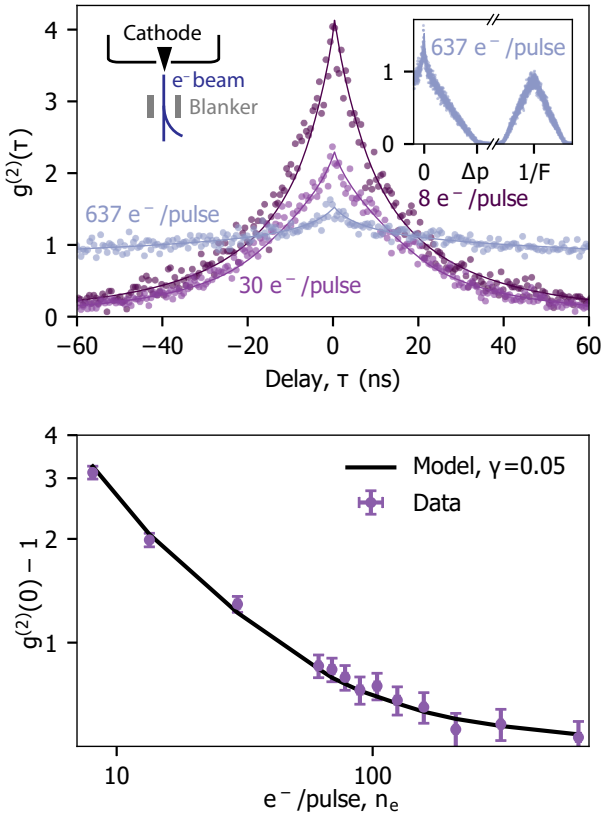


Figure 5.3: $g^{(2)}(\tau)$ measurements with a ns-pulsed electron beam. (a) $g^{(2)}(\tau)$ experiments obtained by changing the electron pulse width $\Delta p$, which leads to a change in the number of electrons per pulse. In this case the electron energy is 8 keV. The points represent the data and the solid lines the fit. Insets: (left) schematic of the beam blanking configuration, (right) example of a $g^{(2)}(\tau)$ measurement shown for a wider delay time range, thus showing the full peak at $\tau = 0$ and the consecutive peak at $\tau = 1/F$, where $F$ is the repetition rate. (b) Experimental results of $g^{(2)}(0) - 1$ vs number of electrons per pulse, obtained from the fits of the curves in (a). The black solid line corresponds to the best fit obtained using Eq. 5.10, which yields an excitation efficiency of $\gamma = 0.05$. The error bars are derived from the uncertainty in the current measurement (horizontal) and fitting procedure (vertical).

not exhibit a linear trend (on the log-log plot). This is due to the fact that in this comparison we are changing $\alpha_{\text{conv}}$ in each measurement. For a fixed beam current, large pulse widths correspond to a higher number of electrons per pulse. So, while we expect decreasing value of $g^{(2)}(0)$ with electrons per pulse, the factor $\alpha_{\text{conv}}$ also becomes larger, thus effectively increasing $g^{(2)}(0)$. The model, which accounts for this effect, shows a good agreement with the data. We can therefore extract an excitation efficiency of $\gamma = 0.05$. The fact that a lower $\gamma$ is found here compared to the continuous case is fully consistent with the fact that the pulsed experiments were performed with an electron energy of 8 keV instead of 10 keV. At this lower electron energy, most bulk plasmons are generated in the top GaN layer, resulting in fewer excitations close to the quantum wells. The spectrum of the QWs and the Monte Carlo simulations of the electron beam trajectory at 8 keV is provided in the Supporting Information (section 5.7.7). Additionally, we can derive the excitation efficiency using Eq. 5.10 by simply dividing the area of the bunching peak by the area of any other peak, from which we obtain $\gamma = 0.06$, which is in good agreement with the value found using the fitting procedure.



## 5.5. ULTRASHORT PULSES

An extreme case of the model for pulsed $g^{(2)}(\tau)$ measurements is when we have ultrashort electron pulses, that is, in the picosecond regime. In this case, the electron pulse width is very small compared to the emitter lifetime, and thus the factor accounting for the convolution of both becomes $\alpha_{\text{conv}} = \alpha_b$. Then, Eq. 5.9 can be further simplified to

$$g^{(2)}_{\text{ultrashort}}(0) = 1 + \frac{b+1}{n_e b} = \frac{A_0^p}{A^p_{\text{uncorr,i}}}, \tag{5.12}$$

where the only remaining parameters are the number of interacting bulk plasmons per electron, which can be also described in terms of excitation efficiency ($\gamma$), and the average number of electrons per pulse $n_e$. In this case the shape of the bunching peak, and thus, the emitter lifetime, do not contribute to the amplitude of $g^{(2)}(0)$. Moreover, $g^{(2)}(0)$ now can be directly obtained from the ratio between the areas of the different peaks, similar to Eq. 5.10. Hence, when analyzing an experiment, we can simply sum all the counts from each of these two peaks (at $\tau = 0$ and $\tau_i = i/F, i = \pm 1, \pm 2, \dots$) and divide them to directly obtain the value of $g^{(2)}(0)$. In this way, the analysis to retrieve the excitation efficiency from $g^{(2)}(\tau)$ measurements becomes even simpler. We should also notice that ultrashort pulses are typically achieved by changing the emission statistics of the electron. For example, in the case of photoemission of electron pulses, as in the experiments shown below, the emission of pulses is determined by laser excitation of the electron cathode, instead of conventional thermionic or Schottky emission. Our derivation of $g^{(2)}(0)$ is general and does not assume any particular emission statistics for the electron beam. In the Supporting Information (section 5.7.3) we show a complementary derivation for electron pulses obtained with photoemission.

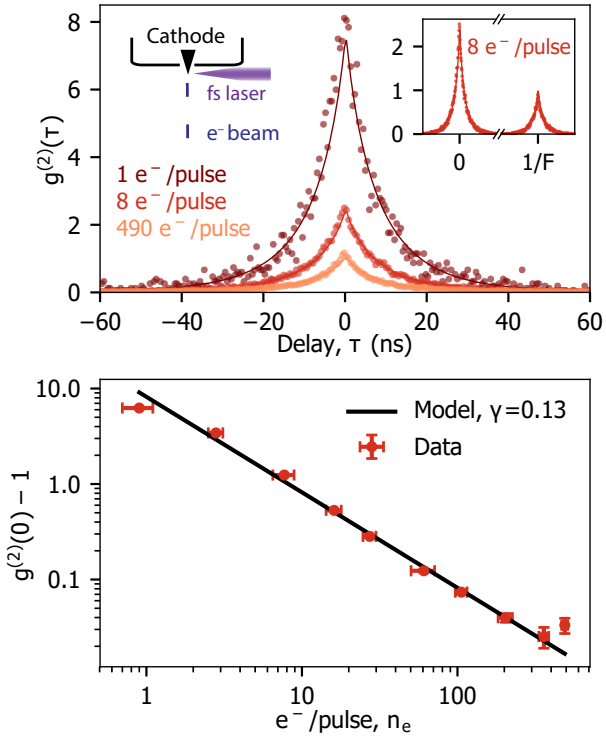


Figure 5.4: $g^{(2)}(\tau)$ measurements with ultrashort (ps) electron pulses. (a) $g^{(2)}(\tau)$ experiments obtained by changing number of electrons per pulse, with electron energy of 10 keV. The experimental data is represented by points, while the solid lines are the fits obtained by solving Eq. 5.7 (with $y_{\text{emitter}}(\tau)$ being a stretched exponential). Insets: (left) schematic of the photoemission setup, (right) zoom-out of a $g^{(2)}(\tau)$ measurement, showing that the shape of the uncorrelated peaks (in this case, $\tau = 1/F = 200$ ns) is now determined only by the emitter decay. (b) $g^{(2)}(0) - 1$ vs number of electrons per pulse, obtained by dividing the area of the bunching peak by the area of any other peak, as discussed in Eq. 5.12. The black solid line corresponds to the best fit obtained using Eq. 5.12, which yields an excitation efficiency of $\gamma = 0.13$.

Figure 5.4a shows a selection of $g^{(2)}(\tau)$ measurements performed using ultrashort pulses (~ 1 ps), obtained by focusing a fs laser into the electron cathode at a repetition rate of 5.04 MHz [72] (see chapter 2). We chose the conditions for which a larger number of electrons per pulse can be achieved (up to 490 in this case) at the expense of spatial resolution [49] (chapter 2). This regime allows us to reach the highest possible electron cascade density, as will be discussed below. The experiments were performed with an electron energy of 10 keV. The figure shows the 0-delay peak for a changing number of electrons per pulse. We observe that with an average of 1 electron per pulse we obtain $g^{(2)}(0) = 7.25$. The right inset in Figure 5.4a shows a measurement including also the first uncorrelated peak, centered at $\tau = 198$ ns. We observe that now both the peaks at $\tau = 0$ and at $\tau = 1/F$ have the same shape, determined by the emitter decay. The solid lines again represent the curves obtained by fitting with Eq. 5.7, given that the emitter decay follows a stretched exponential. The best fit is obtained for $\tau_{\text{emitter}} = 5.84 \pm 0.07$ ns ns and $\beta_{\text{emitter}} = 0.751 \pm 0.004$. Figure 5.4b shows the value of $g^{(2)}(0) - 1$ as a function of the number of electrons per pulse, together with the fit using Eq. 5.12. Here, the data points have been obtained by simply dividing the areas of the bunching peak by the height of peaks at $\tau_i = i/F$. The horizontal error bars represent the uncertainty in current measurement in pulsed, partially due to instability in the power of the laser that excites the tip. The vertical error bars are obtained from the analysis of areas below the peaks. We also correct for the fact that the number of events decreases at long delays due to an experimental artifact (see 5.7.5). We observe that the data follows the trend predicted by Eq. 5.12, yielding the best fit for the model for $\gamma = 0.130 \pm 0.001$, which is in agreement with the excitation efficiency found in the experiments in continuous mode, in which the same electron energy was used. This confirms the feasibility of using the $g^{(2)}(\tau)$ analysis with ultrashort electron pulses to obtain the excitation efficiency, thus enabling many applications of $g^{(2)}(\tau)$ spectroscopy in ultrafast electron microscopy.

Even though the data show a linear trend as in the continuous case, we should note that the electron excitation is very different between the continuous and pulsed cases. In ultrafast pulsed mode, we are exciting the sample with a large number of electrons within a very short time (ps), while in the continuous or beam-blanked cases the average time between two consecutive electrons was never smaller than hundreds of ps (600 ps at 260 pA). We expect that bulk plasmons decay within the first tens of fs after electron excitation, initially creating hot carriers. The thermalization of these carriers typically occurs within tens of ps [207]. Therefore, in the ps-pulsed $g^{(2)}(\tau)$ experiment up to 490 electrons in each pulse excite the sample within the carrier thermalization time, and in a relatively small area. This raises the question whether we are inducing any nonlinear interaction between carriers due, such as Auger recombination, to high carrier concentrations.

Previous work on InGaN/GaN quantum wells under optical excitation showed that a high excitation fluence leads to a decrease in efficiency, typically referred to as "efficiency droop" [241]. Even though the origin of this effect is still under discussion, some works attributed this efficiency droop to Auger recombination due to

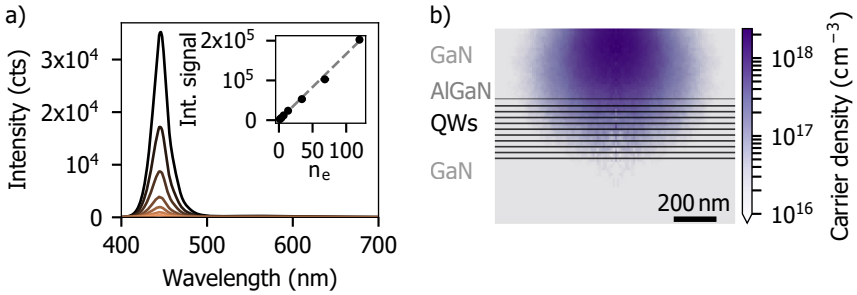


Figure 5.5: (a) Spectra of the QWs obtained when exciting with ultrashort electron pulses, containing from 1.4 (orange) up to 120 (black) electrons per pulse on average (10 keV). Inset: integrated signal of the QW emission as a function of the number of electrons per pulse. The dashed line corresponds to a linear fit. (b) 2D map of the estimated maximum carrier density in the sample obtained after excitation of 490 electrons with an energy of 10 keV.

5

locally-induced high carrier densities [241]. Nevertheless, the trend of $g^{(2)}(0)$ with the number of electrons per pulse exhibits a clear power law, as expected from the $g^{(2)}(\tau)$ model, which neglects nonlinear effects. These results suggest that nonlinear interactions between carriers do not play a significant role in this case, even at the highest number of electrons per pulse. This further suggests that the induced carrier densities are lower than the threshold for Auger recombination to occur.

To further elucidate this absence of nonlinear effects, Figure 5.5a shows CL spectra of the QWs obtained at different number of electrons per pulse. The integrated area below the curve (in the 410-490 nm spectral range) as a function of the number of electrons per pulse is plotted in the inset of Figure 5a. We observe a clear linear trend with increasing number of electrons per pulse. Figure 5.5b shows the calculated maximum carrier density for a 10 keV electron beam containing 490 electrons. Here we have assumed a radius of the electron beam of 200 nm, corresponding to the expected spatial resolution obtained under our pulsed conditions, calculated using the Fourier transform method explained in ref. [49]. We use the Casino software [1] to estimate the number of inelastic collisions of the electron with the sample. We assume that each collision corresponds to the generation of a bulk plasmon and generates 3 electron/hole pairs [28, 242]. We observe that the highest carrier density is in the order of $6 \times 10^{17}$ cm$^{-3}$. Previous works based on optical excitation of InGaN show that Auger processes only become dominant for carrier densities larger than $1 \times 10^{18}$ cm$^{-3}$ [243, 244]. Therefore, the electron-induced carrier density is below that which would create nonlinear effects. Moreover, we expect the initial spatial distribution of carriers to be relatively localized in space after electron excitation, implying that diffusion of carriers plays a larger role than in optical experiments, in which the spot size is typically larger, as it is limited by diffraction. We note that this is the largest number of electrons per pulse that we can obtain in our system at 10 keV. Other pulsed conditions lead to better spatial resolution and hence more confined electron cascades, but at much lower num-

ber of electrons per pulse (less than tens of electrons per pulse) (chapter 2). Other works have shown a spatial resolution in the nm range, but in the regime of few electrons per pulse, and thus small electron density [79, 90].

## 5.6. CONCLUSIONS

In conclusion, we have presented a full description of $g^{(2)}(\tau)$ autocorrelation measurements in incoherent cathodoluminescence spectroscopy for different electron beam configurations. We have developed a fully analytical model to explain the amplitude of bunching ($g^{(2)}(0)$) as a function of electron beam current (or number of electrons per pulse), electron excitation efficiency, emitter lifetime and pulse duration, in the case of pulsed electron beams. The model highlights the inverse dependence of the bunching contribution to $g^{(2)}(\tau)$ as a function of electron beam current or number of electrons per pulse. Moreover, by acquiring a $g^{(2)}(\tau)$ curve at a known electron beam current we can directly extract the electron excitation efficiency by using a simple equation, and the curve can be fitted to obtain the emitter lifetime. This is a major step forward compared to the previous method in which Monte Carlo simulations were needed, given the simplicity of the analysis using our model.



In particular, we show that for a pulsed electron beam, the excitation efficiency can be obtained by simply dividing the areas of the peak at 0 delay by that of any other peak, without the need of fitting the data. The model is generic and independent of the sample under study and prior knowledge of the sample geometry. In order to test the model with experiments, we have studied InGaN/GaN quantum well samples, in which we find an excitation efficiency of 0.13 for 10 keV electrons and 0.05 in the case of 8 keV electrons. Furthermore, we have presented 10 keV CL measurement using ultrashort (ps) electron pulses, with the average number of electrons ranging from less than 1 to ~ 500. The measurements of $g^{(2)}(0)$ as a function of the number of electrons per pulse exhibit the same trend as predicted by the analytical model, suggesting that nonlinear carrier interactions do not play a role, even at a high number of electrons per pulse. We model the induced carrier density in the QW sample and show that it remains lower than typical values for which nonlinear effects in optical excitation are observed. We foresee that the analytical model will make $g^{(2)}(\tau)$ measurements and analysis more accessible, thus allowing to get deeper insights into the fundamentals of electron-matter interaction. Moreover, the $g^{(2)}(\tau)$ experiments with ultrashort pulses pave the way to study photon statistics with dense electron cascades in a wide range of materials.

## 5.7. SUPPORTING INFORMATION

### 5.7.1. COMPARISON TO MONTE CARLO SIMULATIONS

Previous $g^{(2)}(\tau)$ measurements in cathodoluminescence (CL) have been modeled using Monte Carlo (MC) simulations. Here we demonstrate the accuracy of our analytical model by comparing $g^{(2)}(0)$ results obtained with our analytical model

to those produced by MC simulations. The comparison is performed for the three different electron beam configurations (continuous, pulsed with beam blanker and pulsed through photoemission). In all cases, the following steps were considered after the arrival of an electron to the sample:

1. Creation of $b_i$ bulk plasmons, according to a Poisson distribution with expectation value $b$.
2. Decay of each plasmon into $m_i$ electron-hole pairs, described with a Poisson distribution with expectation value $m$.
3. Excitation of a quantum well by an electron-hole pair with probability $\eta$.
4. Emission of a photon, following a given decay mechanism.

The MC simulations with a continuous electron beam have been performed using the same code as in refs. [39, 41, 42]. The code was adapted to represent the blanker experiment, in which only part of the initial continuous beam reaches the sample, thus generating (relatively long) electron pulses. In the MC simulations for the blanker case the current in continuous mode and the repetition rate were set to 20 pA and 1 MHz, respectively, and the pulse width was varied from 8 up to 500 ns, similar to the experiments. We also adapted the initial MC code to simulate electron pulses generated by photoemission. In this case, no continuous electron beam is initially generated, but instead we directly create pulses containing a certain number of electrons per pulse, given by a Poisson distribution with expectation value $n_e$. The pulse width is assumed to be Gaussian, with $\sigma = 1$ ps. The exact value of the pulse width is not critical, given that it is much shorter than the emitter lifetime $\tau_{\text{emitter}}$. The MC simulations with photoemission were performed assuming a repetition rate of $F = 5.04$ MHz. In all cases, the results from the simulations have been analyzed using the same procedure as for the experimental data.

Figure 5.6 shows the values of $g^{(2)}(0) - 1$ obtained from the MC simulations using a continuous electron beam (a), and a pulsed electron beam generated by beam blanking (b) and photoemission (c). In the three cases we show $g^{(2)}(0) - 1$ as a function of electron beam current (a) and number of electrons per pulse (b, c). In all cases we consider an exponential decay for the emitter, with lifetime $\tau_{\text{emitter}} = 12$ ns and an average number of $b = 0.2$ bulk plasmons per electron that interact with the quantum wells, corresponding to an excitation efficiency of $\gamma = 0.18$. We also assume $m = 1$ and $\eta = 1$, even though it has already been shown that these parameters do not play a role in the final result of the MC simulation [41]. In this work we explain this fact by showing that $m$ and $\eta$ cancel out in the development of the analytical model. The time step in the simulations was set to 512 ps, the same as in our experiments.

Figure 5.6 also shows the results of our analytical model, in which we used the same parameters as in the MC simulations. We should note that here no fitting is needed, given that we just fix all the parameters (including $b$). The results show a very good agreement between the MC simulations and the analytical model.

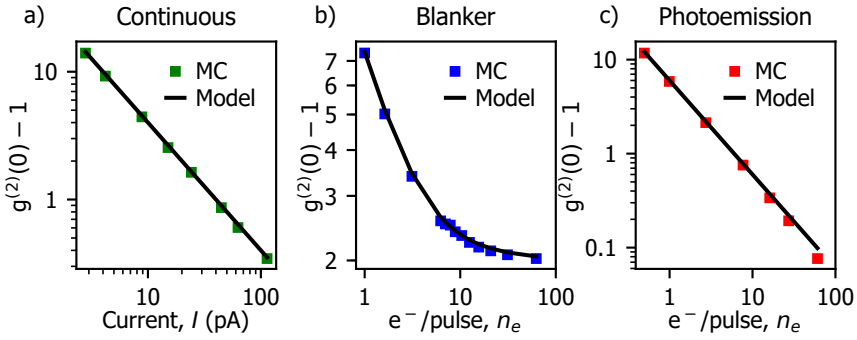


Figure 5.6: Monte Carlo simulations of $g^{(2)}(0)$ amplitude vs. electron beam current or number of electrons per pulse, together with the results from the analytical model. (a) Continuous electron beam, (b) electron beam pulsed using the beam blanking technique and (c) pulsed electron beam generated by photoemission.

5

### 5.7.2. ANALYTICAL MODEL - CONTINUOUS ELECTRON BEAM

A $g^{(2)}(\tau)$ experiment measures the photon statistics of a given emitter or source, and it is therefore based on random processes: the emission of a photon is stochastic, following a certain probability distribution (for example, an exponential decay). Moreover, in typical experimental setups (such as the HBT experiment), the emitted photons are split randomly towards the two detectors, with a 50 % probability of being detected by each detector [140]. The measurement is based on collecting enough statistics such that it can accurately represent the chances of having a correlation at a given delay compared to any other. It is therefore not possible to predict exactly how many photons will correlate with photons from the same electron (thus leading to bunching), and how many with photons from other electrons (uncorrelated events). Instead, we can calculate how likely it is that one scenario happens with respect to the other one. Hence, our analytical model is based on calculating the average number of combinations of correlations that lead to bunching ($A_b$) compared to the average number of combinations that lead to uncorrelated events (photons coming from different electrons, or pulses, in the pulsed case, $A_{\text{uncorr}}$).

We start from Eq. 5.2 of the main text, in which:

$$g^{(2)}_{\text{cont}}(0) = 1 + \frac{A^c_b}{A^c_{\text{uncorr}}} \frac{(2B+1)\,t_B}{2\alpha_b}, \tag{5.13}$$

where $A^c_b$ contains the mean number of combinations of correlations between photons from the same electron (i.e., giving bunching), $A^c_{\text{uncorr}}$ is the mean number of combinations of correlations between photons from different electrons (uncorrelated), $B$ is the total number of bins during the acquisition time $T$, $t_B$ is the bin size and $\alpha_b$ is the shape factor of the bunching peak, defined as the ratio between the area and height of the peak. Hence, we now need to calculate $A^c_b$ and $A^c_{\text{uncorr}}$.

CORRELATIONS BETWEEN PHOTONS FROM THE SAME ELECTRON ($A_b^c$, BUNCHING PEAK)

We consider that when one electron interacts with an emitter (semiconductor, quantum wells, atomic defect, etc), a certain number of photons $k$ will be emitted, each of them with a certain arrival time $t_k$. We should note that this value $k$ is not fixed, but will be different for each electron, given the stochastic nature of all the processes (creation of bulk plasmon, decay into electron-hole pairs, radiative decay of emitter). We want to count the number of combinations of pair-correlation events between photons from the same electron. We define one correlation as the detection of a pair of photons, thus we need to take subsets of 2 from $k$ photons, each photon with a fixed arrival time. Moreover, the order matters, given that this will determine whether the measured delay between photons is positive or negative, and there are no repetitions, i.e., a photon cannot correlate with itself. This is a common problem in combinatorics [245], sometimes referred to as variation without repetition, from which we extract that the number of possible combinations is

$$A_k = \binom{k}{2} = k(k-1)\,. \tag{5.14}$$



Next, we want to relate $A_k$ to physical variables, i.e., expected value of number of bulk plasmons per electron ($b$), expected value of number electron-hole pairs created per plasmon ($m$) and radiative decay efficiency ($\eta$). We will follow steps 1-3 described in the main text (section 5.3), starting from step 3 and building up.

3 Given $m_i$ electron-hole pairs, each of them with a probability $\eta$ of exciting a QW that emits a photon, the expected value of the number of possible combinations of correlations of photons becomes

$$\begin{aligned} A_3 &= \sum_{k=0}^{m_i} A_k \mathrm{Bin}(k; m_i, \eta) = \\ &= \sum_{k=0}^{m_i} k(k-1)\frac{m_i!}{k!(m_i-k)!}\eta^k(1-\eta)^{m_i-k} = \\ &= \eta^2 m_i(m_i-1)\,. \end{aligned} \tag{5.15}$$

2 Each bulk plasmon will create $m_i$ electron-hole pairs, described with a Poisson distribution with expected value $m$ $\left(\mathrm{Poiss}(m_i; m) = \frac{e^{-m}m^{m_i}}{m_i!}\right)$. Hence, we need to account for all the possible values of $m_i$, weighted by their probability. The expected value of the number of possible combinations correlations of photons produced by one bulk plasmon is then

$$\begin{aligned} A_{2,b_i=1} &= \sum_{m_i=0}^{\infty} A_3 \mathrm{Poiss}(m_i; m) = \\ &= \sum_{m_i=0}^{\infty} \eta^2 m_i(m_i-1)\frac{e^{-m}m^{m_i}}{m_i!} = \\ &= m^2\eta^2\,. \end{aligned} \tag{5.16}$$

If an electron creates more than one bulk plasmon, each of these plasmons will decay into a certain amount of electron-hole pairs, with likelihood given by a Poisson distribution with expectation value $m$, as already described. Thus, we need to account for all the possible combinations of correlations of photons produced by an arbitrary number $b_i$ of bulk plasmons. We start with the case of two bulk plasmons, in which the expected value of the number of possible combinations of correlations of photons (the correlations can be from photons from the same or different plasmon) becomes

$$A_{2,b_i=2} = \sum_{m_1=0}^{\infty}\sum_{m_2=0}^{\infty} \eta^2(m_1+m_2)(m_1+m_2-1)\text{Poiss}(m_1;m)\text{Poiss}(m_2;m) = \\ = 4m^2\eta^2 . \tag{5.17}$$

It can be shown by induction (see below) that in the general case of $b_i$ bulk plasmons, which produce photons that can correlate with other photons from the same plasmon or a different plasmon, the expectation value of the number of possible combinations of correlations is

$$A_{2,b_i} = b_i^2 m^2 \eta^2 . \tag{5.18}$$

1 Finally, the number of bulk plasmons produced by a single electron also follows a Poisson distribution with expected value $b$ ($\text{Poiss}(b_i;b)$). Therefore, averaging again over all possible values of $b_i$, we obtain that the average number of possible combinations of correlations produced by one electron is

$$A_1 = \sum_{b_i=0}^{\infty} b_i^2 m^2\eta^2\text{Poiss}(b_i;b) = bm^2\eta^2(b+1) . \tag{5.19}$$

In the case of $n$ electrons, the mean number of possible combinations of correlations between photons from the same electron becomes:

$$A_b^c = nA_1 = nbm^2\eta^2(b+1) . \tag{5.20}$$

CORRELATIONS BETWEEN PHOTONS FROM DIFFERENT ELECTRONS ($A_1^c$)

Next, we need to calculate the number of possible combinations of correlations between photons from different electrons. Taking into account the statistical distributions of each parameter involved in the emission of a photon (bulk plasmons, carriers, emission efficiency), the average number of photons emitted per electron is

$$N_{ph} = \sum_{b_i=0}^{\infty}\sum_{m_i=0}^{\infty}\sum_{k=0}^{m_i} kb_i\text{Poiss}(b_i;b)\text{Poiss}(m_i;m)\text{Bin}(k;m_i,\eta) = \\ = bm\eta . \tag{5.21}$$

We should note that the result is the same as if we would just consider the expected values $b$, $m$ and $\eta$ given that the number of photons scales linearly with these parameters. We now need to create pairs between two photons from different electrons. In this case the order is still important. We calculate the average number of combinations of correlations of photons coming from different electrons as

$$A^c_{\text{uncorr}} = \left[nbm\eta\right]\left[(n-1)bm\eta\right] = n(n-1)b^2m^2\eta^2\,. \tag{5.22}$$

### $g^{(2)}(0)$ FOR A CONTINUOUS BEAM

Finally, we can insert Eqs. 5.20 and 5.22 into Eq. 5.13, rewrite $n$ as a function of the electron current, $I = \frac{nq}{Bt_b}$. Given a typical acquisition time of a $g^{(2)}(\tau)$ experiment of at least 1 min, and bin size of $t_b = 0.512\,\text{ns}$, the total number of bins becomes $B \approx 1\times10^{11}$. It is therefore reasonable to take the limit $B\to\infty$ to obtain

$$\begin{aligned} g^{(2)}_{\text{cont}}(0) &= \lim_{B\to\infty}\left(1+\frac{(2B+1)\,t_b}{2\alpha_b}\frac{b+1}{\left(\frac{It_bB}{q}-1\right)b}\right) = \\ &= 1+\frac{q}{I\alpha_b}\frac{b+1}{b}\,. \end{aligned} \tag{5.23}$$

The last expression can also be expressed in terms of the excitation efficiency $\gamma$ (Eq. 5.6 in the main text, further explained in section 5.7.2) such that

$$g^{(2)}_{\text{cont}}(0) = 1+\frac{q}{I\alpha_b}\frac{\log(\gamma-1)-1}{\log(\gamma-1)}\,. \tag{5.24}$$

### BUNCHING PEAK: DERIVATION OF MEAN NUMBER OF POSSIBLE COMBINATIONS OF PHOTON CORRELATIONS FROM $b_i$ BULK PLASMONS BY INDUCTION

We want to find the expected value for number of combinations of correlations for an arbitrary number of bulk plasmons. Similar to Eq. 5.17, in the case of $j+1$ bulk plasmons, we have

$$\begin{aligned} A_{2,b=j+1} &= \eta^2\sum_{m_1=0}^{\infty}\ldots\sum_{m_j=0}^{\infty}\sum_{m_{j+1}=0}^{\infty}\left(\bar{m}+m_{j+1}\right)\left(\bar{m}+m_{j+1}-1\right)\mathrm{P}_{\bar{m}}\mathrm{P}_{j+1} = \\ &= \eta^2\sum_{m_1=0}^{\infty}\ldots\sum_{m_j=0}^{\infty}\sum_{m_{j+1}=0}^{\infty}\left(m_{j+1}^2+m_{j+1}(2\bar{m}-1)-\bar{m}+\bar{m}^2\right)\mathrm{P}_{\bar{m}}\mathrm{P}_{j+1}\,, \end{aligned} \tag{5.25}$$

where we have defined $\bar{m} = m_1+\ldots+m_j$ and $\mathrm{P}_{\bar{m}}$ is the product of Poisson distributions, i.e., $\mathrm{P}_{\bar{m}} = \text{Poiss}(m_1;m)\ldots\text{Poiss}(m_j;m) = \prod_{i=1}^{j}\frac{e^{-m}m^i}{i!}$. Eq. 5.25 can be further developed into

$$A_{2,b=j+1} = \eta^2\left[m(m+1)+2jm^2-m-jm+\sum_{m_1=0}^{\infty}\ldots\sum_{m_j=0}^{\infty}\bar{m}^2\mathrm{P}_{\bar{m}}\right]. \tag{5.26}$$

Therefore, we need to find an analytical expression for the last term in Eq. 5.26. We assume that

$$\sum_{m_1=0}^{\infty}\ldots\sum_{m_j=0}^{\infty}\bar{m}^2\mathrm{P}_{\bar{m}} = jm(jm+1)\,, \tag{5.27}$$

which we will prove by induction. In the case of $j = 1$,

$$\sum_{m_1=0}^{\infty} m_1^2 \mathrm{P}(m_1; m) = m(m+1)\,. \tag{5.28}$$

Assuming that Eq. 5.27 is true, we need to prove that in the case of $j+1$ bulk plasmons, it becomes $(j+1)m[(j+1)m]$. Hence

$$\begin{aligned}
&\sum_{m_1=0}^{\infty} \cdots \sum_{m_j=0}^{\infty} \sum_{m_{j+1}=0}^{\infty} \left(\bar{m} + m_{j+1}\right)^2 \mathrm{P}_{\bar{m}} \mathrm{P}_{j+1} = \\
&= \sum_{m_1=0}^{\infty} \cdots \sum_{m_j=0}^{\infty} \sum_{m_{j+1}=0}^{\infty} \left(\bar{m}^2 + 2\bar{m}m_{j+1} + m_{j+1}^2\right) \mathrm{P}_{\bar{m}} \mathrm{P}_{j+1} = \\
&= jm(jm+1) + 2jm^2 + m(m+1) = \\
&= (j+1)m\left[(j+1)m\right].
\end{aligned} \tag{5.29}$$

Finally, inserting Eq. 5.27 into Eq. 5.26, we obtain

$$A_{2,b=j+1} = (j+1)^2 m^2 \eta^2\,. \tag{5.30}$$



OBTAINING THE EXCITATION EFFICIENCY ($\gamma$)

For each electron, the probability of interacting, i.e., creating at least one plasmon that can excite the quantum wells, or any other emitter, is

$$P_{\mathrm{int}} = 1 - \mathrm{Poiss}(0; b) = 1 - e^{-b}\,, \tag{5.31}$$

where $b$ is the average number of bulk plasmons generated per electron (around the emitter). We define $\gamma$ as the fraction of electrons that create at least one bulk plasmon near the emitter. Given a certain number of electrons $n_{\mathrm{total}}$, from which $n_{\mathrm{interacting}}$ interact with the emitter, $\gamma$ becomes

$$\gamma = \frac{n_{\mathrm{interacting}}}{n_{\mathrm{total}}} = \frac{n_{\mathrm{total}} P_{\mathrm{int}}}{n_{\mathrm{total}}} = 1 - e^{-b}\,. \tag{5.32}$$

NUMBER OF CORRELATIONS AT LONG DELAYS

We consider that electrons interact with the sample during a certain (square) time window $T = B t_b$, where $B$ is the total number of bins and $t_B$ is the bin size. The distribution of the electrons in time can be represented as a uniform random distribution. The number of possible correlations between photons coming from different electrons as a function of delay $\tau$ exhibits a triangular shape, with base corresponding to $2T$. This shape results from the convolution of two squared signals with width $T$. Thus, in the model, the total number of correlations are spread within an area corresponding to a triangle, with base $(2B+1)t_b$ and height $h_1$. Figure 5.7 shows an example of this effect. In the experiments, the typical acquisition time (at least seconds) is much larger than the time window within which we acquire correlations (30 µs in our case for $t_b = 0.512$ ps), and thus this effect becomes negligible in the

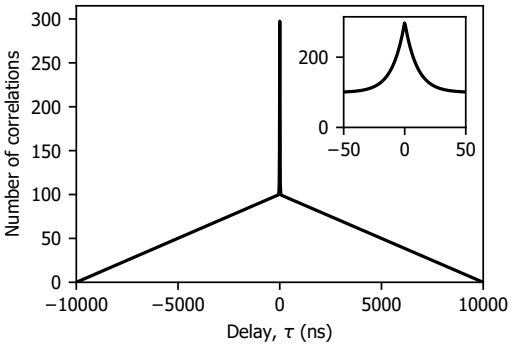


Figure 5.7: Theoretical shape of the number of possible correlations as a function of delay $\tau$ between photons emitted after the exposure of the sample to an electron beam during a time $T$. Here, $T = 10\mu s$. The observed triangular shape results from the convolution of two square pulses with base $T$. The inset shows the curve at small delay, in which the triangular background is not observed.



narrow time window in which we analyze the data, i.e., we only see the very top of the triangle. However, in the case of a pulsed electron beam, the time window corresponds to the pulse width $\Delta p$. The correlations between photons from the same or different pulses then exhibit a triangular shape, with base $2\Delta p$, as a function of $\tau$. This is the shape that we observe in our $g^{(2)}(\tau)$ measurements with the blanker (inset of Fig. 5.3, main text).

#### CALCULATION OF $\alpha_0$. DISCUSSION DISCRETE/CONTINUOUS

A key parameter in our analytical model is the relation between the height and the area of the bunching peak, $\alpha_b$ (shape factor). Given a known decay function of the bunching peak, the shape factor can typically be easily calculated. In the case of a simple exponential we obtain $\alpha_b = 2\tau_b$, while for stretched exponential the shape factor becomes $\alpha_b = 2\frac{\tau}{\beta}\Gamma\left(\frac{1}{\beta}\right)$. Nevertheless, $g^{(2)}(\tau)$ measurements are discrete, and thus these expressions for $\alpha_b$ are only valid if the bin size $t_{\text{bin}}$ is much smaller than the typical decay time, such that we can assume an almost continuous function. Otherwise, the discretized nature of the measurement should be taken into account. For example, the generalized expression for $\alpha_{\text{bunching}}$ in the case of an exponential decay with arbitrary bin size is $\alpha_b = \frac{2t_b}{1-e^{-t_b/\tau_b}}$, which becomes $2\tau_b$ when $t_b \ll \tau_b$.

### 5.7.3. ANALYTICAL MODEL - PULSED ELECRON BEAM

In the case of a pulsed electron beam we need to adapt the definition of $g^{(2)}(0)$ given in Eq. 5.1 of the main text. Here, we need to normalize the height at $\tau = 0$, with respect to the height of any other peak, $H_i$, which represents the uncorrelated

events. Hence

$$g^{(2)}_{\text{pulsed}}(0) = \frac{H(0)}{H_i(i \neq 0)}\,. \tag{5.33}$$

$H(0)$ is the height of the peak at $\tau = 0$. This peak will contain two contributions: correlations between photons from the same electron (with mean number of possible combinations $A^p_b$) and between photons from different electron but same pulse ($A^p_{\text{uncorr},0}$). As discussed in main text, the first contribution will be distributed over a temporal shape (with height $h^p_b$ and area $A^p_b$) determined by the emitter decay, through Eq. 5.7. Hence, the ratio between the area and the height is: $h^p_b = \alpha_b A^p_b$, similar to the bunching contribution in the continuous case. In contrast, the temporal distribution of the correlations between photons from different electrons but same pulse (second contribution of $\tau = 0$ peak) depends not only on the emitter decay but also the shape of the electron pulse. Hence, the shape of this contribution is given by the convolution of two electron pulses, convoluted also with the emitter decay (see 5.7.4). We define the ratio between the area ($A^p_{\text{uncorr},0}$) and the height ($h^p_{\text{uncorr},0}$) of this part as: $A_{\text{uncorr},0} = \alpha_{\text{conv}} h^p_{\text{uncorr},0}$.

$h_{\text{uncorr},i}(i \neq 0)$ is the height of any peak at $\tau \neq 0$, i.e., containing correlations between photons from consecutive pulses ($i = \pm 1$), from every second pulse ($i = \pm 2$) and so on. The shape of any of these peaks is also determined by the electron pulse shape and emitter decay, hence we can define: $A_{\text{uncorr},i} = \alpha_{\text{conv}} h^p_{\text{uncorr},i}$. $A^p_{\text{uncorr},i}$ contains the possible correlations between photons from different pulses.

Taking the previous definitions into account, we can rewrite Eq. 5.33 as

$$g^{(2)}_{\text{pulsed}}(0) = \frac{h^p_b + h^p_{\text{uncorr},0}}{h^p_{\text{uncorr},i}} = \frac{\alpha_{\text{conv}} A^p_b + \alpha_b A_{\text{uncorr},0}}{\alpha_b A_{\text{uncorr},i}}\,. \tag{5.34}$$

#### CORRELATIONS BETWEEN PHOTONS FROM THE SAME PULSE

*Correlations between photons from the same electron ($A^p_b$)*

The mean number of possible combinations of correlations between photons from the same electron, i.e., leading to bunching, is given in Eq. 5.19, which we have to multiply by the number of electrons per pulse and the total number of pulses ($r$)

$$A^p_b = r\,b(b+1)\,m^2\eta^2 \sum_{n_i=0}^{\infty} n_i \text{Poiss}(n_i; n_e) = r\,n_e\,b(b+1)\,m^2\eta^2\,. \tag{5.35}$$

Here we have assumed that the number of electrons per pulse $n_i$ follows a Poisson distribution with expected value $n_e$. This will be the case in most experiments, such as in the beam blanker and photoemission of electron pulses described in the main text. However, we would obtain the same result if we consider the number of electrons per pulse fixed, given that $A^p_b$ scales linearly with $n_i$.

*Correlations between photons from different electrons within the same pulse ($A^p_{uncorr,0}$)*

Given the average number of emitted photons per electron $N_{\text{ph}}$ (Eq. 5.21), the number of combinations of correlations between photons from the same pulse, but

different electron, becomes

$$A^p_{\text{uncorr},0} = b^2 m^2 \eta^2 \sum_{n_i=0}^{\infty} n_i(n_i-1)\text{Poiss}(n_i;n_e) = r\, n_e^2 b^2 m^2 \eta^2 . \tag{5.36}$$

CORRELATIONS BETWEEN PHOTONS FROM DIFFERENT PULSES ($A^p_{\text{UNCORR},i}$)

Following from Eq. 5.21, which gives the average number of photons emitted per electron, and assuming $n_i$ electrons per pulse (Poisson-distributed), the average number of photons emitted per pulse is

$$N_p = bm\eta \sum_{n_i=0}^{\infty} n_i \text{Poiss}(n_i;n_e) = n_e bm\eta . \tag{5.37}$$

The number of possible correlations between photons from different pulses is therefore

$$A^p_{\text{uncorr},r} = r(r-1) n_e^2 b^2 m^2 \eta^2 , \tag{5.38}$$

which is distributed over $2(r-1)$ peaks, given that we do not count the peak at $\tau = 0$, which would contain correlations between photons from the same pulse. We also need to take into account that the peaks at $\tau_i$ are contained within a triangular envelope, given that the number of possible correlations decreases as the delay between pulses increases, as explained in section 5.7.2.

Hence, the area below each peak at $\tau_i$ becomes

$$A^p_{\text{uncorr},i} = \frac{2A^p_{\text{uncorr},r}}{2(r-1)} = r\, n_e^2 b^2 m^2 \eta^2 . \tag{5.39}$$

$g^{(2)}(0)$ FOR A PULSED ELECTRON BEAM

Finally, inserting Eqs. 5.35, 5.36 and 5.39 into Eq. 5.34 we obtain

$$g^{(2)}_{\text{pulsed}}(0) = 1 + \frac{\alpha_{\text{conv}}}{\alpha_b}\frac{b+1}{n_e b} = 1 + \frac{\alpha_{\text{conv}}}{n_e \alpha_b}\frac{\log(\gamma-1)-1}{\log(\gamma-1)} . \tag{5.40}$$

In which again we have used the relation between $b$ and $\gamma$ given in Eq. 5.6 of the main text.

ALTERNATIVE CALCULATION OF $\gamma$ FOR A PULSED ELECTRON BEAM

In the case of a pulsed electron beam, we don't need to calculate $g^{(2)}(0)$ to retrieve the excitation efficiency $\gamma$, but we can simply divide the sum of Eqs. 5.35 and 5.36 by Eq. 5.39, which results in

$$\frac{A^p_b + A^p_{\text{uncorr},0}}{A^p_{\text{uncorr,i}}} = 1 + \frac{b+1}{n_e b} = 1 + \frac{1-\log(1-\gamma)}{n_e \log(1-\gamma)} . \tag{5.41}$$

which corresponds to Eq. 5.10 in the main text. In experiments, this ratio would be equivalent to dividing the sums of all the counts below the peak at 0 delay with the sum of the counts below any other peak.

ALTERNATIVE DERIVATION OF $g^{(2)}_{\text{PULSED}}(0)$ IN PHOTOEMISSION

The previous derivation of $g^{(2)}(0)$ assumes that bunching comes only from correlations between photons from the same electron. However, in the case of electron pulses obtained by photoemission, several electrons might excite the sample instantaneously (i.e., within a ps timescale, much smaller than the emitter decay). In this case bunching comes from correlations between photons from the same pulse, and it doesn't matter whether they come from the same or different electrons. Here we show a derivation of $g^{(2)}(0)$ starting from the point that all electrons within a pulse will create bunching, and show that it results in the same expression as Eq. 5.12 (main text).

We assume that the duration of the electron pulses is much smaller than the emitter lifetime. Hence, all peaks will have the same shape. In particular, the area below the bunching peak (peak at $\tau = 0$) is related to its height as: $A'_b = \alpha_b h'_b$. Similarly, any other peak $\tau_i (i \neq 0)$ follows the same relation: $A'_i = \alpha_b h'_i$. Eq. 5.34 can now be written as

$$g^{(2)}_{\text{ultrashort,v2}}(0) = \frac{A'_b}{A'_i}\,. \tag{5.42}$$



We first calculate the area below the bunching peak, i.e., $A'_b$. The first steps are the same as in the continuous case. From Eq. 5.18 we know that given $b_i$ bulk plasmons, the mean number of combinations of correlations is $b_i^2 m^2 \eta^2$. Assuming that we have $n_i$ electrons per pulse, each of them can create a different number of plasmons $b_i$. The case of $n_i = 1$ is derived in Eq. 5.19. In the case of $n_i = 2$,

$$A_{n_i=2} = \sum_{b_1=0}^{\infty}\sum_{b_2=0}^{\infty} (b_1+b_2)^2 m^2\eta^2 \text{Poiss}(b_1;b)\text{Poiss}(b_2;b) = 2bm^2\eta^2(2b+1)\,. \tag{5.43}$$

In the general case of $n_i$ electrons per pulse, it can be shown (through a similar demonstration by induction as for $A_{2,b_i}$ in section 5.7.2) that

$$A_{n_i} = n_i b m^2 \eta^2 (b n_i + 1)\,. \tag{5.44}$$

Finally, the number of electrons per pulse is not fixed but follows a Poisson distribution with expected value $n_e$. Moreover, we need to multiply this by the total number of pulses exciting the sample during a measurement ($r$). Hence, the average number of combinations of pair-correlations leading to bunching becomes

$$A'_b = r b m^2 \eta^2 \sum_{n_i=0}^{\infty} n_i (b n_i + 1)\text{Poiss}(n_i; n_e) = r n_e b m^2 \eta^2 (n_e b + b + 1)\,. \tag{5.45}$$

The area below each peak $i$, containing the number of combinations of pair-correlations between photons from different pulses (consecutive pulses, every second pulse, etc) was already calculated in Eq. 5.39. Hence,

$$A'_i = A^p_{\text{uncorr},i} = \frac{2A^p_{\text{uncorr},r}}{2(r-1)} = r n_e^2 b^2 m^2 \eta^2\,. \tag{5.46}$$

Inserting Eqs. 5.45 and 5.46 into Eq. 5.42 yields

$$g^{(2)}_{\text{ultrashort,v2}}(0) = 1 + \frac{b+1}{n_e b}, \tag{5.47}$$

which is the same as $g^{(2)}_{\text{ultrashort,v2}}(0)$ given in Eq. 5.12 of the main text, which was obtained by setting $\alpha_{\text{conv}} = \alpha_b$ in Eq. 5.9.

### 5.7.4. FULL DESCRIPTION OF $g^{(2)}(\tau)$

In the previous sections we have derived the value of $g^{(2)}(0)$, but we have not discussed yet the full shape of the autocorrelation function as a function of delay (i.e., $g^{(2)}(\tau)$). In the continuous case, the shape of $g^{(2)}(\tau)$ only depends on the bunching peak, while in pulsed experiments $g^{(2)}(\tau)$ depends also on the temporal shape of the electron pulses, as will be seen below.

#### SHAPE OF THE BUNCHING PEAK



Given a certain function $y(t)$, the result of its autocorrelation is [140]

$$h(\tau) = \int_{-\infty}^{\infty} y(t)\, y(t+\tau)\, dt = y(-\tau) * y(\tau). \tag{5.48}$$

In the case of the bunching peak in a $g^{(2)}(\tau)$ measurement, $y(t) = y_{\text{emitter}}(t)$ and $h(\tau) = y_{\text{bunching}}(\tau)$, as given in Eq. 5.7 in the main text.

#### SHAPE OF UNCORRELATED PEAKS IN A PULSED ELECTRON BEAM

As we have already discussed, a $g^{(2)}(\tau)$ measurement in pulse shows peaks centered at 0-delay and delays $\tau_i (i = \pm 1, \pm 2 \ldots)$ corresponding to the time between pulses. The peak at $\tau = 0$ has contributions from bunching, which result in a shape determined by the emitter (as shown in Eq. 5.48 and Eq. 5.7 in the main text), and from uncorrelated photons, i.e., coming from different electrons. The peaks at $\tau_i (i \neq 0)$ contain uncorrelated photons, i.e., coming from different pulses. In all cases in which there are correlations between photons from different electrons, the shape of the electron pulse also plays a role, together with the emitter decay. The function defining the probability of emitting a photon coming from a pulsed electron beam, as a function of time ($y(t)$), is given by the convolution between the electron pulse shape ($p(t)$) and emitter decay ($y_{\text{emitter}}(t)$), i.e.,

$$y(t) = p(t) * y_{\text{emitter}}(t) \tag{5.49}$$

Using Eq. 5.48, the correlation between two photons with temporal spread $y(t)$ becomes

$$h^{p}_{\text{uncorr}}(\tau) = \left[p(-\tau) * y_{\text{emitter}}(-\tau)\right] * \left[p(\tau) * y_{\text{emitter}}(\tau)\right] = \left[p(\tau) * p(\tau)\right] * h_b(\tau), \tag{5.50}$$

where in the last step we have used the definition of $h_b(\tau)$ from Eq. 5.7 in the main text.

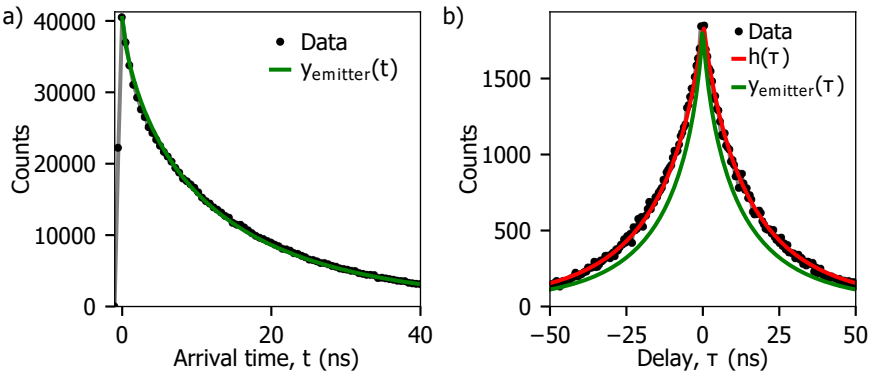


Figure 5.8: (a) TCSPC measurement on quantum wells, performed using a pulsed electron beam generated by photoemission (black) together with the corresponding fit with a stretched exponential (green). The best fit is obtained when $\tau_{\text{emitter}} = 11\,\text{ns}$ and $\beta_{\text{emitter}} = 0.73$. (b) $g^{(2)}(\tau)$ measurement performed on the same area on the sample and identical conditions as in (a) (black), together with the result from Eq. 5.48 using the emitter parameters from (a) (red) and a stretched exponential using the emitter parameters. The model (Eq. 5.48) shows a very good agreement with the data.

5

### COMPARISON TO EXPERIMENTS: STRETCHED EXPONENTIAL DECAY

In order to test the validity of Eq. 5.7 (main text) (same as Eq. 5.48), describing the shape of the bunching peak, we performed time-correlated single-photon counting measurements (TCSPC) on the sample. We subsequently acquired a $g^{(2)}(\tau)$ measurement with exactly the same conditions. The TCSPC measurements were performed using a pulsed electron beam obtained by photoemission, with the same conditions as in the $g^{(2)}(\tau)$ photoemission experiments (here, $n_e = 347$ electrons/pulse), and the data is collected in the same way as explained in chapter 3 (section 3.4.3). In these measurements, a histogram of the arrival time of photons following the electron pulse is built, and thus they directly show the emission decay. Figure 5.8a shows the resulting decay trace. We observe that the trace can be best fitted using a stretched exponential (Eq. 5.8). In this case we find that $\tau_{\text{emitter}} = 11\,\text{ns}$ and $\beta_{\text{emitter}} = 0.73$. The histogram obtained in the corresponding $g^{(2)}(\tau)$ measurement is shown in Figure 5.8b. We observe that the bunching peak cannot be properly described with a stretched exponential using $\tau_{\text{emitter}}$ and $\beta_{\text{emitter}}$ as parameters (green curve). Instead, the result of solving numerically Eq. 5.48 with the emitter parameters exhibits a very good agreement with the data (red curve).

The discrepancy between the shape of the $g^{(2)}(\tau)$ curve and the actual emitter decay when the latter follows a stretched exponential could explain the different lifetimes obtained in ref. [49] when comparing $g^{(2)}(\tau)$ and decay trace measurements.

*Single and double exponential decays*

In most systems, the decay mechanism can be approximated with a single or

double exponential decay. Solving Eq. 5.48 in those cases yields: $y_{\text{bunching}}(\tau) \propto e^{\tau/\tau_1}$ and $y_{\text{bunching}}(\tau) \propto e^{\tau/\tau_1} + e^{\tau/\tau_2}$, for single and double exponential decays, respectively. Therefore, in both cases the decay of the $g^{(2)}(\tau)$ function directly gives the decay of the emitter.

#### COMPARISON TO EXPERIMENTS: SQUARE ELECTRON PULSE

The experiments using the beam blanker are performed using square electron pulses, with pulse width $\Delta p$ determined by the blanking conditions (repetition rate and duty cycle) (see below, section 5.7.6). Hence, the pulse shape is given by

$$p(t) = \begin{cases} 1 & 0 \leq t \leq \Delta p \\ 0 & \text{otherwise} \end{cases} \tag{5.51}$$

and the emitter decay $y_{\text{emitter}}(t)$ follows a stretched exponential (Eq. 5.8). The shape of the peaks at $\tau_i (i \neq 0)$ then become (Eq. 5.50)

$$h^p_{\text{uncorr}}(\tau) = T(\tau) * \left[ y_{\text{emitter}}(-\tau) * y_{\text{emitter}}(\tau) \right] = T(\tau) * h_b(\tau)\,, \tag{5.52}$$

where $T(\tau)$ is a triangular function with base $\Delta p$, resulting from the convolution of $p(t)$ with $p(-t)$.

### 5.7.5. CORRECTION AT LONG DELAYS

In a $g^{(2)}(\tau)$ measurement, when the delay is longer than the typical correlation time (in our case, the emitter lifetime), we expect all events to be uncorrelated, thus exhibiting a constant amplitude. In the case of a continuous electron beam, this means that the $g^{(2)}(\tau)$ curve is constant for $\tau \gg 0$, while in the pulsed case, we still observe peaks at the delays corresponding to the time between pulses, all of them with the same amplitude. Nevertheless, this is not typically what we observe in experiments. Figure 5.9 shows the raw data of two $g^{(2)}(\tau)$ measurements, in continuous (a) and pulsed (b) mode. In both cases we observe that the number of counts decreases with increasing $\tau$, contrary to what we would expect from the theory. This is due to an experimental artifact in the Hanbury-Brown and Twiss experiment. In the experiment, the emitted light is split into two beams with a 50:50 beam splitter. Each beam is directed towards one detector, connected to the time correlator. When one of the detectors receives a photon, the time correlator starts counting until a photon is received on the second detector. Therefore, having a count at a certain delay $\tau$ means that the second detector does not receive any photon during the time $\tau$. This becomes very unlikely with increasing $\tau$, thus producing the effect observed in the figure.

One way to avoid this artifact is by having a very low count rate on each detector, such that the probability of having two (uncorrelated) photons emitted within a time smaller than $\tau$ becomes very low. Nevertheless, this can result in very long acquisition times (in the order of hours) or low signal-to-noise ratios. In our case, we decided to keep the number of counts relatively high (typically $1 \times 10^4$ counts/s) and correct for this artifact during the data analysis. We observe that the evolution

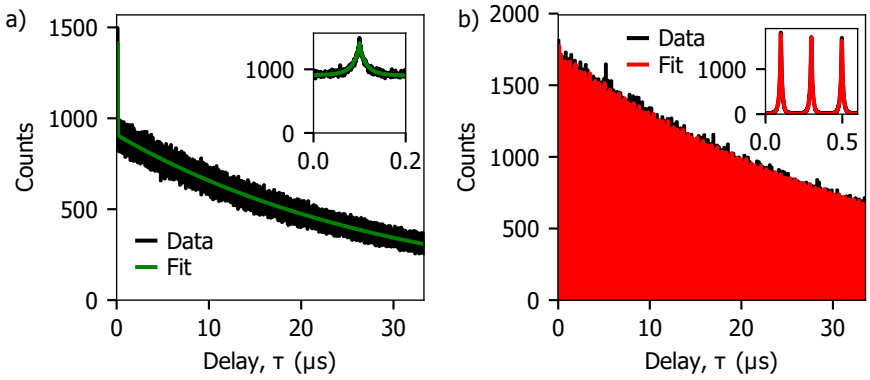


Figure 5.9: Raw data from a $g^{(2)}(\tau)$ experiment with a (a) continuous and (b) pulsed (by photoemission) electron beam. The data show that the number of counts decrease for long delays due to an experimental artifact in the HBT experiment. The green and red curves show the fits using an exponential decay to account for this artifact. The obtained average decays are $\tau_{\text{long}} = 31$ and 769 µs for (a) and (b), respectively. The insets show a zoom in for small delays, in which this artifact is not visible.



of the signal over $\tau$ due to this artifact follows an exponential decay, with average decay $\tau_{\text{long}}$. The fits obtained when applying this decay are shown in Figure 5.9, for which we obtained $\tau_{\text{long}} = 31$ and 769 µs, respectively. This procedure is valid as long as $\tau_{\text{long}}$ is much larger than the bunching decay and pulse width, in the case of a pulsed electron beam. Otherwise, artifacts due to this effect would also affect the value of $g^{(2)}(0)$.

### 5.7.6. EXPERIMENTAL DETAILS

All measurements are performed while focusing the electron beam on a single spot on the sample. The electron current is measured by collecting the beam current through a Faraday cup and reading it with a picoammeter.

#### BEAM BLANKER

The experiments using a beam blanker are performed using the same microscope as in ref. [49]. In our case, a 400 µm aperture is placed right below the pole piece. The distance between the blanking plates is kept to 2 mm for all experiments. In contrast to previous work, here we apply a square signal on one of the blanking plates, with peak-to-peak amplitude of 5 V and offset 2.5 V. The other plate is grounded. This results in a square electron pulse, with pulse width determined by the duty cycle $D$ and repetition rate $F$, i.e., $\Delta p = (1 - D)/F$. In order to confirm the shape of the electron pulse, we performed decay trace measurements on the QWs while blanking the beam. Figure 5.10 shows two examples of traces, both obtained using $D = 0.6$ and repetition rate $F = 0.5$ and 6 MHz, respectively. We fitted the data using

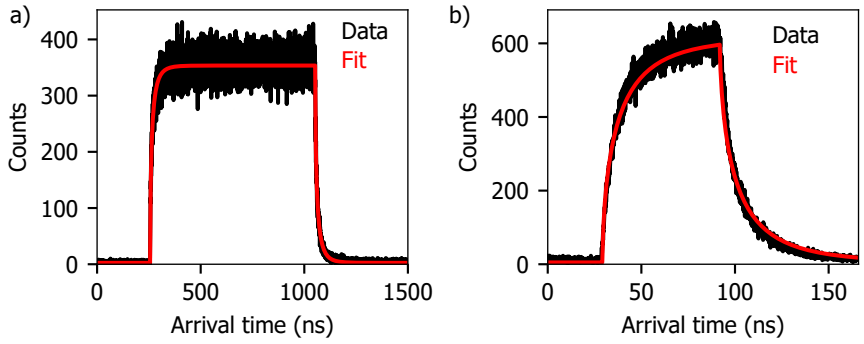


Figure 5.10: Decay traces on the QWs obtained using an electron beam blanker, with repetition rate (a) 0.5 and (b) 6 MHz. The fits are obtained using Eq. 5.53, showing that the electron pulses can be described as a square pulse with pulse width of 796 and 62 ns, for (a) and (b) respectively.

5

the following equation

$$f(t) = \begin{cases} B & t \leq t_0 \\ A\left(1 - e^{-\frac{(t-t_0)^\beta}{\tau}}\right) + B & t_0 \leq t \leq t_1 \\ Ae^{-\frac{(t-t_1)^\beta}{\tau}} + B & t > t_1\,, \end{cases} \tag{5.53}$$

where $\tau = 8.6$ ns and $\beta = 0.63$ are the parameters describing the QW radiative decay, $A$ is the amplitude of the signal and $B$ is the background signal. The pulse width can be obtained from $\Delta p = t_1 - t_0$. In the experiments we obtain pulse widths of 796 and 62 ns, for Figure 5.10(a) and (b) respectively, which are very close to the theoretical values at these conditions (800 and 66 ns, respectively). These experiments were performed using an electron energy of 10 keV, but we do not expect significant deviations when changing the electron energy to 8 keV.

Even though the experimental data shows an almost perfect square electron pulses, small deviations from this can arise when changing parameters, especially when increasing the duty cycle and repetition rate. In order to account for this, we measured the electron current in continuous mode $I_c$ (i.e., in blanking conditions but without any signal driving the blanking plates) and in pulsed $I_p$ (square signal driving one of the plates). The relation between both magnitudes is given by $I_p = I_c(1 - D)$. Figure 5.11a shows the value of electron current in pulsed $I_p$ measured at different repetition rates. These measurements were performed at 8 keV and $D = 0.95$, with the same blanking conditions as for the $g^{(2)}(\tau)$ measurements using the blanker in the main text. The figure also shows the expected value of $I_p$ (red curve), given a continuous current of $I_c = 213.9$ pA. We observe that the measured values are slightly lower than the expected ones, and the discrepancy increases with increasing repetition rate. These measured values of $I_p$ were used to calculate the number of electrons per pulse in Fig. 5.3 of the main text. The pulse

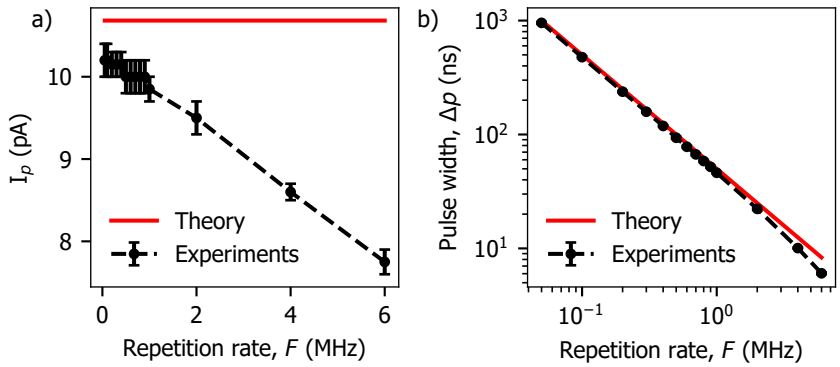


Figure 5.11: (a) Electron beam current measured in pulsed conditions using a beam blanker as a function of repetition rate. The red curve represents the theoretical current that we should obtain given a continuous current of 213.9 pA, and duty cycle of 0.95. (b) Pulse duration extracted from the experimental values of electron current in pulsed in (a), together with the theoretical value of the pulse width (red curve).



duration of the electron beam can also be extracted from these measurements, given that $\Delta p = I_p/(I_c F)$. Figure 5.11b shows the value of pulse width obtained using the experimental values of $I_p$ (black dots) compared to the theoretical values, given by $\Delta p = (1-D)/F$ (red curve).

#### LASER-DRIVEN ELECTRON SOURCE (PHOTOEMISSION)

Ultrashort (ps) pulses are obtained by focusing the 4th harmonic (258 nm) of an Yb-doped femtosecond laser ($\lambda$ = 1035 nm,250 fs pulses) onto the electron cathode. The experiments are performed using a Quanta 250 FEG SEM. In order to suppress continuous emission, the filament current is reduced from 2.35 down to 1.7 A. The extractor voltage is also lowered from the typical 4550 value down to 650 V. These settings allow us to achieve a high number of electrons per pulse, at the expense of lower spatial resolution, as explained in chapter 2.

### 5.7.7. CATHODOLUMINESCENCE WITH 8 KEV ELECTRONS

Figure 5.12 shows the CL spectrum obtained when exciting the sample with a continuous 8 keV electron beam, corresponding to the energy used in the experiments using the beam blanker. Most of the emission comes from the QW emission (410-490 nm). The inset shows a schematic of the structure of the sample together with Monte Carlo simulations of the trajectory of an 8 keV electron inside the sample, performed with the Casino software [1]. Each dot in the plot corresponds to an inelastic collision of the primary electron beam with the sample, while the color indicates the energy of the primary electron beam. We observe that barely any electron reaches the QWs, thus explaining the low excitation efficiency obtained at 8 keV ($\gamma = 0.05$).

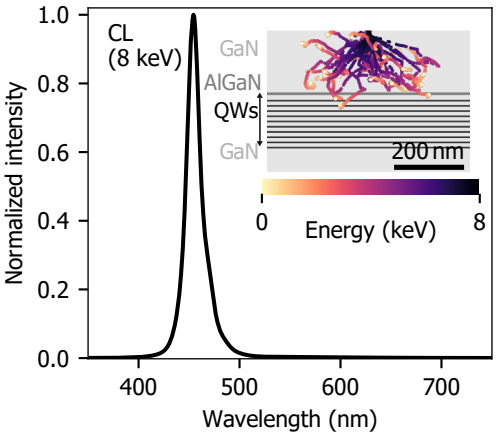


Figure 5.12: CL spectrum obtained after excitation with an 8 keV continuous electron beam (213.5 pA). Inset: schematic of the InGaN/GaN quantum well stack overlaid with the simulations of the trajectory of an 8 keV electron inside the sample.

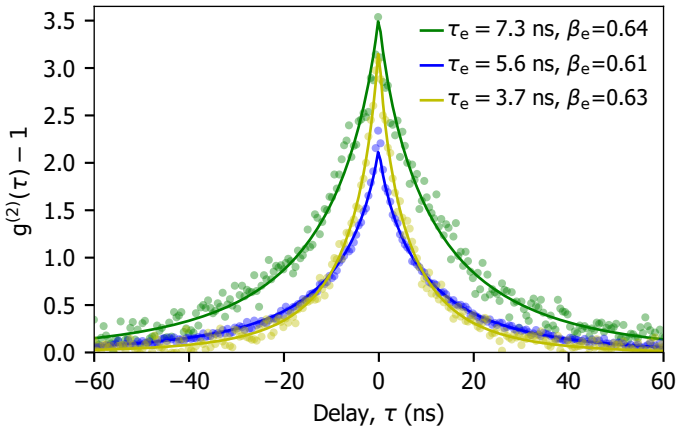


Figure 5.13: $g^{(2)}(\tau)$ measurements obtained with a 10 keV continuous electron beam at three different spots on the sample. The solid lines are the fits from Eq. 5.48 when $y(t)$ is a stretched exponential, with fit parameters $\tau_e = \tau_{\text{emitter}}$ and $\beta_e = \beta_{\text{emitter}}$.

### 5.7.8. DEPENDENCE OF QW EMISSION DECAY ON AREA

In the main text we show $g^{(2)}(\tau)$ measurements performed using the different electron beam configurations (continuous, pulsed with blanker and pulsed with photoemission), in each case exhibiting different decay lifetimes ($\tau_{\text{emitter}}$ and $\beta_{\text{emitter}}$). Here we prove that the main reason for this discrepancy is the inhomogeneity in

the sample. Figure 5.13 shows $g^{(2)}(\tau)$ measurements performed using a continuous electron beam on different spots on the sample. The curves were obtained at 10 keV with beam currents of 10.6, 14.1 and 34 pA (green, blue and yellow curves, respectively). Each experimental curve (data points) is accompanied by the corresponding fit (solid lines), obtained by solving numerically Eq. 5.48 when $y(t)$ is a stretched exponential. We observe that $\tau_{\text{emitter}}$ strongly depends on the position of the sample, ranging from 3.7 to 7.3 in these three examples. Instead, $\beta_{\text{emitter}}$ remains in the 0.61-0.64 range.

# REFERENCES


[1] D. Drouin, A. R. Couture, D. Joly, X. Tastet, V. Aimez, and R. Gauvin, *CASINO V2.42 - A fast and easy-to-use modeling tool for scanning electron microscopy and microanalysis users,* Scanning **29**, 92 (2007).

[2] L. Novotny and B. Hecht, *Principles of Nano-Optics* (Cambridge University Press, Cambridge, 2012).

[3] I. I. Smolyaninov, *Optical microscopy beyond the diffraction limit,* HFSP Journal **2**, 129 (2008).

[4] S. Gigan, *Optical microscopy aims deep,* Nature Photonics **11**, 14 (2017).

[5] P. Hansma, V. Elings, O. Marti, and C. Bracker, *Scanning tunneling microscopy and atomic force microscopy: application to biology and technology,* Science **242**, 209 (1988).

[6] R. Egerton, *Limits to the spatial, energy and momentum resolution of electron energy-loss spectroscopy,* Ultramicroscopy **107**, 575 (2007).

[7] E. Ruska, *The Development of the Electron Microscope and of Electron Microscopy(Nobel Lecture),* Angewandte Chemie International Edition in English **26**, 595 (1987).

[8] R. F. Egerton, *Physical Principles of Electron Microscopy* (Springer US, Boston, MA, 2005) p. 202.

[9] H. Ruska, *Die Sichtbarmachung der bakteriophagen Lyse im Übermikroskop,* Die Naturwissenschaften **28**, 45 (1940).

[10] H.-W. Ackermann, *Ruska H. Visualization of bacteriophage lysis in the hypermicroscope. Naturwissenschaften1940; 28,* Bacteriophage **1**, 183 (2011).

[11] D. McMullan, *Scanning electron microscopy 1928-1965,* Scanning **17**, 175 (1994).

[12] A. Bogner, P.-H. Jouneau, G. Thollet, D. Basset, and C. Gauthier, *A history of scanning electron microscopy developments: Towards "wet-STEM" imaging,* Micron **38**, 390 (2007).

[13] R. F. Egerton, *Electron energy-loss spectroscopy in the TEM,* Reports on Progress in Physics **72**, 016502 (2009).

[14] M. J. Lagos, A. Trügler, U. Hohenester, and P. E. Batson, *Mapping vibrational surface and bulk modes in a single nanocube,* Nature **543**, 529 (2017).

[15] O. Krivanek, N. Dellby, J. Hachtel, J.-C. Idrobo, M. Hotz, B. Plotkin-Swing, N. Bacon, A. Bleloch, G. Corbin, M. Hoffman, C. Meyer, and T. Lovejoy, *Progress in ultrahigh energy resolution EELS,* Ultramicroscopy **203**, 60 (2019).

[16] T. Arabatzis, *Cathode Rays,* in *Compendium of Quantum Physics* (Springer Berlin Heidelberg, Berlin, Heidelberg, 2009) pp. 89–92.

[17] J. Götze, *Application of Cathodoluminescence Microscopy and Spectroscopy in Geosciences,* Microscopy and Microanalysis **18**, 1270 (2012).

[18] B. G. Yacobi and D. B. Holt, *Cathodoluminescence scanning electron microscopy of semiconductors,* Journal of Applied Physics **59**, R1 (1986).

[19] T. Coenen and N. M. Haegel, *Cathodoluminescence for the 21st century: Learning more from light,* Applied Physics Reviews **4**, 031103 (2017).

[20] W. Steinmann, *Experimental Verification of Radiation of Plasma Oscillations in Thin Silver Films,* Physical Review Letters **5**, 470 (1960).

[21] N. Yamamoto, K. Araya, and F. J. García de Abajo, *Photon emission from silver particles induced by a high-energy electron beam,* Physical Review B **64**, 205419 (2001).

[22] E. J. R. Vesseur, R. de Waele, M. Kuttge, and A. Polman, *Direct Observation of Plasmonic Modes in Au Nanowires Using High-Resolution Cathodoluminescence Spectroscopy,* Nano Letters **7**, 2843 (2007).

[23] A. Losquin and T. T. A. Lummen, *Electron microscopy methods for space-, energy-, and time-resolved plasmonics,* Frontiers of Physics **12**, 127301 (2017).

[24] A. Polman, M. Kociak, and F. J. García de Abajo, *Electron-beam spectroscopy for nanophotonics,* Nature Materials **18**, 1158 (2019).

[25] F. J. García de Abajo, *Optical excitations in electron microscopy,* Reviews of Modern Physics **82**, 209 (2010).

[26] B. J. M. Brenny, T. Coenen, and A. Polman, *Quantifying coherent and incoherent cathodoluminescence in semiconductors and metals,* Journal of Applied Physics **115**, 244307 (2014).

[27] C. A. Klein, *Radiation Ionization Energies in Semiconductors: Speculations about the Role of Plasmons,* Journal of the Physical Society of Japan Supp **21**, 307 (1966).

[28] A. Rothwarf, *Plasmon theory of electron-hole pair production: efficiency of cathode ray phosphors,* Journal of Applied Physics **44**, 752 (1973).

[29] M. Kociak and L. Zagonel, *Cathodoluminescence in the scanning transmission electron microscope,* Ultramicroscopy **176**, 112 (2017).

[30] J. Schefold, S. Meuret, N. Schilder, T. Coenen, H. Agrawal, E. C. Garnett, and A. Polman, *Spatial Resolution of Coherent Cathodoluminescence Super-Resolution Microscopy,* ACS Photonics **6**, 1067 (2019).

[31] B. J. Brenny, A. Polman, and F. J. García De Abajo, *Femtosecond plasmon and photon wave packets excited by a high-energy electron on a metal or dielectric surface,* Physical Review B **94**, 1 (2016).

[32] T. Coenen, E. J. R. Vesseur, and A. Polman, *Angle-resolved cathodoluminescence spectroscopy,* Applied Physics Letters **99**, 143103 (2011).

[33] T. Coenen, *Angle-resolved cathodoluminescence nanoscopy*, Ph.D. thesis, University of Amsterdam (2014).

[34] S. Mignuzzi, M. Mota, T. Coenen, Y. Li, A. P. Mihai, P. K. Petrov, R. F. M. Oulton, S. A. Maier, and R. Sapienza, *Energy–Momentum Cathodoluminescence Spectroscopy of Dielectric Nanostructures,* ACS Photonics **5**, 1381 (2018).

[35] T. Coenen and A. Polman, *Energy-Momentum Cathodoluminescence Imaging of Anisotropic Directionality in Elliptical Aluminum Plasmonic Bullseye Antennas,* ACS Photonics **6**, 573 (2019).

[36] C. I. Osorio, T. Coenen, B. J. M. Brenny, A. Polman, and A. F. Koenderink, *Angle-Resolved Cathodoluminescence Imaging Polarimetry,* ACS Photonics **3**, 147 (2016).

[37] T. Sannomiya, A. Konečná, T. Matsukata, Z. Thollar, T. Okamoto, F. J. García de Abajo, and N. Yamamoto, *Cathodoluminescence Phase Extraction of the Coupling between Nanoparticles and Surface Plasmon Polaritons,* Nano Letters **20**, 592 (2020).

[38] N. J. Schilder, H. Agrawal, E. C. Garnett, and A. Polman, *Phase-Resolved Surface Plasmon Scattering Probed by Cathodoluminescence Holography,* ACS Photonics **7**, 1476 (2020).

[39] S. Meuret, L. Tizei, T. Cazimajou, R. Bourrellier, H. Chang, F. Treussart, and M. Kociak, *Photon Bunching in Cathodoluminescence,* Physical Review Letters **114**, 1 (2015).

[40] L. H. Tizei and M. Kociak, *Spatially resolved quantum nano-optics of single photons using an electron microscope,* Physical Review Letters **110**, 153604 (2013).

[41] S. Meuret, T. Coenen, H. Zeijlemaker, M. Latzel, S. Christiansen, S. Conesa-Boj, and A. Polman, *Photon bunching reveals single-electron cathodoluminescence excitation efficiency in InGaN quantum wells,* Physical Review B **96**, 035308 (2017).

[42] S. Meuret, T. Coenen, S. Y. Woo, Y. H. Ra, Z. Mi, and A. Polman, *Nanoscale Relative Emission Efficiency Mapping Using Cathodoluminescence g(2) Imaging,* Nano Letters **18**, 2288 (2018).

[43] A. Arbouet, G. M. Caruso, and F. Houdellier, *Ultrafast Transmission Electron Microscopy: Historical Development, Instrumentation, and Applications,* in *Advances in Imaging and Electron Physics, Volume 207* (Elsevier, 2018) Chap. 1, pp. 1–72.

[44] L. Zhang, J. P. Hoogenboom, B. Cook, and P. Kruit, *Photoemission sources and beam blankers for ultrafast electron microscopy,* Structural Dynamics **6**, 051501 (2019).

[45] G. S. Plows and W. C. Nixon, *Stroboscopic scanning electron microscopy,* Journal of Physics E: Scientific Instruments **1**, 302 (1968).

[46] O. Bostanjoglo and T. Rosin, *Ultrasonically Induced Magnetic Reversals Observed by Stroboscopic Electron Microscopy,* Optica Acta: International Journal of Optics **24**, 657 (1977).

[47] O. Bostanjoglo and T. Rosin, *Resonance oscillations of magnetic domain walls and bloch lines observed by stroboscopic electron microscopy,* Physica Status Solidi (a) **57**, 561 (1980).

[48] R. J. Moerland, I. G. C. Weppelman, M. W. H. Garming, P. Kruit, and J. P. Hoogenboom, *Time-resolved cathodoluminescence microscopy with subnanosecond beam blanking for direct evaluation of the local density of states,* Optics Express **24**, 24760 (2016).

[49] S. Meuret, M. Solà Garcia, T. Coenen, E. Kieft, H. Zeijlemaker, M. Lätzel, S. Christiansen, S. Woo, Y. Ra, Z. Mi, and A. Polman, *Complementary cathodoluminescence lifetime imaging configurations in a scanning electron microscope,* Ultramicroscopy **197**, 28 (2019).

[50] I. Weppelman, R. Moerland, J. Hoogenboom, and P. Kruit, *Concept and design of a beam blanker with integrated photoconductive switch for ultrafast electron microscopy,* Ultramicroscopy **184**, 8 (2018).

[51] J. Fehr, W. Reiners, L. Balk, E. Kubalek, D. Köther, and I. Wolff, *A 100-femtosecond electron beam blanking system,* Microelectronic Engineering **12**, 221 (1990).

[52] A. Lassise, P. H. A. Mutsaers, and O. J. Luiten, *Compact, low power radio frequency cavity for femtosecond electron microscopy,* Review of Scientific Instruments **83**, 043705 (2012).

[53] L. Zhang, M. W. Garming, J. P. Hoogenboom, and P. Kruit, *Beam displacement and blur caused by fast electron beam deflection,* Ultramicroscopy **211**, 112925 (2020).

[54] P. May, J. Halbout, and G. Chiu, *Picosecond photoelectron scanning electron microscope for noncontact testing of integrated circuits,* Applied Physics Letters **51**, 145 (1987).

[55] H. E. Elsayed-Ali and J. W. Herman, *Ultrahigh vacuum picosecond laser-driven electron diffraction system,* Review of Scientific Instruments **61**, 1636 (1990).

[56] S. Kong, J. Kinross-Wright, D. Nguyen, R. Sheffield, and M. Weber, *Performance of cesium telluride photocathodes as an electron source for the Los Alamos Advanced FEL,* Nuclear Instruments and Methods in Physics Research Section A: Accelerators, Spectrometers, Detectors and Associated Equipment **358**, 284 (1995).

[57] T. Nink, F. Galbert, Z. Mao, and O. Bostanjoglo, *Dynamics of laser pulse-induced melts in Ni–P visualized by high-speed transmission electron microscopy,* Applied Surface Science **138-139**, 439 (1999).

[58] H. Dömer and O. Bostanjoglo, *High-speed transmission electron microscope,* Review of Scientific Instruments **74**, 4369 (2003).

[59] T. LaGrange, M. R. Armstrong, K. Boyden, C. G. Brown, G. H. Campbell, J. D. Colvin, W. J. DeHope, A. M. Frank, D. J. Gibson, F. V. Hartemann, J. S. Kim, W. E. King, B. J. Pyke, B. W. Reed, M. D. Shirk, R. M. Shuttlesworth, B. C. Stuart, B. R. Torralva, and N. D. Browning, *Single-shot dynamic transmission electron microscopy,* Applied Physics Letters **89**, 044105 (2006).

[60] J. S. Kim, T. LaGrange, B. W. Reed, M. L. Taheri, M. R. Armstrong, W. E. King, N. D. Browning, and G. H. Campbell, *Imaging of Transient Structures Using Nanosecond in Situ TEM,* Science **321**, 1472 (2008).

[61] H. S. Park, J. S. Baskin, O. H. Kwon, and A. H. Zewail, *Atomic-scale imaging in real and energy space developed in ultrafast electron microscopy,* Nano Letters **7**, 2545 (2007).

[62] B. Barwick, H. S. Park, O.-h. Kwon, J. S. Baskin, and A. H. Zewail, *4D Imaging of Transient Structures and Morphologies in Ultrafast Electron Microscopy,* Science **322**, 1227 (2008).

[63] A. Gahlmann, S. Tae Park, and A. H. Zewail, *Ultrashort electron pulses for diffraction, crystallography and microscopy: theoretical and experimental resolutions,* Physical Chemistry Chemical Physics **10**, 2894 (2008).

[64] D. A. Plemmons and D. J. Flannigan, *Ultrafast electron microscopy: Instrument response from the single-electron to high bunch-charge regimes,* Chemical Physics Letters **683**, 186 (2017).

[65] A. Feist, N. Bach, N. Rubiano da Silva, T. Danz, M. Möller, K. E. Priebe, T. Domröse, J. G. Gatzmann, S. Rost, J. Schauss, S. Strauch, R. Bormann, M. Sivis, S. Schäfer, and C. Ropers, *Ultrafast transmission electron microscopy using a laser-driven field emitter: Femtosecond resolution with a high coherence electron beam,* Ultramicroscopy **176**, 63 (2017).

[66] F. Houdellier, G. M. Caruso, S. Weber, M. Kociak, and A. Arbouet, *Development of a high brightness ultrafast Transmission Electron Microscope based on a laser-driven cold field emission source,* Ultramicroscopy **186**, 128 (2018).

[67] K. Bücker, M. Picher, O. Crégut, T. LaGrange, B. Reed, S. Park, D. Masiel, and F. Banhart, *Electron beam dynamics in an ultrafast transmission electron microscope with Wehnelt electrode,* Ultramicroscopy **171**, 8 (2016).

[68] Y. M. Lee, Y. J. Kim, Y.-J. Kim, and O.-H. Kwon, *Ultrafast electron microscopy integrated with a direct electron detection camera,* Structural Dynamics **4**, 044023 (2017).

[69] E. Pomarico, I. Madan, G. Berruto, G. M. Vanacore, K. Wang, I. Kaminer, F. J. García de Abajo, and F. Carbone, *meV Resolution in Laser-Assisted Energy-Filtered Transmission Electron Microscopy,* ACS Photonics **5**, 759 (2018).

[70] C. Zhu, D. Zheng, H. Wang, M. Zhang, Z. Li, S. Sun, P. Xu, H. Tian, Z. Li, H. Yang, and J. Li, *Development of analytical ultrafast transmission electron microscopy based on laser-driven Schottky field emission,* Ultramicroscopy **209**, 112887 (2020).

[71] K. Wang, R. Dahan, M. Shentcis, Y. Kauffmann, A. Ben Hayun, O. Reinhardt, S. Tsesses, and I. Kaminer, *Coherent interaction between free electrons and a photonic cavity,* Nature **582**, 50 (2020).

[72] M. Merano, S. Sonderegger, A. Crottini, S. Collin, P. Renucci, E. Pelucchi, A. Malko, M. H. Baier, E. Kapon, B. Deveaud, and J.-D. Ganière, *Probing carrier dynamics in nanostructures by picosecond cathodoluminescence.* Nature **438**, 479 (2005).

[73] M. Merano, *Picosecond Cathodoluminescence*, Ph.D. thesis, École Polytechnique Fédérale de Lausanne (2005).

[74] D.-S. Yang, O. F. Mohammed, and A. H. Zewail, *Scanning ultrafast electron microscopy,* Proceedings of the National Academy of Sciences **107**, 14993 (2010).

[75] O. F. Mohammed, D.-S. Yang, S. K. Pal, and A. H. Zewail, *4D Scanning Ultrafast Electron Microscopy: Visualization of Materials Surface Dynamics,* Journal of the American Chemical Society **133**, 7708 (2011).

[76] J. Sun, V. A. Melnikov, J. I. Khan, and O. F. Mohammed, *Real-Space Imaging of Carrier Dynamics of Materials Surfaces by Second-Generation Four-Dimensional Scanning Ultrafast Electron Microscopy,* The Journal of Physical Chemistry Letters **6**, 3884 (2015).

[77] P. Corfdir, J. Ristić, P. Lefebvre, T. Zhu, D. Martin, A. Dussaigne, J. D. Ganière, N. Grandjean, and B. Deveaud-Plédran, *Low-temperature time-resolved cathodoluminescence study of exciton dynamics involving basal stacking faults in a-plane GaN,* Applied Physics Letters **94**, 201115 (2009).

[78] B. G. Mendis, D. Gachet, J. D. Major, and K. Durose, *Long Lifetime Hole Traps at Grain Boundaries in CdTe Thin-Film Photovoltaics,* Physical Review Letters **115**, 218701 (2015).

[79] M. Shahmohammadi, J.-D. Ganière, H. Zhang, R. Ciechonski, G. Vescovi, O. Kryliouk, M. Tchernycheva, and G. Jacopin, *Excitonic Diffusion in InGaN/GaN Core–Shell Nanowires,* Nano Letters **16**, 243 (2016).

[80] T. Zhu, D. Gachet, F. Tang, W. Y. Fu, F. Oehler, M. J. Kappers, P. Dawson, C. J. Humphreys, and R. A. Oliver, *Local carrier recombination and associated dynamics in m -plane InGaN/GaN quantum wells probed by picosecond cathodoluminescence,* Applied Physics Letters **109**, 232103 (2016).

[81] S. Modak, L. Chernyak, I. Lubomirsky, and S. Khodorov, *Continuous and Time-Resolved Cathodoluminescence Studies of Electron Injection Induced Effects in Gallium Nitride,* in *NATO Science for Peace and Security Series B: Physics and Biophysics book series* (2020) pp. 109–117.

[82] A. Feist, N. Rubiano da Silva, W. Liang, C. Ropers, and S. Schäfer, *Nanoscale diffractive probing of strain dynamics in ultrafast transmission electron microscopy,* Structural Dynamics **5**, 014302 (2018).

[83] F. Carbone, O. H. Kwon, and A. H. Zewail, *Dynamics of chemical bonding mapped by energy-resolved 4D electron microscopy,* Science **325**, 181 (2009).

[84] N. Rubiano da Silva, M. Möller, A. Feist, H. Ulrichs, C. Ropers, and S. Schäfer, *Nanoscale Mapping of Ultrafast Magnetization Dynamics with Femtosecond Lorentz Microscopy,* Physical Review X **8**, 031052 (2018).

[85] R. M. van der Veen, O.-H. Kwon, A. Tissot, A. Hauser, and A. H. Zewail, *Single-nanoparticle phase transitions visualized by four-dimensional electron microscopy,* Nature Chemistry **5**, 395 (2013).

[86] T. Danz, T. Domröse, and C. Ropers, *Ultrafast nanoimaging of the order parameter in a structural phase transition,* Science **371**, 371 (2021).

[87] B. Barwick, D. J. Flannigan, and A. H. Zewail, *Photon-induced near-field electron microscopy,* Nature **462**, 902 (2009).

[88] F. J. Garci a de Abajo, A. Asenjo-Garcia, and M. Kociak, *Multiphoton Absorption and Emission by Interaction of Swift Electrons with Evanescent Light Fields,* Nano Letters **10**, 1859 (2010).

[89] A. Feist, K. E. Echternkamp, J. Schauss, S. V. Yalunin, S. Schäfer, and C. Ropers, *Quantum coherent optical phase modulation in an ultrafast transmission electron microscope,* Nature **521**, 200 (2015).

[90] J. Sun, A. Adhikari, B. S. Shaheen, H. Yang, and O. F. Mohammed, *Mapping Carrier Dynamics on Material Surfaces in Space and Time using Scanning Ultrafast Electron Microscopy,* The Journal of Physical Chemistry Letters **7**, 985 (2016).

[91] C. Kealhofer, W. Schneider, D. Ehberger, A. Ryabov, F. Krausz, and P. Baum, *All-optical control and metrology of electron pulses,* Science **352**, 429 (2016).

[92] K. E. Priebe, C. Rathje, S. V. Yalunin, T. Hohage, A. Feist, S. Schäfer, and C. Ropers, *Attosecond electron pulse trains and quantum state reconstruction in ultrafast transmission electron microscopy,* Nature Photonics **11**, 793 (2017).

[93] E. A. Peralta, K. Soong, R. J. England, E. R. Colby, Z. Wu, B. Montazeri, C. McGuinness, J. McNeur, K. J. Leedle, D. Walz, E. B. Sozer, B. Cowan, B. Schwartz, G. Travish, and R. L. Byer, *Demonstration of electron acceleration in a laser-driven dielectric microstructure,* Nature **503**, 91 (2013).

[94] J. Verbeeck, H. Tian, and P. Schattschneider, *Production and application of electron vortex beams,* Nature **467**, 301 (2010).

[95] G. M. Vanacore, G. Berruto, I. Madan, E. Pomarico, P. Biagioni, R. J. Lamb, D. McGrouther, O. Reinhardt, I. Kaminer, B. Barwick, H. Larocque, V. Grillo, E. Karimi, F. J. García de Abajo, and F. Carbone, *Ultrafast generation and control of an electron vortex beam via chiral plasmonic near fields,* Nature Materials **18**, 573 (2019).

[96] A. H. Zewail, *Four-Dimensional Electron Microscopy,* Science **328**, 187 (2010).

[97] D. A. Plemmons, P. K. Suri, and D. J. Flannigan, *Probing Structural and Electronic Dynamics with Ultrafast Electron Microscopy,* Chemistry of Materials **27**, 3178 (2015).

[98] A. Adhikari, J. K. Eliason, J. Sun, R. Bose, D. J. Flannigan, and O. F. Mohammed, *Four-Dimensional Ultrafast Electron Microscopy: Insights into an Emerging Technique,* ACS Applied Materials & Interfaces **9**, 3 (2017).

[99] M. S. Grinolds, V. A. Lobastov, J. Weissenrieder, and A. H. Zewail, *Four-dimensional ultrafast electron microscopy of phase transitions,* Proceedings of the National Academy of Sciences **103**, 18427 (2006).

[100] F. Houdellier, G. Caruso, S. Weber, M. Hÿtch, C. Gatel, and A. Arbouet, *Optimization of off-axis electron holography performed with femtosecond electron pulses,* Ultramicroscopy **202**, 26 (2019).

[101] S. Ji, L. Piazza, G. Cao, S. T. Park, B. W. Reed, D. J. Masiel, and J. Weissenrieder, *Influence of cathode geometry on electron dynamics in an ultrafast electron microscope,* Structural Dynamics **4**, 054303 (2018).

[102] N. Bach, T. Domröse, A. Feist, T. Rittmann, S. Strauch, C. Ropers, and S. Schäfer, *Coulomb interactions in high-coherence femtosecond electron pulses from tip emitters,* Structural Dynamics **6**, 014301 (2019).

[103] P. K. Olshin, M. Drabbels, and U. J. Lorenz, *Characterization of a time-resolved electron microscope with a Schottky field emission gun,* Structural Dynamics **7**, 054304 (2020).

[104] M. Merano, S. Collin, P. Renucci, M. Gatri, S. Sonderegger, A. Crottini, J. D. Ganière, and B. Deveaud, *High brightness picosecond electron gun,* Review of Scientific Instruments **76**, 085108 (2005).

[105] M. Bronsgeest, *Physics of Schottky electron sources*, Ph.D. thesis, Delft University of Technology (2009).

[106] S. Yamamoto, *Fundamental physics of vacuum electron sources,* Reports on Progress in Physics **69**, 181 (2006).

[107] P. Kruit, *Electron Sources,* in *Transmission Electron Microscopy: Diffraction, Imaging and Spectrometry*, edited by B. Carter and D. B. Williams (Springer, 2016) pp. 1–15.

[108] B. Barwick, C. Corder, J. Strohaber, N. Chandler-Smith, C. Uiterwaal, and H. Batelaan, *Laser-induced ultrafast electron emission from a field emission tip,* New Journal of Physics **9**, 142 (2007).

[109] H. Yanagisawa, C. Hafner, P. Doná, M. Klöckner, D. Leuenberger, T. Greber, J. Osterwalder, and M. Hengsberger, *Laser-induced field emission from a tungsten tip: Optical control of emission sites and the emission process,* Physical Review B **81**, 115429 (2010).

[110] R. Bormann, S. Strauch, S. Schäfer, and C. Ropers, *An ultrafast electron microscope gun driven by two-photon photoemission from a nanotip cathode,* Journal of Applied Physics **118**, 173105 (2015).

[111] J. Venables and G. Cox, *Computer modelling of field emission gun scanning electron microscope columns,* Ultramicroscopy **21**, 33 (1987).

[112] M. S. Bronsgeest, J. E. Barth, G. A. Schwind, L. W. Swanson, and P. Kruit, *Extracting the Boersch effect contribution from experimental energy spread measurements for Schottky electron emitters,* Journal of Vacuum Science & Technology B: Microelectronics and Nanometer Structures **25**, 2049 (2007).

[113] Marco van der Heijden, *Energy spread measurement of the Nano Aperture Ion Source*, Master thesis, Delft University of Technology (2011).

[114] M. Aidelsburger, F. O. Kirchner, F. Krausz, and P. Baum, *Single-electron pulses for ultrafast diffraction,* Proceedings of the National Academy of Sciences **107**, 19714 (2010).

[115] G. H. Jansen, *Coulomb Interactions in Particle Beams*, Ph.D. thesis, Delft University of Technology (1988).

[116] M. Ammosov, *Influence of the Coulomb repulsion between electrons on their energy spectrum in the case of the nonlinear surface photoeffect,* Journal of the Optical Society of America B **8**, 2260 (1991).

[117] B. J. Siwick, J. R. Dwyer, R. E. Jordan, and R. J. D. Miller, *Ultrafast electron optics: Propagation dynamics of femtosecond electron packets,* Journal of Applied Physics **92**, 1643 (2012).

[118] A. Phys, *The Boersch effect in a picosecond pulsed electron beam emitted from a semiconductor photocathode,* Applied Physics Letters **109**, 013108 (2016).

[119] D. C. Joy, Y.-U. Ko, and J. J. Hwu, *Metrics of resolution and performance for CD-SEMs,* in *Proceedings SPIE*, edited by N. T. Sullivan (2000) pp. 108–114.

[120] B. L. Qian and H. E. Elsayed-Ali, *Electron pulse broadening due to space charge effects in a photoelectron gun for electron diffraction and streak camera systems,* Journal of Applied Physics **91**, 462 (2002).

[121] S. Collin, M. Merano, M. Gatri, S. Sonderegger, P. Renucci, J.-D. Ganière, and B. Deveaud, *Transverse and longitudinal space-charge-induced broadenings of ultrafast electron packets,* Journal of Applied Physics **98**, 094910 (2005).

[122] W. E. King, G. H. Campbell, A. Frank, B. Reed, J. F. Schmerge, B. J. Siwick, B. C. Stuart, and P. M. Weber, *Ultrafast electron microscopy in materials science, biology, and chemistry,* Journal of Applied Physics **97**, 111101 (2005).

[123] S. Sonderegger, E. Feltin, M. Merano, A. Crottini, J. F. Carlin, R. Sachot, B. Deveaud, N. Grandjean, and J. D. Ganière, *High spatial resolution picosecond cathodoluminescence of InGaN quantum wells,* Applied Physics Letters **89**, 232109 (2006).

[124] R. J. Moerland, I. G. C. Weppelman, M. W. H. Garming, P. Kruit, and J. P. Hoogenboom, *Time-resolved cathodoluminescence microscopy with subnanosecond beam blanking for direct evaluation of the local density of states,* Optics Express **24**, 24760 (2016).

[125] M. Fushitani, *Applications of pump-probe spectroscopy,* Annual Reports Section "C" (Physical Chemistry) **104**, 272 (2008).

[126] J. Cabanillas-Gonzalez, G. Grancini, and G. Lanzani, *Pump-Probe Spectroscopy in Organic Semiconductors: Monitoring Fundamental Processes of Relevance in Optoelectronics,* Advanced Materials **23**, 5468 (2011).

[127] E. M. Grumstrup, M. M. Gabriel, E. E. Cating, E. M. Van Goethem, and J. M. Papanikolas, *Pump–probe microscopy: Visualization and spectroscopy of ultrafast dynamics at the nanoscale,* Chemical Physics **458**, 30 (2015).

[128] M. Nakajima, N. Takubo, Z. Hiroi, Y. Ueda, and T. Suemoto, *Photoinduced metallic state in VO2 proved by the terahertz pump-probe spectroscopy,* Applied Physics Letters **92**, 011907 (2008).

[129] A. Picón, C. S. Lehmann, C. Bostedt, A. Rudenko, A. Marinelli, T. Osipov, D. Rolles, N. Berrah, C. Bomme, M. Bucher, G. Doumy, B. Erk, K. R. Ferguson, T. Gorkhover, P. J. Ho, E. P. Kanter, B. Krässig, J. Krzywinski, A. A. Lutman, A. M. March, D. Moonshiram, D. Ray, L. Young, S. T. Pratt, and S. H. Southworth, *Hetero-site-specific X-ray pump-probe spectroscopy for femtosecond intramolecular dynamics,* Nature Communications **7**, 11652 (2016).

[130] J. Murawski, T. Graupner, P. Milde, R. Raupach, U. Zerweck-Trogisch, and L. M. Eng, *Pump-probe Kelvin-probe force microscopy: Principle of operation and resolution limits,* Journal of Applied Physics **118**, 154302 (2015).

[131] J. Jahng, J. Brocious, D. A. Fishman, S. Yampolsky, D. Nowak, F. Huang, V. A. Apkarian, H. K. Wickramasinghe, and E. O. Potma, *Ultrafast pump-probe force microscopy with nanoscale resolution,* Applied Physics Letters **106**, 083113 (2015).

[132] V. A. Lobastov, R. Srinivasan, and A. H. Zewail, *Four-dimensional ultrafast electron microscopy,* Proceedings of the National Academy of Sciences **102**, 7069 (2005).

[133] K. B. Schliep, P. Quarterman, J.-P. Wang, and D. J. Flannigan, *Picosecond Fresnel transmission electron microscopy,* Applied Physics Letters **110**, 222404 (2017).

[134] D. R. Cremons, D. A. Plemmons, and D. J. Flannigan, *Femtosecond electron imaging of defect-modulated phonon dynamics,* Nature Communications **7**, 11230 (2016).

[135] D. T. Valley, V. E. Ferry, and D. J. Flannigan, *Imaging Intra- and Interparticle Acousto-plasmonic Vibrational Dynamics with Ultrafast Electron Microscopy,* Nano Letters **16**, 7302 (2016).

[136] B. Liao and E. Najafi, *Scanning ultrafast electron microscopy: A novel technique to probe photocarrier dynamics with high spatial and temporal resolutions,* Materials Today Physics **2**, 46 (2017).

[137] M. W. H. Garming, M. Bolhuis, S. Conesa-Boj, P. Kruit, and J. P. Hoogenboom, *Lock-in Ultrafast Electron Microscopy Simultaneously Visualizes Carrier Recombination and Interface-Mediated Trapping,* The Journal of Physical Chemistry Letters **11**, 8880 (2020).

[138] B. J. Brenny, *Probing light emission at the nanoscale with cathodoluminescence*, Ph.D. thesis, University of Amsterdam (2016).

[139] E. J. R. Vesseur, *Electron beam imaging and spectroscopy of plasmonic nanoantenna resonances*, Ph.D. thesis, Utrecht University (2011).

[140] M. Fox, *Quantum Optics: An Introduction* (Oxford University Press, 2006) p. 397.

[141] R. Hanbury Brown and R. Q. Twiss, *Correlation between photons in two coherent beams of light,* Nature **177**, 27 (1956).

[142] I. Rech, A. Ingargiola, R. Spinelli, I. Labanca, S. Marangoni, M. Ghioni, and S. Cova, *Optical crosstalk in single photon avalanche diode arrays: a new complete model,* Optics Express **16**, 8381 (2008).

[143] J. E. Howard, *Imaging properties of off-axis parabolic mirrors,* Applied Optics **18**, 2714 (1979).

[144] A. Drechsler, M. Lieb, C. Debus, A. Meixner, and G. Tarrach, *Confocal microscopy with a high numerical aperture parabolic mirror,* Optics Express **9**, 637 (2001).

[145] P. G. Eliseev, H.-B. Sun, S. Juodkazis, T. Sugahara, S. Sakai, and H. Misawa, *Laser-Induced Damage Threshold and Surface Processing of GaN at 400 nm Wavelength,* Japanese Journal of Applied Physics **38**, L839 (1999).

[146] T. Akane, K. Sugioka, H. Ogino, H. Takai, and K. Midorikawa, *KrF excimer laser induced ablation–planarization of GaN surface,* Applied Surface Science **148**, 133 (1999).

[147] J. J. Dubowski, S. Moisa, B. Komorowski, H. Tang, and J. B. Webb, *Laser polishing of GaN,* in *Proc. SPIE 4274, Laser Applications in Microelectronic and Optoelectronic Manufacturing VI,*, edited by M. C. Gower, H. Helvajian, K. Sugioka, and J. J. Dubowski (2001) pp. 442–447.

[148] A. Vladar and M. Postek, *Electron Beam-Induced Sample Contamination in the SEM,* Microscopy and Microanalysis **11**, 764 (2005).

[149] A. J. V. Griffiths and T. Walther, *Quantification of carbon contamination under electron beam irradiation in a scanning transmission electron microscope and its suppression by plasma cleaning,* Journal of Physics: Conference Series **241**, 012017 (2010).

[150] K. Papatryfonos, T. Angelova, A. Brimont, B. Reid, S. Guldin, P. R. Smith, M. Tang, K. Li, A. J. Seeds, H. Liu, and D. R. Selviah, *Refractive indices of MBE-grown AlxGa(1- x)As ternary alloys in the transparent wavelength region,* AIP Advances **11** (2021), 10.1063/5.0039631.

[151] T. Kawashima, H. Yoshikawa, S. Adachi, S. Fuke, and K. Ohtsuka, *Optical properties of hexagonal GaN,* Journal of Applied Physics **82**, 3528 (1997).

[152] E. Grilli, M. Guzzi, R. Zamboni, and L. Pavesi, *High-precision determination of the temperature dependence of the fundamental energy gap in gallium arsenide,* Physical Review B **45**, 1638 (1992).

[153] H. Birey and J. Sites, *Radiative transitions induced in gallium arsenide by modest heat treatment,* Journal of Applied Physics **51**, 619 (1980).

[154] R. C. Roca, K. Fukui, H. Mizuno, M. Suzuki, and I. Kamiya, *Below-Bandgap Photoluminescence from GaAs,* physica status solidi (b) **257**, 1900391 (2020).

[155] V. F. Amaliya, A. Yuniati, and P. van Dommelen, *Photoluminesence study of undoped GaAs at temperatures 300 K and 77 K,* Journal of Physics: Conference Series **1825**, 012046 (2021).

[156] Y. Varshni, *Temperature dependence of the energy gap in semiconductors,* Physica **34**, 149 (1967).

[157] M. B. Panish and H. C. Casey, *Temperature Dependence of the Energy Gap in GaAs and GaP,* Journal of Applied Physics **40**, 163 (1969).

[158] K. P. O'Donnell and X. Chen, *Temperature dependence of semiconductor band gaps,* Applied Physics Letters **58**, 2924 (1991).

[159] K. W. Mauser, M. Solà-Garcia, M. Liebtrau, B. Damilano, P.-M. Coulon, S. Vézian, P. Shields, S. Meuret, and A. Polman, *Probing nanoscale thermal transport with cathodoluminescence thermometry,* (2020), arXiv:2012.14890 .

[160] L. Quang Phuong, M. Okano, Y. Yamada, A. Nagaoka, K. Yoshino, and Y. Kanemitsu, *Photocarrier localization and recombination dynamics in Cu 2 ZnSnS 4 single crystals,* Applied Physics Letters **103**, 191902 (2013).

[161] B. Monemar, J. Bergman, I. Buyanova, H. Amano, I. Akasaki, T. Detchprohm, K. Hiramatsu, and N. Sawaki, *The excitonic bandgap of GaN: Dependence on substrate,* Solid-State Electronics **41**, 239 (1997).

[162] M. A. Reshchikov and H. Morkoç, *Luminescence properties of defects in GaN,* Journal of Applied Physics **97**, 061301 (2005).

[163] T. Suski, P. Perlin, H. Teisseyre, M. Leszczyński, I. Grzegory, J. Jun, M. Boćkowski, S. Porowski, and T. D. Moustakas, *Mechanism of yellow luminescence in GaN,* Applied Physics Letters **67**, 2188 (1995).

[164] M. Roesler and W. Brauer, *Theory of Secondary Electron Emission . I. General theory for NFE metals.* Physica Status Solidi (b) **104**, 161 (1981).

[165] W. S. M. Werner, A. Ruocco, F. Offi, S. Iacobucci, W. Smekal, H. Winter, and G. Stefani, *Role of surface and bulk plasmon decay in secondary electron emission,* Physical Review B **78**, 233403 (2008).

[166] J. C. de Mello, H. F. Wittmann, and R. H. Friend, *An improved experimental determination of external photoluminescence quantum efficiency,* Advanced Materials **9**, 230 (1997).

[167] X. Zou, C. Li, X. Su, Y. Liu, D. Finkelstein-Shapiro, W. Zhang, and A. Yartsev, *Carrier Recombination Processes in GaAs Wafers Passivated by Wet Nitridation,* ACS Applied Materials & Interfaces **12**, 28360 (2020).

[168] M. A. Reshchikov and R. Y. Korotkov, *Analysis of the temperature and excitation intensity dependencies of photoluminescence in undoped GaN films,* Physical Review B **64**, 115205 (2001).

[169] K. Fleischer, M. Toth, M. R. Phillips, J. Zou, G. Li, and S. J. Chua, *Depth profiling of GaN by cathodoluminescence microanalysis,* Applied Physics Letters **74**, 1114 (1999).

[170] G. L. Martinez, M. R. Curiel, B. J. Skromme, and R. J. Molnar, *Surface recombination and sulfide passivation of GaN,* Journal of Electronic Materials **29**, 325 (2000).

[171] M. Leroux, N. Grandjean, B. Beaumont, G. Nataf, F. Semond, J. Massies, and P. Gibart, *Temperature quenching of photoluminescence intensities in undoped and doped GaN,* Journal of Applied Physics **86**, 3721 (1999).

[172] M. W. Gerber, *A study of recombination mechanisms in GaAs using temperature-dependent time-resolved photoluminescence*, Ph.D. thesis, McMaster University (2016).

[173] I. Pelant and J. Valenta, *Luminescence Spectroscopy of Semiconductors* (Oxford University Press, 2012).

[174] R. K. Ahrenkiel, B. M. Keyes, and D. J. Dunlavy, *Intensity-dependent minority-carrier lifetime in III-V semiconductors due to saturation of recombination centers,* Journal of Applied Physics **70**, 225 (1991).

[175] T. S. Sosnowski, T. B. Norris, H. H. Wang, P. Grenier, J. F. Whitaker, and C. Y. Sung, *High-carrier-density electron dynamics in low-temperature-grown GaAs,* Applied Physics Letters **70**, 3245 (1997).

[176] G. Segschneider, F. Jacob, T. Löffler, H. G. Roskos, S. Tautz, P. Kiesel, and G. Döhler, *Free-carrier dynamics in low-temperature-grown GaAs at high excitation densities investigated by time-domain terahertz spectroscopy,* Physical Review B **65**, 125205 (2002).

[177] S. Rihani, R. Faulks, H. Beere, H. Page, I. Gregory, M. Evans, D. A. Ritchie, and M. Pepper, *Effect of defect saturation on terahertz emission and detection properties of low temperature GaAs photoconductive switches,* Applied Physics Letters **95**, 051106 (2009).

[178] A. Polman, M. Knight, E. C. Garnett, B. Ehrler, and W. C. Sinke, *Photovoltaic materials: Present efficiencies and future challenges,* Science **352**, aad4424 (2016).

[179] F. Liu, Q. Zeng, J. Li, X. Hao, A. Ho-Baillie, J. Tang, and M. A. Green, *Emerging inorganic compound thin film photovoltaic materials: Progress, challenges and strategies,* Materials Today **41**, 120 (2020).

[180] R. Brouri, A. Beveratos, J.-P. Poizat, and P. Grangier, *Photon antibunching in the fluorescence of individual color centers in diamond,* Optics Letters **25**, 1294 (2000).

[181] M. W. Doherty, N. B. Manson, P. Delaney, F. Jelezko, J. Wrachtrup, and L. C. Hollenberg, *The nitrogen-vacancy colour centre in diamond,* Physics Reports **528**, 1 (2013).

[182] M. Berthel, O. Mollet, G. Dantelle, T. Gacoin, S. Huant, and A. Drezet, *Photophysics of single nitrogen-vacancy centers in diamond nanocrystals,* Physical Review B **91**, 035308 (2015).

[183] A. Gruber, A. Dräbenstedt, C. Tietz, L. Fleury, J. Wrachtrup, and C. von Borczyskowski, *Scanning Confocal Optical Microscopy and Magnetic Resonance on Single Defect Centers,* Science **276**, 2012 (2012).

[184] C. Kurtsiefer, S. Mayer, P. Zarda, and H. Weinfurter, *Stable Solid-State Source of Single Photons,* Physical Review Letters **85**, 290 (2000).

[185] I. Aharonovich, D. Englund, and M. Toth, *Solid-state single-photon emitters,* Nature Photonics **10**, 631 (2016).

[186] D. D. Awschalom, R. Hanson, J. Wrachtrup, and B. B. Zhou, *Quantum technologies with optically interfaced solid-state spins,* Nature Photonics **12**, 516 (2018).

[187] B. J. M. Hausmann, B. Shields, Q. Quan, P. Maletinsky, M. McCutcheon, J. T. Choy, T. M. Babinec, A. Kubanek, A. Yacoby, M. D. Lukin, and M. Loncar, *Integrated Diamond Networks for Quantum Nanophotonics,* Nano Letters **12**, 1578 (2012).

[188] G. Balasubramanian, P. Neumann, D. Twitchen, M. Markham, R. Kolesov, N. Mizuochi, J. Isoya, J. Achard, J. Beck, J. Tissler, V. Jacques, P. R. Hemmer, F. Jelezko, and J. Wrachtrup, *Ultralong spin coherence time in isotopically engineered diamond,* Nature Materials **8**, 383 (2009).

[189] B. Hensen, H. Bernien, A. E. Dréau, A. Reiserer, N. Kalb, M. S. Blok, J. Ruitenberg, R. F. L. Vermeulen, R. N. Schouten, C. Abellán, W. Amaya, V. Pruneri, M. W. Mitchell, M. Markham, D. J. Twitchen, D. Elkouss, S. Wehner, T. H. Taminiau, and R. Hanson, *Loophole-free Bell inequality violation using electron spins separated by 1.3 kilometres,* Nature **526**, 682 (2015).

[190] K. Nemoto, M. Trupke, S. J. Devitt, B. Scharfenberger, K. Buczak, J. Schmiedmayer, and W. J. Munro, *Photonic Quantum Networks formed from NV- centers,* Scientific Reports **6**, 26284 (2016).

[191] H. J. Mamin, M. Kim, M. H. Sherwood, C. T. Rettner, K. Ohno, D. D. Awschalom, and D. Rugar, *Nanoscale Nuclear Magnetic Resonance with a Nitrogen-Vacancy Spin Sensor,* Science **339**, 557 (2013).

[192] J. M. Taylor, P. Cappellaro, L. Childress, L. Jiang, D. Budker, P. R. Hemmer, A. Yacoby, R. Walsworth, and M. D. Lukin, *High-sensitivity diamond magnetometer with nanoscale resolution,* Nature Physics **4**, 810 (2008).

[193] R. Kolesov, B. Grotz, G. Balasubramanian, R. J. Stöhr, A. A. L. Nicolet, P. R. Hemmer, F. Jelezko, and J. Wrachtrup, *Wave-particle duality of single surface plasmon polaritons,* Nature Physics **5**, 470 (2009).

[194] G. Kucsko, P. C. Maurer, N. Y. Yao, M. Kubo, H. J. Noh, P. K. Lo, H. Park, and M. D. Lukin, *Nanometre-scale thermometry in a living cell,* Nature **500**, 54 (2013).

[195] N. Aslam, G. Waldherr, P. Neumann, F. Jelezko, and J. Wrachtrup, *Photo-induced ionization dynamics of the nitrogen vacancy defect in diamond investigated by single-shot charge state detection,* New Journal of Physics **15**, 013064 (2013).

[196] L. Hacquebard and L. Childress, *Charge-state dynamics during excitation and depletion of the nitrogen-vacancy center in diamond,* Physical Review A **97**, 063408 (2018).

[197] P. Siyushev, H. Pinto, M. Vörös, A. Gali, F. Jelezko, and J. Wrachtrup, *Optically controlled switching of the charge state of a single nitrogen-vacancy center in diamond at cryogenic temperatures,* Physical Review Letters **110**, 167402 (2013).

[198] K.-M. C. Fu, C. Santori, P. E. Barclay, and R. G. Beausoleil, *Conversion of neutral nitrogen-vacancy centers to negatively charged nitrogen-vacancy centers through selective oxidation,* Applied Physics Letters **96**, 121907 (2010).

[199] M. V. Hauf, B. Grotz, B. Naydenov, M. Dankerl, S. Pezzagna, J. Meijer, F. Jelezko, J. Wrachtrup, M. Stutzmann, F. Reinhard, and J. A. Garrido, *Chemical control of the charge state of nitrogen-vacancy centers in diamond,* Physical Review B **83**, 081304 (2011).

[200] L. Rondin, G. Dantelle, A. Slablab, F. Grosshans, F. Treussart, P. Bergonzo, S. Perruchas, T. Gacoin, M. Chaigneau, H.-C. Chang, V. Jacques, and J.-F. Roch, *Surface-induced charge state conversion of nitrogen-vacancy defects in nanodiamonds,* Physical Review B **82**, 115449 (2010).

[201] B. Grotz, M. V. Hauf, M. Dankerl, B. Naydenov, S. Pezzagna, J. Meijer, F. Jelezko, J. Wrachtrup, M. Stutzmann, F. Reinhard, and J. A. Garrido, *Charge state manipulation of qubits in diamond,* Nature Communications **3**, 729 (2012).

[202] H. Kato, M. Wolfer, C. Schreyvogel, M. Kunzer, W. Müller-Sebert, H. Obloh, S. Yamasaki, and C. Nebel, *Tunable light emission from nitrogen-vacancy centers in single crystal diamond PIN diodes,* Applied Physics Letters **102**, 151101 (2013).

[203] L. H. G. Tizei and M. Kociak, *Spectrally and spatially resolved cathodoluminescence of nanodiamonds: local variations of the NV0 emission properties,* Nanotechnology **23**, 175702 (2012).

[204] S. Kumar, A. Huck, and U. L. Andersen, *Efficient Coupling of a Single Diamond Color Center to Propagating Plasmonic Gap Modes,* Nano Letters **13**, 1221 (2013).

[205] H. Lourenço-Martins, M. Kociak, S. Meuret, F. Treussart, Y. H. Lee, X. Y. Ling, H.-C. Chang, and L. H. Galvão Tizei, *Probing Plasmon-NV0 Coupling at the Nanometer Scale with Photons and Fast Electrons,* ACS Photonics **5**, 324 (2018).

[206] C. A. Klein, *Bandgap Dependence and Related Features of Radiation Ionization Energies in Semiconductors,* Journal of Applied Physics **39**, 2029 (1968).

[207] M. Kociak and L. F. Zagonel, *Publisher's Note,* Ultramicroscopy **174**, 50 (2017).

[208] G. Davies, *Dynamic Jahn-Teller distortions at trigonal optical centres in diamond,* Journal of Physics C: Solid State Physics **12**, 2551 (1979).

[209] L. H. Robins, L. P. Cook, E. N. Farabaugh, and A. Feldman, *Cathodoluminescence of defects in diamond films and particles grown by hot-filament chemical-vapor deposition,* Physical Review B **39**, 13367 (1989).

[210] S. A. Malykhin, J. Houard, R. R. Ismagilov, A. S. Orekhov, A. Vella, and A. N. Obraztsov, *Luminescent Characteristics of Needle-Like Single Crystal Diamonds,* physica status solidi (b) **255**, 1700189 (2018).

[211] A. Tallaire, A. Collins, D. Charles, J. Achard, R. Sussmann, A. Gicquel, M. Newton, A. Edmonds, and R. Cruddace, *Characterisation of high-quality thick single-crystal diamond grown by CVD with a low nitrogen addition,* Diamond and Related Materials **15**, 1700 (2006).

[212] H. Watanabe, T. Kitamura, S. Nakashima, and S. Shikata, *Cathodoluminescence characterization of a nitrogen-doped homoepitaxial diamond thin film,* Journal of Applied Physics **105**, 093529 (2009).

[213] H. Zhang, D. R. Glenn, R. Schalek, J. W. Lichtman, and R. L. Walsworth, *Efficiency of Cathodoluminescence Emission by Nitrogen-Vacancy Color Centers in Nanodiamonds,* Small **13**, 1700543 (2017).

[214] F. Carbone, B. Barwick, O.-H. Kwon, H. S. Park, J. Spencer Baskin, and A. H. Zewail, *EELS femtosecond resolved in 4D ultrafast electron microscopy,* Chemical Physics Letters **468**, 107 (2009).

[215] D. Krishnamurti, *The Raman spectrum of diamond,* Proceedings of the Indian Academy of Sciences - Section A **40**, 211 (1954).

[216] K. Iakoubovskii and G. J. Adriaenssens, *Luminescence excitation spectra in diamond,* Physical Review B **61**, 10174 (2000).

[217] A. M. Zaitsev, *Optical properties of diamond: A data handbook* (Springer, 2001).

[218] H. Demers, N. Poirier-Demers, A. R. Couture, D. Joly, M. Guilmain, N. de Jonge, and D. Drouin, *Three-dimensional electron microscopy simulation with the CASINO Monte Carlo software,* Scanning **33**, 135 (2011).

[219] K. Beha, A. Batalov, N. B. Manson, R. Bratschitsch, and A. Leitenstorfer, *Optimum photoluminescence excitation and recharging cycle of single nitrogen-vacancy centers in ultrapure diamond,* Physical Review Letters **109**, 097404 (2012).

[220] D. A. Hopper, R. R. Grote, A. L. Exarhos, and L. C. Bassett, *Near-infrared-assisted charge control and spin readout of the nitrogen-vacancy center in diamond,* Physical Review B **94**, 241201 (2016).

[221] N. B. Manson and J. P. Harrison, *Photo-ionization of the nitrogen-vacancy center in diamond,* Diamond and Related Materials **14**, 1705 (2005).

[222] H.-C. Lu, Y.-C. Peng, S.-L. Chou, J.-I. Lo, B.-M. Cheng, and H.-C. Chang, *Far-UV-Excited Luminescence of Nitrogen-Vacancy Centers: Evidence for Diamonds in Space,* Angewandte Chemie International Edition **56**, 14469 (2017).

[223] A. Lohrmann, S. Pezzagna, I. Dobrinets, P. Spinicelli, V. Jacques, J.-F. Roch, J. Meijer, and A. M. Zaitsev, *Diamond based light-emitting diode for visible single-photon emission at room temperature,* Applied Physics Letters **99**, 251106 (2011).

[224] N. Mizuochi, T. Makino, H. Kato, D. Takeuchi, M. Ogura, H. Okushi, M. Nothaft, P. Neumann, A. Gali, F. Jelezko, J. Wrachtrup, and S. Yamasaki, *Electrically driven single-photon source at room temperature in diamond,* Nature Photonics **6**, 299 (2012).

[225] T. Malinauskas, K. Jarasiunas, E. Ivakin, V. Ralchenko, A. Gontar, and S. Ivakhnenko, *Optical evaluation of carrier lifetime and diffusion length in synthetic diamonds,* Diamond and Related Materials **17**, 1212 (2008).

[226] T. Shimomura, Y. Kubo, J. Barjon, N. Tokuda, I. Akimoto, and N. Naka, *Quantitative relevance of substitutional impurities to carrier dynamics in diamond,* Physical Review Materials **2**, 094601 (2018).

[227] M. Kozák, F. Trojánek, and P. Malý, *Optical study of carrier diffusion and recombination in CVD diamond,* Physica Status Solidi (A) Applications and Materials Science **210**, 2008 (2013).

[228] M. A. Feldman, E. F. Dumitrescu, D. Bridges, M. F. Chisholm, R. B. Davidson, P. G. Evans, J. A. Hachtel, A. Hu, R. C. Pooser, R. F. Haglund, and B. J. Lawrie, *Colossal photon bunching in quasiparticle-mediated nanodiamond cathodoluminescence,* Physical Review B **97**, 1 (2018).

[229] D. J. Flannigan, B. Barwick, and A. H. Zewail, *Biological imaging with 4D ultrafast electron microscopy,* Proceedings of the National Academy of Sciences **107**, 9933 (2010).

[230] A. Hanisch-Blicharski, A. Janzen, B. Krenzer, S. Wall, F. Klasing, A. Kalus, T. Frigge, M. Kammler, and M. Horn-von Hoegen, *Ultra-fast electron diffraction at surfaces: From nanoscale heat transport to driven phase transitions,* Ultramicroscopy **127**, 2 (2013).

[231] V. Di Giulio, M. Kociak, and F. J. G. de Abajo, *Probing quantum optical excitations with fast electrons,* Optica **6**, 1524 (2019).

[232] Y. Ji, Z. H. Zhang, Z. Kyaw, S. Tiam Tan, Z. Gang Ju, X. Liang Zhang, W. Liu, X. Wei Sun, and H. Volkan Demir, *Influence of n-type versus p-type AlGaN electron-blocking layer on InGaN/GaN multiple quantum wells light-emitting diodes,* Applied Physics Letters **103**, 1 (2013).

[233] M. Julkarnain, N. Kamata, T. Fukuda, and Y. Arakawa, *Yellow luminescence band in undoped GaN revealed by two-wavelength excited photoluminescence,* Optical Materials **60**, 481 (2016).

[234] H. J. Kimble, M. Dagenais, and L. Mandel, *Photon antibunching in resonance fluorescence,* Physical Review Letters **39**, 691 (1977).

[235] B. Lounis, H. A. Bechtel, D. Gerion, P. Alivisatos, and W. E. Moerner, *Photon antibunching in single CdSe/ZnS quantum dot fluorescence,* Chemical Physics Letters **329**, 399 (2000).

[236] B. L. Morgan and L. Mandel, *Measurement of Photon Bunching in a Thermal Light Beam,* Physical Review Letters **16**, 1012 (1966).

[237] P. K. Tan, G. H. Yeo, H. S. Poh, A. H. Chan, and C. Kurtsiefer, *Measuring temporal photon bunching in blackbody radiation,* The Astrophysical Journal **789**, L10 (2014).

[238] D. Bhatti, J. Von Zanthier, and G. S. Agarwal, *Superbunching and Nonclassicality as new Hallmarks of Superradiance,* Scientific Reports **5**, 1 (2015).

[239] C. Bradac, M. T. Johnsson, M. Van Breugel, B. Q. Baragiola, R. Martin, M. L. Juan, G. K. Brennen, and T. Volz, *Room-temperature spontaneous superradiance from single diamond nanocrystals,* Nature Communications **8**, 1 (2017).

[240] K. C. Benny Lee, J. Siegel, S. E. Webb, S. Lévêque-Fort, M. J. Cole, R. Jones, K. Dowling, M. J. Lever, and P. M. French, *Application of the stretched exponential function to fluorescence lifetime imaging,* Biophysical Journal **81**, 1265 (2001).

[241] A. David, N. G. Young, C. Lund, and M. D. Craven, *Review—The Physics of Recombinations in III-Nitride Emitters,* ECS Journal of Solid State Science and Technology **9**, 016021 (2020).

[242] V. J. Keast, A. J. Scott, M. J. Kappers, C. T. Foxon, and C. J. Humphreys, *Electronic structure of GaN and InxGa1-xN measured with electron energy-loss spectroscopy,* Physical Review B - Condensed Matter and Materials Physics **66**, 1253191 (2002).

[243] Y. C. Shen, G. O. Mueller, S. Watanabe, N. F. Gardner, A. Munkholm, and M. R. Krames, *Auger recombination in InGaN measured by photoluminescence,* Applied Physics Letters **91**, 141101 (2007).

[244] K. W. Williams, N. R. Monahan, D. D. Koleske, M. H. Crawford, and X.-Y. Zhu, *Ultrafast and band-selective Auger recombination in InGaN quantum wells,* Applied Physics Letters **108**, 141105 (2016).

[245] M. Bóna, *Who Knows What It Looks Like, But It Exists. The Probabilistic Method,* in *A Walk Through Combinatorics* (World Scientific, 2016) pp. 381–416.

# LIST OF PUBLICATIONS

This thesis is based on the following publications:

- *Electron energy spread measurements in an ultrafast scanning electron microscope.* M. Solà-Garcia, M.Liebtrau, K. W. Mauser, S. Meuret, A. Polman, in preparation. (part of **Chapter 2**)
  M.S.G., S.M. and K.W.M. designed and implemented the ultrafast SEM setup. M.S.G. and M.L. performed the experiments. M.S.G. analyzed the data with the help of M.L., S.M. and A.P. All authors participated in the critical review of the manuscript.

- *Complementary cathodoluminescence lifetime imaging configurations in a scanning electron microscope.* S. Meuret, M. Solà-Garcia, T. Coenen, E. Kieft, H. Zeijlemaker, M. Lätzel, S. Christiansen, S.Y. Woo, Y.H. Ra, Z. Mi, A. Polman, Ultramicroscopy **197**, 28-38 (2019). (part of **Chapter 2**)
  S.M. and M.S.G. designed and implemented the experimental setup of the laser-driven SEM. M.S.G. and S.M. performed the experiments for the characterization of the laser-driven SEM. S.M. designed, implemented and performed the experiments of the electrostatic beam-blanker. T.C. performed the Fourier analysis for spatial resolution. E.K., T.C. and H.Z. assisted in the design, implementation and analysis of the results for the electrostatic beam blanker and laser-driven cathode. M.L. and S.C. provided the sample containing InGaN/GaN quantum wells in a planar geometry. S.Y.W., Y.H.R. and Z.M. provided the sample containing InGaN/GaN quantum wells embedded in GaN nanowires. A.P. supervised the project and assisted in the analysis of the results. All authors participated in the critical review of the manuscript.

- *Pump-probe cathodoluminescence microscopy: design and characterization.* M. Solà-Garcia, K. W. Mauser, N. van Nielen, M. Vreugdenhil, S. Meuret, A. Polman, in preparation. (part of **Chapter 3**)
  M.S.G., S.M. and K.W.M. designed and implemented the pump-probe CL setup. N.N. participated in further improvements of the setup. M.S.G., K.W.M. and N.N. performed the characterization of the setup. M.S.G. and M.V. performed the experiments and data analysis of the PL/CL comparison. All authors discussed the results and participated in the critical review of the manuscript.

- *Electron-induced state conversion in diamond NV centers measured with pump-probe cathodoluminescence spectroscopy.* M. Solà-Garcia, S. Meuret, T. Coenen, A. Polman, ACS Photonics **7**, 232-240 (2020). **(Chapter 4)**
  S.M. designed the experiment. M.S.G. and S.M. designed and implemented the pump-probe setup. M.S.G. performed the experiments and developed the rate-equation model. M.S.G., S.M., T.C. and A.P. analyzed the experimental data. All authors participated in the critical review of the manuscript.

- *Photon statistics of incoherent cathodoluminescence using continuous and pulsed electron beams.* M. Solà-Garcia, K. W. Mauser, M. Liebtrau, T. Coenen, S. Christiansen, S.

Meuret, A. Polman, ACS Photonics **8**, 916-925 (2021). **(Chapter 5)**
M.S.G. developed the analytical model, performed the experiments and analyzed the data. M.S.G., S.M. and K.W.M. designed and implemented the ultrafast SEM. S.M. and T.C. participated in the design and implementation of the electrostatic beam-blanker, which was further optimized by M.L. T.C. performed the Fourier analysis for the electron beam size. S.C. provided the sample. A.P. conceived the initial idea and supervised the project. All authors participated in the critical review of the manuscript.

Other publications by the author:

- *Employing cathodoluminescence for nanothermometry and thermal transport measurements in semiconductor nanowires.* K. W. Mauser, M. Solà-Garcia, M. Liebtrau, B. Damilano, P.-M. Coulon, S. Vézian, P. Shields, S. Meuret, A. Polman, submitted.

- *Enabling silicon-on-silicon photonics with pedestalled Mie resonators.* M. Garín, M. Solà-Garcia, A. Julian, P. Ortega, Nanoscale **10**, 14406-14413 (2018).

- *Optoelectronic enhancement of ultrathin $CuIn_{1-x}Ga_xSe_2$ solar cells by nanophotonic contacts.* G. Yin, M.W. Knight, M.C. van Lare, M. Solà-Garcia, A. Polman, M. Schmid, Advanced Optical Materials **5**, 1600637 (2017).

# SUMMARY

Since their emergence in the 1930s, electron microscopes have become an essential tool for the study of matter down to the sub-nanometer resolution, several orders of magnitude beyond that of conventional optical imaging. Nowadays, the capabilities of both transmission (TEM) and scanning (SEM) electron microscopes go beyond imaging, offering new methods to characterize matter at the nanoscale. Information such as chemical composition and electrical properties can now be obtained using either TEM or SEMs. In particular, cathodoluminescence (CL) microscopy, which analyzes the light emitted by matter after excitation with a high-energy electron, allows us to study the optical properties of a material with a high spatial resolution.

In parallel to the development of electron-based analysis techniques, ultrafast electron microscopy (UEM) has emerged to access to the temporal dimension of electron-matter interaction, thus enabling the study of ultrafast processes in a material at the nanoscale. Moreover, pump-probe techniques inside UEMs have been developed, which are based on the excitation of a material with both electrons and light, thus combining high spatial and temporal resolution. Until now, most electron-based pump-probe schemes have been developed in TEMs, and only a few pump-probe experiments based on SEMs have been realized. Hence, the full potential of USEM still needs to be explored. Additionally, the development of UEM has enabled the control of electron excitation of materials up to the single-electron regime, thus demanding a deep understanding of the dynamics of electron-matter interactions.

In this thesis we investigate the processes involved in the interaction of electrons with materials through the analysis of CL emission. In the first part of the thesis we introduce the design and implementation of pump-probe CL (PP-CL) microscopy, a new SEM-based technique to study the luminescence after synchronous excitation of matter with electron and light pulses. In contrast to previous techniques, in which the electron always acts as a probe, here we can use the electron either as a pump or as a probe, thus allowing us to gain new insights into the dynamics of excitation of matter with electrons. In the second part of the thesis, we apply PP-CL, together with second-order autocorrelation measurements of the CL emission, to investigate the dynamics of electron-matter interaction.

In Chapter 2, we present the design and characterization of our ultrafast scanning electron microscope (USEM), which is based on a laser-driven Schottky field-emission gun. We review the fundamentals of continuous and pulsed electron emission, and the main parameters that regulate each process. We continue by describing the technical aspects of our USEM, including the alignment procedure of the fs laser on the electron cathode. We provide a characterization of the pho-

togenerated electron pulses and discuss the different regimes in which the USEM can operate, for either high current or good spatial resolution. We present measurements of electron energy spread in a USEM for continuous (~ 0.72 eV) and pulsed electron emission. In the latter, we find that the lowest energy spread is 0.77 eV for pulses containing less than one electron, on average, corresponding to an estimated pulse duration on the sample of 416 fs. In the case of ~ 1000 electrons per pulse, the energy spread increases to 14.4 eV (6.4 ps) due to Coulomb repulsion between electrons from the same pulse. Finally, we characterize the spatial resolution of the USEM for different operating regimes. We obtain a resolution of ~ 90 nm and discuss the parameters that affect the resolution, as well as possible improvements to bring it down to the 5 – 10 nm range.

In Chapter 3 we introduce the first pump-probe CL microscope, combining the generation of ultrafast electron pulses from Chapter 2 with the injection of laser light into the sample. In the first part of the chapter we discuss the technical aspects and different methods to analyze the luminescence of the sample, including spectroscopic, time-correlated and lock-in measurements. In the second part we evaluate the differences and similarities between electron and laser excitation of a semiconductor, which should be considered in PP-CL experiments. We present a systematic comparison of CL and photoluminescence (PL) measurements on GaAs and GaN substrates, and discuss the deposited energy density, absorption depth, spectra, quantum efficiency and carrier dynamics. Finally, we present initial investigations of PP-CL measurements on $Cu_2ZnSnS_4$, in which we observe up to a ~ 20 % enhancement of CL emission in the nanosecond timescale after excitation of the sample. In this case, the electron is used as a probe to evaluate the changes in carrier dynamics induced by the laser.

One of the advantages of PP-CL microscopy is that it allows us to use the electron as a pump, thus providing complementary insights of electron and light excitation. In Chapter 4 we exploit this capability by showing charge-state conversion in diamond nitrogen-vacancy (NV) centers upon 5 keV pulsed electron irradiation. NV centers are promising single-photon sources that are present in two charge states: $NV^0$ and $NV^-$. In particular, centers in the $NV^-$ state have received attention for applications in quantum technology, given their long electron spin coherence time. While both states can be probed in PL, each with a characteristic emission spectrum (575 nm for $NV^0$, 637 nm for $NV^-$), in CL only emission from the $NV^0$ state is observed. Here we use our PP-CL setup to show that excitation of NV centers through electron-generated carriers results in the transition of centers from the $NV^-$ to the $NV^0$ state. We develop a rate-equation model based on the experimental data accounting for carrier diffusion (with a characteristic time of 0.8 ns), $NV^0$ spontaneous emission (~ 20 ns) and $NV^0 \rightarrow NV^-$ back transfer (500 ms). These results show new insights into the differences between electron excitation of NV centers and conventional laser excitation.

In Chapter 5 we continue exploring the fundamental properties of electron-matter interaction, this time through the investigation of photon correlations of CL emission. CL measurements of the second-order autocorrelation ($g^{(2)}(\tau)$) func-

tion exhibit strong photon bunching ($g^{(2)}(0) \gg 1$), due to the fact that excitation of a sample with a single high-energy electron can result in the emission of multiple photons. Until now, photon bunching in CL was described by means of numerical (Monte-Carlo) modelling. Here we develop a fully analytical model to describe the amplitude of bunching ($g^{(2)}(0)$) as a function of electron beam current (or number of electrons per pulse), emitter lifetime, electron pulse width (in the case of pulsed electron beams) and electron excitation probability ($\gamma$). The latter is defined as the probability that an electron creates at least one interaction (bulk plasmon) around the emitter, and thus provides a way to quantify electron-matter interaction. We test our model with $g^{(2)}(\tau)$ measurements on InGaN/GaN quantum wells, and further expand it theoretically and experimentally using pulsed beams generated with an electrostatic beam blanker (ns pulses) and a laser-driven cathode (ps pulses). In this particular sample we obtain excitation efficiencies of $\gamma = 0.13$ and 0.05 (for 10 and 8 keV electron beams, respectively), and we conclude that excitation with ultrashort and dense electron pulses ($\sim 500$ electrons per pulse) does not induce nonlinear effects in these quantum wells.

Overall, this thesis gives new insights into how high-energy electrons interact with matter through state of the art cathodoluminescence experiments and theoretical analysis. It introduces pump-probe cathodoluminescence (PP-CL) microscopy as a new method to study material excitation at ultrafast timescales. We envision that PP-CL can be further exploited to give new insights into key processes in materials, such as carrier dynamics and defect saturation in semiconductors, including photovoltaic materials, reversible phase transformations, and hot-carrier generation and thermal relaxation in nanostructures. The pump-probe configuration also enables to perform Raman spectroscopy measurements, in which electron-induced material excitations can be probed at the ps timescale. Moreover, it inspires the development of photon-induced near-field electron microscopy in an SEM, thus bringing new capabilities to ultrafast SEMs.

# SAMENVATTING

Sinds hun opkomst in de jaren dertig van de vorige eeuw zijn elektronenmicroscopen essentieel geworden in het bestuderen van materie met sub-nanometer resolutie, een aantal ordes van grootte beter dan die van conventionele optische beeldvorming. Tegenwoordig gaan de mogelijkheden van zowel transmissie- (TEM) als scanning- (SEM) elektronenmicroscopen verder dan beeldvorming en bieden ze nieuwe methoden om materie op nanoschaal te karakteriseren. Informatie zoals chemische samenstelling en elektrische eigenschappen kan nu worden verkregen met behulp van TEMs en SEMs. In het bijzonder stelt kathodoluminescentiemicroscopie (KL) ons in staat om de optische eigenschappen van een materiaal te bestuderen met hoge ruimtelijke resolutie. Een KL microscoop analyseert het licht dat wordt uitgezonden door materie nadat het is geëxciteerd met een hoogenergetisch elektron.

Parallel aan de ontwikkeling van analysetechnieken op basis van elektronen, is ultrasnelle elektronenmicroscopie (UEM) opgekomen. Met UEM kan een temporele resolutie worden behaald in de orde van grootte van de tijdsschaal van interacties tussen elektronen en materie. Hierdoor wordt het mogelijk om ultrasnelle processen in een materiaal op nanoschaal te bestuderen. Bovendien zijn er pomp-sondeer (*pump-probe*) technieken ontwikkeld binnen UEMs die zijn gebaseerd op de excitatie van een materiaal met zowel elektronen als licht, waardoor hoge ruimtelijke en temporele resolutie wordt gecombineerd. Tot nu toe zijn de meeste op elektronen gebaseerde pump-sondeer technieken ontwikkeld in TEMs en er zijn slechts een paar experimenten gerealiseerd voor pump-sondeer in SEMs. Daarom moet de volledige potentie van ultrasnelle scanning-elektronenmicroscopie (USEM) nog worden onderzocht. Daarnaast kunnen we door de ontwikkeling van UEM de elektronenexcitatie van een materiaal controleren tot op het niveau van enkele elektronen, wat ons diepgaand begrip verschaft van de interacties tussen elektronen en materie.

In dit proefschrift onderzoeken we de processen die betrokken zijn bij de interactie van elektronen met materialen door middel van de analyse van KL-emissie. In het eerste deel van het proefschrift introduceren we het ontwerp en de implementatie van pomp-sondeer KL (PS-KL) microscopie, een nieuwe op SEM gebaseerde techniek om de luminescentie te bestuderen na synchrone excitatie van materie met elektronen- en lichtpulsen. In tegenstelling tot eerdere technieken, waarbij het elektron altijd als sonde fungeert, kunnen we het elektron hier zowel als pomp of als sonde gebruiken, waardoor we nieuwe inzichten kunnen krijgen in de dynamica van de excitatie van materie met elektronen. In het tweede deel van het proefschrift passen we PS-KL toe, samen met tweede-orde autocorrelatiemetingen van de KL-emissie, om de dynamica van elektronen-materie-interactie te onderzoeken.

In Hoofdstuk 2 presenteren we het ontwerp en de karakterisering van onze USEM die is gebaseerd op een lasergedreven Schottky-veldemissiebron. We bespreken de grondbeginselen van continue en gepulseerde elektronenemissie en de belangrijkste parameters die elk proces beïnvloeden. Vervolgens beschrijven we de technische aspecten van onze USEM, inclusief de uitlijnprocedure van de femtoseconde laser op de elektronenkathode. We karakteriseren de fotogegenereerde elektronenpulsen en bespreken de verschillende regimes waarin de USEM kan werken, voor zowel hoge stroomsterkte als een goede ruimtelijke resolutie. We presenteren metingen van elektronenenergiespreiding in een USEM voor continue ($\sim 0.72$ eV) en gepulseerde elektronenemissie. In het laatste geval vinden we de laagste energiespreiding 0.77 eV voor pulsen die gemiddeld minder dan één elektron bevatten, wat overeenkomt met een geschatte pulsduur op het preparaat van 416 fs. In het geval van $\sim 1000$ elektronen per puls neemt de energiespreiding toe tot 14.4 eV (6.4 ps) als gevolg van Coulomb-afstoting tussen elektronen binnen dezelfde puls. Ten slotte karakteriseren we de ruimtelijke resolutie van de USEM voor verschillende operationele regimes. We verkrijgen een resolutie van $\sim 90$ nm en bespreken de parameters die de resolutie beïnvloeden, evenals mogelijke verbeteringen om deze terug te brengen tot het bereik van $5-10$ nm.

In Hoofdstuk 3 introduceren we de eerste pomp-sondeer KL-microscoop die de generatie van ultrasnelle elektronenpulsen uit Hoofdstuk 2 combineert met de injectie van laserlicht in het preparaat. In het eerste deel van het hoofdstuk bespreken we de technische aspecten en verschillende methoden om de luminescentie van het monster te analyseren, inclusief spectroscopische, tijdgecorreleerde en lock-in metingen. In het tweede deel evalueren we de verschillen en overeenkomsten tussen elektronen- en laserexcitatie van een halfgeleider waarmee rekening moet worden gehouden in PS-KL-experimenten. We presenteren een systematische vergelijking van KL- en fotoluminescentie (FL)-metingen op GaAs- en GaN-substraten en bespreken de gedeponeerde energiedichtheid, absorptiediepte, spectra, het kwantumrendement en de ladingsdragerdynamica. Ten slotte presenteren we PS-KL-metingen van $Cu_2ZnSnS_4$, waarin we tot $\sim 20\,\%$ verhoging van KL-emissie zien op de nanoseconde-tijdschaal na excitatie van het preparaat. In dit geval wordt het elektron gebruikt als een sonde om de veranderingen in de dynamica van ladingsdragers te analyseren die door de laser worden geïnduceerd.

Eén van de voordelen van PS-KL-microscopie is dat het ons in staat stelt het elektron als pomp te gebruiken, waardoor aanvullende inzichten worden verkregen in elektronen- en lichtexcitatie. In Hoofdstuk 4 maken we gebruik van deze mogelijkheid door de omzetting van de ladingstoestand in diamantstikstof-defect (NV) centra te laten zien bij 5 keV gepulseerde elektronenbestraling. NV-centra zijn veelbelovende bronnen van individuele fotonen en kennen twee specifieke ladingstoestanden: $NV^0$ en $NV^-$. Met name centra in de $NV^-$-toestand hebben aandacht gekregen voor toepassingen in de kwantumtechnologie, gezien de lange coherentietijd van de elektronenspin. Hoewel beide toestanden kunnen worden onderzocht in FL, elk met een karakteristiek emissiespectrum (piekend bij 575 nm voor $NV^0$, en 637 nm voor $NV^-$), wordt in KL alleen emissie van de $NV^0$-toestand waargenomen.

Hier gebruiken we onze PS-KL-opstelling om aan te tonen dat excitatie van NV-centra via elektronen-gegenereerde ladingsdragers resulteert in de overgang van centra van de $NV^-$- naar de $NV^0$-toestand. We ontwikkelen een reactiesnelheids-vergelijkingsmodel op basis van de experimentele gegevens dat rekening houdt met diffusie van ladingsdragers (met een karakteristieke tijd van 0.8 ns), spontane emissie van de $NV^0$ centrar ($\sim$ 20 ns) en $NV^0 \rightarrow NV^-$ terugoverdracht (500 ms). Deze resultaten geven nieuwe inzichten in de verschillen tussen elektronenexcitatie van NV-centra en conventionele laserexcitatie.

In Hoofdstuk 5 gaan we verder met het onderzoeken van de fundamentele aspecten van elektronen-materie interactie, deze keer door fotoncorrelaties van KL-emissie te onderzoeken. KL-metingen van de tweede-orde autocorrelatiefunctie ($g^{(2)}(\tau)$) vertonen sterke fotonenbundeling ($g^{(2)}(0) \gg 1$) vanwege het feit dat excitatie van het preparaat met één hoogenergetisch elektron kan resulteren in de emissie van meerdere fotonen. Tot nu toe werd het bundelen van fotonen in KL beschreven door middel van numerieke (Monte-Carlo) modellering. Hier ontwikkelen we een volledig analytisch model om de amplitude van bundeling ($g^{(2)}(0)$) te beschrijven als een functie van de stroom van de elektronenstraal (of aantal elektronen per puls), emitterlevensduur, duur van de elektronenpuls (in het geval van gepulseerde elektronenbundels) en de waarschijnlijkheid van elektronenexcitatie ($\gamma$). De laatste wordt gedefinieerd als de kans dat een elektron ten minste één interactie (bulkplasmon) rond de emitter creëert en biedt dus een manier om de interactie tussen elektronen en materie te kwantificeren. We testen ons model met $g^{(2)}(\tau)$-metingen op InGaN / GaN-kwantumputten en breiden het theoretisch en experimenteel verder uit voor gepulseerde stralen die worden gegenereerd met een elektrostatische straalonderdrukker (ns-pulsen) en een lasergestuurde kathode (ps-pulsen). In dit specifieke preparaat vinden we excitatie-rendementen van $\gamma = 0.13$ en 0.05 (voor respectievelijk elektronenbundels van 10 en 8 keV) en concluderen we dat excitatie met ultrakorte en compacte elektronenpulsen ($\sim$ 500 elektronen per puls) geen niet-lineaire effecten veroorzaakt in deze kwantumputten.

Dit proefschrift geeft nieuwe inzichten in hoe hoogenergetische elektronen interacteren met materie door middel van state-of-the-art kathodoluminescentie-experimenten en theoretische analyse. Het introduceert pump-sondeer kathodoluminescentie (PS-KL) microscopie als een nieuwe methode om materiaalexcitatie op ultrasnelle tijdschalen te bestuderen. We stellen ons voor dat PS-KL verder kan worden benut om nieuwe inzichten te geven in belangrijke processen in materialen, zoals ladingsdrager-dynamica en verzadiging van defecten in halfgeleiders inclusief fotovoltaïsche materialen, omkeerbare fasetransformaties, het genereren van hete ladingsdragers, en thermische relaxatie in nanostructuren. De pomp-sondeer configuratie maakt het ook mogelijk om Raman-spectroscopiemetingen uit te voeren waarbij elektronengeïnduceerde materiaalexcitaties kunnen worden onderzocht op de ps-tijdschaal. Bovendien inspireert het de ontwikkeling van foton-geïnduceerde nabije-veld-elektronenmicroscopie in een SEM, wat nieuwe mogelijkheden biedt voor ultrasnelle SEMs.

# RESUMEN

Desde su aparición en los años 30, los microscopios electrónicos se han convertido en una herramienta esencial para el estudio de la materia a escala sub-nanométrica, más allá del límite de resolución de la microscopia óptica convencional. Actualmente, los microscopios electrónicos, tanto los de transmisión (TEM) como los de barrido (MEB o SEM, por sus siglas en inglés), sirven para formar imágenes y ofrecen nuevos métodos para estudiar características de los materiales, tales como la composición química o las propiedades eléctricas, a escala nanomètrica. En particular, la microscopía de catodoluminiscencia (CL) se basa en el análisis de la luz emitida por la materia tras ser excitada por un electrón de alta energía, permitiendo estudiar las propiedades ópticas de un material con una alta resolución espacial.

Paralelamente al avance en técnicas de análisis basadas en microscopios electrónicos, en los últimos años se ha desarrollado la microscopía electrónica ultrarrápida (UEM). La UEM brinda acceso a estudiar la dinámica de la interacción entre electrones y materia, dando lugar al análisis de procesos ultrarrápidos a escala nanométrica. Además, se han desarrollado técnicas de estilo bomba-sonda (*pump-probe*) dentro de los UEMs, basadas en la excitación de un material con electrones y luz de forma sincronizada. Esta técnica permite obtener una alta resolución tanto espacial como temporal. Sin embargo, hasta ahora la configuración de tipo bomba-sonda se ha realizado mayoritariamente en TEMs y sólo en algunos casos se han desarrollado experimentos en SEMs. Por lo tanto, aún queda por explorar el potencial de los microscopios electrónicos de barrido ultrarrápidos (USEM). Asimismo, el progreso en UEMs ofrece un gran control sobre la excitación de materia con electrones, pudiendo acceder al límite en el que sólo un electrón a la vez interacciona con la muestra. Para poder explotar esta gran precisión necesitamos una comprensión profunda de la dinámica de la interacción electrón-materia.

En esta tesis investigamos los procesos relacionados con la interacción de electrones con materiales a través del análisis de CL. En la primera parte de la tesis introducimos el diseño e implementación del microscopio de CL de tipo bomba-sonda (BS-CL o PP-CL, por sus siglas en inglés). Esta nueva técnica está desarrollada en un SEM y permite estudiar la luminiscencia de un material tras ser excitado con pulsos de luz y de electrones de forma sincronizada. Hasta ahora, los experimentos de tipo bomba-sonda en microscopios electrónicos se han limitado al uso de electrones para monitorear el estado de la muestra tras ser excitada ópticamente. Sin embargo, aquí también podemos utilizar los electrones para excitar la muestra, lo que aporta nueva información sobre cómo los electrones de alta energía excitan un material. En la segunda parte de la tesis, aplicamos la técnica de BS-CL, junto con medidas de autocorrelación de CL, para investigar la dinámica de interacción entre electrones y materia.

En el Capítulo 2 presentamos el diseño y caracterización de nuestro USEM, que está basado en un emisor de electrones de tipo Schottky excitado con un láser. Revisamos los procesos fundamentales de la emisión continua y pulsada de electrones, junto con los parámetros más importantes que rigen cada proceso. Seguidamente, describimos los aspectos técnicos de nuestro USEM, incluyendo el proceso de alineamiento de un láser de femtosegundos sobre el emisor de electrones. Discutimos la caracterización de los pulsos de electrones fotogenerados y analizamos los diferentes modos en los que nuestro USEM puede operar, permitiendo obtener una elevada corriente eléctrica o una buena resolución espacial. Presentamos medidas de la dispersión de energía de los electrones cuando son emitidos de forma continua ($\sim 0.72\,\mathrm{eV}$) o pulsada. En el caso de pulsos de electrones obtenemos que la dispersión de energía más baja es de 0.77 eV, correspondiendo a pulsos que contienen menos de un electrón de media. Calculamos que esta dispersión equivale a una duración del pulso de electrones de aproximadamente 416 fs. En el caso de pulsos con aproximadamente 1000 electrones, la dispersión asciende a 14.4 eV (6.4 ps) debido a las repulsiones de Coulomb entre electrones del mismo pulso. Finalmente, en el capítulo caracterizamos la resolución espacial del USEM en función de la cantidad de electrones emitidos. Obtenemos una resolución de $\sim 90\,\mathrm{nm}$ y discutimos los parámetros determinantes y posibles mejoras para llegar al rango de $5-10\,\mathrm{nm}$.

En el Capítulo 3 introducimos el primer microscopio de BS-CL, que combina la excitación de una muestra con pulsos de luz y con los pulsos de electrones ultrarrápidos descritos en el Capítulo 2. En la primera parte del capítulo discutimos los aspectos técnicos y métodos para analizar la luminiscencia de la muestra, incluyendo medidas espectroscópicas, de correlación temporal y mediante un amplificador lock-in. En la segunda parte evaluamos las diferencias entre la excitación de un semiconductor con electrones y con luz, las cuáles deben ser consideradas en cualquier experimento de BS-CL. Comparamos de forma sistemática experimentos de CL y fotoluminiscencia (FL) en muestras de GaAs y GaN, estudiando en cada caso la densidad de energía depositada, profundidad de absorción, espectro, eficiencia cuántica y dinámica de los portadores de carga (pares electrón-hueco). Finalmente, presentamos investigaciones preliminares de medidas de BS-CL en $Cu_2ZnSnS_4$. Observamos que la emisión de CL aumenta hasta un $\sim 20\,\%$ tras excitar la muestra con luz y que este incremento desaparece en una escala de tiempo de nanosegundos. En este experimento utilizamos el electrón como sonda para evaluar los cambios inducidos por el láser en la dinámica de los portadores de carga.

Una de las ventajas de la microscopía BS-CL es que permite usar el electrón para excitar la muestra y el láser para monitorear los cambios inducidos por el electrón. Con esta configuración podemos acceder a información complementaria sobre cómo los electrones excitan una muestra en comparación con la luz. En el Capítulo 4 utilizamos esta configuración para demostrar la conversión del estado de carga de centros nitrógeno-vacante (NV) en diamante tras ser excitados por pulsos de electrones de 5 keV. Los centros NV son fuentes de fotones individuales y pueden existir en dos estados de carga diferentes: $NV^0$ y $NV^-$. En particular, los centros en el estado $NV^-$ son los que más atención suelen recibir para aplicacio-

nes en tecnologías cuánticas, dado su largo tiempo de coherencia del espín. En FL, ambos estados pueden ser detectados y cada uno exhibe un espectro de emisión característico (575 nm en el caso de $NV^0$, 637 nm en el de $NV^-$). Sin embargo, en CL normalmente sólo se observa emisión del estado $NV^0$. En este capítulo utilizamos nuestro microscopio BS-CL para demostrar que cuando los electrones inciden sobre los centros NV provocan la conversión de centros del estado $NV^-$ al $NV^0$. Desarrollamos un modelo basado en los datos experimentales, teniendo en cuenta la difusión de portadores de carga (en un tiempo característico de 0.8 ns), emisión espontánea de $NV^0$ ($\sim$ 20 ns) y transición de centros $NV^0$ de vuelta al estado $NV^-$ (500 ms). Estos resultados ofrecen una mayor comprensión sobre las diferencias entre la excitación de centros NV con electrones y con luz.

En el Capítulo 5 continuamos explorando las propiedades fundamentales de la interacción de electrones con la materia, esta vez investigando las correlaciones entre fotones en CL. Medidas de la función de autocorrelación de segundo orden ($g^{(2)}(\tau)$) de CL demuestran que los fotones se emiten en grupos ($g^{(2)}(0) \gg 1$). Este hecho es debido a que la excitación de la muestra con un solo electrón de alta energía puede causar la emisión de más de un fotón a la vez. Sin embargo, hasta ahora este fenómeno se ha evaluado mediante modelos numéricos (de tipo Monte-Carlo). En este capítulo desarrollamos un modelo íntegramente analítico que describe la magnitud del agrupamiento de fotones ($g^{(2)}(0)$) en función de la corriente eléctrica (o número de electrones por pulso), el tiempo de vida del emisor de luz, la duración del pulso de electrones (en el caso de un haz de electrones pulsado) y la probabilidad de excitación por electrón ($\gamma$). Esta última se define como la probabilidad de que un electrón cree al menos una interacción (plasmón de volumen) alrededor del emisor de luz, por lo que ofrece una forma de cuantificar la interacción entre electrones y materia. Evaluamos nuestro modelo con medidas de $g^{(2)}(\tau)$ en pozos cuánticos de InGaN/GaN usando haces de electrones continuos. Además, expandimos el modelo tanto teórica como experimentalmente para casos de pulsos de electrones generados mediante dos técnicas diferentes: la desviación electrostática con bloqueo parcial del haz de electrones (pulsos de ns) y la fotoemisión de electrones al focalizar un láser de femtosegundos sobre el emisor de electrones (pulsos de ps). Obtenemos que la probabilidad de excitación de los pozos cuánticos es de $\gamma = 0{,}13$ y 0.05 en el caso de electrones con energía de 10 y 8 keV, respectivamente. Asimismo, concluimos que no se observan efectos no-lineales en la luminiscencia de los pozos cuánticos aun cuando estos son excitados con pulsos de electrones ultrarrápidos y densos ($\sim$ 500 electrones por pulso).

En conclusión, esta tesis ofrece nueva información sobre cómo los electrones de alta energía interaccionan con la materia a través de experimentos de catodoluminiscencia de vanguardia y análisis teóricos. La tesis introduce la microscopía de catodoluminiscencia de tipo bomba-sonda como un método nuevo para estudiar la excitación de materiales en una escala temporal muy corta. Prevemos que el microscopio BS-CL pueda aprovecharse más para brindar una mayor comprensión de procesos clave en materiales, como la dinámica de los portadores de carga y saturación de defectos en semiconductores, incluyendo materiales fotovoltaicos,

transformaciones de fase reversibles, la generación de portadores de carga calientes y la relajación térmica en nanoestructuras. La configuración de tipo bomba-sonda también permite llevar a cabo medidas de espectroscopía de Raman, en la que podemos monitorear los procesos inducidos por el electrón en la materia en una escala de tiempo de ps. Además, este microscopio inspira el desarrollo de la microscopía electrónica de campo cercano inducido por fotones (PINEM, por sus siglas en inglés) dentro de un SEM, aportando así nuevas capacidades a los SEMs ultrarrápidos.

# RESUM

Des de la seva aparició en els anys 30, els microscopis electrònics s'han convertit en una eina essencial per a l'estudi de la matèria a escala sub-nanomètrica, més enllà del límit de resolució de la microscòpia òptica convencional. Actualment, els microscopis electrònics tant de transmissió (TEM) com de rastreig (SEM, per les seves sigles en anglès) permeten formar imatges i estudiar característiques d'un material, tal com la composició quimica o les propietats elèctriques, a escala nanomètrica. En particular, la microscòpia de catodoluminescència (CL), basada en l'anàlisi de la llum emesa quan un electró d'alta energia incideix sobre un material, ens permet estudiar les propietats òptiques de la matèria amb una alta resolució espacial.

Paral·lelament al desenvolupament de tècniques d'anàlisi basades en microscopis electrònics, en els últims anys ha sorgit la microscòpia electrònica ultraràpida (UEM). La UEM permet estudiar la dinàmica de la interacció d'electrons amb la matèria i, per tant, estudiar els processos ultraràpids que s'esdevenen en un material a escala nanomètrica. A més a més, s'han desenvolupat tècniques de tipus bomba-sonda (*pump-probe*) en els UEMs basades en l'excitació sincronitzada d'un material amb electrons i llum. Aquesta configuració permet obtenir una alta resolució tant espacial com temporal. Fins ara, la configuració de tipus bomba-sonda s'ha desenvolupat sobretot en TEMs i només s'han realitzat alguns experiments en SEMs. Per tant, encara queda per explorar el potencial dels microscopis electrònics de rastreig ultraràpids (USEM). Addicionalment, el desenvolupament de la UEM ofereix un gran control sobre l'excitació de la matèria amb electrons fins a l'extrem en què només un electró alhora interacciona amb la mostra. Per poder explotar aquesta precisió en l'excitació amb electrons necessitem una comprensió profunda de la dinàmica de la interacció entre electrons i matèria.

En aquesta tesi investiguem els processos implicats en la interacció d'electrons amb materials a través de l'anàlisi de CL. En la primera part de la tesi introduïm el disseny i implementació del microscopi de catodoluminescència de tipus bomba-sonda (BS-CL). Aquesta nova tècnica, que està desenvolupada dins un SEM, ens permet estudiar la luminescència d'un material quan és excitat amb polsos tant de llum com d'electrons. Fins ara, les tècniques de bomba-sonda desenvolupades en microscopis electrònics s'han limitat a l'ús de l'electró com a sonda, és a dir, per monitorar l'estat de la mostra després de ser excitada òpticament. En canvi, aquí també podem utilitzar l'electró per excitar la mostra, fet que ens permet obtenir nova informació sobre com els electrons d'alta energia exciten un material. En la segona part de la tesi, apliquem la microscòpia BS-CL, junt amb mesures d'autocorrelació de CL, per tal d'investigar la dinàmica de la interacció dels electrons amb la matèria.

En el Capítol 2 presentem el disseny i caracterització del nostre USEM, basat en

una font d'electrons de tipus Schottky excitada amb un làser. Revisem els processos fonamentals de l'emissió de feixos d'electrons continus i polsats i els paràmetres més importants que regulen cada procés. Continuem descrivint els aspectes tècnics del nostre USEM, com per exemple el posicionament del làser de femtosegons sobre la font d'electrons. Seguidament, caracteritzem els polsos d'electrons fotogenerats i considerem els diferents modes d'operació en els que el nostre USEM pot operar, per tal d'obtenir una gran quantitat de corrent elèctric o una bona resolució espacial. Presentem mesures de la dispersió energètica dels electrons en un USEM tant en el cas d'emissió d'electrons contínua ($\sim 0.72\,\text{eV}$) com polsada. En el cas de polsos d'electrons obtenim una dispersió d'energia mínima de 0.77 eV, que es correspon al cas de polsos que contenen menys d'un electró de mitja. Calculem que aquesta dispersió energètica correspon a una duració estimada del pols de 416 fs. En el cas de polsos amb aproximadament 1000 electrons, la dispersió augmenta fins a 14.4 eV (6.4 ps) a causa de la repulsió de Coulomb entre electrons dins del mateix pols. Finalment, caracteritzem la resolució espacial del USEM en funció de la quantitat d'electrons emesos. Obtenim una resolució de $\sim 90\,\text{nm}$ i descrivim els paràmetres determinants i les possibles millores que cal portar a terme per arribar al rang de $5-10\,\text{nm}$.

En el Capítol 3 introduïm el primer microscopi de catodoluminescència de BS-CL, en el qual combinem l'excitació d'una mostra amb polsos de llum i els polsos d'electrons ultraràpids descrits en el Capítol 2. En la primera part del capítol considerem els aspectes tècnics i diversos mètodes per analitzar la luminescència de la mostra. Aquestes formes de detecció de llum inclouen mesures espectroscòpiques, de correlació temporal i amb un amplificador lock-in. En la segona part avaluem les diferències entre l'excitació d'un semiconductor amb electrons i amb llum, les quals són essencials en qualsevol experiment de BS-CL. Comparem de forma sistemàtica mesures de CL i fotoluminescència (FL) en mostres de GaAs i GaN mitjançant l'estudi en cada cas de la densitat d'energia dipositada, profunditat d'absorció, espectre, eficiència quàntica i dinàmica dels portadors de càrrega (parells d'electró-forat). Finalment, presentem els primers resultats de mesures de BS-CL en una mostra de $Cu_2ZnSnS_4$. Obtenim que l'emissió de CL augmenta fins a un $\sim 20\,\%$ quan el làser ha excitat prèviament la mostra i que aquest efecte desapareix en una escala de temps de nanosegons. En aquest experiment, emprem l'electró com a sonda per avaluar els canvis en la dinàmica dels portadors de càrrega induïts per l'excitació amb el làser.

Un dels avantatges de la microscòpia de BS-CL és que ens permet emprar l'electró per excitar la mostra i el làser per avaluar els canvis induïts per l'electró. Amb aquesta configuració podem obtenir informació complementària sobre la diferència entre excitació amb llum i amb electrons. En el Capítol 4 explorem aquesta capacitat per demostrar la conversió de l'estat de càrrega de centres nitrogen-vacant (NV) en diamant després de ser excitats amb polsos d'electrons de 5 keV. Els centres NV són fonts de fotons individuals i poden existir en dos estats de càrrega diferents: $NV^0$ i $NV^-$. En particular, els centres en l'estat $NV^-$ són els més estudiats per a aplicacions en tecnologies quàntiques, gràcies al seu llarg temps de

coherència d'espí. Ambdós estats són detectats en mesures de FL, cadascun amb un espectre característic (575 nm per $NV^0$, 637 nm per $NV^-$). Malgrat això, en CL normalment només podem observar l'emissió de l'estat $NV^0$. En aquest capítol emprem el nostre microscopi de BS-CL per demostrar que quan els electrons incideixen sobre els centres NV provoquen la conversió de centres en l'estat $NV^-$ a l'estat $NV^0$. Desenvolupem un model basat en les dades experimentals que té en compte la difusió dels portadors de càrrega (amb un temps característic de 0.8 ns), l'emissió espontània de $NV^0$ ($\sim$ 20 ns) i la conversió de centres en l'estat $NV^0$ un altre cop cap a l'estat $NV^-$ (500 ms). Aquests resultats ofereixen nova informació sobre com els electrons exciten els centres NV en comparació amb l'excitació òptica convencional.

En el Capítol 5 continuem explorant les propietats fonamentals de la interacció dels electrons amb la matèria, aquest cop mitjançant la investigació de correlacions entre fotons de CL. Mesures de la funció d'autocorrelació de segon ordre ($g^{(2)}(\tau)$) de CL demostren que els fotons s'emeten en grups ($g^{(2)}(0) \gg 1$). Aquest agrupament de fotons es dóna perquè l'excitació d'una mostra amb un sol electró d'alta energia pot resultar en l'emissió de més d'un fotó. Fins ara, l'agrupament de fotons en CL s'ha estudiat mitjançant models numèrics (de tipus Monte-Carlo). En aquest capítol desenvolupament un model completament analític per descriure la magnitud d'aquest agrupament de fotons ($g^{(2)}(0)$) en funció de la quantitat de corrent elèctric (o nombre d'electrons per pols), temps de vida de l'emissor de llum, duració del pols d'electrons (en el cas d'un feix d'electrons polsat) i la probabilitat d'excitació per electró ($\gamma$). Aquesta última es defineix com la probabilitat que un electró creï com a mínim una interacció (plasmó de volum) prop l'emissor de llum. Per tant, $\gamma$ ens permet quantificar la interacció d'electrons amb matèria. Avaluem el nostre model amb mesures de $g^{(2)}(\tau)$ de pous quàntics de InGaN/GaN utilitzant un feix d'electrons continu. A més a més, ampliem el model tan teòricament com experimentalment emprant feixos polsats d'electrons generats amb mètodes diferents: la desviació i bloqueig parcial del feix (polsos de ns) o la fotoemissió d'electrons quan s'excita la font d'electrons amb un làser (polsos de ps). Obtenim que l'eficiència d'excitació dels pous quàntics en aquesta mostra en concret és de $\gamma = 0.13$ i 0.05 en el cas d'electrons amb energia de 10 i 8 keV, respectivament. També concloem que la mostra no exhibeix efectes no-lineals tot i ser excitada per polsos d'electrons ultraràpids i densos ($\sim$ 500 electrons per pols).

En conclusió, aquesta tesi dóna nova informació sobre com els electrons interaccionen amb la matèria mitjançant experiments de catodoluminescència d'avantguarda i anàlisis teòriques. Introduïm la microscòpia de catodoluminescència de tipus bomba-sonda com un mètode nou per estudiar l'excitació de materials a escales temporals ultracurtes. Preveiem que la microscòpia de BS-CL es pot explorar més per oferir nova informació sobre processos claus en materials, tals com la dinàmica de parells d'electró-forat i saturació de defectes en semiconductors, tals com materials fotovoltaics, transformacions de fase reversibles, la generació de portadors de càrrega calents i la relaxació tèrmica en nanoestructures. La configuració de tipus bomba-sonda també permet realitzar mesures d'espectroscòpia Ra-

man que permeten estudiar els processos generats per l'electró dins d'un material a una escala temporal de ps. A més, aquesta configuració inspira el desenvolupament de microscòpia electrònica de camp proper induït per fotons (PINEM, per les seves sigles en anglès) dins d'un SEM, que proporciona noves capacitats als SEMs ultraràpids.

# ACKNOWLEDGEMENTS

Doing a PhD is a journey that has shaped me at a professional and personal level. Luckily, I have not been alone in this journey, but I have been surrounded by extraordinary people that have made it possible and have helped me in many different ways. I would like to thank everybody that has supported me during these four years, directly or indirectly.

First of all, I want to thank my supervisor, Albert. I feel very lucky that I could be part of your group. I have learned a lot from you, not only about physics but also about doing research and managing a group with passion and honesty. I am always impressed by your creative and innovative ideas, and your constant drive to reach new levels of understanding of physics and technology development. You also have the ability to motivate me by sharing your constant enthusiasm and good energy, even when experiements don't work as I expected. Thank you for always keeping your door (or Teams window) open to discuss anything, you always have a good piece of advice for any problem. Moreover, you also deeply care about your students, and I appreciate all the support that you have given me over these years. You are a truly inspiring supervisor, and I know that what I've learned from you will shape my career.

I've been lucky to have an also amazing co-supervisor. Sophie, I cannot express in words how grateful I am that you have been part of my PhD. I feel very lucky that I got to spend the first year of my PhD with you so that I could learn about electron microscopes, laser alignment, CL and models. But most importantly, you are a very generous, open-minded and empathetic supervisor and colleague, which set a great example for me to further develop as a researcher. Thank you for always believing in me. I love and admire your true love towards physics and research and your constant energy and good mood. Your passion for electrons is so contagious that I now have a whole thesis devoted to them :D

The Photonic Materials group truly feels like a small family, and I feel that I have learned something from each single member of the group. First of all, I am happy that the pump-probe CL sub-community grew along the years with amazing people that really pushed forward the development of the setup, and made me feel less lonely. Kelly, I am incredibly happy that you joined the group. You brought the setup to a new level, and I know that I can always count on you to have creative solutions to problems and critical feedback for any project. Working with you has been a pleasure, not only I learned a lot, but also I have personally enjoyed it: thank you very much for your sense of humour, your willingness to help and for being my friend. Nika, working with you has been a wonderful discovery. You are such a quick and critical learner and working with you has always been very fun and easy, even during the most stressful moments of my PhD. Thank you also for being such a

cheerful and empathetic colleague, I love having you around. Marnix, thank you for being such an independent and nice Master student. I really learned about carrier dynamics from you, and despite the complexity of the project you obtained beautiful and systematic comparison of PL/CL dynamics, as well as new insights, which have become part of this thesis. I know that you have a very successful research path ahead.

Outside of the little Quanta lab, many other group members have contributed to my PhD. Verena, you were one of the reasons why I wanted to stay at AMOLF, and you have been a pilar for me during all these years. Thank you for being such a good friend, for always understanding me and cheering me up. I admire your kindness, sharpness and your drive to make the world a better place: you definitely made the office a happier place for me! Matthias, thank you so much for all the help that you have always given me, especially for helping me with the energy spread measurements, which have become one of the most satisfying datasets of the thesis. I really enjoyed being your officemate and making fun of your food particularities! Nick, thank you for always being available to discuss anything, your passion for physics and eagerness to learn new things has been inspiring. Thank you also for caring about all of us and making sure that we had enough social life, I truly enjoyed our discussions about society and Dutch/Spanish/French cultures :) Toon, thank you for always being available to help me, I feel privileged to have such an experience CL user that I can count on. Tom, we started our journey together (almost) and I have really enjoyed seeing how you have become such a great researcher. I admire your organization skills, your capacity to formulate good questions and your eagerness to help: thank you for taking care that the group doesn't fall apart (or ends up without Lumerical licenses, which might be the same :P). Andrea, you bring so much energy and fun to the group! I am amazed that you can be such a great cook and host, making sure that we keep our social group-life active, while also doing an amazing and complex PhD: eres la leche ;) Stefan, it is great to have you in the group even if you're far away: I have always enjoyed talking to you and I love your attitude towards your research. Heleen, thanks for bringing such a positive energy to the group! Joris, I admire your sharpness and ability to make everybody feel understood and comfortable. You were an awesome officemate and half-roomate! I also want to thank the rest of the group, present and past members, for building such a strong and warm community: Evelijn, Daphne, Floris, Kyra, Cyrian, Benjamin B. and Mark K. Floortje: thank you very much for all your help (most of it 'in the shadow'). I am sure that the group would collapse without you!

A big part of my PhD has been devoted to building a setup, which I could have not been done without the amazing technical support that I have had. Dion, thank you for always being ready to help, the pump-probe setup would not be the same without you. Thanks for your creativity in finding new solutions and for listening to my ideas on how to improve the setup, and then building something a hundred times better. Hans Z., I feel very lucky that we have someone so experienced that dares to even lift a completely new microscope. Thank you for all your constant help and for always keeping a good dose of sense of humour in the lab. Erik Kieft,

thank you for always being available to answer nicely all of my questions and teaching me about electron optics. Igor, thank you for saving the Quanta from a shutdown and for taking care of it. I also want to thank the people from Delmic who have helped me with the developments and trouble-shooting of the setup: Éric Piel, Anders Muskens and Rallou Mygiaki.

Being at AMOLF is an inspiring experience: it is full of talented people with common features, such as enthusiasm and creativity, and at the same time very different interests, backgrounds and personalities. I want to thank everybody that contributes to building this sense of community at AMOLF. Kevin, thank you for being an awesome roomate, introducing me to Star Wars (with Sophie) and allowing me to be every time a bit meaner to you :P Nasim, it is always a pleasure being around you. Thank you for always bringing your bit of happiness, empathy and open mind. I also want to thank many other people with whom I have shared nice coffee and tea breaks (when they were a social event) or have simply make my time at AMOLF more pleasant: Robin, Sarah G., Alexander (thanks for being the best catsitter!), Lucie, Sangeetha, Julia, Isabelle, Mareike, Galja, Ruslan, Jenny, Parisa, Ilan and many more that I am probably forgetting. I also want to thank the group leaders of the nanophotonics department from creating a critical but still pleasant and familiar community: Femius, Esther, Erik, Said, Bruno and Ewold. And I want to extend my acknowledgement to all of the support people at AMOLF: ICT, electronics department, workshop, finance, reception, library, secretaries and more: you make working at AMOLF so easy.

Doing a PhD can be very absorbing and it can be difficult to disconnect from it, especially during the low times, but I have been extremely lucky to have a supporting and warm second family at home. Jans, I feel so lucky that I met you at the beginning of my adventure in Amsterdam. You are an amazing friend and roomate. Thank you for cheering me up with your lively attitude and for always taking care of me, either by making amazing birthday cakes (with Ferran) or by making sure that I was (almost) never skipping a meal, especially while writing my thesis :P Ferran, gràcies per portar una mica més de l'essència mediterrània a casa. Gràcies pels teus genials risottos, pero escoltar les meves queixes sobre el PhD i per fer que el pis es senti més com casa. Només em queda poder-te guanyar a algun joc de taula. Alona, I am very happy that I got the chance to know you more. I loved our conversations at home, and I admire your creativity, your energy and your strong commitment to sustainability. And finally, I want to thank Alpha, who will never read this but brings me so much joy and is the best (non-human) quarantine companion.

I also want to thank other people that have stayed with me during these years, either in Amsterdam or further away. Noor, thank you for being my first friend in Amsterdam. Álvaro, Maria y Ferran: gracias por no desistir en vuestro intento de ser amigos de un ser diminuto. Hacer skypes con vosotros me hace sentir como si no hubiesen pasado los años y hace que se me olvide cualquier preocupación. Anna, recordo sempre les nostres converses, tot i que esporàdiques, que em van ajudar molt a mantenir els peus a terra i sentir-me una mica més com a casa, especialment

a l'inici del doctorat. Joan i Alfredo, espero que quedin molts més Eurovisions per veure o anar junts! Maya, som una mica desastres per veure'ns tot i estar tan a prop, però m'encanta tenir una amiga de fa tant de temps tan a prop :) I also want to thank every single person that participated in the Vinyasa TT: thank you for creating such a supportive and open-minded community, and for bringing me out of my little physics bubble.

This thesis would not have been possible without the continuous support of my family. Mamà, papà: gràcies per motivar-me sempre a fer el que m'agrada, tot i que impliqués anar-me'n cada vegada una mica més enfora de vosaltres. Gràcies per sa vostra paciència i suport i per recordar-me cada vegada que torn a casa el que és realment important. Antònia Maria, gràcies per ser sa millor germana que puc demanar tot i que me passi temps sense contestar :P And finally, I want to thank Noel, who has probably had the most diverse number of roles in my PhD, ranging from partner to optics consultant. Eres mi base, quien me apoya incondicionalmente y me recuerda constamente lo que me hace feliz. Gracias por hacer del sentido del humor nuestra mejor arma, por sacar la mejor versión de mi misma, por tu optimismo y generosidad, por tu escepticismo y simplemente por compartir tu vida conmigo.

# ABOUT THE AUTHOR

M. Magdalena (Magda) Solà Garcia was born on April 11th 1992 in Binissalem (Mallorca, Spain), where she grew up and obtained her high school diploma from IES Binissalem. In 2010 she moved to Barcelona to study Engineering Physics at the Polytechnic University of Catalonia, where she graduated with a Bachelor thesis about fabrication of Si microspheres at high temperatures, supervised by dr. Moisés Garín and prof. dr. Ramon Alcubilla. She continued her studies at the Universtiy of Amsterdam with a Master's degree in Advanced Matter and Energy Physics. In 2017 she graduated with a thesis about light-trapping in thin film solar cells, under the supervision of prof. dr. Albert Polman, developed at AMOLF, in Amsterdam. After graduation, she stayed at AMOLF as a PhD student working on the study of electron-matter interaction through cathodoluminescence. The results of her research are shown in this thesis.

In her free time, Magda enjoys practicing Vinyasa yoga, playing board games, discovering new cities, listening to podcasts, swimming in the sea and hiking.